Rocking Connection between a Precast Bridge Column and Cap Beam

Bryan Kennedy

A thesis
submitted in partial fulfillment of the
requirements for the degree of

Master of Science in Civil Engineering

University of Washington

2015

Committee:

John F. Stanton

Marc O. Eberhard

Donald J. Janssen

Program authorized to offer degree:
Department of Civil and Environmental Engineering

University of Washington

Abstract

Rocking Connection between a Precast Bridge Column and Cap Beam

Bryan Kennedy

Chair of the Supervisory Committee:
Professor John F. Stanton
Department of Civil and Environmental Engineering

Traditional cast-in-place, concrete bridge construction is often a lengthy undertaking, which is burdensome to the motoring public because of the traffic delays that it causes. Precast construction can accelerate the process by moving fabrication offsite, and then rapidly erecting and connecting bridge components onsite. However, designing connections that are both easy to complete and are robust under seismic loading is challenging.

This thesis describes a connection that is intended to meet those criteria, and builds on previous work to do so. Experimental, precast, pre-tensioned specimens developed by Davis et al. (2012) showed good seismic performance, but had significant damage at low drift levels. Adding experimental, ductile materials resulted in less structural damage (Finnsson, 2013), but required unconventional construction materials and awkward fabrication.

A new precast, pre-tensioned, column-to-cap beam connection has been developed. The design utilizes (1) unbonded prestressing strands to help the column re-center, (2) bonded reinforcing bars to dissipate energy, (3) a baseplate to permit rigid-body, rocking behavior of the column, and (4) a steel tube to confine the column concrete at the rocking interface. The strands are pre-tensioned when the column is cast, so the connection can be completed without any onsite stressing operations.

The connection's seismic performance was evaluated with pseudo-static, cyclic testing of one subassembly. The test results showed that the specimen was stiff at low loads, re-centered well, dissipated energy, and was ductile and durable. Damage to the concrete was negligible and the peak moment strength was measured at drifts exceeding 10%. The system offers a method for achieving accelerated bridge construction that also provides excellent seismic performance and uses only conventional construction materials.

Acknowledgements

This work was supported by the State of California through the Transportation Systems Research Program of the Pacific Earthquake Engineering Research Center (PEER). The National Science Foundation also provided funding (grant number CMM 1207903) through the George Brown National Earthquake Engineering Simulations program (NEES). Any opinions, findings, conclusions, or recommendations expressed in this material are those of the author and do not necessarily reflect those of the funding agencies.

Foremost, I would like to express my sincere gratitude to Professors John Stanton and Marc Eberhard for giving me the opportunity to work on this project. My research experience would not have been possible without their continual patience, guidance, enthusiasm, and support. I would also like to thank Professor Donald Janssen for serving on my committee, reviewing my thesis, providing many insightful comments, and lending his expertise during the consideration, design, and testing of construction materials.

I also received an immeasurable amount of help from my colleagues at the University of Washington. In particular, I would like to thank Chase Young, who kept the construction trenches lively, entertaining, and light-hearted. David Lam and Matt Brosman made outstanding contributions to this project, through their PEER internships. Furthermore, life was made indescribably easier with Spencer Livermore's materials testing, Travis Thonstad's instrumentation guidance, Olafur Haraldsson's fabrication advice, Max Stephens's tutorials on Abaqus FEA, and Hung Viet Tran's assistance with camera setup and construction equipment. I thank all of them whole-heartedly.

Finally, a fellowship from the Valle Scholarship and Scandinavian Exchange Program at the University of Washington partially funded my time as a research assistant.

Contents

List of Figures

List of Tables

List of Variables

A_{accel}	-design acceleration coefficient
$A_{box(i)}$	-area of the box that encloses the force-displacement response during the i^{th} cycle
$A_{cracked}$	-cracked area of column cross-section, as defined by Priestley et al., (1994)
A_g	-gross area of column cross-section
$A_{loop(i)}$	-area enclosed by the force-displacement response during the i^{th} cycle
A_p	-area of prestressing steel
A_{plate}	-area of the 20 in. diameter circular, steel baseplate
A_s	-area of bonded, longitudinal, reinforcing steel
A_t	-transformed area of column cross-section
A_v	-area of shear reinforcement
a	-position vector between pairs of Optotrak LED targets, established at the start of the test
$B_{damping}$	-design constant related to the damping coefficient
b	-position vector between pairs of Optotrak LED targets, during an applied column displacement
c	-neutral axis location; measured from the midsection of the rocking joint
c_{fit}	-the approximated neutral axis location, determined by functions that were fitted to the experimental envelope
D	-column diameter
D’	-center-to-center diameter of spiral
d	-section depth of column; measured from compression face of column to furthest tension rebar
d_b	-diameter of reinforcing bar
d_{comp}	-the depth of the compressive bearing reaction

d_{deck} -displacement of bridge deck

d_i -distance from midsection of column to i^{th} prestressing strand, longitudinal reinforcing bar, or discretized grout pad slice

$d_{pad,i}$ -distance between the i^{th} slice of the discretized grout pad and the joint midsection

d_{result} -the distance between the compressive resultant of the bearing reaction and the midsection of the joint

$drift_{out}$ -the outputted drift from the moment-rotation model

E_c -modulus of elasticity for concrete or grout

E_cI_g -gross bending stiffness of column

$(E_cI_{g,eff})_{calc}$ -effective bending stiffness for reinforced concrete beam column, as predicted by Elwood and Eberhard (2009)

$(E_cI_{eff,eqv})_{meas}$ -effective, measured bending stiffness of specimen, relative to a continuous medium

E_p -modulus of elasticity for prestressing strand

E_s -modulus of elasticity for steel

E_{sec} -secant modulus of elasticity in Mander's model for confined concrete

E_{true} -the true modulus of elasticity for a material; required by Abaqus CAE material input

e_{pot} -the horizontal distance between a tube potentiometer and the rocking neutral axis of the joint

F_{bond} -bond force between concrete and prestressing strands at the top of the column

F_{eff} -effective lateral force at top of column

$F_{eff,\ decomp}$ -effective force causing joint decompression

$F_{eff,y}$ -effective force causing first yield of longitudinal reinforcement

$F_{friction}$ -estimated frictional force resulting from the contact between the top of the column and the loading plate of the Baldwin Universal Testing Machine

$F_{friction,max}$ -peak frictional force in the Brown (2008) model, resulting from the contact between the top of the column and the loading plate of the Baldwin Universal Testing Machine

F_i -the axial force of the i^{th} element on the joint cross-section

F_{LC} -force reading from the strand load cells at the top of the column

F_{max} -the maximum effective force observed during the test

F_{min} -the minimum effective force observed during the test

F_{strand} -prestressing strand tensile force

f_c -concrete or grout compressive strength

f'_{cc} -the peak, confined, compressive strength for concrete in Mander's model for confined concrete

f_{ct} -concrete splitting tension strength

$f_{M\text{-}P}(x)$ -output of Menegotto-Pinto function for strand constitutive model, with "x" as input

f_p -strand stress as function of strand strain, ε_p

f_{pe} -design effective prestressing stress

$f_{p(i)}$ -strand stress for the i^{th} data point in strain record

f_{py} -yield stress of prestressing strand

f_r -concrete modulus of rupture

$f_{t,joint}$ -tensile strength between grout pad and steel baseplate (assumed to be zero)

f_u -ultimate strength of reinforcing steel

f_y -yield stress of reinforcing steel

f_{yt} -yield stress of transverse reinforcement

$f_{y,tube}$ -yield stress of steel tube

H -applied lateral load from 220-kip MTS actuator

h_1 -distance from rocking interface to centroid of applied lateral load (59.813 in.)

h_2 -distance from rocking interface to point of application of vertical load (96.5 in.)

$h_{i+1} - h_i$ -vertical distance between a pair of successive string potentiometers

I_g -gross moment of inertia for column

I_{strand} -moment of inertia for single prestressing strand

I_t -transformed moment of inertia for column

i -index for i^{th} data point in strand strain record

K -Menegotto-Pinto parameter in constitutive model for prestressing strand

k -effective length factor for Euler buckling load

$k_{ductility}$ -displacement ductility parameter for member

$k_{eff,mod,y}$ -the column effective stiffness at first yield of longitudinal rebar, but from a modified calculation that used the preceding cross-over displacement

$k_{eff,y}$ -the effective stiffness of the column, measured at first yield of longitudinal rebar

$k'_{eff,y}$ -the predicted effective stiffness of the column, implied by the Elwood and Eberhard (2009) predictive model for stiffness degradation

$k_{friction}$ -frictional spring stiffness in Brown (2008) model

$k_{pre\text{-}decomp}$ -the experimentally determined, primary stiffness of the system

$k_{post\text{-}decomp}$ -the experimentally determined, secondary stiffness of the system

$k_{uncracked}$ -the theoretical, uncracked stiffness of the column

$l_{No.4}$ -unbonded length of longitudinal, No. 4, column reinforcement

l_{strand} -unbonded length of prestressing strands

M - moment applied to column-to-cap beam interface

M_{cr} -cracking moment of 20 in. wide, octagonal cross-section

M_{decomp} -joint decompression moment of the rocking connection

M_i -the contribution of the i^{th} element to the cross-sectional moment

$M_{re\text{-}center}$ -moment created by re-centering forces on column (vertical load and prestressing force)

$M_{resisting}$ -moment from cross-sectional forces resisting the column's re-centering (i.e., from the bonded reinforcing steel)

M_{out} -the outputted moment from the moment-rotation model

m -calculated model parameter for the full response for rebar steel

N -Menegotto-Pinto parameter in constitutive model for prestressing strand

n -modal factor for Euler critical buckling load

P_{col} -applied vertical load from Baldwin Universal Testing Machine

P_{crit} -Euler critical buckling load

P_{pt} -total prestressing force in column

P_s -total yield force of all bonded, longitudinal reinforcing bars

P_{total} -total axial load on column: applied vertical load from Baldwin Universal Testing Machine and total force from internal prestressing strands

Q -Menegotto-Pinto parameter in constitutive model for prestressing strand

R -radius of a greased, spherical bearing fixture placed between the top of the column and the Baldwin Universal Testing Machine

r -calculated model parameter for the full response for rebar steel

r_{Mander} -calculated parameter in Mander's model for confined concrete

r_{plate} -radius of the annular, steel baseplate

S_{plate} -section modulus of the circular, steel, baseplate

S_{site} -design site coefficient

s -spacing of shear reinforcement

T_{eff} -period of a seismically isolated structure

V_c -concrete contribution to shear capacity of member

V_n -nominal shear capacity of member

V_p -axial load contribution to shear capacity of member

V_s -reinforcement contribution to shear capacity of member

w_c -unit weight of concrete or grout

$w_{pad,i}$ -the out-of-plane width of the discretized grout pad slice *i*

x -calculated parameter in Mander's model for confined concrete

αD -distance between center of column cross-section and the center of the compression block

γ_p -principal shear strain of steel tube

γ_{xy} -shear strain of steel tube in x-y plane

Δ_1 -measured displacement at the centroid of applied lateral load

Δ_2 -the horizontal displacement at the application point of the vertical load (not measured)

Δ_{bar} -elongation of No. 4 rebar due to opening of rocking connection

$\Delta_{bending}$ -the contribution from bending deformation to the horizontal displacement of the top of the column

$\Delta_{calc,bb}$ -predicted column displacement at the onset of bar buckling

$\Delta_{calc,bf}$ -predicted column displacement at the onset of bar fracture

$\Delta_{calc,sp}$ -predicted column displacement for onset of concrete spalling

$\Delta_{cross,1}$ -displacement at which zero force reading is measured during the (positive) peak-to-zero phase of a particular cycle

$\Delta_{cross,2}$ -displacement at which zero force reading is measured during the (negative) valley-to-zero phase of a particular cycle

Δ_{decomp} -measured column deformation when the effective force causing joint decompression is applied

Δ_{joint} -the joint rotation's contribution to the horizontal displacement of the top of the column

Δ_i -elongation of i^{th} prestressing strand or longitudinal rebar

$\Delta_{i+1} - \Delta_i$ -difference in displacement readings between a pair of successive string potentiometers

Δ_{max} -maximum (peak) applied displacement of the test

$\Delta_{max(i)}$ -maximum (peak) applied displacement of the i^{th} cycle

Δ_{min} -minimum (valley) applied displacement of the test

$\Delta_{min(i)}$ -minimum (valley) applied displacement of the i^{th} cycle

$\Delta_{peak,1}$ -the first absolute maximum (peak) displacement during a cycle, equivalent to $\Delta_{max(i)}$

$\Delta_{peak,2}$ -the second absolute maximum (valley) displacement during a cycle, equivalent to $\Delta_{min(i)}$

$\Delta_{pot,correct}$ -corrected reading for tube potentiometer, due to the instrument's rotation

$\Delta_{pot,E/W}$ -average of the corrected readings from the vertical potentiometers placed on the east and west sides of the steel tube

$\Delta_{pot,measure}$ -raw reading of tube potentiometer that included a contribution from the instrument's rotation

$\Delta_{pot,N}$ -corrected reading from north, vertical potentiometer placed on the steel tube

$\Delta_{y,bar}$ -yield elongation of No. 4 for its 12 in. unbonded length

$\Delta_{y,cross}$ -the cross-over displacement preceding the first applied yield drift

$\Delta_{y,top}$ -top displacement of column (measured at h_1) at first yield

ε_0 -strain measured by the horizontal gauge of the strain-gauge rosette

ε_{45} -strain measured by the inclined gauge of the strain-gauge rosette

ε_{90} -strain measured by the vertical gauge of the strain-gauge rosette

ε_c -strain of concrete or grout

ε_{cc} -strain corresponding to peak strength in Mander's model for confined concrete

ε_{cu} -crushing strain of concrete or grout

ε_i -strand strain measurement for i^{th} data point of record

$\varepsilon_{max,i}$ -previous maximum strand strain measurement, up to i^{th} data point of record

ε_{nom} -nominal (engineering) strain

ε_p -strand strain, measured by pairs of strain gauges

ε_{p1} -first principal strain of steel tube

ε_{p2} -second principal strain of steel tube

ε_{p3} -third principal strain of steel tube

$\varepsilon_{plastic,true}$ -true plastic strain; required by Abaqus CAE material input

ε_{py} -strand yield strain

ε_r -rupture strain for longitudinal reinforcing steel

ε_{SH} -steel strain hardening strain

ε_s -strain of longitudinal reinforcing steel

ε_{true} -true strain; required by Abaqus CAE material input

ε_u -steel strain at ultimate stress

ε_y -yield strain for longitudinal, No. 4, column rebar

ε_z -out of plane strain of steel tube

$\zeta_{(i)}$ -equivalent viscous damping for i^{th} cycle

η -the resultant factor; the ratio of the distance between the compressive resultant and neutral axis and the depth of the compression zone. Similar to the k_2 factor described in other texts (e.g., Wight and MacGregor).

$\theta_{baseplate}$ -the rotation angle of the baseplate during the experiment

$\theta_{i,string}$ -average column rotation between a pair of successive string potentiometers

θ_j -joint rotation angle of rocking interface

θ_{opto} -column rotation calculated from displacements recorded by the Optotrak motion capture system

θ_p -principal angle of strain state for steel tube

λ_{re} -column re-centering ratio

μ_{curved} -frictional coefficient to account for the rotational friction within a spherical bearing plate placed between the top of the column and the Baldwin Universal Testing Machine

μ_{eff}	-effective frictional coefficient for the contact between the top of the column and the loading plate of the Baldwin Universal Testing Machine
μ_{flat}	-frictional coefficient to account for the translational friction between the top of the column and the loading plate of the Baldwin Universal Testing Machine
ν	-Poisson's ratio
π	-pi; 3.14159 …
ρ_{eff}	-effective transverse reinforcing ratio for column
ρ_s	-volumetric spiral reinforcing ratio
σ_{nom}	-nominal (engineering) stress
σ_{p1}	-first principal stress of steel tube
σ_{p2}	-second principal stress of steel tube
σ_{true}	-true stress; required by Abaqus CAE material input
σ_x	-hoop stress of steel tube
σ_y	-longitudinal stress of steel tube
τ_{max}	-maximum shear stress of steel tube
ψ_t	-development length factor for top-cast bars, as described by *ACI 318-11*

1 Introduction

Traditional cast-in-place, concrete bridge construction often requires a lengthy onsite operation, which can severely impede the motoring public. Precast concrete construction offers a solution by moving the fabrication of the bridge's components offsite, and then rapidly erecting and connecting them onsite. Precast and prefabricated superstructure components (such as girders) have been successfully used for over 50 years. However, the engineering community has been hesitant to use precast substructure elements (foundations, columns, and cap beams) in seismically active regions because earthquake loading creates moment and inelastic deformation demands that are highest at the locations of the connections.

Previous researchers have demonstrated that precast, non-prestressed systems can be designed to perform during earthquakes as well as conventional cast-in-place systems. For example, Pang et al. (2008) developed a precast concrete column-to-cap beam connection, while Haraldsson et al. (2011b) developed a precast concrete column-to-footing connection. Both designs were successfully implemented together in the field, and they were found to be constructible and to accelerate the construction (Khaleghi et al., 2012). However, they contained no prestressing and were not designed to re-center after an earthquake, so they represented a precast implementation of conventional cast-in-place designs.

Other connections between precast concrete bridge beams and columns have been developed. For example Matsumoto et al. (2009) designed a connection in which bars projecting from the top of the column were fitted into an opening in the cap beam that was only slightly smaller than the column, and which was then filled with concrete. While the system proved to be readily constructible, the cap beam was weakened by the large opening in it and led to significant shear cracking there.

To provide a higher level of seismic performance, Davis et al. (2012) then further developed the two precast designs by introducing prestressing to re-center the columns after an earthquake. They designed and tested two precast, prestressed bridge columns. These had the desired re-centering properties, but they also displayed significant column spalling and bar buckling at lower drift ratios relative to comparable non-prestressed, reinforced concrete.

To reduce the damage, Finnsson (2013) then tested two designs that used high-performance materials. These columns (PreT-SF-HyFRC and PreT-SF-SS-HyFRC) used stainless steel and Hybrid Fiber-Reinforced Concrete (HyFRC, a steel and plastic fiber-reinforced concrete developed by Kumar et al., 2011). These materials have more ductile behavior, and were intended to improve the column's resistance to cyclic loading. The resulting specimens provided more durable and ductile response than Davis's, but their designs required unconventional and uncommon materials, and relatively cumbersome fabrication operations.

Others have also pursued the goal of having the columns re-center, but have used post-tensioning. For example, Restrepo et al. (2011) developed and tested a "dual shell" column system. In it, the column was made from two concentric steel tubes, with the annular space between them filled with concrete. That prefabricated column was then erected on site, and was secured with a post-tensioned bar tendon down the middle. The system was intended to undergo rigid body rocking, like Davis's columns. It exhibited that behavior, but early deterioration of the grout pad between the column and foundation led to premature system failure.

Additionally, Billington and Yoon (2004) developed a post-tensioned column system that was assembled from segmental, reinforced concrete blocks. The top and bottom blocks of their columns (in the plastic hinging regions) were cast with a ductile, fiber-reinforced concrete. Finnsson's precast, pre-tensioned, HyFRC columns were very similar to Billington's conceptual design. However, the lack of bonded steel between the precast column segments limited the system's energy dissipation at low drifts. Furthermore, post-tensioning adds a site operation, which would likely slow and complicate its construction.

Finally, Hewes and Priestley (2002) also developed a segmental, unbonded, post-tensioned, column system that had a steel confining jacket for the base element. Those systems were very ductile (minor strength drops after 5% drift), and re-centered well. However, one of their columns had unanticipated, significant spalling above the steel jacket, and had some concrete spalling below. Additionally, the jacketed columns did not have bonded reinforcing crossing the joints between segments, and therefore provided very low energy dissipation.

This thesis documents and discusses the design, testing, and performance of a new, precast, bridge column-to-cap-beam connection. The system was developed from the previously described work to provide a viable solution for accelerated bridge construction in seismically active regions. The specific design goals and strategies for the system were to:

- accelerate bridge construction by incorporating whole, non-segmental, precast columns and beams,
- limit residual displacements after the removal of lateral loads by using unbonded prestressing tendons,
- limit structural damage from seismic loading by using a steel tube confining detail,
- dissipate energy by using bonded mild steel reinforcement,
- maintain structural strength at large deformations, and
- limit costs and improve constructability by using only conventional construction materials.

A prototype bridge bent system developed following these strategies is schematically depicted in Figure 1.1.

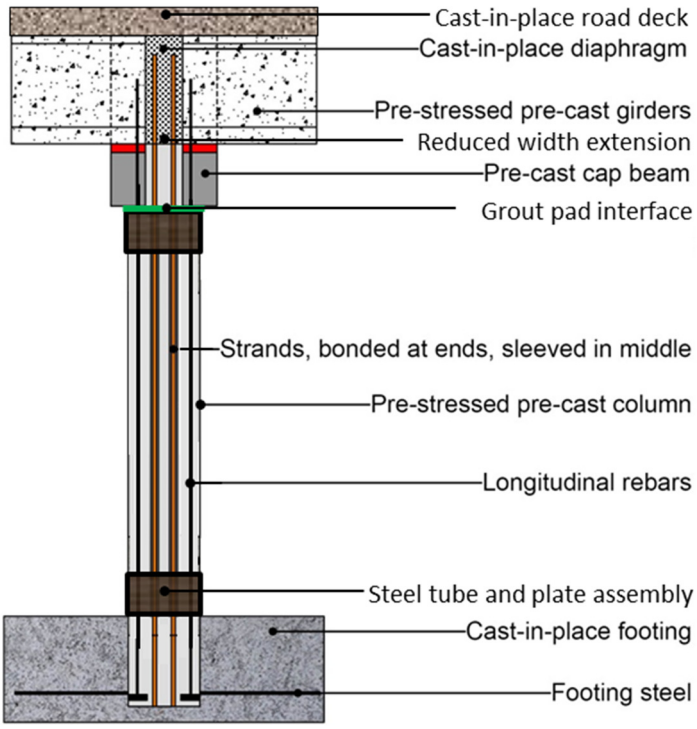

Figure 1.1 Schematic for rocking column, prototype bridge bent (adapted from Finnsson, 2013).

1.1 PRECASTING FOR ACCELERATED BRIDGE CONSTRUCTION

Bridge substructure elements (e.g., foundations, columns, cap beams) are most often built using cast-in-place concrete construction. While it is the most economical for difficult or irregular site conditions, it can be time consuming. Construction duration is often a significant contributor to the direct cost of a project. Furthermore, construction of transportation infrastructure almost inevitably affects and delays the adjacent motoring public, especially in dense, urbanized regions that already suffer from traffic congestion.

Using precast structural elements offers several advantages over traditional cast-in-place construction. Onsite construction time can be reduced by moving fabrication to an offsite facility. This reduction in onsite time can mitigate the total required time for construction and the inconvenience to the public. Furthermore, building in a controlled, centralized facility can improve quality of construction. Finally, moving construction to an offsite facility reduces the required onsite staging area for the project, which is environmentally beneficial.

Precast bridge girders have been successfully implemented in all regions of the United States, and precast bridge substructures have been used in regions of low seismicity. In contrast, use of precast substructure systems in seismically active areas has been avoided because the most common and convenient places to join precast components are the column-to-cap beam and column-to-footing interfaces; but these connection points experience the greatest moment and inelastic deformation demands during earthquake events.

1.2 NAMING CONVENTION FOR EXPERIMENTAL SPECIMENS

The work described in this thesis builds on a long line of accelerated bridge construction research at the University of Washington. The specimens identified here were all precast substructure subassemblies tested at the University of Washington. Test results have significantly influenced the design, testing, and analysis of subsequent systems. For clarity, a naming convention for relevant tests is presented in Table 1.1.

Table 1.1 Naming convention for related tests.

Reference	Specimen Designation		
	Type of Construction	Connection	Detail
Haraldsson et al. (2011b)	PCC	SF	THK1
	PCC	SF	THK2
Davis et al. (2012)	PreT	CB	CONC
	PreT	SF	CONC
Finnsson (2013)	PreT	SF	HyFRC
	PreT	SF	SS-HyFRC
Schaefer et al. (2014a)	PreT	SF	ROCK
	PreT	SF	ROCK-HyFRC
Kennedy (2014) - this thesis	PreT	CB	ROCK

In Table 1.1, the naming codes are defined as:

- PCC - Precast concrete column.
- PreT - Precast, pre-tensioned column.
- SF - Spread footing connection.
- CB - Cap beam connection.
- THK1/THK2 - Footing thickness one/two.
- CONC - Conventional concrete, only.
- HyFRC - Hybrid Fiber-Reinforced Concrete.
- SS - Stainless steel longitudinal reinforcement.
- ROCK - Rocking detail at column base.

According to this convention, the column-to-cap beam specimen tested by Davis is referred to as "PreT-CB-CONC", whereas the specimen documented in this thesis is "PreT-CB-ROCK". This convention was first proposed for this thesis, and previous work may have referenced other tests differently.

1.3 ROCKING DETAIL

The column detailed in this thesis had a steel tube and baseplate at its interface with the cap beam (the top "plastic hinge" region of the column, see the system schematic in Figure 1.1). The steel tube was added to confine the concrete and reduce damage. The baseplate was designed to allow the connection to deform in a "rocking" behavior. This rocking detail was intended to concentrate the deformation of the system at the connection interface (as opposed to distributing the deformation along the length of the column) and limit the overall damage of the system during cyclic loading.

Furthermore, the column's otherwise bonded longitudinal reinforcement was intentionally debonded at the rocking connection with the cap beam. This was done because, as the rocking gap opened during horizontal loading, a concentrated rotation was anticipated at the interface. Such concentrated deformations would have produced infinite axial strains in the bars, initiating fracture at the instant of joint decompression. Granted, this would only have been true for perfectly bonded rebars, but the general mechanism still applied to the behavior of the conceptual design.

1.4 PRESTRESSING TO LIMIT RESIDUAL DISPLACEMENTS

Prestressing can be used to reduce residual displacements after seismic events, and various manifestations of it have been investigated. Such residual displacements, if large, could compromise a bridge's structural stability, or at least, its function. Mitigating residual displacements could ensure a bridge's safe operation for the emergency response immediately after an earthquake, and reduce the repair costs following the earthquake. Pre-tensioning (as opposed to post-tensioning) was selected for this system for several reasons:

- post-tensioning is an in situ operation, which lengthens the duration of on-site construction operations,
- post-tensioning is typically done by a specialty subcontractor, which can be costly and requires smooth interaction with an additional party,
- precasters typically have pre-tensioning capabilities, and can conduct the prestressing under conditions of good quality control,
- pre-tensioning prevents overlapping work conflicts among contractors (post-tensioning is often subcontracted to a specialist outfit),
- post-tensioning the strands would require external anchorages, which can be susceptible to corrosion, and
- pre-tensioning the column results in a more structurally robust element for any unintentional loading during transportation and column erection.

Davis et al. (2012) incorporated unbonded, pre-tensioned strands into a precast bridge column. According to the concept, the strands are intentionally unbonded in the central region so that strand elongations are uniformly distributed along that unbonded length. Therefore, the strands can be designed to remain elastic up to a target drift level. Such a configuration will tend to provide a restoring force (from the strands) for the system following the removal of transverse loads (Stanton et al., 1997).

Figure 1.2 shows the theoretical, cyclic, hysteretic responses for several reinforced concrete systems. During cyclic loading, typical reinforced concrete structures (shown in Figure 1.2a) reach a yield loading, undergo inelastic deformation, and return to a non-zero displacement upon the removal of load. A prestressed-only system (shown in Figure 1.2b), designed to remain elastic through the use of unbonded strands, will tend to exhibit an initial stiffness followed by a secondary, post-decompression stiffness. While such a structure remains elastic and regains the system's original stiffness after loading (Priestley et al., 1993), energy is not dissipated (a key performance criterion of modern earthquake engineering). Therefore, conventional bonded steel reinforcing can be added to an unbonded, prestressed element to create a "hybrid" system (shown in Figure 1.2c). For the hybrid system, energy is dissipated in the flag-shaped loops (due to cyclic yielding of the rebar), but the system returns to its original orientation upon unloading (due to the elastic restoring force in the unbonded strands).

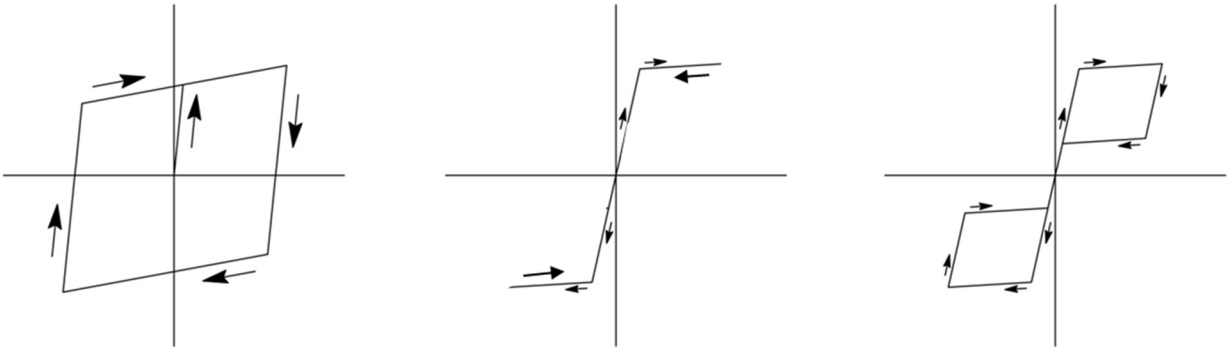

Figure 1.2 The cyclic, force-deformation responses of conventional reinforced concrete (a – on left), unbonded prestressed (b - center), and hybrid systems (c – on right), (adapted from Stanton et al., 1997).

Re-centering design has been used successfully for test specimens at the University of Washington. Davis's specimens exhibited good re-centering but the strength deteriorated due to damage to the concrete, as shown in Figure 1.3. The PreT-SF-ROCK specimen had improved re-centering and better ductility (Schaefer et al., 2014a) because the addition of a steel confining tube (in the column's plastic hinge region) virtually eliminated damage to the concrete. The response of the rocking column is shown in Figure 1.4.

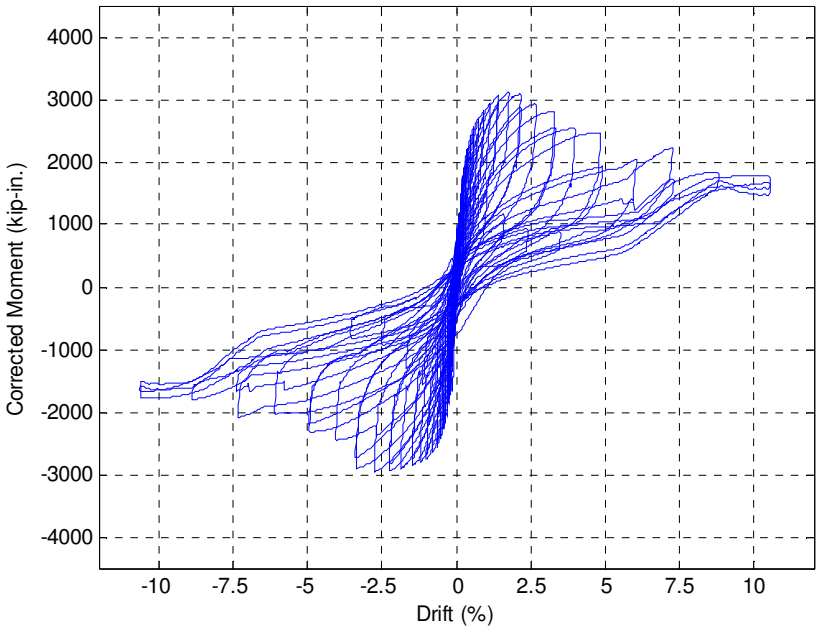

Figure 1.3 Moment drift response of PreT-CB-CONC (Davis et al., 2012).

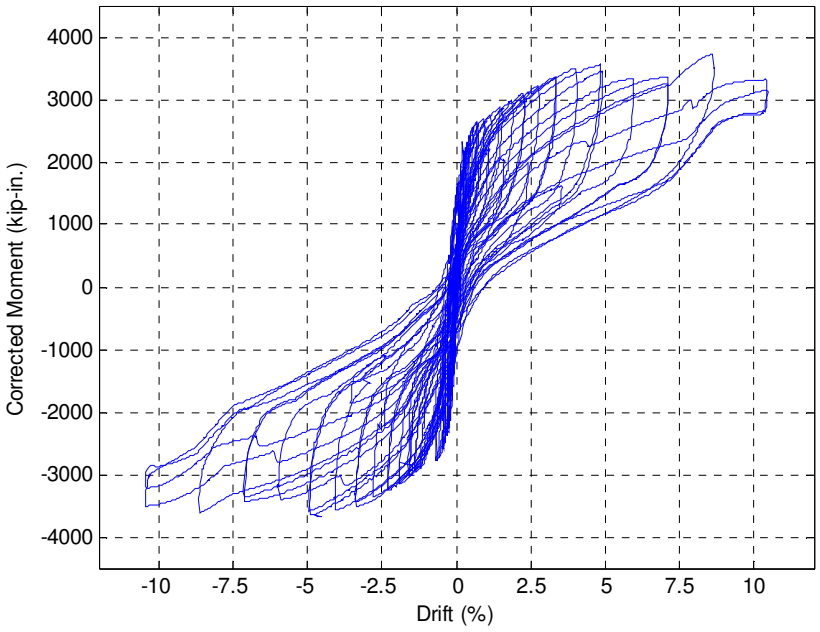

Figure 1.4 Moment drift response of PreT-SF-ROCK (Schaefer et al., 2014a).

1.5 SOCKET CONNECTIONS

1.5.1 Column-to-Footing Connection

Haraldsson et al. (2011b) developed a method for connecting a precast, reinforced concrete column with a cast-in-place, reinforced concrete, spread footing. It is referred to here as a "wet socket", because the concrete surrounding the column is cast in place. For this design, the column is precast and reinforced with straight, longitudinal rebars anchored by heads. No rebar protrudes from the column into the footing. The column is erected in the footing excavation, in which the foundation reinforcement has already been placed, and the footing concrete is then cast around the bottom of the column. The bottom, embedded portion of the column features an intentionally roughened surface in order to help transfer forces from the column to the footing. Figure 1.5 shows the embedded portion of a prestressed, precast column that used this socket connection. Several additional column-to-footing designs followed.

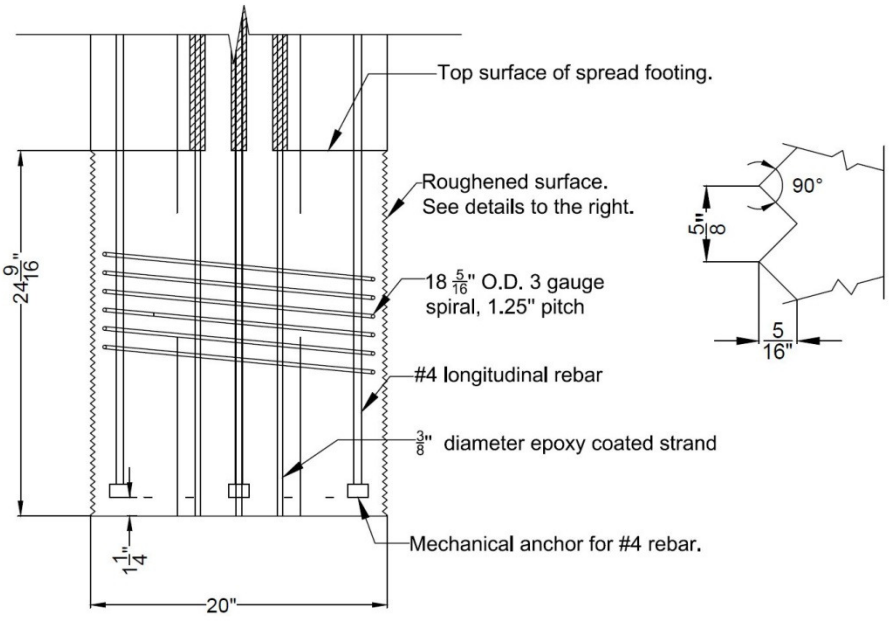

Figure 1.5 Example footing socket connection detail (Finnsson, 2013).

1.5.2 Column-to-Cap Beam Connection

While a wet socket is practical for column-to-footing connections (Khaleghi et al., 2012), use of a comparable wet socket connection at the cap beam would require the cap beam to be cast in place. It has been found (Haraldsson et al, 2011a) that precasting the cap beam represents the largest time savings of any component, so casting it in place would be counter-productive for accelerated bridge construction. Use of a "dry socket" connection, in which the pre-tensioned column is grouted into a full width opening in the cap beam, is impractical because it would require a large opening (wider than the column itself) to be precast in the cap beam. This would force the cap beam to be excessively wide and heavy (unfavorable in precast construction), or could result in

joint shear damage at the connection, such as occurred in Matsumoto's (2009) connection because the opening removed so much of the cap beam section.

Therefore, Davis et al. (2012) developed the detail shown in Figure 1.6. The pre-tensioned strands are bonded at the top and bottom of the column, but not in the middle region. In order to maximize the unbonded length, and to have the column rock at the bottom face of the cap beam, the strands must be bonded within the depth of the cap beam. This was achieved by placing the strands in the middle of the column cross-section, and reducing the column diameter at its top over a length equal to the depth of the cap beam. Deformed reinforcing bars, situated around the outside edge of the column section, were grouted into individual, matching ducts in the cap beam. The design produced a connection in which both unbonded prestressing strands and conventional, bonded, mild steel reinforcement crossed the interface of the components, which is referred to as a "hybrid connection". The opening in the cap beam was small enough not to jeopardize the cap beam's strength, and the shoulder on the column provided a useful surface on which to rest the cap beam during erection so that no column clamps or other temporary supports were needed. Figure 1.6 shows a schematic and photograph of the top end of the Davis column, and the assembly of his column-to-cap beam connection.

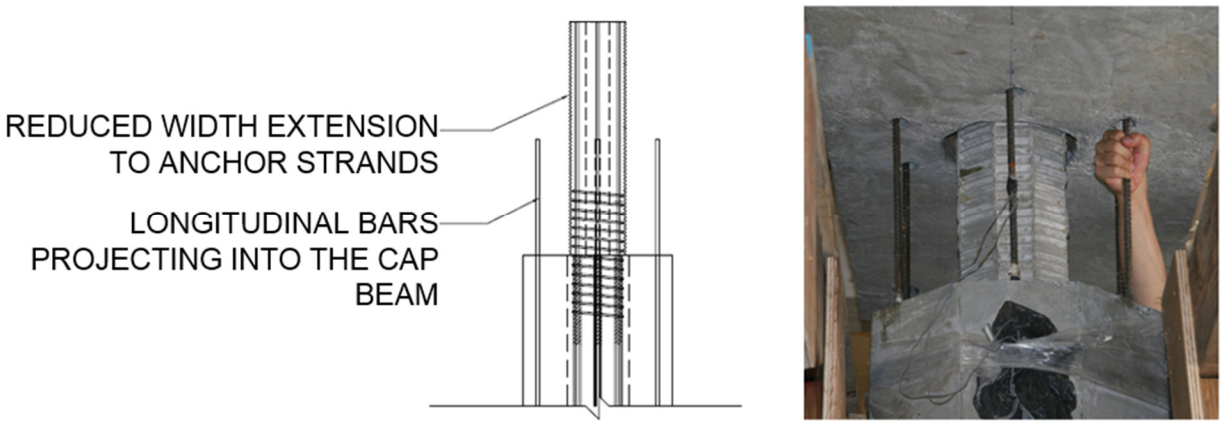

Figure 1.6 The column-to-cap-beam connection tested by Davis (adapted from Davis et al., 2012).

1.6 RESEARCH OBJECTIVES AND SCOPE

The goal of this research was to evaluate the performance and feasibility of a connection between a precast, prestressed column with a rocking detail and a precast cap beam. The connection used the large bar-large duct concept for the deformed reinforcement (Pang et al., 2010) and the reduced diameter column extension for the strands that have been developed in previous work at the University of Washington.

The primary goals of the research were to:

- evaluate the extent to which the steel confining tube would delay damage to the concrete and partial rebar debonding would delay bar fracture,
- analyze the rocking behavior of the column,

- determine the ability of the system to re-center,
- determine the ability of the system to dissipate energy, and
- to identify any other unforeseen behavioral responses.

The rest of this thesis details the specimen design (Chapter 2, pg. 11), testing procedure (Chapter 3, pg. 49), observed response and damage (Chapter 4, pg. 62), measured response (Chapter 5, pg. 77), quantitative analysis and comparison with other previous tests (Chapter 6, pg. 119), comparison with predictive models (Chapter 7, pg. 186), and research findings and recommendations (Chapter 8, pg. 230) for a 42%-scale test subassembly.

Supplemental information can be found in the appendices: materials testing (A, pg. 246), detailed drawings (B, pg. 257), test photos (C, pg. 279), construction photos (D, pg. 282), calculations (E, pg. 293), and experimental instrumentation details (F, pg. 296).

2 Design of Test Specimen

2.1 PREVIOUS DESIGNS

The design of the specimen was influenced by the results of several previous tests.

The prestressed, precast columns tested by Davis et al. (2012) provided decent ductility and re-centering (compared to a non-prestressed system), but had significant damage at lower drifts than for conventional reinforced concrete systems.

Finnsson (2013) then tested prestressed columns that were similar to the post-tensioned system developed by Billington and Yoon (2004). Finnsson used HyFRC (a steel and plastic fiber-reinforced concrete with a more ductile response than conventional concrete) for the plastic hinging regions of the column, and continuous, bonded stainless steel reinforcement (which is more ductile than conventional, mild steel reinforcement). Finnsson observed less damage, more ductility, and good energy dissipation in his specimens (PreT-SF-HyFRC and PreT-SF-SS-HyFRC). However, they required non-standard materials and fabrication was difficult because the HyFRC was used only in the plastic hinge region, which necessitated two separate pours, and the HyFRC did not flow well through tightly spaced reinforcement.

The conceptual design for the Hewes and Priestley (2002) columns was very similar to the rocking design considered in this thesis, but differed in several ways. Their columns were strictly unbonded systems, and therefore lacked the energy dissipation provided by cyclic yielding of bonded reinforcement. Their columns also lacked the baseplate detail (see Section 2.5.3), which led to concrete crushing and spalling below the steel confining jacket. Finally, their post-tensioned columns were assembled from individually precast segments, which would then have to be assembled and post-tensioned together onsite. The pre-tensioned columns examined in this thesis were entirely prefabricated products, and would not require any onsite construction operations besides the initial erection and top/bottom connection pours.

2.2 OVERALL DESIGN PHILOSOPHY

The PreT-CB-ROCK specimen detailed in this thesis was designed in parallel with PreT-SF-ROCK (Schaefer et al., 2014a). These designs were identical in principle, but they differed in their implementation because the specimen tested by Schaefer was for a column-to-footing connection and the one discussed here was for a column-to-cap beam.

The design goals for the rocking columns were to:

- maintain system strength, even at large drift ratios,
- minimize residual displacements,
- provide adequate energy dissipation,
- minimize column damage, even after large drift ratios,
- maintain constructability to facilitate accelerated bridge construction, and

- use only conventional construction materials.

2.3 EXPERIMENTAL CONSIDERATIONS

The testing of a full-scale, complete bent system would have been extremely difficult. Therefore, the size of the test specimen was reduced to 42% of full scale, and only the upper half of the column was tested, as a cantilever. The scaling influenced several design parameters (selection of rebar and strand areas, plate thicknesses, etc.).

The specimen was tested in an "up-side-down" orientation. That is, the cap beam portion of the specimen served as the base, and moment was applied to the connection by applying a horizontal force at the top of the column. An idealized, fixed-fixed column system that is subjected to lateral end deformations has zero moment at its mid-height, and testing the connection with an equivalent cantilever was assumed to represent half of such a system. Figure 2.1 illustrates these ideas: a fixed-fixed column has zero moment at mid-height when subjected to lateral deformation (top left), an equivalent, half-length cantilever can be used to represent the top connection (top right), the structure was rotated for experimental testing (bottom). Furthermore, the "up-side-down" orientation also affected the construction operation used to complete the socket connection (discussed in Section 2.9.3).

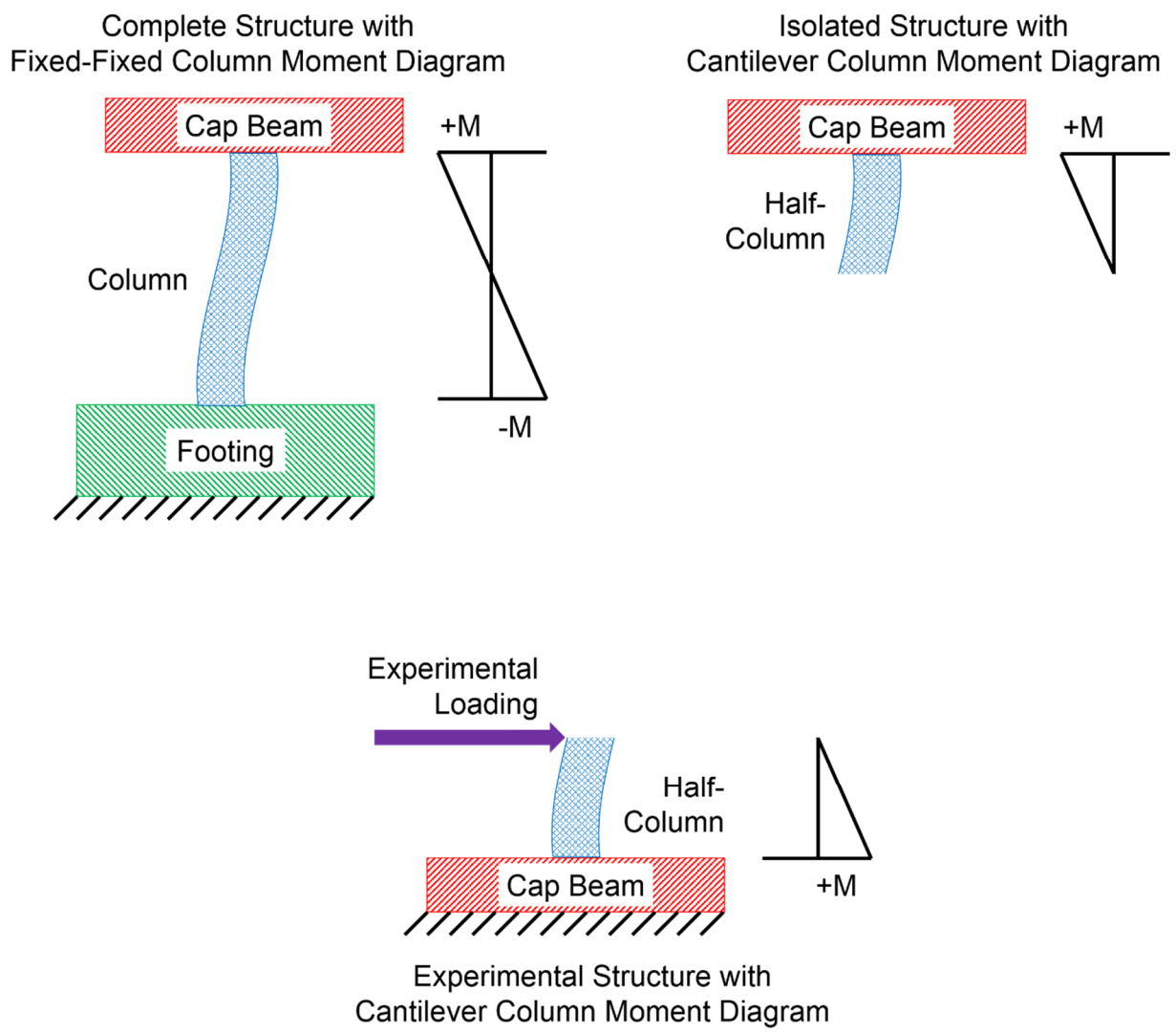

Figure 2.1 Complete (top left), isolated (top right), and experimental (bottom) column schematics with corresponding moment diagrams.

Finally, it should be noted that the coordinates used to describe the specimen (north-most rebar, west column face, etc.) refer to the orientation of the specimen during the test. Additionally, the elevation references for the specimen (top of cap beam, bottom of column, etc.) are made with respect to the testing orientation of the specimen (that is, the reverse of the field condition).

2.4 GENERAL GEOMETRY OF THE SPECIMEN

The column design was adapted from PreT-CB-CONC (Davis et al., 2012), and corresponded to a 48 in. wide full-sized bridge column. The basic column cross-section was octagonal and 20 in. across flats.

Mild steel reinforcement was used to dissipate energy through cyclic yielding. Unbonded, prestressing strands were used to limit residual displacements after the removal of lateral loads. Davis had originally designed the column so that approximately 40% of the reinforcing moment

strength was from the rebar, and 60% came from the prestressing strands (the design strength from the strands was 1.5 times that for the rebars). A steel tube and baseplate were added to confine the concrete in the plastic hinge region of the column, and to focus the system deformation at the connection interface (through rocking behavior). Deformations within the body of the column were inhibited by providing additional bars (omitted for clarity from Figure 1.1) that were welded to the tube assembly but did not cross the rocking interface. The column was a total of 103.5 in. long and had four distinct segments. These segments are identified in Figure 2.2 as:

- a 31.5 in. long, reduced diameter section for the socket connection to the cap beam,
- a 10 in. long, 20 in. diameter, circular, steel tube confined segment,
- a 41 in. long segment with a 20 in. wide octagonal section, and
- a 21 in. long section with modified geometry to permit attachment of the horizontal actuator.

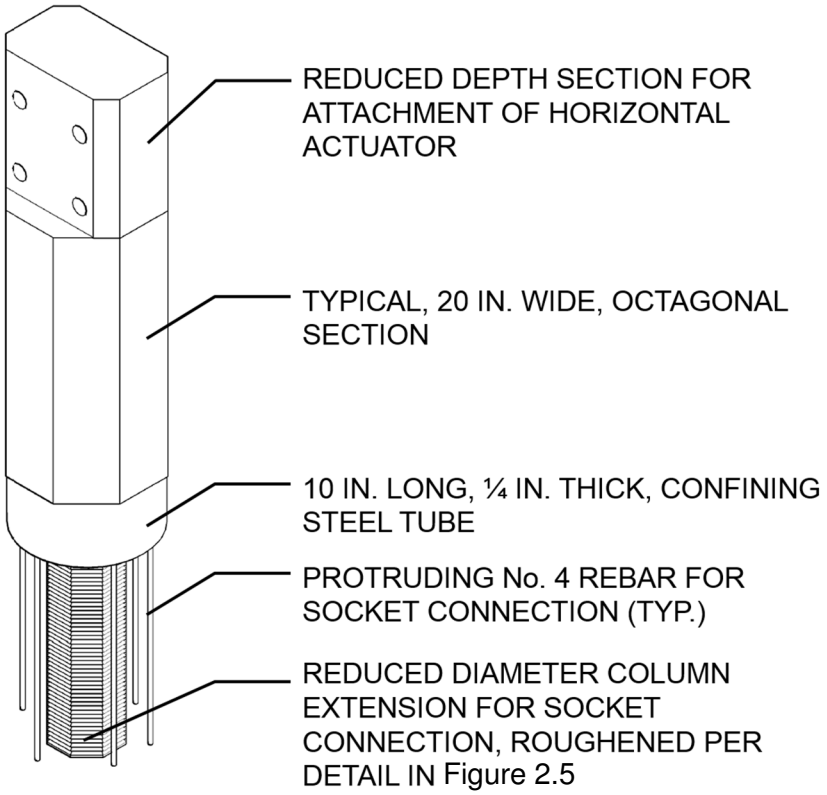

Figure 2.2 Isometric view of column (from southeast perspective).

Figure 2.3 shows the cap beam specimen. It was a total of 78 in. long, 28 in. wide, and 31.5 in. deep. In the field, the cap beam is typically stronger than the column by virtue of its size. The result is that damage from lateral loading is almost inevitably concentrated in the column, so the test cap beam was also designed to be stronger than the column. The cap beam was precast, but reinforced only with mild steel reinforcement (i.e., not prestressed). Additional, detailed drawings of the cap beam and column can be found in Appendix B.

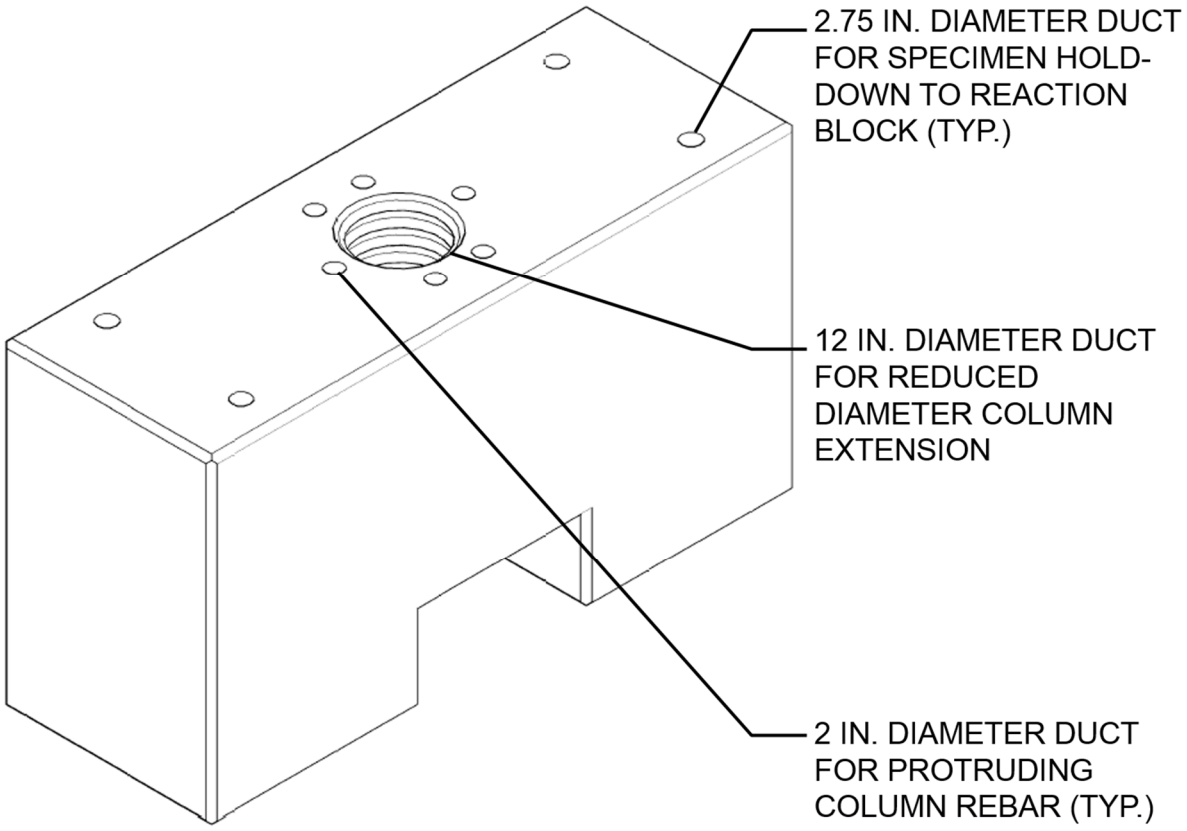

Figure 2.3 Isometric view of cap beam (from southeast perspective).

The column-to-cap beam connection was completed by grouting extensions from the column (the 31.5 in. reduced diameter section and protruding rebars) into ducts that were set in the cap beam. The reduced diameter of the column extension permitted the cap beam to be roughly the same width as the column. A grout pad was used between the column's baseplate and the top of the cap beam.

2.5 DETAILED DESIGN OF THE COLUMN

2.5.1 Column Geometry

2.5.1.1 Typical Column Cross-Section

Figure 2.4 shows the column cross-section. It was octagonal, with a width of 20 in. across flats, which resulted in a cross-sectional area of 331.4 in.^{2}. The shape was chosen because it is close to a circle, but has flat sides. A circular shape is optimal for seismic resistance because it offers the same stiffness and strength in all directions and it allows the use of spiral transverse reinforcement, which is more effective than rectangular ties. However, pre-tensioned products have to be cast horizontally (because the prestressing bed is horizontal), so the top surface must be hand-finished rather than being cast against formwork. Hand-finishing a curved surface to match the rest of the form-cast surface could be difficult, and the use of a polygonal shape solves the problem. The

octagonal cross-section still allows for circular spiral, and contractors are familiar with similar members used as precast piles (e.g., WSDOT 2013).

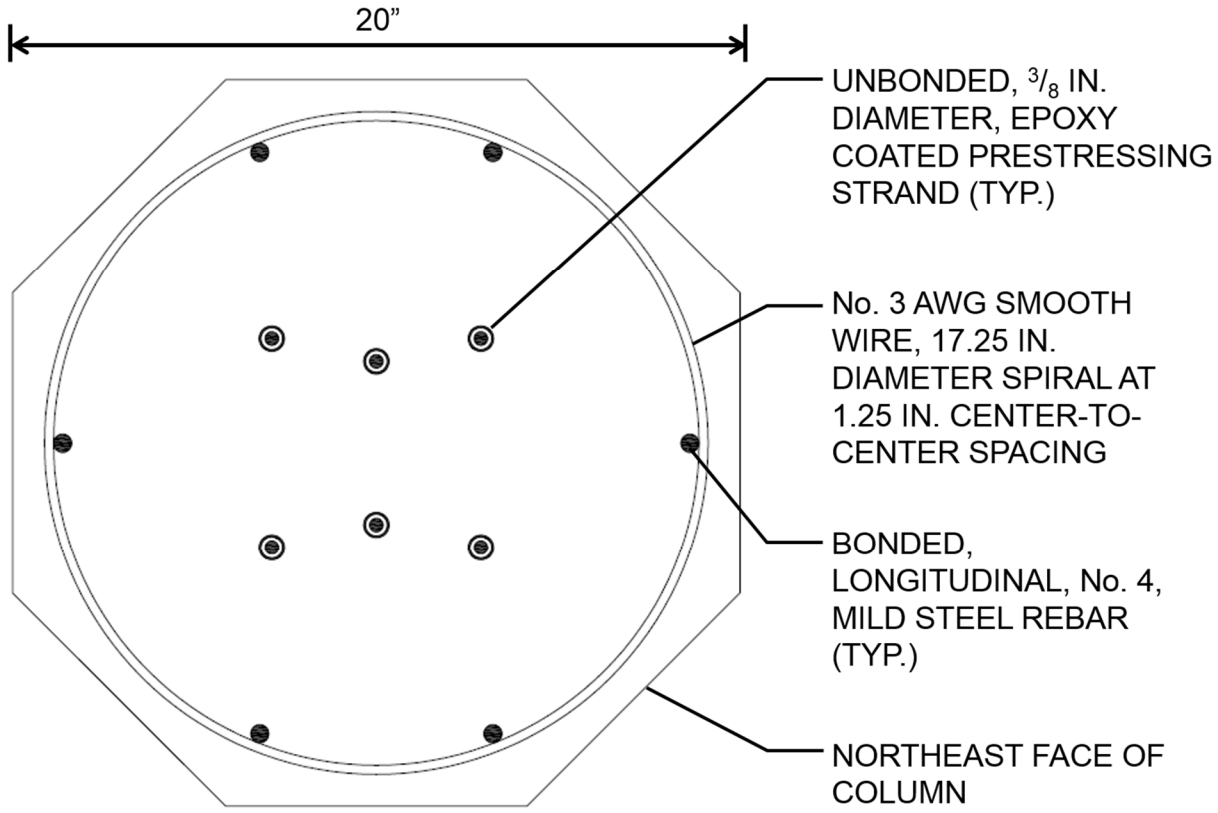

Figure 2.4 Cross-section of 20 in. wide column.

2.5.1.2 Reduced Diameter Column Extension

The bottom 31.5 in. of the column was reduced from the full 20 in. width to a 9.75 in. wide, octagonal cross-section; Figure 2.5 shows the reduced diameter section. This change in section width was done in order to complete the socket connection with the cap beam. This narrower length of the column was fitted and grouted into a central duct in the cap beam.

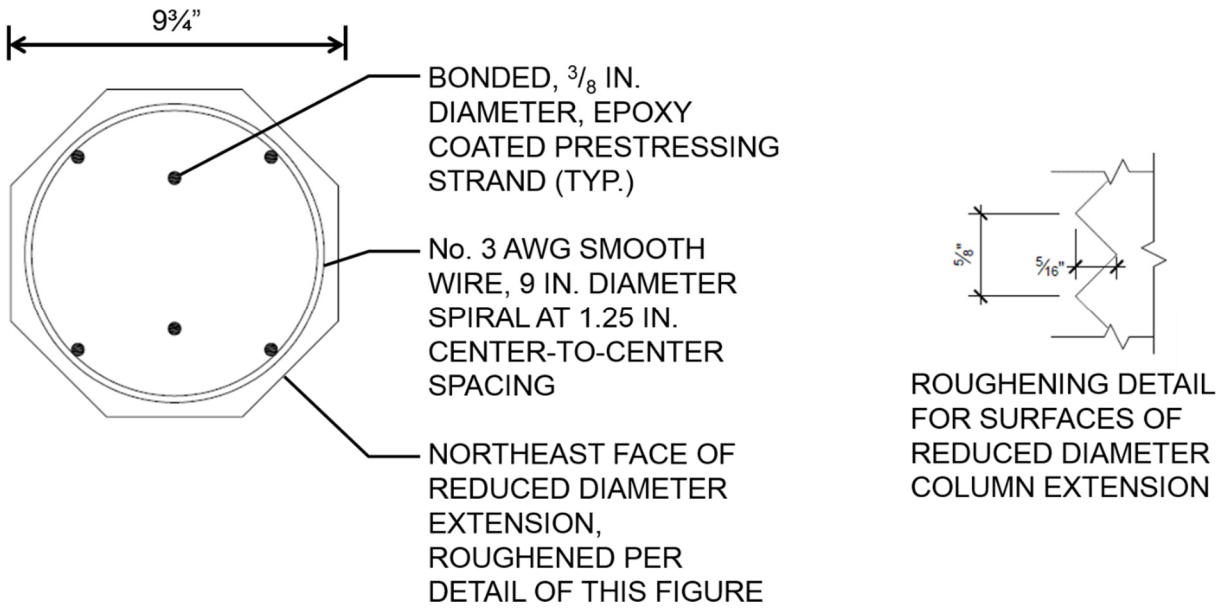

Figure 2.5 Cross-section of reduced diameter column extension and roughening detail.

The surfaces of this segment were intentionally roughened (per detail in Figure 2.5) in order to improve the transfer of forces from the column to the cap beam. This was the same roughened surface detail used in the column-footing socket connection for PreT-SF-ROCK (Schaefer et al., 2014a). It is possible that the surface of the extension could have been left smooth, without the special roughening detail. The projection of the column into the cap beam had length/diameter ratio of 3.23, as opposed to 1.23 for the length that would be embedded into the footing (Schaefer et al., 2014a). However, in the absence of convincing evidence about the surface bond properties, the roughened surface was used to reduce the risk of a spurious failure.

Normally, the strands would be placed in a circular pattern. However, a different pattern was used here in order to accommodate the existing hole pattern in the end plates of the stressing rig at The University of Washington.

2.5.1.3 Reduced Depth at Column Top

The cross-section for the top 21 in. of the column was also altered from the typical octagonal cross-section; this modified section is shown in Figure 2.6. This was done in order to attach a horizontal actuator to the top of the column. This portion maintained the same 20 in. width of the octagon, but had a reduced, 13 in. depth. Wider column faces resulted from the reduction in depth, which permitted the attachment of a flat adapter plate for the actuator.

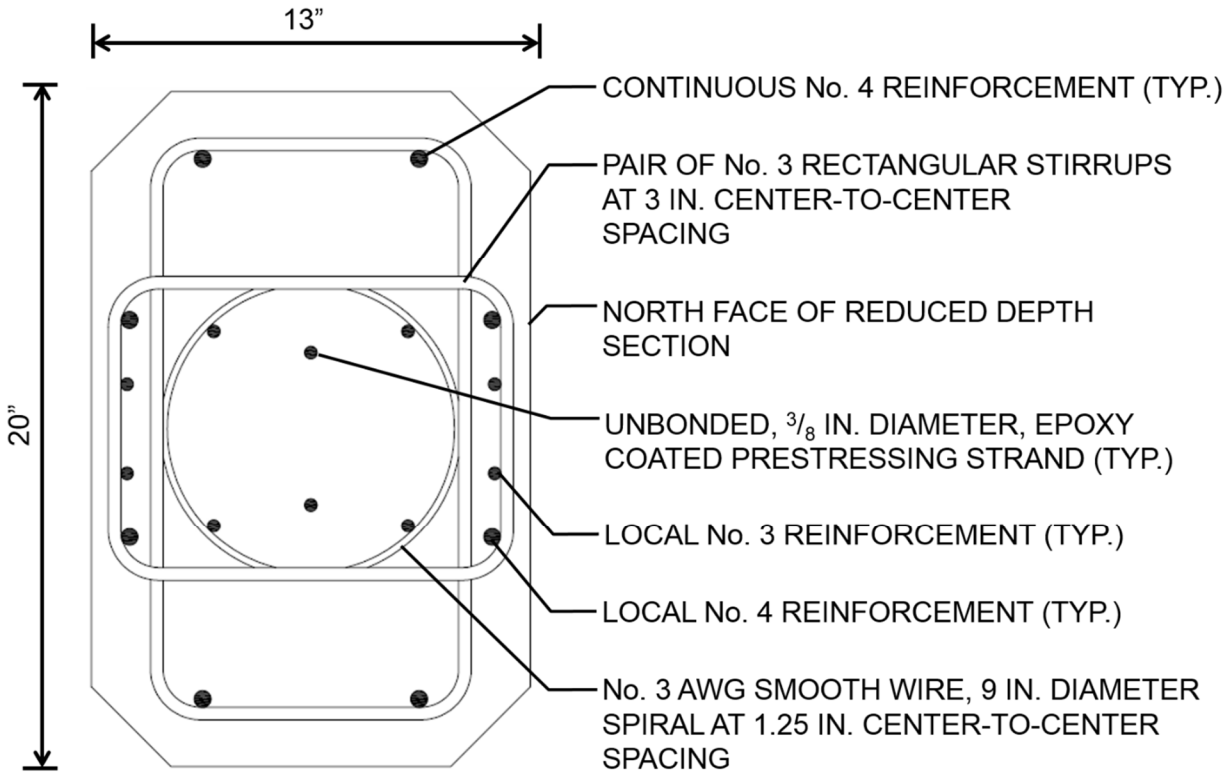

Figure 2.6 Reduced depth section for actuator attachment.

2.5.2 Column Reinforcement

The entire reinforcing cage, prestressing strands, steel tube and plate assembly can be seen in Figure 2.7; Table 2.1 provides the color coding for the figure. See Figure B.1 through Figure B.17 in Appendix B for additional detailed drawings of the column.

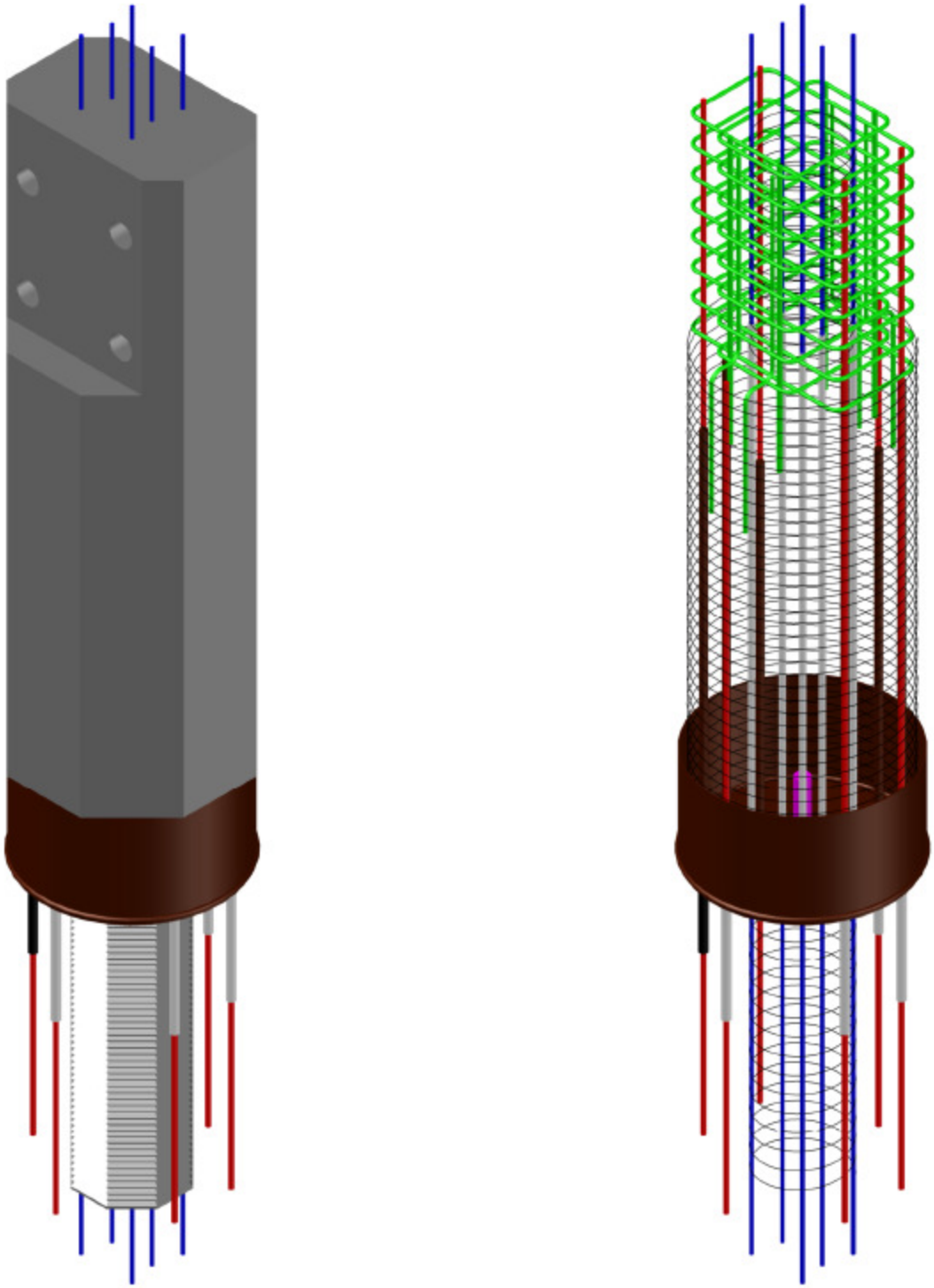

Figure 2.7 Fully cast column (left), and internal reinforcement (right), as seen from southeast perspective.

Table 2.1 Color code of items in Figure 2.7.

Color	Specimen Component	Note	See Section
White	Debonding tube	12 in. long PVC on north No. 4 bars, 12 in. long steel on south No. 4 bars, 54 in. long PVC on prestressing strands.	2.5.2.1, 2.5.2.5
Blue	⅜ in. dia., epoxy coated, prestressing strand	-	2.5.2.5
Red	Continuous No. 4 longitudinal reinforcement	-	2.5.2.1
Black (solid line)	No. 3 AWG, smooth wire spiral	17.25 in. diameter in the 20 in. wide segment, 9 in. diameter in the modified sections at the top and bottom.	2.5.2.3
Brown	Steel confining tube, No. 6 discontinuous bars		2.5.2.2, 2.5.3
Magenta	Dowel bar assembly	Housing fixture not shown in figure	2.5.4
Green	Local No. 3 and No. 4 longitudinal bars, No. 3 stirrups	Additional reinforcement for the reduced depth section.	2.5.2.4

2.5.2.1 Continuous No. 4 Bars

Six No. 4 bars were used for the column's longitudinal reinforcement (Figure 2.4 shows the typical column cross-section). These bars were set on a 17.25 in. pitch circle, which was consistent with the design of previous specimens (Davis et al., 2012 and Schaefer et al., 2014a, for example). The rocking detail was designed to concentrate the deformation of the system at the column base. If the reinforcing bars had been fully bonded, the concentrated rotation would have led to a strain concentration and the possibility of premature fracture. Therefore, the No. 4 rebars were debonded for 12 inches at the connection interface in order to distribute elongations caused by the rocking. The debonded length was selected so that first yield of the rebar would occur at 0.2% column drift. The following assumptions were made for PreT-CB-ROCK's design: rigid body motion of the column and baseplate, a neutral axis depth, c, of 6 in., and a rebar yield strain of 0.00207 in./in. (corresponding to Grade 60 steel). The design resulted in a 12 in. debonded length for the rebars. The assumed kinematics of the connection are presented in Figure 2.8.

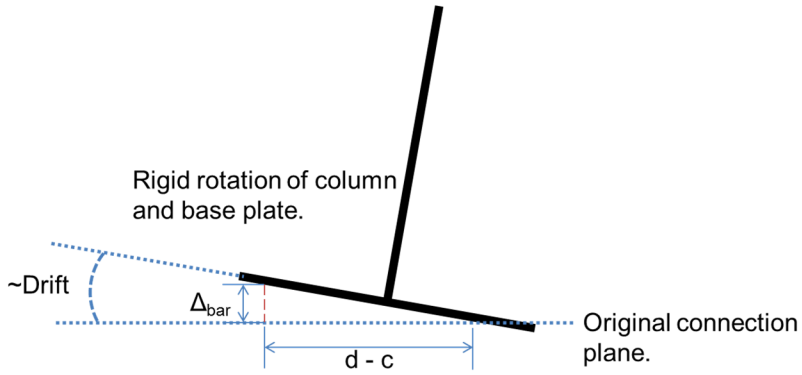

Figure 2.8 Assumed kinematics of rocking interface.

The debonding details of the No. 4 longitudinal bars are shown in Figure 2.9 and were determined as follows. In specimen PreT-SF-ROCK, the rebars were debonded for a total of 8 in., with 4 in. on either side of the rocking interface, using PVC pipes only. For PreT-CB-ROCK, the rebars were debonded for a total of 12 in., with the intention of reducing the bar strain for a given drift and thereby delaying bar fracture. The rebars were debonded entirely on the cap beam side of the connection. In previous rocking specimens, the bars had been debonded equally on both sides of the interface. Here, the decision was made to place all the debonding on the cap beam side, because the debonding may hasten the onset of bar buckling. Initiation of bar buckling in the column region, with its smaller cover, would likely lead to more local damage and spalling than buckling in the larger mass of the cap beam. The extent of deliberate debonding might be limited by the need for anchorage of the bar within the depth of the cap beam. Estimates based on the work of Steuck et al. (2009) showed that the anchorage length was sufficient, even with 12 inches of deliberate debonding.

The three north-most rebars were debonded with ordinary PVC pipe, while the three south-most rebars were debonded with steel pipes. The two schemes were used to investigate their effectiveness in inhibiting bar buckling. While both were embedded in a large block of concrete (the cap beam), there was some uncertainty as to whether the softer PVC would allow enough deformation to initiate buckling. The steel pipes were selected so that the elastic, Euler buckling load of the pipe was twice the yield force of the rebar (detailed design not presented in this thesis).

Figure 2.9 Debonding of protruding No. 4 bars. The PVC sheathed, north bars are on the right side of the photograph.

2.5.2.2 Discontinuous No. 6 Bars

Six No. 6 bars were welded to the steel baseplate, and were then carried up 44 in. into the column (previously introduced, see Figure 2.10). These bars were intended to limit the width of the potential crack at the top of the steel tube on the tension side of the column, and to serve as compression reinforcement on the compression side. These bars were also set in a 17.25 in. diameter pitch circle (the same pattern as the continuous No. 4 bars, but rotated 90° about the longitudinal axis of the column). The design of the No. 6 bars was guided by a preliminary finite element analysis (not presented in this thesis), and consideration of scaling.

2.5.2.3 Spiral Reinforcement

No. 3 AWG smooth wire was used for the column's transverse reinforcement. This wire had a diameter of 0.23 in., and a cross-sectional area of 0.041 in.^{2}. The wire was used as a continuous spiral, with a center-to-center pitch of 1.25 inches and a resulting transverse reinforcement ratio, ρ_s, of 0.93%. The spiral used in the 20 in. wide section of the column had an outside diameter of 18 $^5/_{16}$ in., which resulted in concrete cover of $^{13}/_{16}$ in.

This wire was also used for spiral reinforcement in the modified sections of the column (the extension for the socket connection and the top of the column). The spiral for these portions of the column provided local confinement for the bonded lengths of the prestressing strands. Here, the spiral only wrapped around the strand pattern, and therefore had an outside diameter of 9 inches. In the reduced diameter extension, cover ranged from ¼ to ½ in. (variance came from the roughening protrusions); the same 1.25 in. pitch was used at both locations.

A standard detail for precast piles was used to terminate and anchor the spiral: three successive turns and a 135° bend into the core of the column (WSDOT 2013). This termination detail was used for the 18 $^{5}/_{16}$ in. diameter spiral at the bottom of the steel tube and at the transition in section depth from 20 in. to 13 in. (for the horizontal actuator connection). However, the final 135° bend was not possible for the 9 in. diameter spiral in the reduced diameter region due to reinforcement congestion.

2.5.2.4 Over Reinforced Top

The top 21 in. of the column (where the depth was reduced in order to accommodate the attachment of an actuator) was intentionally over-reinforced per Figure 2.6. This was done to prevent premature failure of that segment of the column during the test. Four No. 4 longitudinal rebars were carried up the full height of the column, and four additional No. 4 rebars were added for flexural reinforcement. Furthermore, four No. 3 bars were added in order to provide reinforcement across a potential crack plane at the transition between the two sections. Pairs of rectangular No. 3 stirrups (spaced at 3 in. center-to-center) were used for transverse reinforcement, and the strand group was confined with a 9 in. diameter spiral (as previously discussed).

2.5.2.5 Column Prestressing

Six epoxy-coated, $^{3}/_{8}$ in. diameter strands were used to prestress the column, as shown in Figure 2.4. The strands were placed in a doubly symmetric, non-circular pattern (the east and west strands of the pattern were moved closer to the center of the section). The corner strands of the pattern lay on an 8 $^{1}/_{8}$ in. diameter circle. This pattern was used to fit the end plates in the stressing rig at the University of Washington, and had previously been used for the columns tested by Finnsson (2013) and Schaefer et al. (2014a). PreT-CB-CONC had a more typical circular pattern because that specimen was constructed by a professional precaster. The prestressing strands were bonded for the entire 31.5 in. length of the reduced diameter section at the bottom of the column, and for 18 in. at the top of the column. This resulted in an unbonded length of 54 in. for the column. The strands were debonded by simply sheathing them with a commercially available, ½ in. diameter, PVC pipe.

The unbonded lengths of the strands in this column and its predecessors have been 54 inches in most cases and 48 inches in PreT-SF-ROCK-HyFRC and PreT-SF-ROCK (Schaefer et al., 2014a). The latter was an unintended error caused by the fact that most of the columns had a cantilever length of 60 inches to the actuator axis, but Finnsson's (2013) PreT-SF-HyFRC and –SS-HyFRC columns were 66 inches long, in order to encourage a crack plane that was raised 6 inches above the footing. Due to the additional column height, Finnsson was able to bond strands for 24 in. at the top of the column. In specimen PreT-SF-ROCK, which was 60 inches long, that top bonded length of 24 inches, rather than the unbonded length of 54 inches, was mistakenly selected for consistency to Finnsson's specimens.

The prestressing design was originally done by Davis et al. (2012) for the PreT-CB-CONC and PreT-SF-CONC specimens. The prestressing of PreT-CB-ROCK generally followed that design. Each strand was initially jacked to a stress of approximately 180 ksi (15.3 kips), which resulted an effective stress of 178 ksi after elastic shortening of the column (assuming E_c = 4000 ksi). Davis estimated the loss due to creep as 4 ksi (twice the elastic loss), and a shrinkage loss of 9 ksi (from an assumed shrinkage strain of 300 $\mu\varepsilon$). Accounting for all losses resulted in a stress of 165 ksi for each strand (14.0 kips), and a concrete compressive stress of 253 psi for the 20 in.

wide octagonal section. The calculated compressive stress was 1068 psi in the reduced diameter column extension (which had an area of 78.7 in.^{2}). The minimum concrete strength at release of the strands was selected to be 5000 psi, which was achieved within one week of casting the specimen.

As discussed by Davis et al. (2012), it was necessary to provide strand chucks as back up anchorage for the strands. The strands should have been approximately 0.20 inches diameter at the correct scale factor, but the smallest commercially available strands were 3/8 inch diameter. For full development, the larger diameter strands required bond stresses higher than those that would be needed in the full-scale prototype, so back-up anchorages were used to prevent spurious bond failure from ending the test prematurely. Details of the arrangements are given in Section 2.9.

2.5.3 Steel Tube and Baseplate Detail

A steel tube and baseplate detail was used for the plastic hinge region of the column. This detail was used to provide significant confinement for the concrete (from the tube) and to allow the shoulder of the column to rock on top of the cap beam (due to the baseplate).

The expected demands on the tube were hoop tension (from the confining force acting on the concrete) and vertical compression (arising from the column's rocking). The tube was a straight-seam, steel tube with an outside diameter of 20 in. (matching the width of the main octagonal section). It had a thickness of ¼ in., which gave a diameter/thickness ratio of 80. Such a ratio is equivalent to a transverse spiral with a 5.0% volumetric ratio. The tube steel had a nominal yield strength of 49 ksi. Finally, the tube had a length of 10 in. (resulting in a tube length-to-column diameter ratio of ½). The length of the tube was a compromise; it needed to be long enough to inhibit spalling of the column concrete in the region of the rocking interface, but it needed to be short enough to permit the concrete to flow easily into the tube during casting. Spalling observations from the PreT-CB-CONC and PreT-SF-CONC tests (Davis et al., 2012) and a preliminary finite element analysis were used to estimate the required length of the tube.

The bottom of the steel tube was welded to a circular, steel, baseplate, as shown in Figure 2.10. This plate had a 20 in. diameter (matching the tube) and was ½ in. thick. The plate had a 10 in. diameter hole cut from its center, which allowed the passage of the prestressing strands into the reduced diameter section of the column. The plate also had six ¾ in. diameter holes cut into it, which allowed the longitudinal, No. 4 reinforcing bars to project through the plate and to be subsequently fitted into ducts in the cap beam. Finally, six additional ¾ in. diameter holes were drilled into the steel plate, which were then used as plug-weld points for the discontinuous, longitudinal, No. 6 bars that extended back into the body of the column.

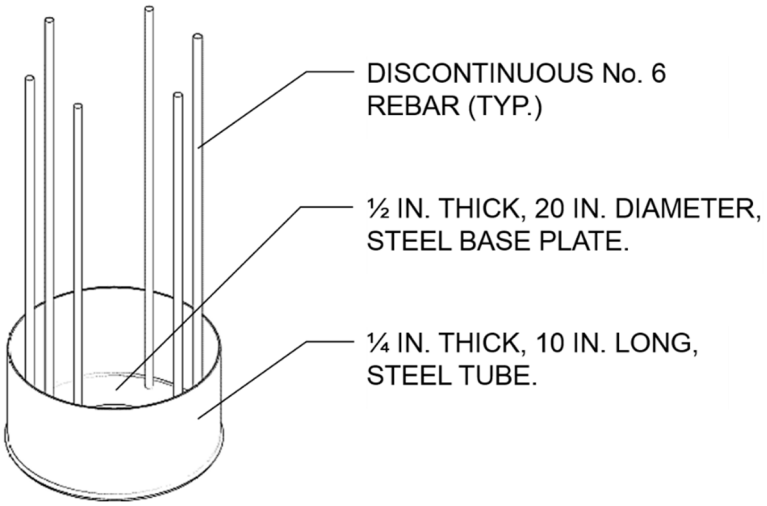

Figure 2.10 Isometric view of rocking detail: steel plate, tube, and discontinuous No. 6 bars (from southeast perspective).

2.5.4 Dowel Bar Assembly

A dowel bar and housing fixture was included in the specimen. It is shown in Figure 2.11 (after the dowel bar had been instrumented with strain gauges and the opening sealed with silicone caulk to prevent ingress of concrete) and in Figure 2.12. The purpose of this assembly was to help transfer column shear forces through the column-to-cap beam connection, without affecting the column's ability to re-center.

Figure 2.11 Dowel bar and housing fixture.

The bar had a diameter of 2 in., a length of 11 in., and was made of high strength steel in order to limit its required size. The bar was located at the center of the column cross-section, and was embedded for approximately 7.5 in. in the steel tube segment of the column. The bar then extended into a housing located inside the reduced diameter section of the column. The housing was designed to allow free rotation and vertical displacement, but to resist shear forces in the horizontal plane of the column-cap beam joint. It was constructed of a 4 in. diameter, ¼ in. thick, steel pipe (HSS4x0.250) with ¼ in. thick, circular, steel plates welded to both ends. The top plate of the housing had a 2 in. diameter hole cut in it in order to receive the dowel bar.

Figure 2.12 shows an approximation of the intended load path for the column shear force through the dowel bar, into the cap beam. The dowel was expected to bear against the interior edge of the top steel plate of the housing, which would then force the housing to bear against the concrete of the reduced diameter segment (which was grouted in a duct in the cap beam). Because the dowel bar was only bonded to the concrete on one side of the connection (the housing fixture was hollow), any inelastic bending of the bar was not expected to inhibit the re-centering of the column.

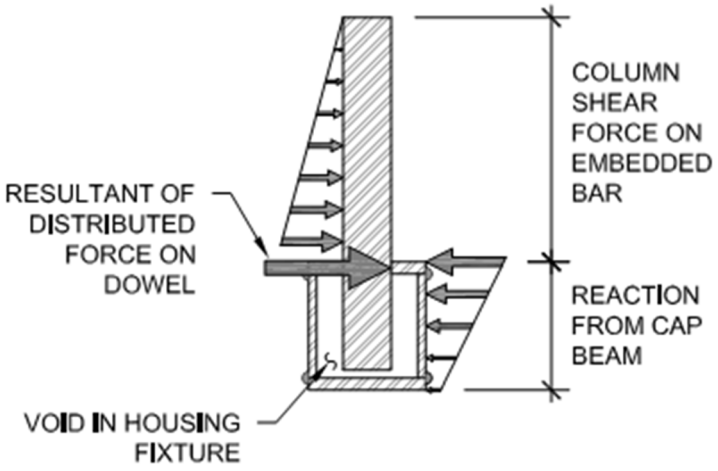

Figure 2.12 Intended load path for transfer of shear force through dowel bar.

2.6 DETAILED DESIGN OF THE CAP BEAM

2.6.1 Design Philosophy

The design for the cap beam was adapted from the PreT-CB-CONC specimen (Davis et al., 2012). That cap beam was designed to provide shear and moment capacities such that damage and deformation would be concentrated in the column, and was originally designed according to the specifications of *ACI 318-08*. The design was believed to be far stronger than necessary, but was used to avoid any possibility of failure in the cap beam. This was considered prudent, because the objective of the test was to investigate the behavior of the column. For field implementation, the cap beam reinforcement should be re-considered.

See Figure B.18 through Figure B.25 in Appendix B for detailed drawings of the cap beam geometry and reinforcement.

2.6.2 Overall Cap Beam Geometry

Figure 2.13 and Figure 2.14 show the basic geometry. The PreT-CB-ROCK cap beam was 28 in. wide, 78 in. long, and 31.5 in. deep.

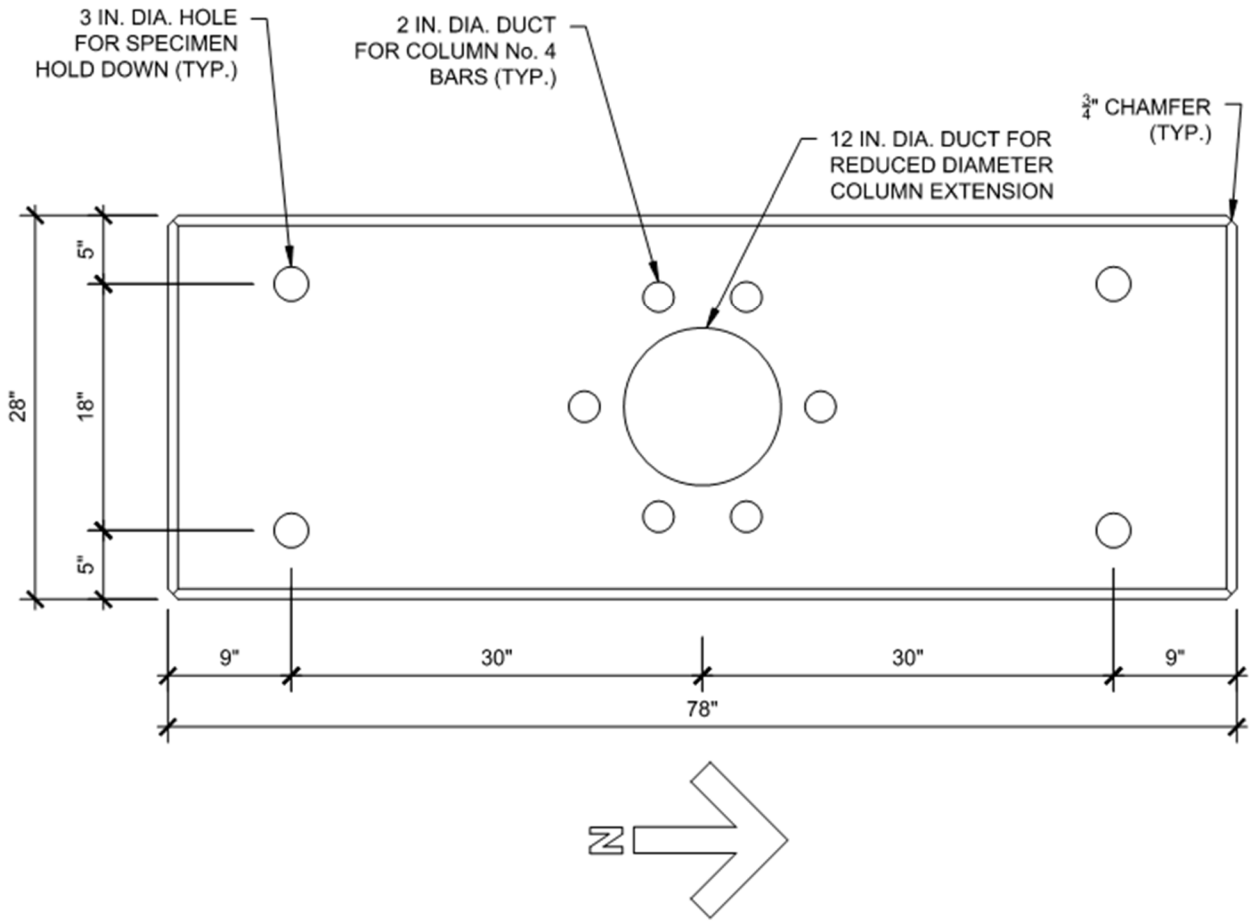

Figure 2.13 Cap beam plan.

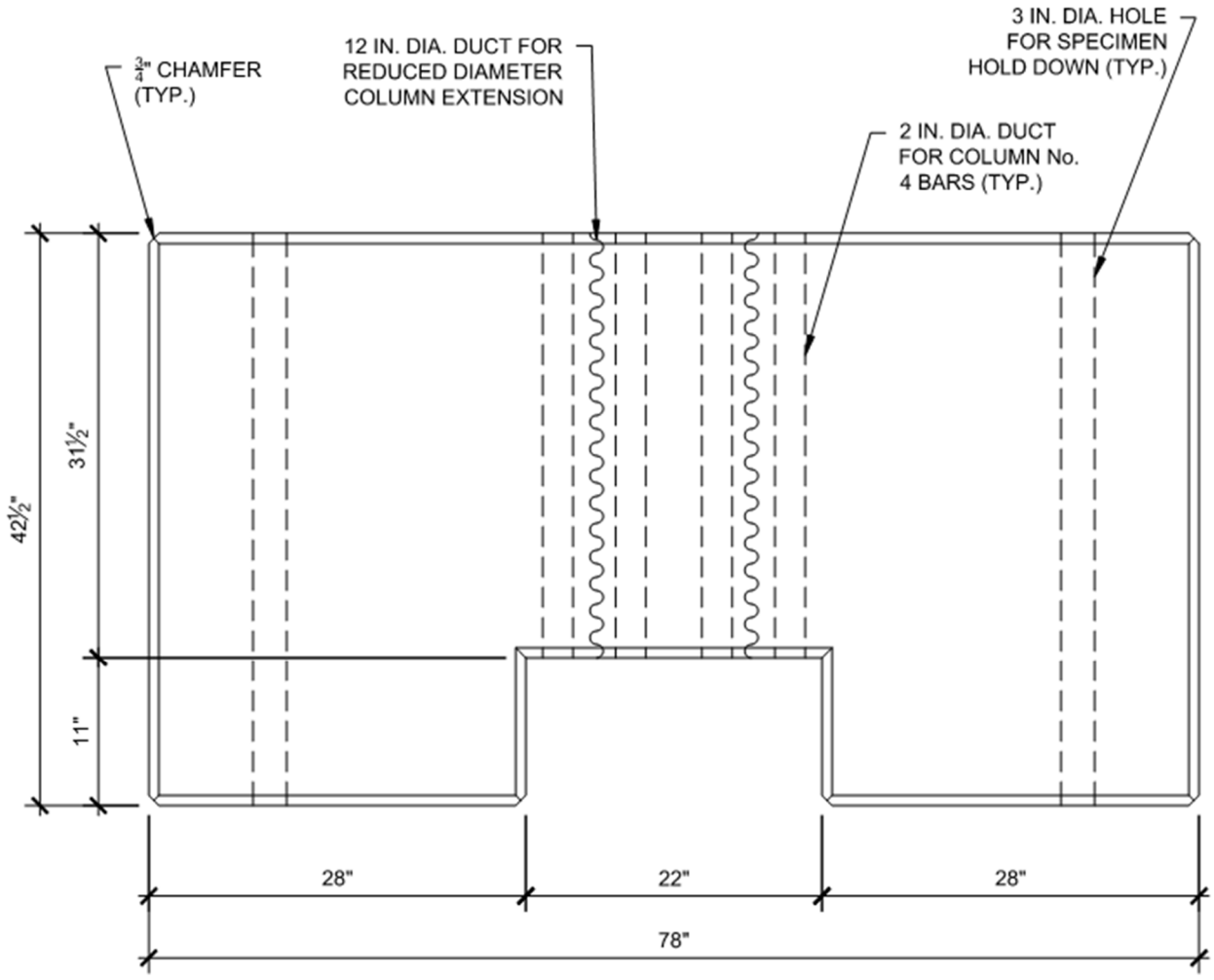

Figure 2.14 Cap beam east elevation.

In order to accommodate screw thread devices (STD's) and strand chucks that were left on the reduced diameter end of the column (shown in Figure 2.15 and further discussed in Section 2.9.1.1), an 11 in. deep void space was required at the beam's middle, underneath the socket connection. This was accomplished by adding 11 in. deep, "standoff" sections on both ends of the cap beam. This resulted in a 42.5 in. deep cap beam at the ends, and a 31.5 in. depth at the middle. These dimensions were consistent with the PreT-CB-CONC cap beam.

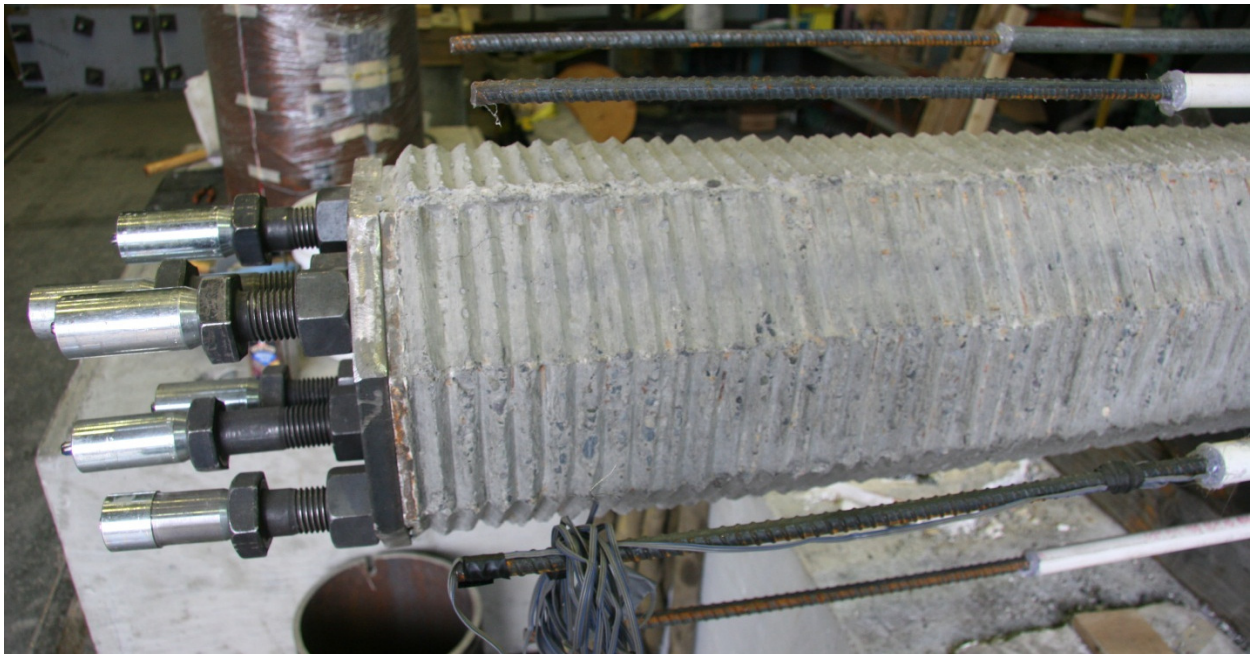

Figure 2.15 Steel bearing plate, STD's, and strand chuck anchorage assembly on end of reduced diameter section.

2.6.3 Cap Beam Reinforcement

Figure 2.16 shows the cap beam's reinforcing cage and connection ductwork; Table 2.2 provides the color coding for the figure. It is noted that this figure does not include additional skin steel placed in the bottom of the 42.5 in. tall, "stand-off" ends of the cap beam – which can be seen in various construction photos (Figure 2.22, for example).

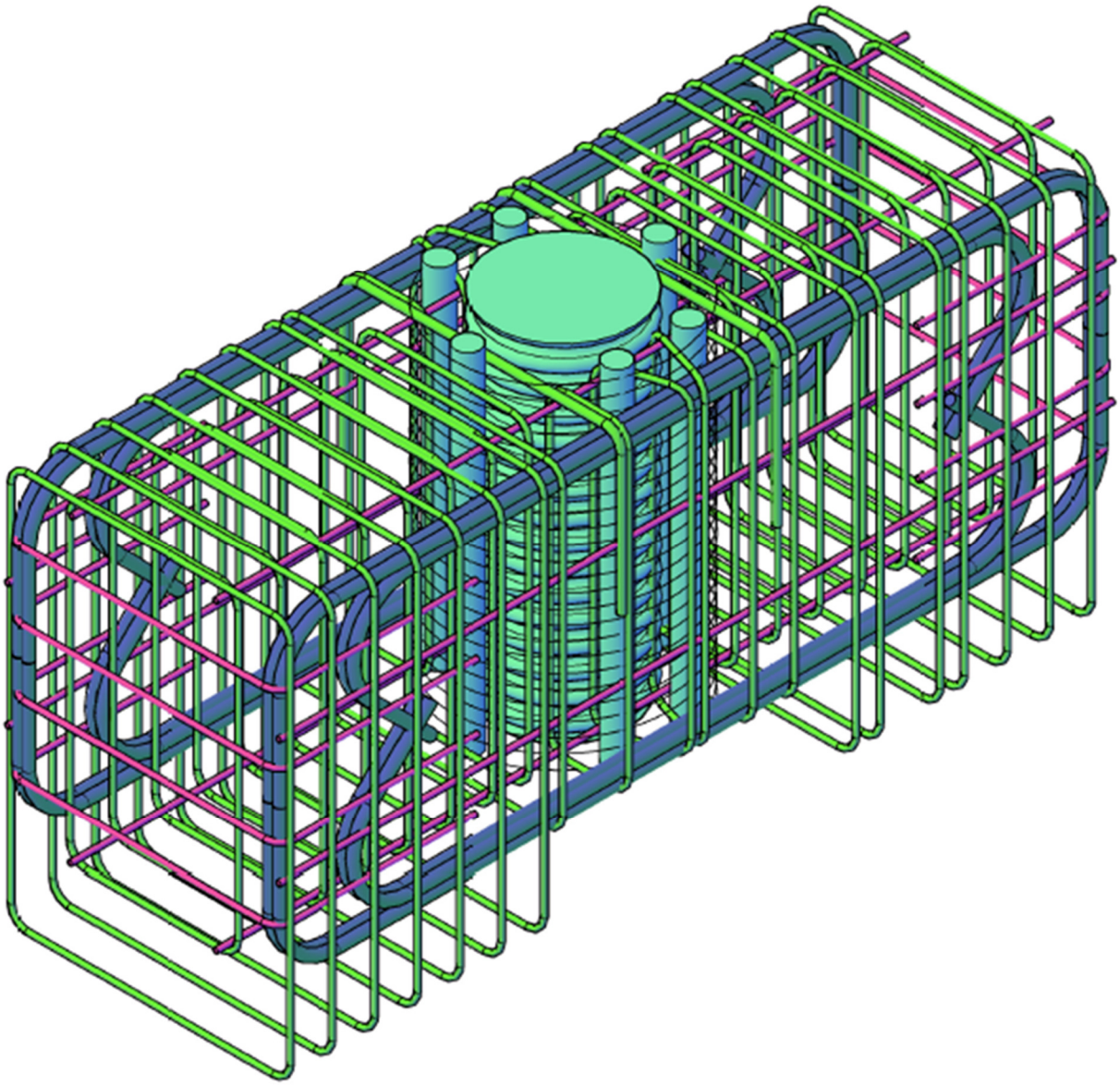

Figure 2.16 Reinforcing and connection ductwork of cap beam (from southeast perspective).

Table 2.2 Color coding of items in Figure 2.16.

Color	Specimen Component	Note
Dark Blue	No. 7 longitudinal reinforcement	Main flexural reinforcement for cap beam.
Magenta	No. 3 longitudinal bars, No. 3 end ties	Straight bars added for cage rigidity and to provide an longitudinal force at the corners of the narrow stirrups, end ties for No. 7 hooks, No. 3 skin steel.
Black (solid line)	No. 3 AWG smooth wire hoops	Additional reinforcement around connection ductwork.
Cyan	Connection ductwork	Six 2 in. diameter post-tensioning ducts for the rebars, one 12 in. diameter, corrougated drainage pipe for reduced diameter column extension.
Green	No. 3 stirrups, local No. 5 transverse reinforcement	Transverse reinforcement for cap beam.

The primary flexural reinforcement consisted of sixteen No. 7 bars (colored dark blue in Figure 2.16). These were bundled in groups of four, with one bundle in each corner of the rectangular cross-section of the beam (eight top bars and eight bottom bars). The "outer" bars of the bundles were anchored with 90° hooks on the end, while the "inner" bars had 135° hooks. Transverse reinforcement consisted of pairs of closed, No. 3 rectangular stirrups (colored green in Figure 2.16). These stirrups had different widths and heights depending on their location within the cap beam. Each stirrup was terminated with a hook bending into the interior of the hoop (either a 135° or 90° bend depending on the stirrup size). Additional transverse reinforcement was added near the socket connection in order to improve local concrete confinement. This was done by adding No. 5 U-bars to either side of the connection. No. 3 skin steel was used at the mid-height of the section (colored magenta in Figure 2.16), and in the 11 in. deep standoff sections at the ends of the beam. No. 3 U-bars were used to enclose the end hooks of the longitudinal reinforcement (also colored magenta in Figure 2.16).

The No. 3 AWG smooth wire that was used for the spiral reinforcement in the column was also used in the cap beam (shown with a solid, black line in Figure 2.16). Here, the wire was used as additional joint reinforcement for the socket connection. However, placement difficulties prevented the wire from being used in a continuous spiral. Therefore, the wire was cut and bent into individual, 20 in. diameter, circular hoops that were wrapped around the group of outer 2 in. diameter ducts (colored light blue in Figure 2.16). The hoops had an end overlapping length of 10 in. (~43.5 times the wire diameter). These hoops were placed after tying the rebar cage, and therefore, the overlapping ends could not be welded. The hoops were set at a target center-to-center spacing of 1.25 in. along the height of the cap beam.

2.6.4 Ductwork for Socket Connection

The socket connection in the cap beam was prepared by fixing ductwork in the rebar cage at the beam's mid-length. A 12 in. nominal diameter, corrugated, galvanized steel drainage pipe was used for the central duct of the connection (to receive the reduced diameter column extension). However, the actual, average, outer diameter of this duct was closer to 12.5 in., and the outward corrugations of the duct resulted in a maximum diameter of 13 in. in some places. Davis was able to use an 8.5 in. diameter pipe for this duct in the PreT-CB-CONC specimen because his circular strand pattern had a smaller diameter than the one used on this project. The use of the nominal 12 in. duct here resulted in conflicts with the cap beam's primary flexural rebar. A 10 in. duct would have been preferable, but was not available commercially.

The six smaller ducts (to receive the protruding No. 4 rebars from the column) were 2 in. diameter, post-tensioning ducts. Davis used 1.25 in. diameter ducts, which resulted in a significant alignment problem during the socket connection fitting of PreT-CB-CONC. Therefore, it was decided to use larger ducts for the column rebars in order to improve construction tolerance. All ductwork extended the full 31.5 in. height of the cap beam.

All ductwork was set in the cap beam formwork so it was centrally aligned with the corresponding column extension.

2.7 BEAM-COLUMN INTERFACE

During field erection, the shoulder of the column and the bottom face of the cap beam are unlikely to be perfectly plumb with one another. This may result from errors in the column erection or the fact that the underside of the cap beam is not truly horizontal. Therefore a pad of interfacial material is needed to ensure an even bearing surface between the two components. In the PreT-CB-ROCK specimen, the interface was equipped with a ½ in. thick, fiber-reinforced grout pad between the bottom of the steel plate and the top of the cap beam; this material is further described in Section 2.8.5. The method of installation is described in Section 2.9.3.

2.8 MATERIALS

2.8.1 Reinforcing Steel

Steel rebar conforming to ASTM A706, Grade 60 was used for the longitudinal rebar in the specimen (No. 4 and No. 6 bars in the column, and No. 7 bars in the cap beam). The No. 3 rebar was not available according to A706 specifications, so A615, Grade 60 was used for that rebar. However, no No. 3 rebar was used in a region where yielding was anticipated. The smooth wire conformed to ASTM A82 specifications (Finnsson, 2013).

2.8.2 Prestressing Strands

The prestressing strands were epoxy coated, 3/8 in. diameter, grade 270 steel. Epoxy coating was chosen because previous research (Jimenez 2012, and Cousins et al., 1990) had shown that it offered better bond properties than uncoated "black" strand and because it provides additional corrosion resistance.

2.8.3 Steel Tube, Plate, and Dowel

The confining tube around the column was a 20 in. diameter, straight-seam welded, steel tube. The tube's wall thickness was ¼ in., and its steel designation was "API 5LB PSL1 43rd Edition". The nominal properties of the steel were: yield stress of 49 ksi, ultimate stress of 60 ksi, and a toughness of 86.5 ft-lb (Lee, 2011). This tube was being used on a concrete-filled-tube experimental project at the University of Washington, so it was readily available.

The annular plate that was welded to the bottom of the tube was a ½ in. thick, A36 steel plate. This thickness was twice that of the 20 in. diameter tube, but was selected because the baseplate had to resist some bending, whereas the tube largely resists in-plane tension and compression.

The dowel bar was made from high strength steel (with a specified yield stress of 80 ksi) in order to minimize its required size. The tube of the housing fixture was an HSS4x0.250 section (ASTM A500 Gr. B steel), and the top and bottom circular plates were made from ¼ in. A36 plate steel.

2.8.4 Conventional Concrete

2.8.4.1 Mix Design

Table 2.3 gives the mix design for one cubic yard of concrete. The column and cap beam were cast from the same batch of concrete, which was supplied by a ready-mix plant operated by CalPortland (a construction materials company based in the western United States). The concrete was a cement-rich, non-air entrained, pea gravel mixture. The mix design was selected for its workability and from consideration of scaling (the maximum aggregate size was 3/8 in., which corresponds to ~7/8 in. at full-scale). The concrete had a target compressive strength of 5000 psi (at 28 days), and a nine inch slump on delivery. CalPortland's mix code for this concrete was 0171.

Table 2.3 Mix design for conventional concrete.

Constituent	Design Quantity (per cubic yard)	Notes
Fine Aggregate	1250 lb	Class II Sand
Coarse Aggregate	1980 lb	$^3/_8$" maximum aggregate size, AASHTO #8
Cement	752 lb	Type I/II, Corresponds to 8-sack mix design.
Water	240.0 lb	Additional 2 gallons of water added onsite to 4.25 cyd load.
Water Reducing Admixture (WRA)	30.00 oz	-
High Range Water Reducer (HRWR)	30.00 oz	ADVA 195, Additional 0.2 gallons of HRWR added onsite to 4.25 cyd load.

2.8.4.2 Site-Added Materials

The slump of the concrete load was only 5.75 in. on delivery, resulting in a stiffer mix than desired. However, the batch time for the load compared to the known workability time for the mix design suggested that the batching procedure simply resulted in a stiffer material, and that the concrete was not prematurely setting up. Therefore, a total of 2 gallons of water and 0.2 gallons of high range water reducer were added to the 4.25 cubic yard load (both quantities were within the allowable range for site-added materials). The ratio between the added HRWR and the added water was far larger than for the original mix design. The additional two gallons of water were included to evenly disperse the added HRWR in the batch – not to maintain the design ratio between the constituents.

The resulting concrete had a slump of 8.75 in., and placement proceeded without complication. The concrete was internally vibrated during the casting of both the column and cap beam in order to ensure consolidation and a good finish against the formwork. Minimal bleed water was observed as a result of the vibration.

Furthermore, the compressive strength of the concrete was 6990 psi at 7 days and 9830 psi at 28 days (versus a specified compressive strength of 5000 psi at 28 days), suggesting that the additional water did not deteriorate the strength properties of the mixture. Appendix A: Materials Testing gives the concrete strength as a function of time.

2.8.5 Grout

Dayton Superior's Sure-Grip® High Performance Grout was used for the specimen, shown in Figure 2.17. This is a contractor's grade, non-metallic, high early strength, cementitious material. The manufacturer recommends this grout for interior/exterior structural precast components, structural column baseplates, and bearing pads (Dayton Superior, 2015). The product has many state DOT approvals, including Caltrans. The material was mixed and placed according to the directions of the manufacturer. Appendix A: Materials Testing provides strength testing results for the grout mixtures used on this project.

Figure 2.17 Sample bag of grout used for PreT-CB-ROCK grout pad.

2.8.5.1 Fiber-Reinforced Grout for Grout Pad

Fiber-reinforced grout was used for the grout pad between the column shoulder and the cap beam. The selection of this grout was influenced by the experience of Restrepo et al. (2011) during a test at the University of California, San Diego. Restrepo tested a connection between a hollow, precast concrete column and a precast cap beam, with a grout bed between the column and cap beam.

During his test, the deterioration of the grout bed significantly diminished the strength of the connection for large drift cycles and allowed some shear slip. His grout contained no fibers and the stress on it may have been exacerbated by the small contact area resulting from the hollow column.

For the grout pad of the PreT-CB-ROCK specimen, the grout was mixed according to the "flowable" consistency recommended by Dayton Superior (3.25 quarts of mix water to a 50 pound bag of grout). Propex's Fibermesh 300 fibers (shown in Figure 2.18) were then added to this grout mixture. These fibers were made from virgin polypropylene, and came in a blended length profile (fiber lengths ranged from ½ in. to ¾ in. long). These fibers were selected for their similarity to the fibers used for another similar concrete filled tube project at UC San Diego (Guerrini et al., 2012); the fiber-reinforced mortar bedding used on that project performed satisfactorily. The grout for PreT-CB-ROCK's connection was dosed at 3 pounds of fibers per cubic yard of grout. The fiber manufacturer recommended a concrete dosing of 1.5 pounds per cubic yard; the dosing was doubled because of the much higher cement content of grout compared to concrete (Janssen, 2013). The higher fiber dosing did not hinder the workability of the material, and the grout pad was placed without complication.

Figure 2.18 Fibermesh 300 polypropylene fibers used for grout pad.

2.8.5.2 Pumped Grout for Cap Beam Ductwork

The grout material used for the cap beam ducts was not fiber-reinforced. This grout was mixed according to the pump-able, "fluid" consistency recommended by Dayton Superior (4.0 quarts of mix water to 50 pound bag of grout). Previous research (Steuck et al., 2009) had shown that fibers in the grout did not increase bond strength and in some cases reduced it.

2.9 CONSTRUCTION OF SPECIMEN

The specimen was entirely constructed at the Structural Research Laboratory at the University of Washington. Additional construction photos can be found in Appendix D.

2.9.1 Column Construction

Column construction began with the steel tube and baseplate assembly. One end of the tube was welded to the circular plate using a full-penetration, ¼" radius weld. The discontinuous No. 6 bars at the bottom of the column were then plug-welded into holes that were drilled into the baseplate. The welding was performed by a professional welder, but was not inspected according to any standard. Construction then proceeded to the tying of the spiral cage and the erection of formwork for the column. The longitudinal rebars and the spiral were instrumented with strain gauges prior to the construction of the cage. The reduced diameter extension of the column was prepared with secondary formwork that fitted inside the main column form, and the reduced depth section for the actuator connection at the top of the column was formed with a foam blockout and PVC ductwork. Finally, the dowel bar fixture was set into the cage, at the bottom of the steel plate.

The prestressing operation was completed with $^3/_8$ in. strand chucks, a 100 kip center-hole hydraulic ram (powered by an electric pump), a custom fabricated steel standoff, and a steel reaction frame. The strands were stressed individually. A local precaster had found that the special chucks marketed for use with epoxy coated strand allowed significant slip, so standard chucks were used after locally stripping the epoxy coating from the strand.

Two stressing passes were completed; after stressing all six strands in a first pass, each strand was re-stressed to correct for losses from the shortening of the steel reaction frame. The prestressing force was monitored with load cells at the dead end of the strands, strain gauges applied at the mid-length of the strands, and pressure readings from the pump at the live end. After the concrete had been cast and reached a compressive strength greater than 5000 psi, the strands were released, and the total prestressing load was transferred to the column.

It is noted that the specimen was cast such that the east face of the column was the top, finished surface. Furthermore, the concrete was internally vibrated during the casting.

2.9.1.1 External Anchorage of Strands at Column Ends

After the release, the strands were "re-stressed" and anchored with chucks and custom-made Screw Thread Devices at the top and bottom of the column, in an operation similar to post-tensioning (although the strands were also bonded at the column ends). This was done so that if a strand started to slip prematurely during the test, the slip would be arrested by the chuck and most of the prestressing force could still be maintained in the strand.

The column concrete was allowed to cure for seven days before releasing the prestressing strands. After the release and removal of the specimen from the prestressing rig, the strands were then re-stressed and anchored at each end of the member, using the following procedure. An assembly consisting of a screw thread device (STD), a load cell, and then a strand chuck were first slipped over the length of strand that protruded from the end of the column. This strand chuck was actually half of a strand coupler, because internal screw threads were needed, as discussed below. A photograph of this assembly is shown in Figure 2.19, and a schematic can be seen in

Figure 2.20. The STD consisted of a 1.25" ASTM A490 nut and bolt, which had a $^{7}/_{16}$" diameter hole drilled longitudinally through the center of its head and shank.

The bolt was first turned into the nut for full engagement. The strand was then jacked using a stand-off to resist the jacking force, and the strand chuck was seated with the use of a purpose-built device that is shown in Figure 2.21. This device was fabricated from a steel tube that had a series of male threads on one end (which was screwed into the female threads of the strand chuck), and a head on the other end (which was engaged by the ram piston during stressing). After seating the chuck onto the strand, the STD bolt was backed out of the nut until the head of the bolt engaged the load cell. The strand was then released, allowing the chuck to bear onto the load cell, which bore onto the STD, which bore onto a steel plate that was embedded into the end of the column. Some stress was inevitably lost as the chuck seated fully (the pull-in slip of the chucks was approximately ¼ in.), but that stress was regained by manually turning the bolt outwards until the load cell indicated that the desired 6 kips load was in the strand.

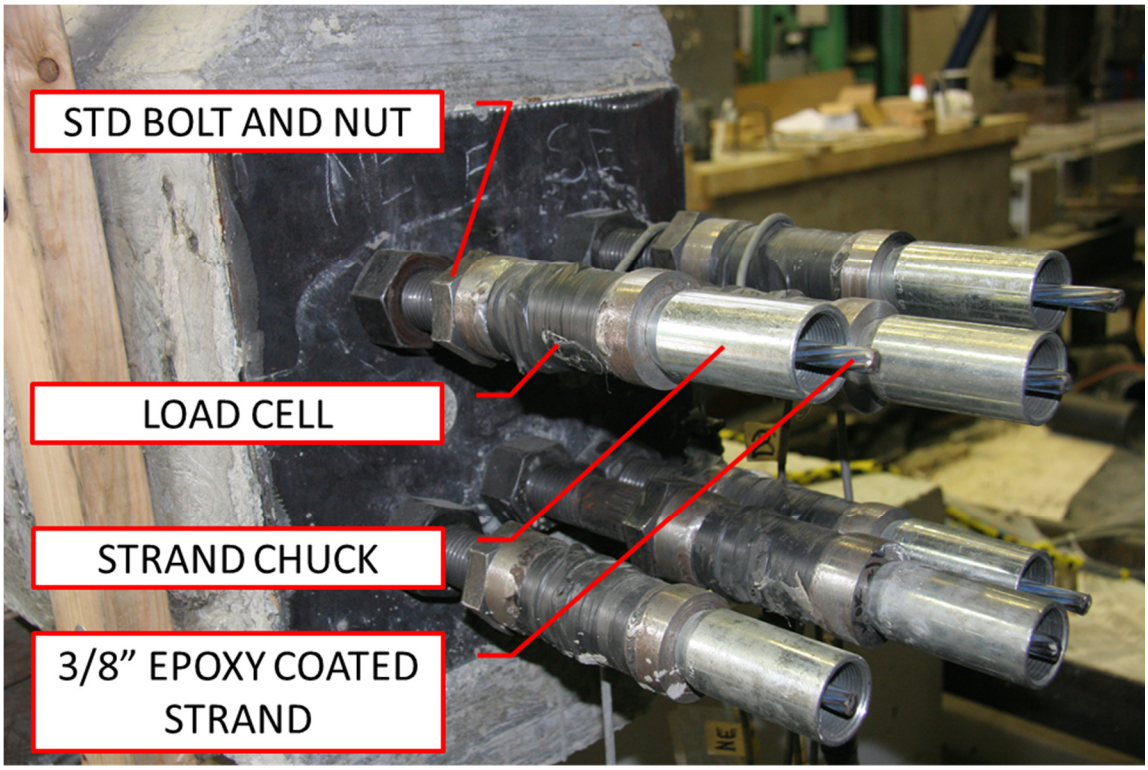

Figure 2.19 STD's, load cells, and chucks used to externally anchor the strands at the top of the column.

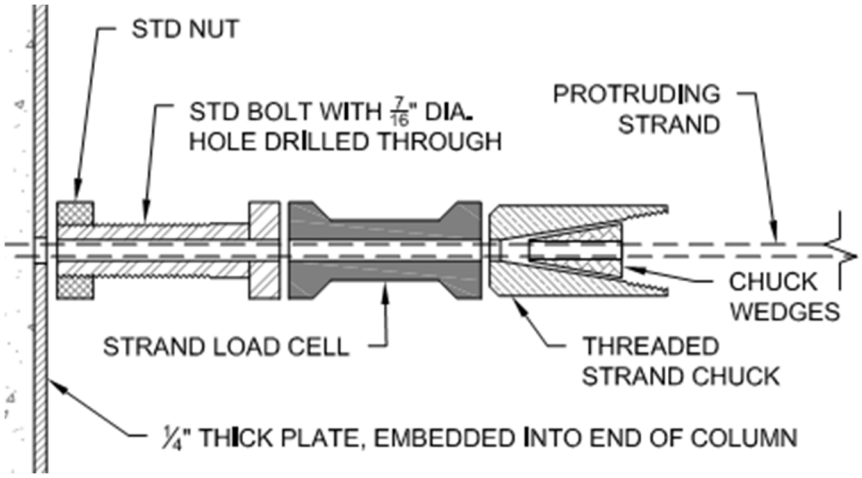

Figure 2.20 Schematic of strand anchorage at end of column.

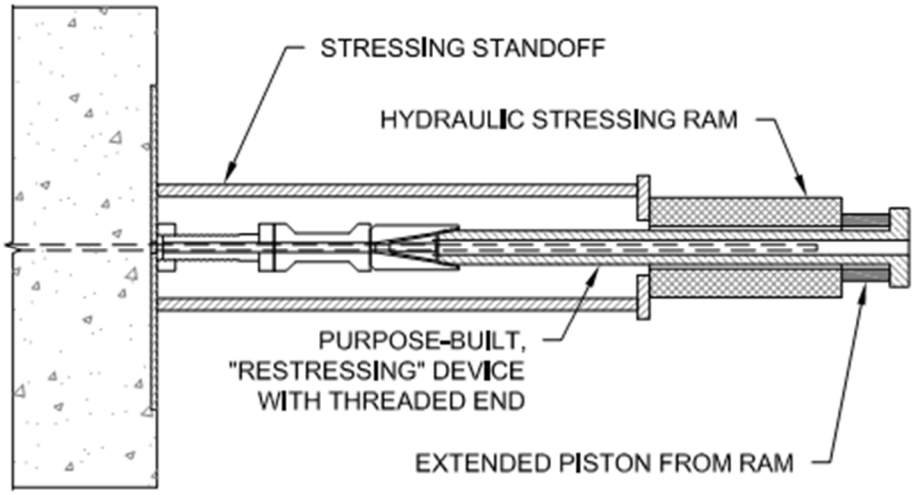

Figure 2.21 Schematic of re-stressing assembly.

This procedure, and especially the presence of the STD's, was adopted for three reasons. First, the strand chucks were needed to prevent system failure if the bond failed. Second, the re-stressing technique allowed some prestress in the strand between the chuck and the end of the column, thereby reducing the strain change before the chuck takes up the full load after a bond failure. Last, the STD's facilitated removal of the load cell and chuck after the test.

The strain gauges on the west-most strand indicated that it had slipped during the release and had lost a significant amount of its prestressing strain. Therefore, this strand was set to an anchorage load of 14 kips (165 ksi), which corresponded to Davis's design for the effective prestressing force on each strand.

2.9.2 Cap Beam Construction

The cap beam was built with ordinary techniques used in precast, non-prestressed construction. The increased sizes of the socket connection ductwork (relative to the PreT-CB-CONC specimen)

did not allow for passage of the longitudinal No. 7 bar bundles between the central 12 in. duct and the outer 2 in. ducts. As a result, all longitudinal rebar was concentrated in the corners of the beam's cross-section. Figure 2.22 shows the end elevation of the cap beam cage.

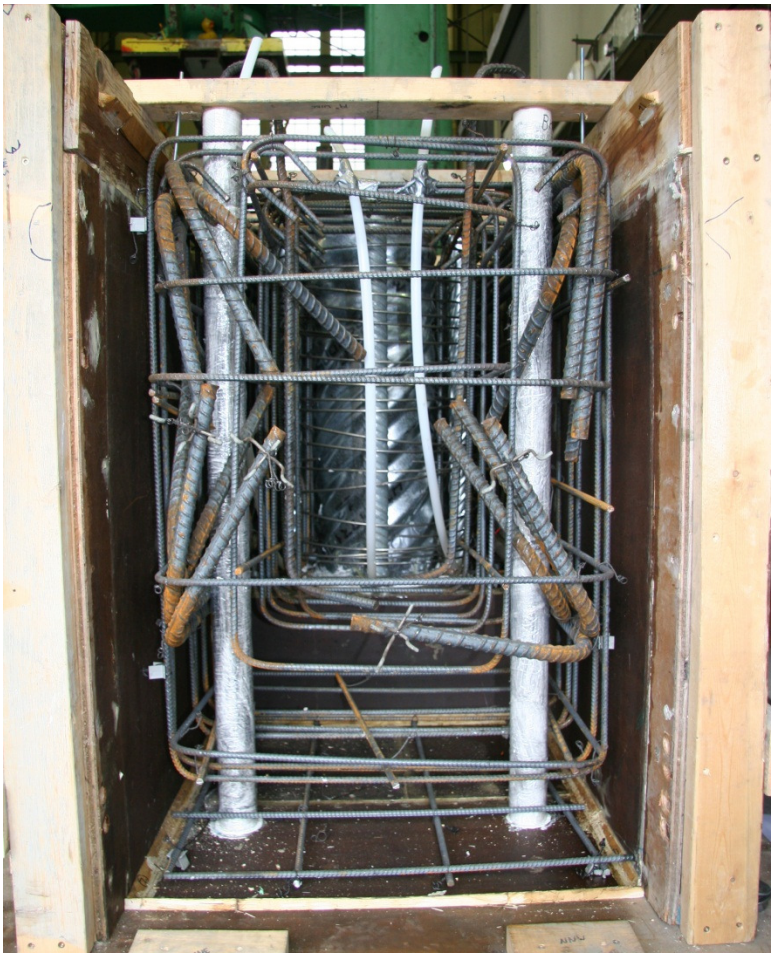

Figure 2.22 End elevation of cap beam reinforcing cage.

The hoop widths of the rectangular stirrups for the cap beam were not changed. Therefore, the relocation of the longitudinal reinforcement produced "empty" corners in the stirrups. In strut-and-tie terms, if one of these empty corners were to act as a node for a compression strut, there would be no longitudinal tension force available to maintain equilibrium of the node. Therefore, longitudinal No. 3 bars were added to the beam cage at these corners. However, the inclusion of these No. 3 bars was still made difficult by the size of the central duct. Therefore, the top and bottom of the duct was permanently compressed such that the duct's cross-section became elliptical at the ends (with a 10.5 in. narrow diameter). This narrowing of the duct permitted the passage of No. 3 bars between the large central duct and smaller exterior ducts, but did not jeopardize the fitting of the column extension into the cap beam.

The cap beam was cast at the same time as the column (from the same concrete load). The cap beam concrete was also internally vibrated during placement, and the form sides were continually tapped to prevent honeycombing or bug hole defects.

2.9.3 Socket Connection

2.9.3.1 Construction Orientation for Specimen

The socket connection between the column and cap beam was completed in the experimental ("upside-down") orientation. That is, the cap beam was placed on the ground, the column was lifted with a crane, and then the extensions of the column were fitted into the beam's ductwork.

This process differed from the field construction of the connection (which was used by Davis et al. for PreT-CB-CONC), where the bent columns would be erected and braced, and the precast cap beam would then be lifted and set onto the columns. The "upside-down" erection procedure was adopted to avoid the need for inverting the system in the laboratory, but it affected the grouting operation for the connection. In the field, it would be expected that the shoulder of the column (the circular steel plate) would be buttered with the fiber-reinforced grout, and then the cap beam would be lowered onto it. Then, the connection ductwork could be filled with grout by simply pouring fluid grout into the open tops of the ducts, which was done for PreT-CB-CONC (Davis, 2013).

2.9.3.2 Alignment, Fitting, and Shimming

The PreT-CB-ROCK connection, was completed by first dry-fitting the column extensions with the ducts in the cap beam. Alignment proved to be straightforward, and is shown in Figure 2.23 and Figure 2.24.

Figure 2.23 Fitting of the column-to-cap beam socket connection.

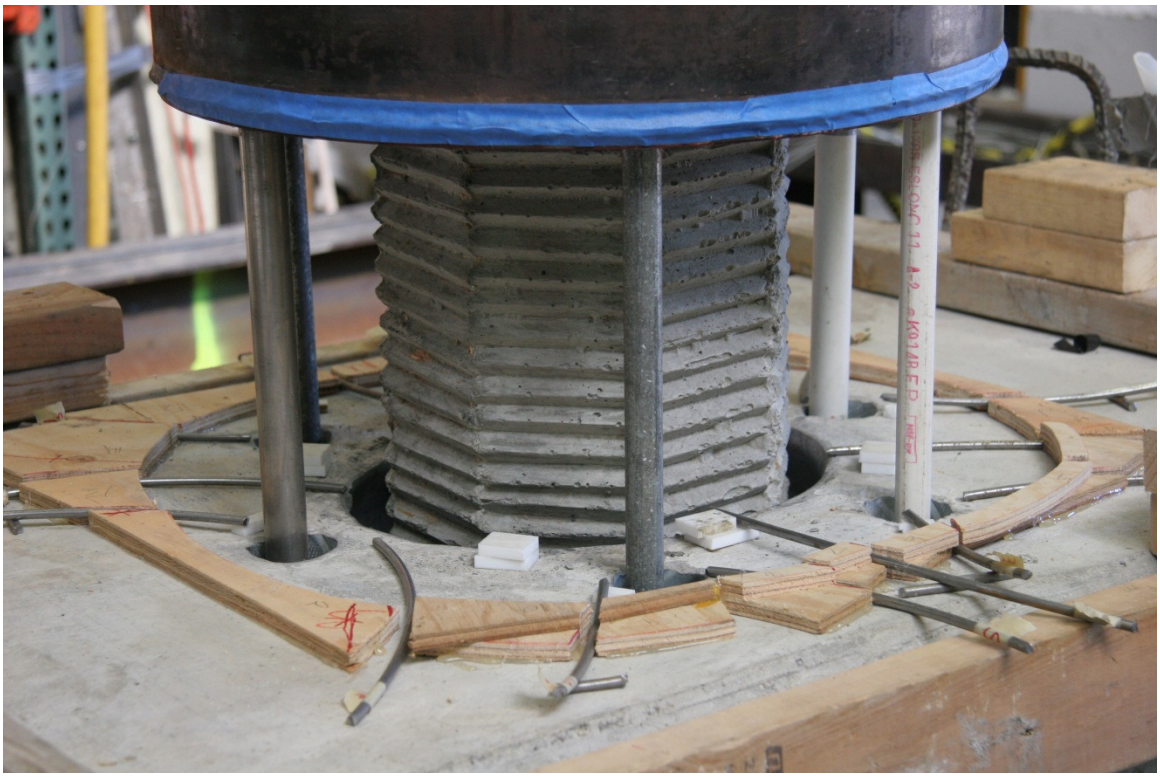

Figure 2.24 Alignment of column extensions into cap beam ducts.

Half-inch thick pieces of PTFE were laid on the top surface of the cap beam, around the central duct, in order to serve as shims for the column (which can also be seen in Figure 2.24). Additional shimming was used in order to ensure an orthogonal alignment between the column and cap beam.

2.9.3.3 Grout Pad Placement

Before placing the fiber-reinforced grout for the pad, flexible, ¼ in. diameter, plastic tubing was laid on top of the cap beam in order to form bleed vents in the grout pad. The tubes were used to form two bleed vents between each duct and the perimeter of the pad (two additional vents were formed for the central duct). In Figure 2.24, it is noted that pieces of steel wire are shown on top of the cap beam; these were not used for the actual construction operation, and were eventually replaced with the tubing (photo was not available).

Fiber-reinforced grout was then placed on top of the cap beam, around the connection ductwork. The column was lowered so that any excess grout squeezed out of the ½" thick space between the baseplate and cap beam (the grout material either fell through the then-empty ductwork or seeped outward past the perimeter of the column's steel tube). The grout was allowed to stiffen and any excess material that had squeezed out of the space between the column plate and cap beam was cut away so that the perimeter of the grout pad matched the circumference of the baseplate; the plastic tubing was also extracted from the pad at this time.

This operation left a residual "cusp" in the grout pad underneath the fillet weld with the tube, which is shown schematically in Figure 2.25. It had no structural significance.

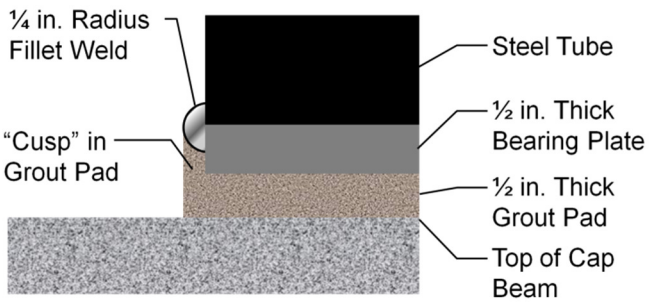

Figure 2.25 Section of grout pad interface showing cusp in pad.

Furthermore, because the finished, top face of the cap beam was not perfectly smooth around the connection ductwork, and the baseplate was shimmed so that the column and cap beam were orthogonal, the resulting grout pad was not exactly ½ in. thick at all locations. After shimming, the void space between the cap beam and baseplate was ~$^{7}/_{16}$ in. on the north side, but ~$^{12}/_{16}$ in. on the south side. Figure 2.26 shows measurements of the two dimensions.

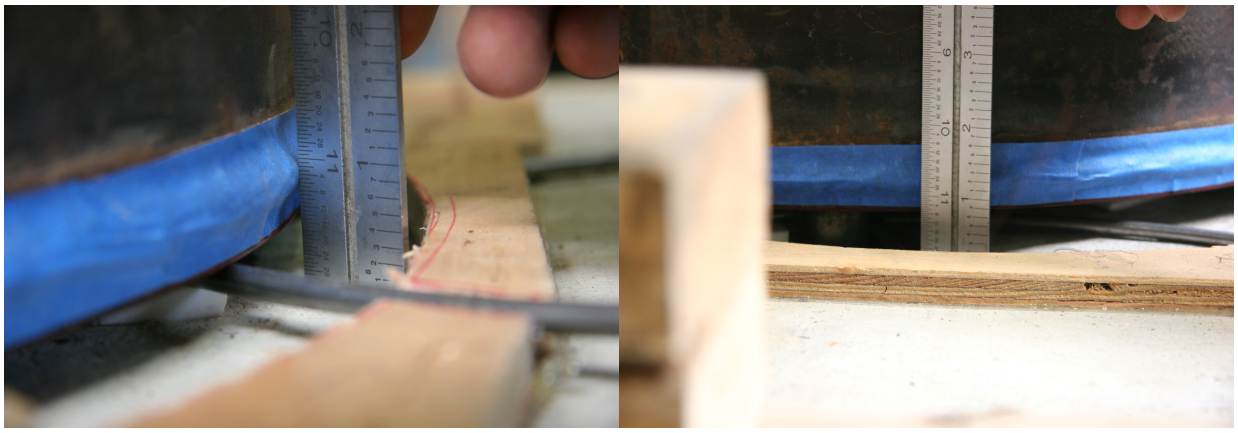

Figure 2.26 Void between baseplate and cap beam on connection's north side (left) and south side (right).

2.9.3.4 Ductwork Grouting

After the grout pad had set up, the ductwork was grouted. This was done by first plugging the bottom of each duct (the duct openings at the bottom of the 31.5" depth section). Half-inch diameter, plastic grout tubes were then used to pump fluid grout into each duct, using. These grout tubes were set into the cap beam cage prior to the concrete pour, and were specifically manufactured for grout pumping operations. The grout tubes ran from the top of the finished face of the cap beam to holes cut into the bottoms of each duct. Figure 2.27 offers a schematic of one such grout tube in the specimen, Figure 2.28 shows several grout tubes running to their respective ducts, and Figure 2.29 is a photograph of a typical connection of a grout tube to the bottom of a duct. A low-pressure, commercially available grout pump was used for the operation.

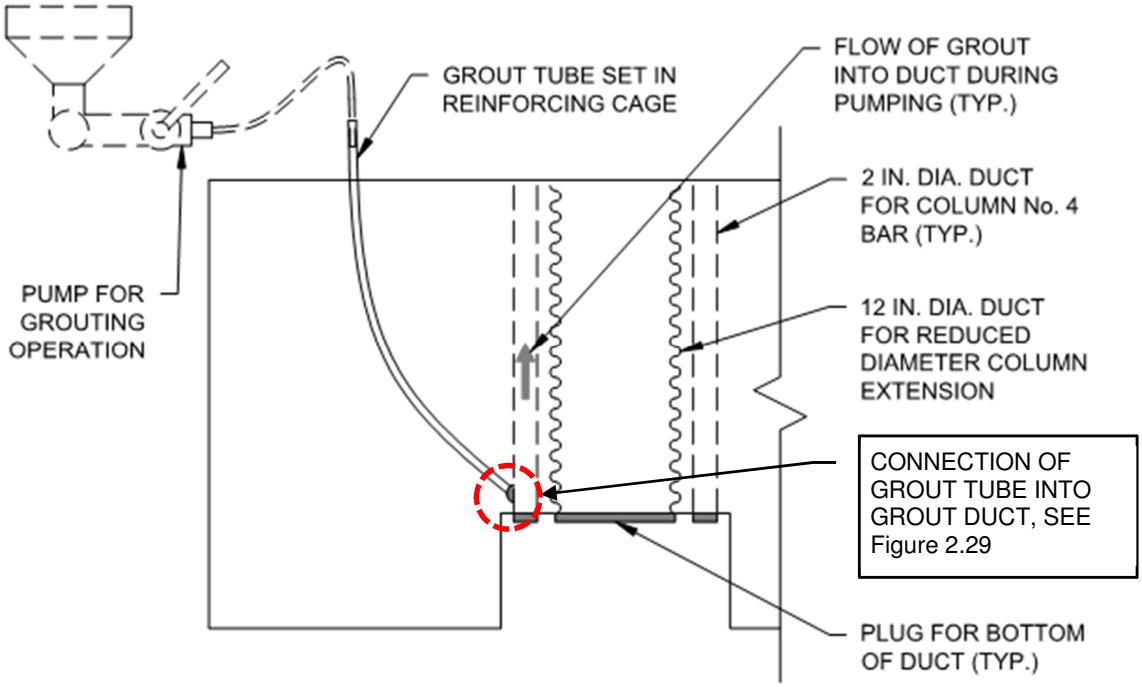

Figure 2.27 Schematic of grout tube in cap beam.

Figure 2.28 Grout tubes running to connection ductwork.

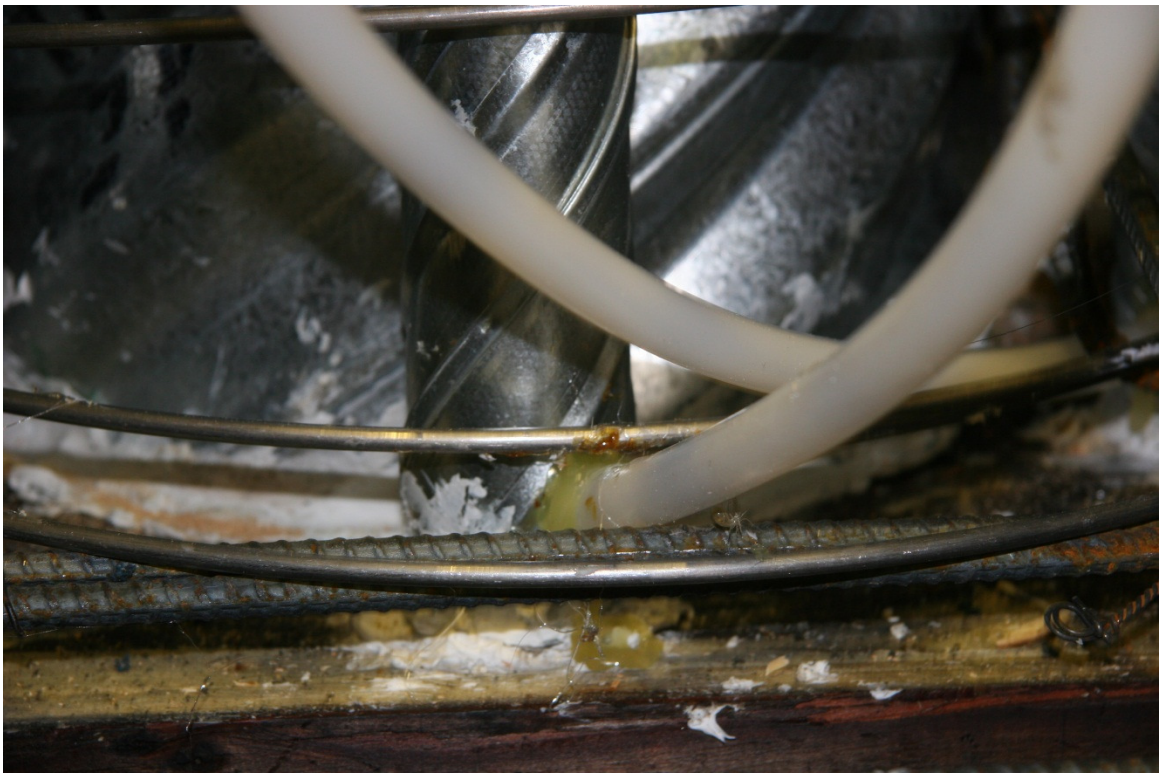

Figure 2.29 Typical connection of a grout tube into bottom of duct.

The grout was pumped into each duct until grout squirted from the bleed vents that were formed in the grout pad. Figure 2.30 shows pumped grout seeping from the bleed vents.

Figure 2.30 Pumped grout seeping from a bleed vent in the grout pad (excess grout was allowed to stiffen, and was then removed).

2.9.3.5 Summary

The connection required two days to complete: one day for the grout pad placement and one day for the pumping operation. The two different operations were chosen because fibers were used for the interface grout but not for the ducts. The latter choice was made because pumping fiber-reinforced grout into a duct might be difficult without a high-pressure pump, and because previous work (Steuck et al., 2009) had shown that using fiber-reinforced grout produced results that were no better, and were in some cases worse, than grout without fibers (with respect to bond with longitudinal reinforcement).

In the field, the duct grout would be poured from above, so no pump would be needed and the fluid pressure in the grout would be very low. Therefore, it may be possible to install both grouts in a single day because the buttered fiber-reinforced grout at the interface would likely provide a seal good enough to prevent leakage of the duct grout, even before the former had fully set up.

3 Experimental Setup

This chapter discusses the test setup (Section 3.1), instrumentation (Section 3.2), and testing protocol (Section 3.3).

3.1 TEST SETUP

The test setup is shown in Figure 3.1. A servo-controlled MTS actuator, attached to a self-reacting frame, provided the horizontal loads, while the laboratory Baldwin Universal Testing Machine provided the vertical loading.

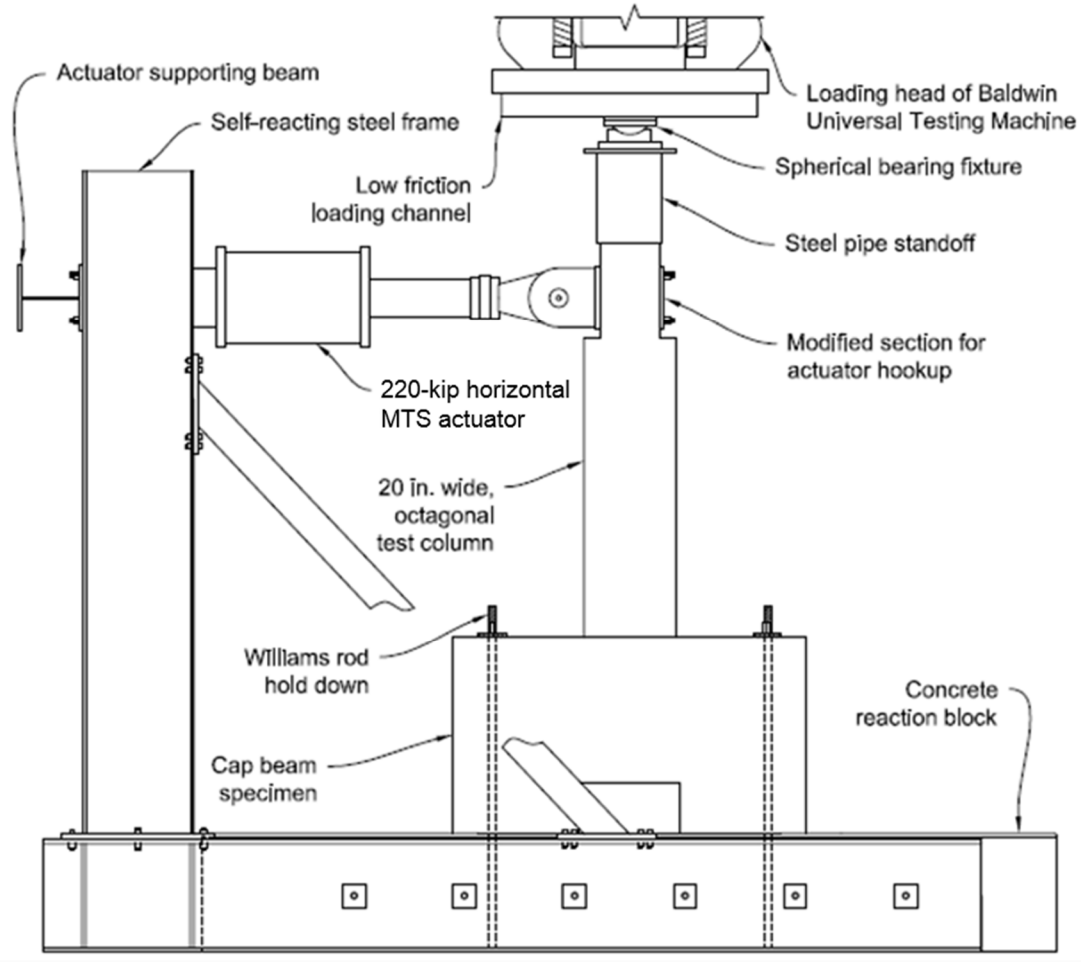

Figure 3.1 Self-reacting frame and Baldwin Universal Testing Machine (adapted from Stephens, 2014).

The self-reacting frame was constructed of structural steel sections and a large reinforced concrete reaction block. Two steel W24x103 sections, which were tensioned to the sides of the reaction block, formed the base of the reaction frame. These horizontal beams were connected to

two W24x94 steel columns, which were stiffened by diagonal, HSS 6x6x$^3/_8$ braces. Finally, a W14x90 crossbeam bridged between the two columns of the frame, and supported a horizontal 220-kip MTS actuator.

The PreT-CB-ROCK specimen was lifted and placed at the center of the concrete reaction block. The cap beam was then shimmed so that the column was vertically plumb. Hydrostone (a high-strength, fast curing gypsum plaster) was then poured into the gap between the cap beam and reaction block to ensure that the specimen was fully in contact with the reaction block. Finally, 1.25-inch-diameter, threaded Williams rods were used to secure the cap beam to the reaction block. The Williams rods ran through four preformed ducts in the cap beam to anchor points in the reaction block. Each rod was then tensioned to a force of approximately 80 kips. This arrangement prevented overturning and sliding of the specimen on the block.

The horizontal load from the 220-kip MTS actuator was applied to the 13 in., reduced depth section at the top of the column (detailed in Section 2.5). The actuator was connected to the column with the use of four, tensioned, one-inch-diameter, threaded rods. These rods were run through ducts in the reduced depth section of the column and they bolted the head of the actuator to a steel plate placed on the opposite face of the column.

The vertical load from the Baldwin Universal Testing Machine was applied to the top of the specimen with the use of several bearing components, which are shown in Figure 3.2. The entire assembly is shown in Figure 3.3. A channel lined with greased stainless steel was bolted to the Baldwin loading head in order to prevent lateral motion, but to permit longitudinal motion, of the top of the column during the test. A greased, PTFE clad, bearing plate was then inserted in the channel in order to minimize sliding friction from the column's movement. This plate transferred the vertical load to a greased, spherical bearing fixture that accommodated the rotation of the top of the column during the test. Finally, the spherical bearing fixture transferred the vertical load to a standoff placed on top of the column. The standoff was composed of a steel tube with a square plate welded at one end. This standoff was required to accommodate the STD's (the "screw thread devices" discussed in Section 2.9), load cells, chucks, and strands that protruded from the top of the column.

Figure 3.2 From upper-left: PTFE clad bearing plate, ungreased top spherical bearing, greased bottom spherical bearing, and standoff used to transfer the vertical load from the Baldwin.

Figure 3.3 Bearing assembly with stand-off on top of PreT-SF-ROCK (Schaefer et al., 2014a), an identical setup was used for the PreT-CB-COCK test.

3.2 INSTRUMENTATION

A summary of the instrumentation used during the PreT-CB-ROCK test is given in Table 3.1. Figure 3.4 shows the typical locations of each type of external instrument used for the experiment; see Figure 3.6 for the strain gauge plan.

Table 3.1 Summary of instrumentation.

Instrument Type	Measured Response	Total Used	Number in Figure 3.4
Baldwin load cell	Vertical load	1	-
MTS load cell	Horizontal load	1	-
MTS LVDT	Actuator displacement	1	-
Linear potentiometers	Specimen displacements	7	1 – 3
String potentiometers	Column displacements	6	4 - 9
Inclinometers	Column rotations	4	10 – 13
Linear potentiometers	Rocking plate displacements	4	14 – 16
Load cells	Force changes in anchored end of strands	6	17 – 19
Three-wire strain gauges	Strains in reinforcing bars and spiral	48	-
Two-wire strain gauges	Strains in strands and dowel bar	14	-
Strain-gauge rosettes	Strain state of steel tube	2	-
Motion capture cameras	Column displacements	2	-
Analog video camera	Video recording of test	1	-

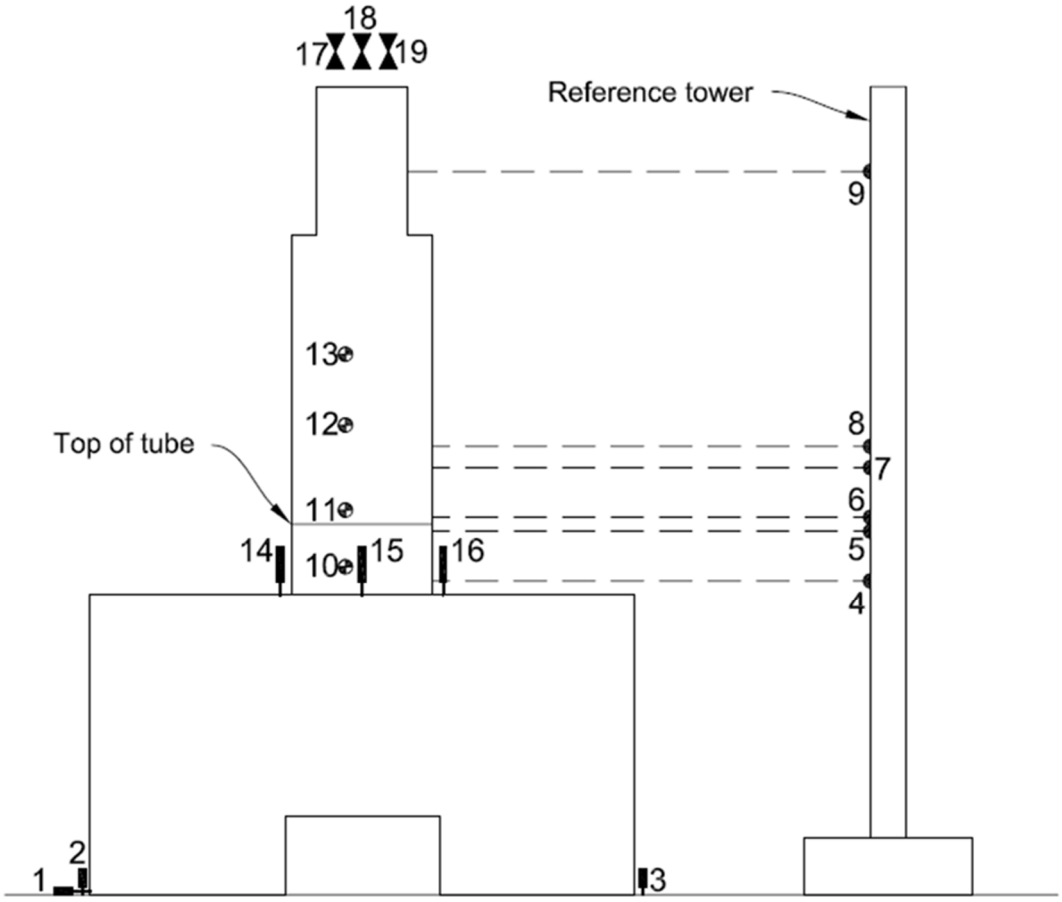

Figure 3.4 East elevation of external instrumentation setup; load cells for applied forces, Optotrak system, and rig displacement instruments not shown. The instrument numbering follows Table 3.1.

3.2.1 Applied Loads

The horizontal and vertical loads from the MTS actuator and Baldwin Universal Testing Machine were recorded with internal load cells.

3.2.2 MTS LVDT

The displacement of the MTS actuator's piston relative to its body was recorded with an internal linear variable differential transformer (LVDT).

3.2.3 Linear Potentiometers to Measure Rig and Specimen Base Displacement

A linear potentiometer was used to measure the deflection of the W14x90 actuator beam. This potentiometer was anchored to a fixed reference tower throughout the test. The sum of this displacement and the MTS LVDT reading gave the total displacement of the column at the centerline of the MTS actuator. This value was later compared with the displacement recorded by a string potentiometer in the same location (see Section 3.2.4).

Linear potentiometers were also used to measure the potential overturning and slip of the concrete reaction block on the floor of the structures laboratory. Additional linear potentiometers were used to measure the potential relative motion (slip and overturning) of the cap beam relative to the reaction block (instruments 1-3 in Figure 3.4).

3.2.4 String Potentiometers

String potentiometers were used to measure the column's lateral displacement. The string potentiometers ran from attachment points on the north face of the column to an unloaded reference tower that was anchored to the reaction block. The string potentiometers were attached at column elevations of 2", 9 $^3/_8$", 11 ½", 17 $^3/_8$", 22 ½", and 60" (the centroid of the applied lateral load) above the top of the cap beam.

The elevation of 2" was selected in order to detect any significant slipping of the baseplate on top of the mortar pad. As a pair, the potentiometers at 9 $^3/_8$" and 11 ½" were expected to detect concentrated deformation of the column where its section transitioned from the confining tube to 20" diameter octagon. The pair of potentiometers at 17 $^3/_8$" and 22 ½" were used to maintain instrumentation consistency with the PreT-SF-ROCK-HyFRC test. That column specimen had hybrid fiber-reinforced concrete (HyFRC) in its bottom 20", and a crack plane was anticipated at the transition from HyFRC to normal concrete. Finally, the potentiometer at 60" provided an additional measurement for the top displacement of the column. Redundancy in this measurement was deemed desirable because it was the most important displacement of the test.

3.2.5 Inclinometers

Inclinometers were used to directly measure the rotation of the column. These instruments were attached to the east face of the column at elevations of 4", 12", 24", and 34" above the cap beam. These elevations were selected in order to provide consistency with the string potentiometer instruments, and with previous pre-tensioned column experiments.

3.2.6 Linear Potentiometers to Measure Tube Movement

Linear potentiometers with their axes vertical were attached to the north, south, east, and west sides of the steel tube. The plunger tips of these potentiometers were set on glass microscope slides, which were glued to aluminum plates set on top face of the cap beam. These potentiometers measured the local vertical displacements at locations around the tube as entire assembly rocked on the grout pad. The instruments were used in order to determine the location of the connection's neutral axis. Figure 3.5 shows the potentiometer that was placed on the west side of the tube.

Figure 3.5 Linear potentiometer used to measure movement of steel tube.

3.2.7 Strand Load Cells

Load cells were placed between the STD and chuck of each strand at the top of the column, as shown in Figure 2.20. These load cells were custom-built for this purpose, and were calibrated before use. During the test, a significant change in the force measured by the load cell would indicate slipping of the strand along its bonded length at the top of the column. Load cells were only used at the top, because the bonded length was shorter in that end of the column (18 in. at the top versus 31.5 in. in the reduced diameter section). It was expected that if strand slip were to occur, it would happen first at the top, and slip would be detected by the load cells there.

3.2.8 Strain Gauges

Two-wire strain gauges, three-wire temperature-compensating strain gauges, and strain-gauge rosettes were used in the experiment. Figure 3.6 shows the locations of the strain gauges.

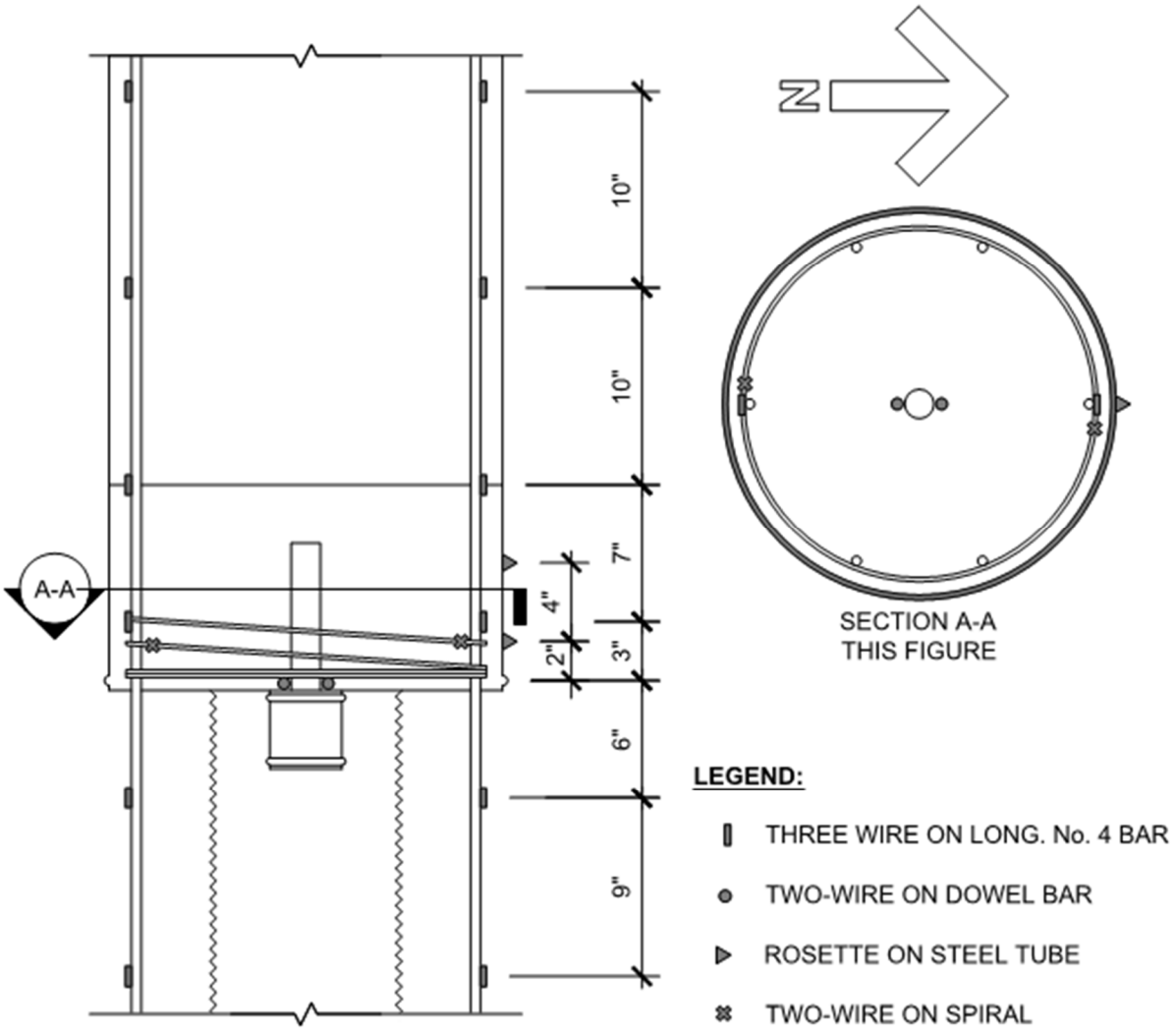

Figure 3.6 East elevation (left) and section (right) of strain gauge plan; strands and No. 6 bars are not shown.

3.2.8.1 Prestressing Strands

Before stressing, pairs of two-wire strain gauges were applied to each prestressing strand. Pairs of gauges were used at each location to provide instrumentation redundancy. Two-wire gauges were used because the strand wires were too narrow for the placement of available three-wire gauges. Prior to placement, the epoxy coating was stripped off the strand using a power-operated wire brush at the application point for the gauges. The individual strain gauges of each pair were applied to different wires on the strand, on approximately opposite sides of the strand. These strain gauges were applied to each strand so that they would be roughly 15 in. above the rocking interface during the test.

The data acquisition system used during the prestressing operation only had the twelve strand strain gauges and the strand load cells hooked up. Prior to the test, these instruments were disconnected from the original acquisition system, connected to another data acquisition system (along with the rest of the testing instrumentation), and zeroed. The offset readings for these

instruments were recorded prior to switching data acquisition systems, which were added to the measurements recorded during the test.

3.2.8.2 Bonded Reinforcement

The north and south No. 4 reinforcing bars were instrumented with pairs of three-wire strain gauges. Taking the rocking interface as a "zero-elevation", the pairs were applied at elevations of -15" (three inches below the debonded length of the rebar), -6" (midpoint of the debonded length), +3", +10", +20", and +30". The gauges were applied on opposite faces of the bars at these elevations.

The northeast and southwest (discontinuous) No. 6 reinforcing bars were also instrumented with pairs of three-wire strain gauges. Using the previously defined elevation reference, these bars were instrumented at elevations of +3", +6", +10", +20", and +30". These locations were chosen to detect important stains in the bar, which were expected to be tension strain at or near the potential crack at the top of the steel tube on the tension side, and compression near the baseplate on the compression side.

The spiral was instrumented with a total of four strain gauges (two pairs of three-wire gauges). These pairs were applied as close as possible to the interior face of the rocking plate. Because of the anchorage detail used to terminate the spiral inside the steel tube, the gauge pairs were applied at elevations of roughly 2.5" on the north face of the column and 3.25" on the south face of the column.

3.2.8.3 Dowel Bar and Steel Tube

The dowel bar was also instrumented with strain gauges. This bar was intended to provide shear resistance across the rocking interface in addition to the shear friction between the grout pad and steel baseplate (as discussed in Section 2.5.3). The bar was placed so that it was embedded in the steel-tube confined concrete and ran into a tubular housing placed inside the reduced diameter section of the column, as shown in Figure 2.11. As the top of the column was displaced, the free end of the bar was meant to bear against the side of the housing fixture, effectively behaving as a cantilever beam (see force diagram of Figure 2.12). Two-wire strain gauges were placed on the north and south faces of the dowel in order to measure the bending strains of the bar from which the shear force could be deduced.

Before the test, strain-gauge rosettes were applied to the northern, exterior face of the steel tube. These instruments were applied in order to determine the two-dimensional strain state of the steel tube during the test. The rosettes were composed of three, stacked, two-wire strain gauges that were oriented at 0°, 45°, and 90°. Rosettes were placed at elevations of +2" and +6", and can be seen in Figure 3.7.

3.2.9 Optotrak Motion Capture System

A three-dimensional motion capture system was used to record the kinematics of the specimen. Two Optotrak cameras, which can track the three-dimensional motion of specialized light emitting diodes (LED's), were used in the system. LED's were applied on the center of the north, west, and south faces of the column at vertical spacings of 2 in. (for the bottom 20 in. of column) and 4 in. (for the middle 20 in. of column). Figure 3.7 shows the placement of some of these LED's.

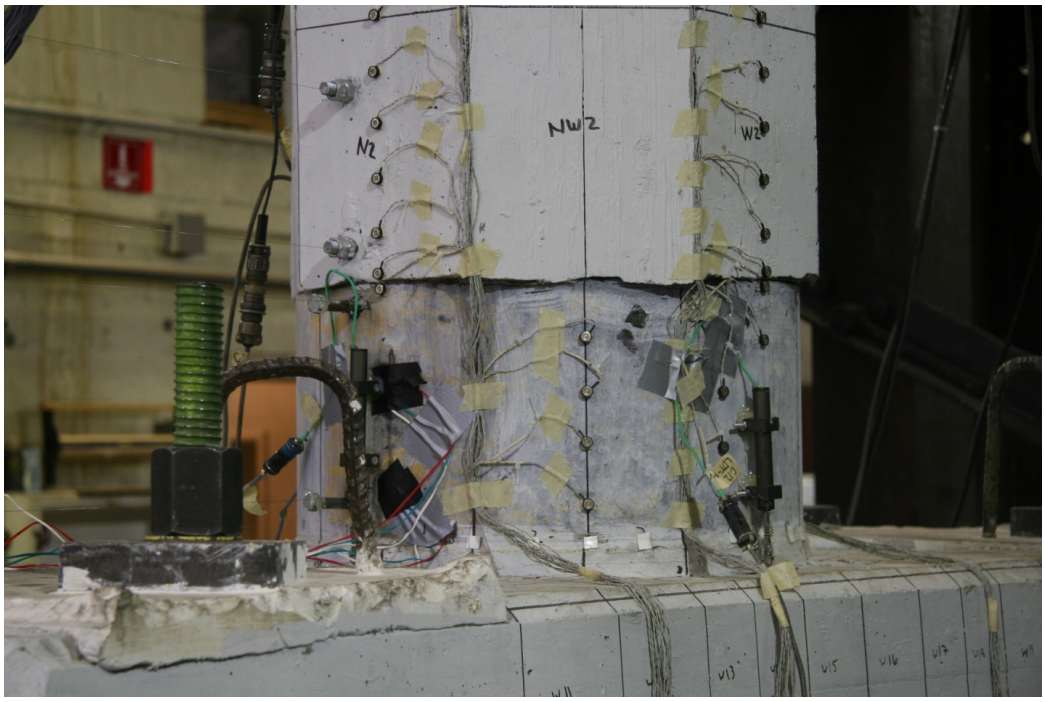

Figure 3.7 LED's applied to north and west faces of column.

LED's were also placed along the bottom edge of the steel tube. Some of these LED's can be seen in Figure 3.7. Many of the LED targets at the base, however, were largely obstructed from the view of the motion capture cameras and rarely gave readings during the test.

3.2.10 Analog Video Camera

To act as a backup, the entire test was video recorded.

3.3 TESTING PROTOCOL

3.3.1 Primary Test

The PreT-CB-ROCK specimen was loaded both vertically and laterally. A vertical load of 159 kips was applied to the column. This load was calculated as the unfactored dead load for a prototype bridge column (scaled to 42% lab scale) according to AASHTO LRFD Specifications (AASHTO, 2009). It was kept constant during the test using servo-controls on the Baldwin Universal Testing Machine. The lateral displacement history was modified from the NEHRP recommendation for the testing of precast structural walls (Building Seismic Safety Council, 2004). Both the vertical loading and lateral displacement history have been used in similar tests at the University of Washington (Davis et al., 2012 and Schaefer et al., 2014a, for example).

A trial cycle was completed the day before the large-displacement test. This trial was done to ensure that: the Baldwin Universal Testing Machine and 220-kip horizontal actuator were operating properly, all external instruments were functioning, and the strain gauges were correctly connected to the data acquisition computer. A reduced vertical load of 90 kips and a continuous drift cycle of ±0.05% were applied to the column for the trial cycle.

The test lateral displacement history is given in Table 3.2 and is shown in Figure 3.8. It was composed of ten sets of cycles, with four drift cycles per set (for a total of 40 cycles for the entire test). The target drift ratios of the first set were selected so that the system would remain elastic. For the four cycles of each succeeding set, the target drift ratios were selected according to the following algorithm: 1.2X, 1.44X, 1.44X, and 0.48X (where "X" is the maximum drift ratio of the preceding set). Furthermore, the amplitude coefficients within one set were related: $1.2^2 = 1.44$ and $1.44 / 3 = 0.48$.

Table 3.2 Target displacement history (adapted from Finnsson, 2013).

Set	Cycle	Drift (%)	Displacement (in.)
1	1	± 0.33	± 0.20
	2	± 0.40	± 0.24
	3	± 0.40	± 0.24
	4	± 0.13	± 0.08
2	1	± 0.48	± 0.29
	2	± 0.58	± 0.35
	3	± 0.58	± 0.35
	4	± 0.19	± 0.12
3	1	± 0.69	± 0.41
	2	± 0.83	± 0.50
	3	± 0.83	± 0.50
	4	± 0.28	± 0.17
4	1	± 1.00	± 0.60
	2	± 1.19	± 0.72
	3	± 1.19	± 0.72
	4	± 0.40	± 0.24
5	1	± 1.43	± 0.86
	2	± 1.72	± 1.03
	3	± 1.72	± 1.03
	4	± 0.57	± 0.34
6	1	± 2.06	± 1.24
	2	± 2.48	± 1.49
	3	± 2.48	± 1.49
	4	± 0.83	± 0.50
7	1	± 2.97	± 1.78
	2	± 3.57	± 2.14
	3	± 3.57	± 2.14
	4	± 1.19	± 0.71
8	1	± 4.28	± 2.57
	2	± 5.14	± 3.08
	3	± 5.14	± 3.08
	4	± 1.71	± 1.03
9	1	± 6.16	± 3.70
	2	± 7.40	± 4.44
	3	± 7.40	± 4.44
	4	± 2.47	± 1.48
10	1	± 8.87	± 5.32
	2	± 10.65	± 6.39
	3	± 10.65	± 6.39
	4	± 3.55	± 2.13

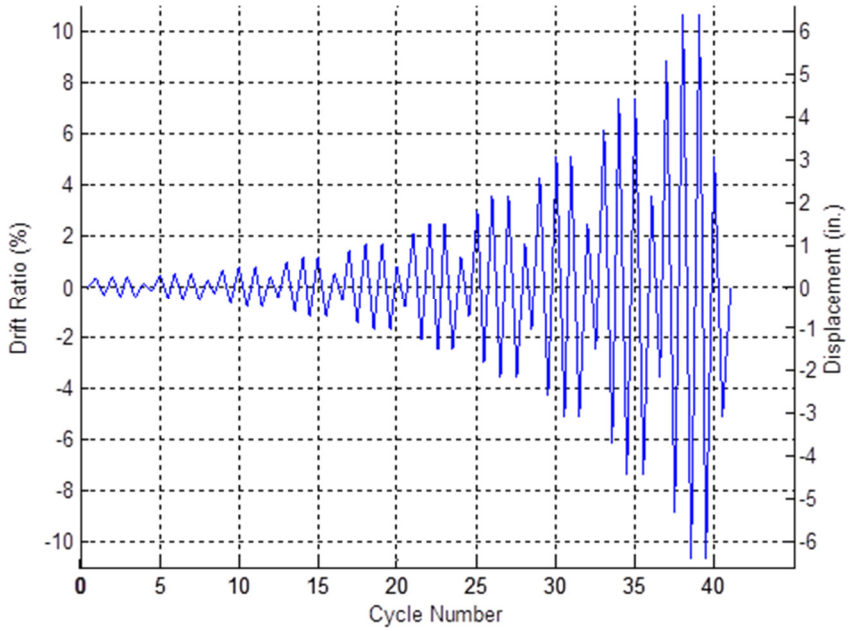

Figure 3.8 Graphical representation of target displacement (adapted from Finnsson, 2013).

The experiment was conducted under displacement control. The cycle displacements for the horizontal actuator were calculated by multiplying the target drifts by 60 in. (the distance between the center of the horizontal actuator and the top of the cap beam). These target displacements were input directly into the MTS controller, and were not increased to compensate for the deformation of the self-reacting steel frame (shown in Figure 3.1). Therefore, the actual, imposed drifts were slightly smaller than those listed in Table 3.2.

For the test, drifts in the south direction of the laboratory were identified as positive drifts, and drifts in the north direction were identified as negative. The maximum positive and max-absolute negative drifts for a cycle were referred to as the "peak" and "valley" drifts respectively. The displacement was paused at peak and valley drifts for the first two cycles of every set. The specimen was inspected for damage and crack propagation during these pauses. The third and fourth cycles of each set were run continuously, with inspection occurring only at zero drift after the end of each cycle.

For the first six sets of the test, each displacement cycle had a total time of 80 seconds (not including the pauses after peaks and valleys). The cycles of sets seven, eight, and nine were completed in a total time of 120 seconds each, and the tenth set cycles were completed in 4 minutes each. This control setup provided an approximately constant displacement rate for the test.

3.3.2 Residual Displacement Cycles

Several residual displacement cycles were completed after the primary testing. These cycles were completed in order to observe the response of the system without axial load, and to determine the extent of strand yielding from the main test by observing the residual displacement when the lateral load was removed. Before the residual displacement cycles were imposed, the remaining, unfractured, northwest, No. 4 longitudinal bar of the column was deliberately cut (five of the six

No. 4 bars fractured during the primary test). This resulted in a connection in which only the yielded column strands crossed the column-to-cap beam interface.

The residual cycles were also conducted under displacement control. The top of the column was displaced to incrementing drift ratios (±1.0%, ±2.0%, ±3.0%, ±4.0%). The additional testing was stopped after the ±.4.0% cycle because the bearing configuration became unstable in the absence of vertical load.

The following instruments were used during these cycles:

- horizontal actuator load cell and LVDT,
- strand load cells, and
- linear potentiometers on the north and south faces of the tube (measuring the tube liftoff from the grout pad).

The remaining external instrumentation was disconnected before the residual cycles, and the column strain gauges were not reconfigured prior to the additional testing. All cycles were run continuously and the specimen was not photographed or inspected for damage during the residual testing.

4 Observed Response

Visual and audible observations were made to evaluate the behavior and damage progression of the PreT-CB-ROCK subassembly test. The damage progression was documented with crack width measurements, crack sketches, photographs, videotaping, and qualitative assessments. Prior to the testing, thinned latex paint was used to whitewash the specimen, which aided the visual detection of cracking. The observed damage progression of PreT-CB-ROCK is detailed in this chapter. Additional test photographs can be found in Appendix C.

4.1 GENERAL OBSERVATIONS

The system deformed with the intended, rocking behavior. That is, it appeared that most of the applied displacement at the top of the column was accommodated by the concentrated rotation of the connection. Especially for higher drifts, the baseplate bore on the outer quarters of the grout pad, although physical measurements were not taken for this dimension. Figure 4.1 shows the column rocking on the south side of the grout pad, during the Set 10-Cycle 3 peak near the end of the test (drift ratio of ~+10.42%). Figure 4.2 shows the entire column during the applied valley drift of that same cycle (drift ratio of ~-10.40%).

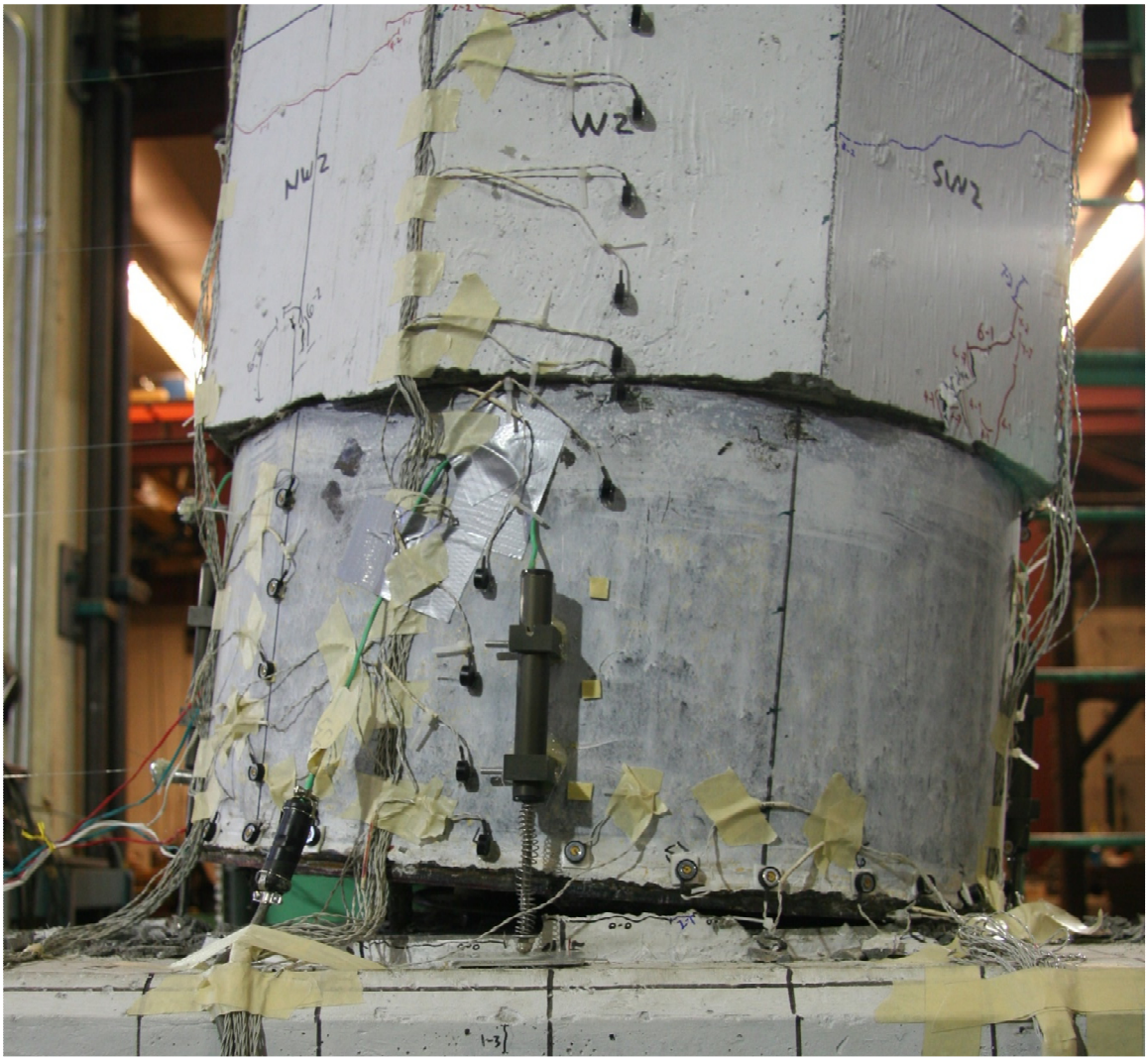

Figure 4.1 The column base rocking on the south side of the grout pad during the maximum positive drift of the test (photo taken from west side of specimen).

Figure 4.2 PreT-CB-ROCK being displaced to the minimum valley drift of the test (photo taken from southwest of specimen).

Uplift or rocking of the cap beam base on the reaction block was not observed. No problems or issues with the testing setup or loading assemblies were observed.

4.2 DEFINITIONS OF DAMAGE STATES IN SPECIMEN

The PreT-CB-ROCK specimen was monitored to identify the damage states established by Berry et al., (2004). These key damage states are defined in Table 4.1, and have been used during similar tests of reinforced concrete columns at the University of Washington to describe damage progression. It is noted, however, that the damage states given in Table 4.1 were developed for conventional, cast-in-place columns, so they are not all fully applicable to the behavior of precast, prestressed, rocking columns.

Table 4.1 Definitions of damage states in specimens.

Damage state	Description/observation
First significant horizontal crack	Crack width ≥ 0.5 mm
First significant diagonal crack	Crack width ≥ 0.5 mm and crack extends ¼ of column diameter
First open residual crack	Residual crack width ≥ 0.25 mm
First yield of longitudinal rebar	First strain gauge that reaches yield strain
First yield of transverse reinforcement	First strain gauge that reached yield strain
First spalling in cap beam	Observed spalling on surface
First spalling in column	Observed flaking, minor spalling
Significant spalling in column	Spalled height ≥ ¼ of column diameter
Fully spalled	Spalling height no longer increases with increasing deformation
Exposure of longitudinal reinforcement	First observation of column longitudinal reinforcement
Buckling of longitudinal reinforcement	First observation of buckling of longitudinal reinforcement bars
Large cracks in concrete core	Crack width ≥ 2.0 mm
Fracture of transverse reinforcement	Observation or sound
Fracture of longitudinal reinforcement	Observation or sound
Instability of column	Loss of axial capacity

4.3 INITIAL DAMAGE

While attaching the horizontal actuator to the specimen, the gap between the grout pad and the steel rocking plate likely opened, causing a horizontal crack in the grout at the bottom of the steel plate. A photo of this crack is presented in Figure 4.3. During the cyclic testing, it was determined that this crack separated the cusp of the grout pad from the main, ½-in. thickness of the pad (see Figure 2.25 for identification of the cusp). No damage to the actual pad was observed.

Figure 4.3 Crack below grout pad cusp that resulted from attachment of actuator.

It is noted that this crack in the grout pad was the only evidence of joint decompression. The joint was not continuously monitored during the attachment of the actuator, and was never directly observed to have opened.

Additionally, the specimen was subjected to an elastic, trial cycle the day before the full test. This trial cycle was conducted in order to ensure that the instruments were properly connected to the specimen, and that the actuators were properly functioning. The instrumentation data from this cycle was temporarily recorded and examined, but was not saved for future data analysis. Finally, during the preliminary cycle, several small, horizontal hairline cracks were observed in the column, but these cracks closed once the specimen was returned to its original position (zero drift).

4.4 DRIFT RATIOS AT KEY DAMAGE STATES

The PreT-CB-ROCK specimen was subjected to the forty drift cycles previously defined in the Section 3.3.1. Table 4.2 lists the set, cycle, and drift ratio at which each damage state was reached or observed. The strain gauge readings are marked as “not available” because of problems with the gauges themselves and the data acquisition system. The reported drift ratios were calculated from the displacement measured at the top of the column by the MTS LVDT (after correcting the LVDT data by subtracting the deflection of the actuator beam). The LVDT measurements were used as the master measurements, because the string pots have limited precision. The LVDT data was consistent with the deflection measurements recorded relative to the unloaded instrumentation reference frame.

Table 4.2 Summary of damage state progression for both specimens.

Damage state	PreT-CB-ROCK		
	Set	Cycle	Drift (%)
First significant horizontal crack	Not observed		
First significant diagonal crack	Not observed		
First open residual crack	Not observed		
First yield of longitudinal rebar (south drift)*	1	2	+0.342
First yield of longitudinal rebar (north drift)*	2	2	-0.477
First yield of transverse reinforcement	Not available		
First spalling in cap beam	After test		
First spalling in column	4	1	+0.86 / -0.84
Exposure of longitudinal reinforcement	6	2	+2.30 / -2.31
Significant spalling of column	Not observed		
Full spalling of the column	Not observed		
Exposure of longitudinal reinforcement	Not observed		
Buckling of longitudinal reinforcement	Not observed		
Large cracks in concrete core	Not observed		
Fracture of transverse reinforcement	Not observed		
Fracture of longitudinal reinforcement	9	3	+7.05 / -7.04
Loss of axial capacity	Not observed		

*The first yield was indirectly estimated with analysis of the tube potentiometer data (see Section 6.8.2.1), strain gauge data was not available.

4.5 DAMAGE TO CONCRETE

Little concrete damage was observed during the test. Most cracks remained at hairline widths, and no diagonal cracks were observed.

4.5.1 Column Concrete Cracking

A maximum crack width of approximately 0.4 mm was observed during Set 5-Cycle 2 (-1.53% drift). This crack occurred at the transition between the top of the steel tube and the concrete column. It should be noted, however, that the crack at this transition was difficult to measure during the test. However, a pair of LED's was used to measure this potential crack plane with the Optotrak motion capture system; see Section 5.5.3 for this data. Figure 4.4 shows this crack on the north side of the column.

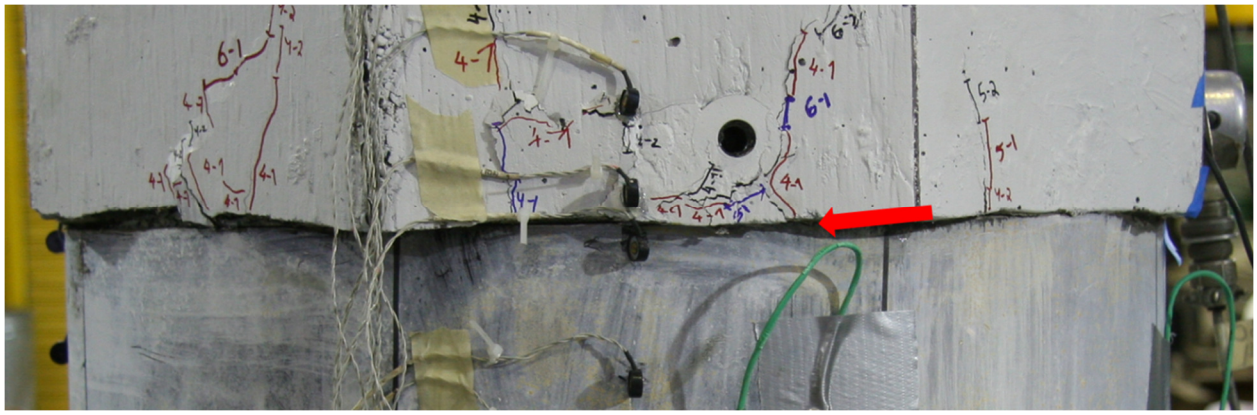

Figure 4.4 Horizontal crack at transition from tube to concrete.

The crack through the reduced diameter extension of the column was observed during Set 7-Cycle 1 (+2.76% drift ratio). However, this crack occurred due to the gap created by the column's rocking behavior, and was therefore not considered a crack through the column core (as described by the damage state given in Table 4.1). At the end of each cycle, column cracks typically closed shut, or closed to a hairline width.

4.5.2 Column Concrete Spalling

Very little column spalling occurred and it resulted in cosmetic damage only. During the test, minor concrete flaking was observed where concrete at the vertices of the octagon overhung the top edge of the steel tube. This spalling never led to exposure of the reinforcement. Figure 4.5 shows some of this surface flaking, which was first observed during the Set 4-Cycle 1 (+0.85 / -0.84% drift ratio).

Figure 4.5 Minor surface flaking observed at the top of the steel tube.

After the test, it was apparent that spalling cracks developed through the overhanging corners of the octagonal section. Removing these spalled concrete chips did not expose any steel

reinforcement, leaving damage similar to what was observed during the PreT-SF-ROCK test. Figure 4.6 shows this damage on the PreT-SF-ROCK specimen (photographs of this damage for the PreT-CB-ROCK specimen were not available). Furthermore, the heights of these spalls were no greater than one quarter of the column diameter. Therefore, these spalls were considered *cosmetic damage* that resulted from the geometric incompatibility between the circular steel tube and the overhanging vertices of the octagonal section of the column, as opposed to the *significant spalling* damage state (as described by the damage state given in Table 4.1).

Figure 4.6 Corner spalling of PreT-SF-ROCK specimen.

After a column drift of 3.0%, Hewes and Priestley observed similar spalling above the jacketed segment of one of their high aspect ratio columns. However, that spalling exposed the column's transverse, spiral reinforcement, and they identified it as significant damage. Their other columns did not exhibit this type of damage, however.

4.5.3 Cap Beam Concrete Damage

Minor vertical cracks were observed in the top (in the testing orientation) of the cap beam after the second and third cycles of the first set (drift ratios of ±0.38% and ±0.35%, respectively). These cracks were located very close to the socket connection, and were indicative of flexural, tension cracking. However, due to their very short lengths (relative to the cap beam's depth), these cracks could have resulted from thermal stresses while the specimen cured, which then opened during mechanical loading. Regardless, these cracks remained hairline for the duration of the test and crack propagation was minimal. Figure 4.7 shows this cracking on the west face of the cap beam.

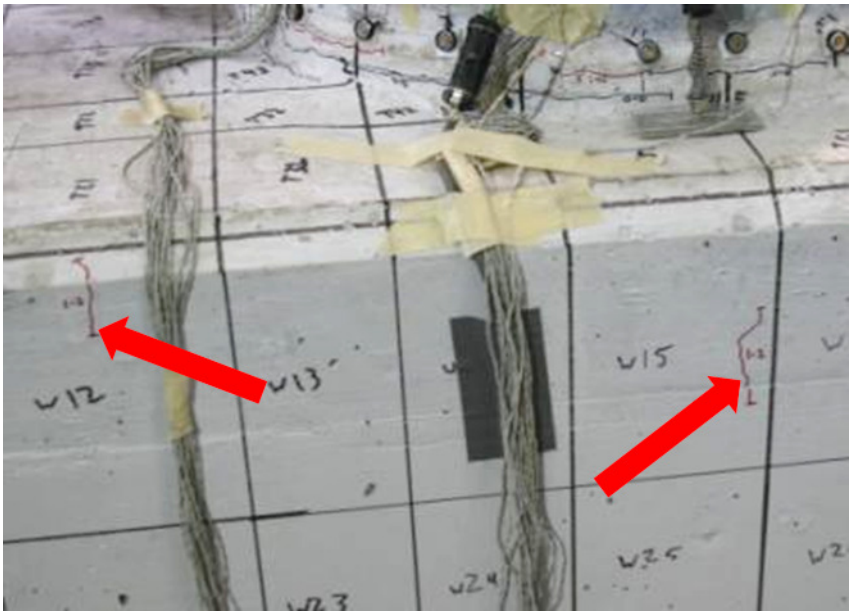

Figure 4.7 Hairline cracking on west face of cap beam.

After the test, surface spalling was observed on the horizontal face of the cap beam, just north of the grout pad. The chip that spalled was approximately ¼" thick, no cap beam reinforcement was visible after its removal, and the spalling was considered cosmetic damage. Figure 4.8 shows the approximate location and relative size of this spalled concrete chip (no photograph of the actual damage was available).

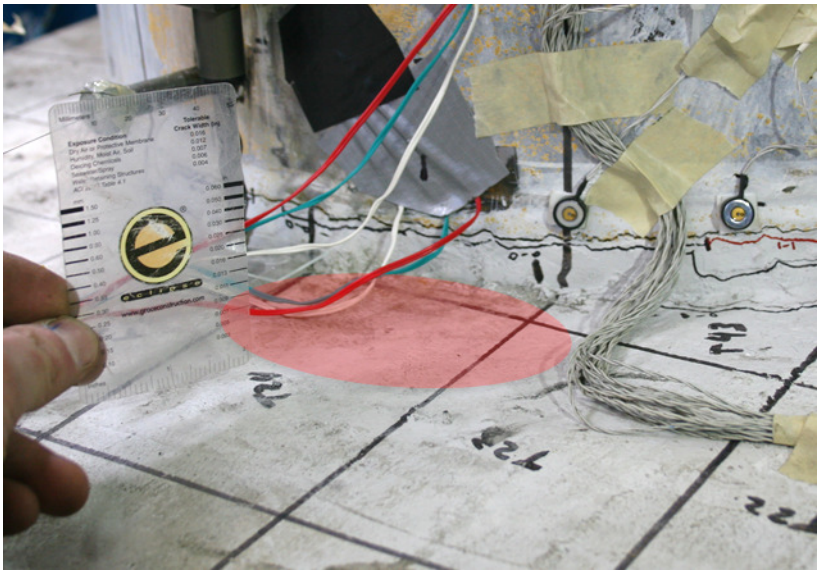

Figure 4.8 Approximate size and location of cap beam spalling.

4.6 DAMAGE TO GROUT PAD

During the test, the grout pad cusp underneath the steel tube's fillet weld quickly flaked off, and was then removed. This flaking was considered cosmetic damage. Figure 4.9 shows the cracking

and removal of this material from the main part of the grout pad (these photos were taken during a peak drift hold).

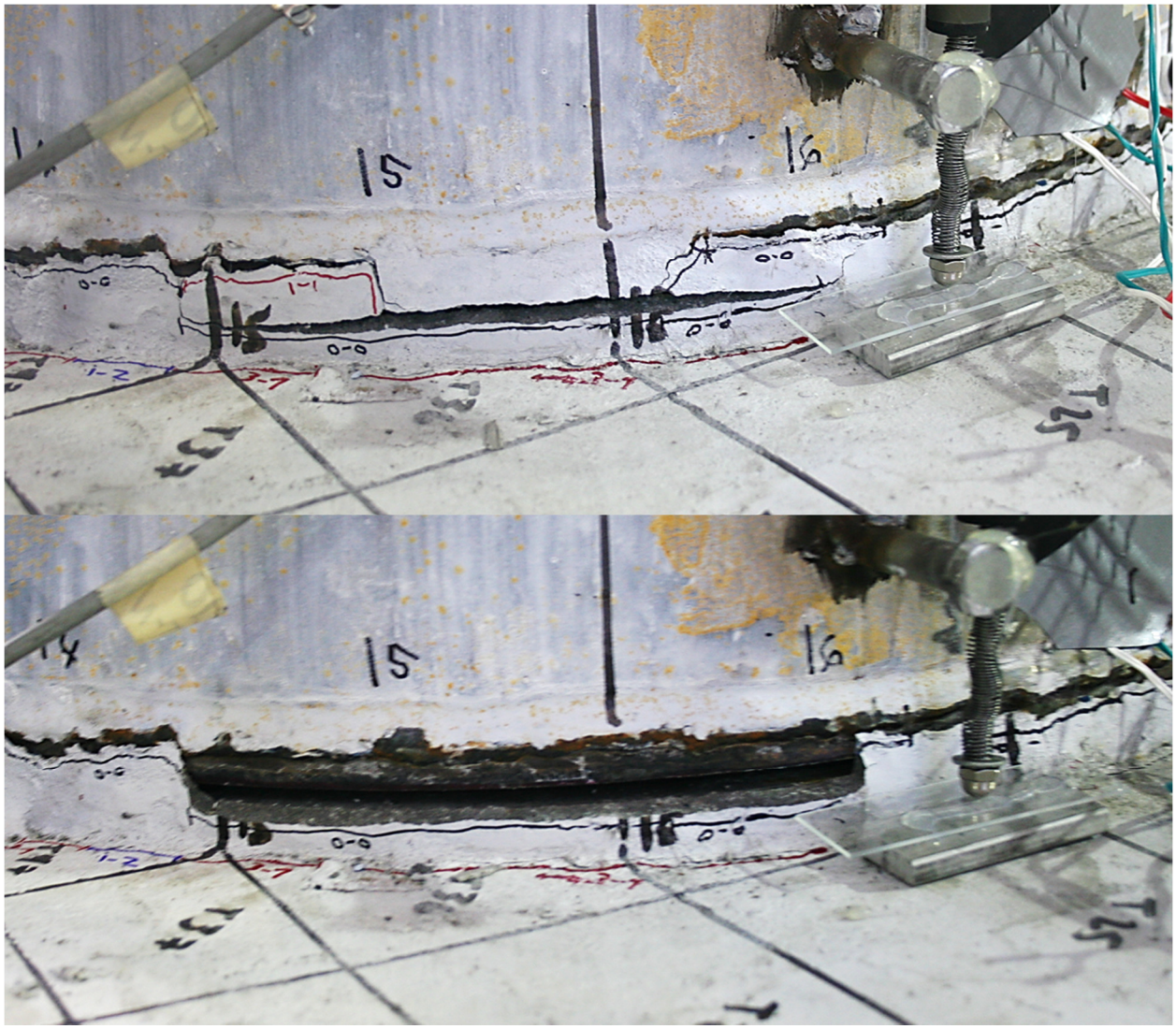

Figure 4.9 Early cracking (top) and removal (bottom) of the cusp underneath the tube weld.

4.6.1 Grout Crushing

Hairline vertical cracks, which may be analogous to the columnar or splitting fracture type applicable to concrete cylinder and mortar cube compressive testing, were first observed in the grout pad during Set 1-Cycle 3 (±0.35% drift ratio). Additional vertical cracks were again observed during the second and fourth sets (drift ratios of ±0.49% and ±1.00%, respectively). Vertical cracking in the grout pad was last observed after the Set 6-Cycle 4 (maximum drift of +0.72%).

Grout crushing, defined as a complete loss of material from the main body of the grout pad, began along the north and south edges of the pad at drifts of +7.02% / -7.05% (Set 9-Cycle 2).

Crushing continued in the following drift cycle and in the Set 10-Cycle 2 (±10.33% drift ratio). Minimal grout crushing was observed in the following, continuous ±10.41% drift cycle. Figure 4.10 to Figure 4.12 demonstrate the progression of crushing in the grout pad. The maximum depth of this crushing (measured radially from the perimeter of the baseplate) totaled approximately 3/8" by the end of the test.

Figure 4.10 Crushing of south side of grout pad resulting from +7.02% / -7.05% drift cycles.

Figure 4.11 Crushing of south side of grout pad resulting from first ±10.33% drift cycle (Set 10-Cycle 2).

Figure 4.12 Minimal grout crushing after ±10.41% drift cycle (Set 10-Cycle 3) -- before initiating the cycle, the previously crushed grout was removed.

4.6.2 Permanent Compression of Grout Pad

By the end of the test, the grout pad had been plastically compressed by the rocking of the steel baseplate. This resulted in a rounding of the grout pad. That is, the pad appeared undamaged and at its original thickness near the middle of the cross-section, and was permanently compressed on the north and south sides of the connection. Figure 4.13 and Figure 4.14 illustrate this deformation.

Figure 4.13 South side of grout pad after test completion; note the gap between the baseplate and grout pad caused by permanent compression of the grout.

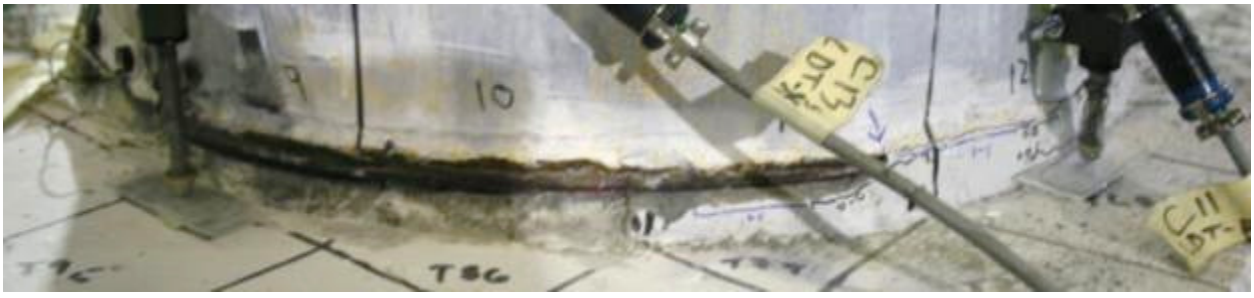

Figure 4.14 Southeast side of grout pad after test completion. The pad nearer the center of the connection remained largely intact.

The north and south sides of the grout pad were monitored during the test. Changes in the residual gap between the pad and baseplate were recorded after the column was returned to zero

drift at the end of each cycle. Increases in the widths of these gaps were assumed to be indicative of plastic compression of the underlying pad. Table 4.3 provides the observation data, and Figure 4.15 shows a plot of these measurements against the applied drift.

Table 4.3 Measurements of residual gap between baseplate and grout pad, following removal of applied drifts.

Set	7				8				9				10			
Cycle	1	2	3	4	1	2	3	4	1	2	3	4	1	2	3	4
Average Applied Drift (%)	2.76	3.27	3.28	1.04	3.98	4.89	4.88	1.54	5.85	7.03	7.05	2.35	8.49	10.3	10.4	2.51
North Side (mm)	0	-	-	0	-	-	-	0.8	2	-	3	3	3.5	4	4.5	6
South Side (mm)	0.25	0.25	0.25	0.25	.55	1	1.75	1.75	3	3	3	3	4	5	5	6

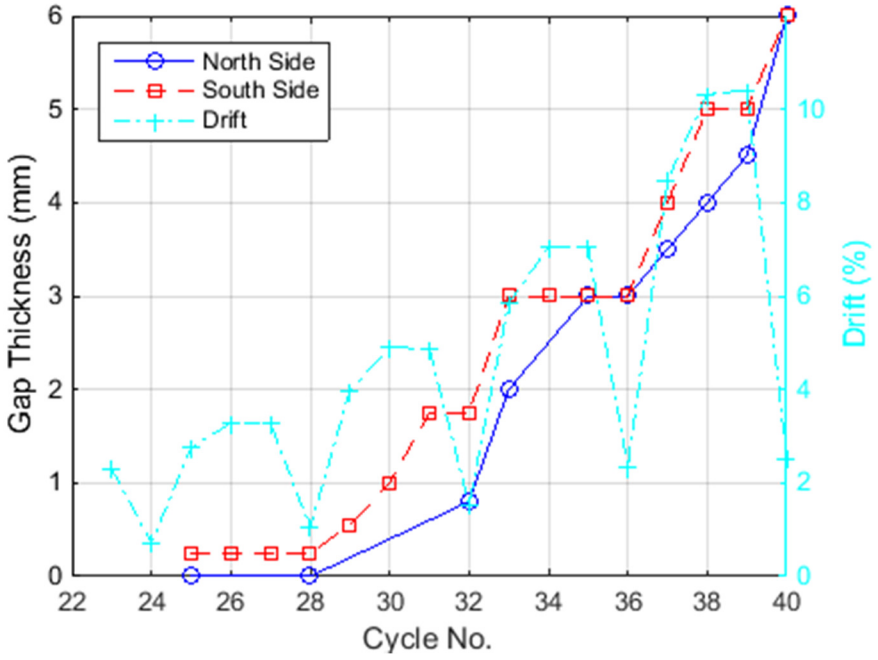

Figure 4.15 Measured thickness of the gap between the baseplate and grout pad.

The measurements of the residual gap between the grout pad and baseplate indicated that the physically measureable, plastic compression of the pad began after Set 7-Cycle 1 (an average drift ratio of 2.76%). The permanent compression continued for the rest of the test, and resulted in a maximum, measured gap width of 6 mm for both the north and south sides. However, the observations suggested that greater plastic compression resulted at lower drifts for the south side

than for the north. This could have been due to the varying placement thickness of the pad: ~$^{7}/_{16}$ in. on the north side and ~$^{12}/_{16}$ in. on the south side (see Section 2.9.3.3). Because the north side was thinner, it may have had a greater axial stiffness through its thickness than the south side.

4.7 DAMAGE TO REINFORCEMENT

Readings from the three-wire strain gauges on the reinforcing bars were not properly recorded by the data acquisition system. Therefore, no direct information regarding the first yielding of the longitudinal and transverse reinforcement was available. However, the yield drifts were estimated with an analysis of the potentiometers that were placed on the steel tube (see Section 6.8.2.1). The corresponding south and north yield drifts were +0.342% (Set 1-Cycle 2) and -0.477% (Set 2-Cycle 2), respectively.

No buckling was observed in any of the reinforcement. The extreme north and south No. 4 bars fractured after the specimen reached the Set 9-Cycle 2 drifts of +7.02 / - 7.05%; fracture of both these bars came in the following cycle. Figure 4.16 shows the gap between the steel rocking plate and grout pad after the first bar fracture. Rupture of the northeast, southeast, and southwest No. 4 rebars followed. All of these bars fractured during Set 10-Cycle 3 (after the column was subjected to the first drift cycle of ±10.41%). Fracture was not observed for the following reinforcement: northwest No. 4 bar, prestressing strands, spiral, and all of the No. 6 bars.

Figure 4.16 Rocking gap after rupture of north most rebar (intact northeast rebar visible in photograph).

The internal reinforcement of the column was observed through the gap that formed at the baseplate. Rebar was first observed during the Set 6-Cycle 2 (±2.31% drift ratio). This first observation of longitudinal reinforcement roughly matched the rocking specimens tested by Schaefer et al. (2014a); first exposure occurred during Set 6-Cycle 2 and during Set 6-Cycle 1 for the PreT-SF-ROCK-HyFRC and PreT-SF-ROCK specimens, respectively. The spiral of the reduced diameter column extension was first observed in Set 7-Cycle 2 (+3.23% drift ratio).

Prestressing strands first became visible during Set 8-Cycle 1 (+3.98% drift ratio). Finally, the dowel bar was first observed during Set 9-Cycle 1 (+5.83% drift ratio). However, it should be noted that these visual observations required the removal of the cusp on the grout pad.

It should be noted that the damage state of "exposure of longitudinal reinforcement" was originally developed to indicate loss of concrete cover, and the susceptibility of the reinforcement to bar buckling. In this test, the longitudinal reinforcing bars were indeed observed, but it was through the gap at the rocking interface rather than through concrete damaged by bars starting to buckle. Thus the observation met the letter, but not the spirit, of the damage state.

4.8 DAMAGE TO ROCKING DETAIL COMPONENTS

Buckling of the steel tube was not observed. Yield lines were not observed on the steel tube.

5 Measured Response

This chapter reports the measured response of the PreT-CB-ROCK test specimen, including the measured material properties, moment-drift response, effective forces, displaced shape, rotations, curvatures, baseplate rotation, steel strains, and strand slippage data.

Furthermore, the data gathered during the residual cycles is presented in this chapter.

5.1 MATERIAL PROPERTIES

The PreT-CB-ROCK specimen was constructed entirely in the Structural Research Laboratory at the University of Washington. The column and cap beam were cast from the same batch of concrete, supplied by CalPortland. During the concrete casting, 6 in. by 12 in. cylinders, and 6 in. by 6 in. by 22 in. beams were cast and then cured in the fog room at the University of Washington. During the grouting operations, two-inch mortar cubes were made and also cured in the fog room. Steel reinforcing bars were tested; these bars came from the same batch used to construct the specimen.

This section summarizes the measured material properties. Appendix A: Materials Testing provides additional details.

5.1.1 Conventional Concrete

Table 5.1 summarizes the results of all the concrete materials testing from the date of the specimen test. Complete details are given in Table A.1 of Appendix A: Materials Testing. Compression, splitting tension, and modulus of elasticity tests were performed at 7 days, 14 days, 28 days, and on the test day (the modulus elasticity test was completed the following week). Additionally, flexural beams were tested at 28 days after casting and on the test day.

The measured tensile strength and elastic modulus correspond to 5.89 times and 51900 times the square root of the compressive strength (psi units).

Table 5.1 Concrete materials testing results for PreT-CB-ROCK test date.

	Compressive Strength, f_c	**Cylinder Splitting Tension, f_{ct}**	**Modulus of Rupture, f_r**	**Modulus of Elasticity, E_c**
Age	57 days	57 days	57 days	64 days
Test Result	9030 psi	560 psi	909 psi	4930 ksi
$\frac{Test\ Result}{\sqrt{f_c}}$	Not Applicable	5.89	9.57	51900

5.1.2 Grout

Table 5.2 gives the results of the grout compression tests. Compression tests were performed at 7 days, 14 days, 28 days, and on the test day. Since the results of several of the test-day compression

results seemed to be inconsistent, additional compression tests were conducted; these additional results are given in Table A.2 of Appendix A: Materials Testing.

Table 5.2 Mortar materials testing results for PreT-CB-ROCK test date.

	Fiber Grout	Rebar Duct Grout	Central Duct Grout
Age	31 days	30 days	28 days
Compression Test Result, f_c	6875 psi	9196 psi	9217 psi

5.1.3 Mild Steel Reinforcement

Samples of the reinforcing bars were tested on the 300-kip Baldwin testing machine at the University of Washington. The results of these tests are summarized in Table 5.3. Stresses were calculated by dividing the force from the loading machine by the nominal area of the reinforcing bar. Strain was determined with the use of an extensometer with a 3.5-in. gauge length; strain was calculated by dividing the displacement reading of the potentiometer in the extensometer by its gauge length. Strain results were also obtained with the use of strain gauges for some pull tests. The yield stress was determined from the yield plateau of a specimen's stress-strain response, and the ultimate stress was determined from the maximum load reading of the testing machine. Complete details, including measured stress-strain curves, are given in Appendix A: Materials Testing.

Table 5.3 Summary of steel reinforcement properties.

Size	Construction Use	f_y (ksi)	f_u (ksi)	E_s (ksi)
No. 3	Cap Beam Transverse	73.4	105.3	35610
No. 4	Column Longitudinal	73.1	107.3	30950
No. 6	Column Longitudinal	72.4	106.0	29550
No. 7	Cap Beam Longitudinal	70.5	97.8	27150
No. 3 AWG	Column Spiral	86.3*	96.0*	30500*

*Results for No. 3 AWG from Finnsson (2013).

It is noted that mild steels have a modulus of elasticity of approximately 29,000 ksi. Any deviation from that standard value could be due to variance in the actual area of the delivered reinforcing bars. That is, if a particular bar were rolled to an area greater than the specified nominal area, it would have an increased axial stiffness, which would result in a higher calculated modulus of elasticity (in which nominal areas were used).

5.1.4 Prestressing Steel

Samples of the epoxy coated prestressing strand were also tested on the 300-kip Baldwin at the University of Washington. Stress was calculated by dividing the force from the loading machine by the nominal area of the strand. Strain was determined through the use of an extensometer and

strain gauges. Two strand samples were tested monotonically, and two were tested cyclically. All four of these tests used a specimen strand length of approximately 32 inches. The cyclic tests were intended to simulate the loading history of the strand: the strands were elongated to the design, effective prestress of approximately 165 ksi, and then cycled to increasing levels of strain. The cyclic tests showed that once a strand was elongated by approximately 0.0179 in./in., it had zero stress when returned to its initial prestressing strain. Table 5.4 summarizes the strand test results, and additional information is given in Appendix A: Materials Testing.

Table 5.4 Summary of prestressing strand properties.

Test Number	Test Type	Specimen Anchorage	f_u (ksi)	E_p (ksi)
1	Monotonic	300-kip Baldwin Jaws	267.8	30020
2	Monotonic	300-kip Baldwin Jaws	268.5	31540
3	Cyclic	300-kip Baldwin Jaws	270.4	32090
4	Cyclic	Strand Chucks	>301.4*	32610

*Strand could not be fractured due to the geometric configuration of the test setup. The reported stress is the highest measured during the test.

It is noted that the modulus of elasticity values were calculated from the strain gauge data. The strain gauges were placed in-line with the wires (as opposed to the longitudinal axis of the strand). Therefore, for any net longitudinal strain, the gauge measured a slightly smaller value on the wire. This instrumentation detail may explain the disagreement between the reported E_p values and the often used value of 28,500 ksi for prestressing strand.

The strands in Tests 1-3 were gripped in the serrated jaws of the test machine, and failed at the jaws. The result from Test 4, in which the anchorage at each end was supplied by a strand chuck, was believed to be most representative of the true strand strength.

5.1.5 Steel Tube, Plate, and Dowel

The steel used for the confining tube, rocking plate, and dowel bar was not tested for this project.

5.2 MOMENT-DRIFT RESPONSE

The moment at the column-cap beam interface, including P-Δ effects, was calculated using Equation 5.1.

$$M = h_1 \cdot H + \Delta_1 \cdot \frac{h_2}{h_1} \cdot P - F_{friction} \cdot h_2 \qquad \textbf{Equation 5.1}$$

The variables in this equation are graphically defined in Figure 5.1; *M* is the moment at the base of the column, *H* is the lateral load from the 220-kip MTS actuator, *P* is the vertical load from the Baldwin Universal Testing Machine, $F_{friction}$ is the estimated frictional force resulting from the relative motion across the greased, stainless-steel, bearing interface, h_1 is the distance from the

rocking interface to the centroid of the applied lateral load (59.813 in.), h_2 is the distance from the rocking interface to the point of application of the vertical load (96.5 in.), and Δ_1 is the measured displacement at the location of the applied lateral load.

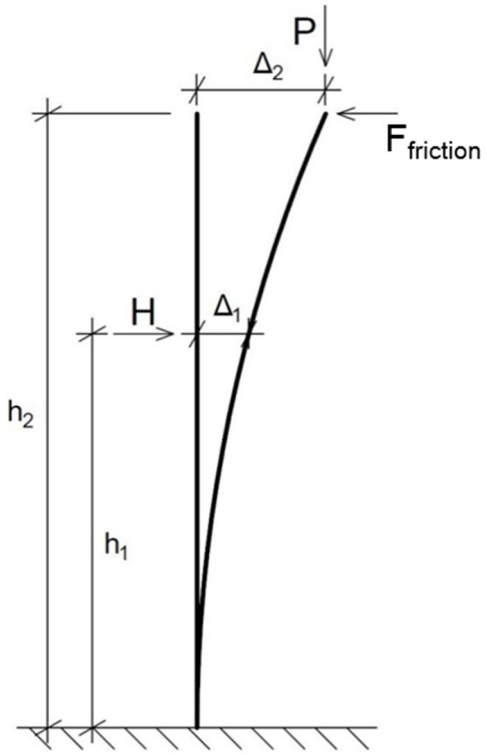

Figure 5.1 Graphical definition of variables for Equation 5.1 (adapted from Finnsson, 2013).

The lateral displacement at the elevation at which the vertical load was applied, Δ_2 in Figure 5.1, was not measured. Instead, the term $\left(\Delta_1 \cdot \frac{h_2}{h_1}\right)$ was used to approximate this displacement. This adjustment was based on an assumption of rigid-body motion of the various loading fixtures that were used to transfer the vertical load from the Baldwin to the top of the column.

The frictional force, $F_{friction}$, resulted from the sliding of the bearing plate along the loading channel and from the rotational friction within the spherical bearing itself. This frictional force was estimated using a model from Brown (2008). This model was developed for the experimental testing of reinforced concrete columns at The University of Washington. The loading setup for PreT-CB-ROCK was similar to Brown's tests. The frictional model can be seen in Figure 5.2, and an effective coefficient of friction was calculated using Equation 5.2.

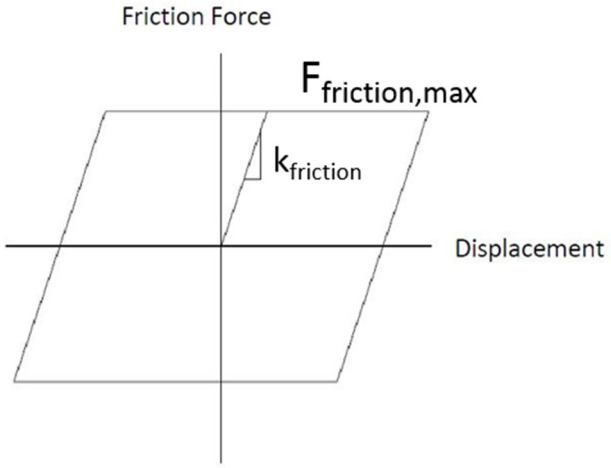

Figure 5.2 Friction correction model (adapted from Brown, 2008)

$$\mu_{eff} = \mu_{flat} + \mu_{curved} \cdot \frac{R}{h_2} \qquad \textbf{Equation 5.2}$$

The terms of Equation 5.2 are: μ_{eff} (an effective frictional coefficient), μ_{flat} (the translational component of the friction from the bearing plate sliding in the loading channel), μ_{curved} (the rotational contribution to the friction from the spherical bearing fixture), R (the radius of the greased spherical bearing fixture), and h_2 (the distance from the rocking interface to the application point of the vertical load). The frictional model (shown in Figure 5.2) is bilinear with a spring stiffness ($k_{friction}$) of 60 kips/in. and a peak force ($F_{friction,max}$) of μ_{eff} *P. Brown (2008) determined that $\mu_{eff} \approx 1.6\%$, resulting in a maximum frictional force of 2.54 kips for the applied vertical load of 159 kips.

Figure 5.3 through Figure 5.5 show the resulting moment-drift responses for PreT-CB-ROCK. Davis et al. (2012) determined that using Brown's recommended stiffness of 60 kips/in. in the frictional model resulted in implausible behavior for corrected moment-drift responses. Davis modified the model by reducing the stiffness to 5 kips/in.; this modification was also adopted for similar pre-tensioned column tests at the University of Washington (Finnsson, 2013 and Schaefer et al., 2014a). The reduced frictional stiffness of 5 kips/in. was selected to correct the moment-drift response for PreT-CB-ROCK (shown in Figure 5.5).

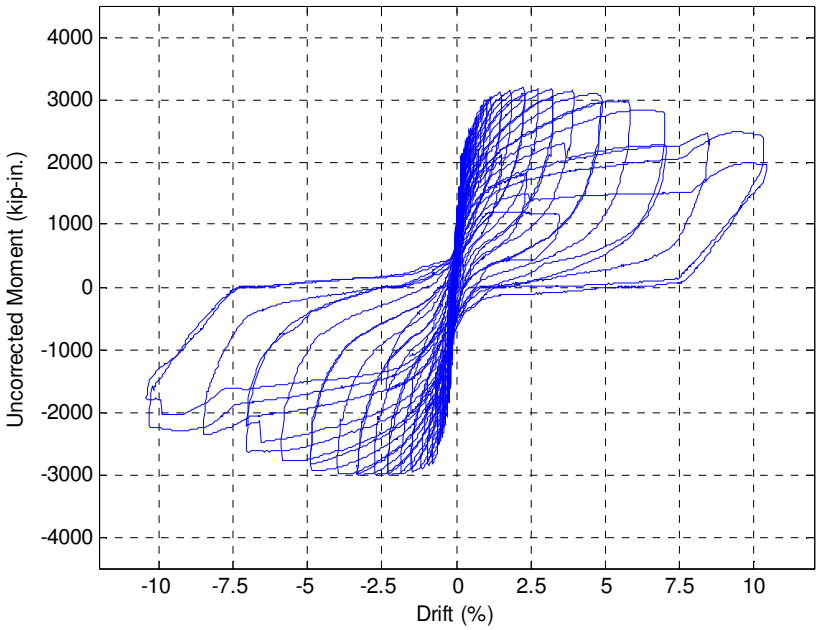

Figure 5.3 Uncorrected moment vs. drift response without added P-delta effects.

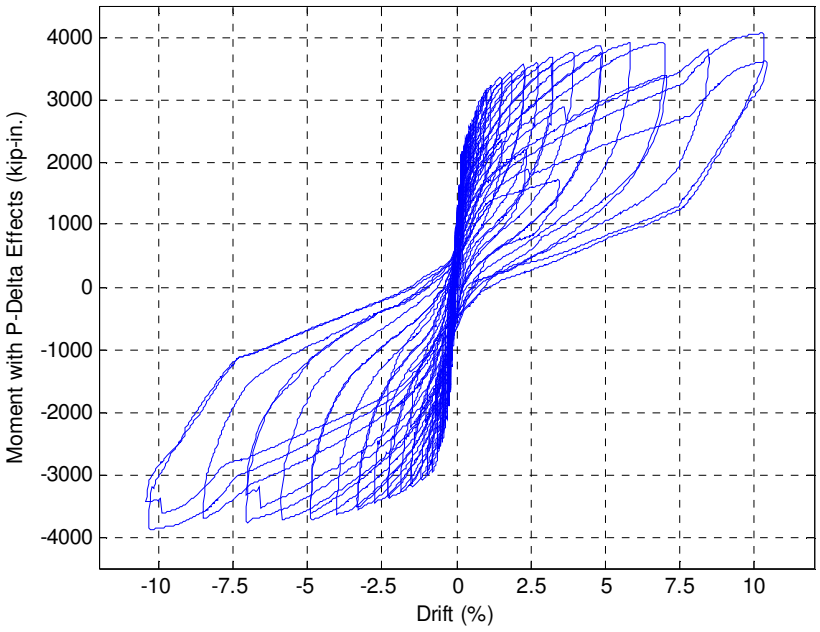

Figure 5.4 Uncorrected moment vs. drift response including P-delta effects.

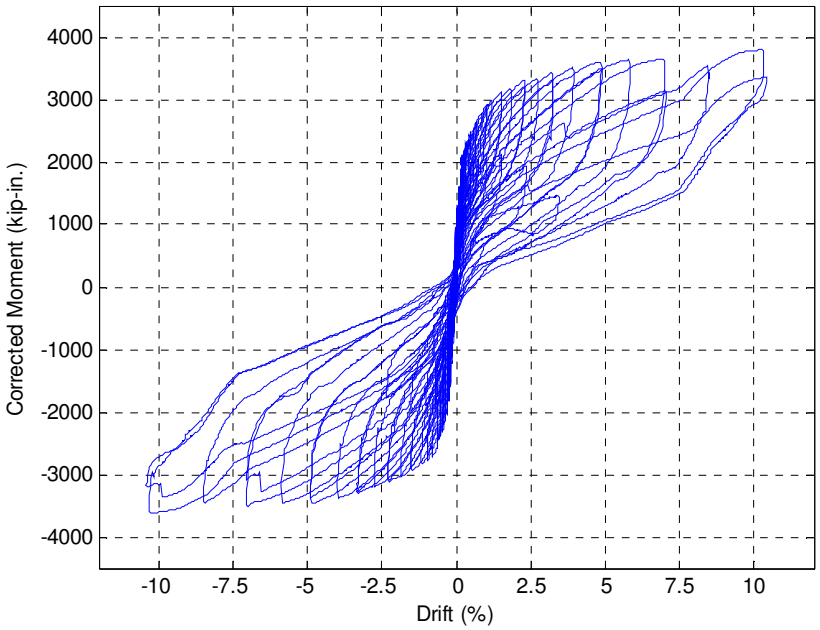

Figure 5.5 Corrected moment vs. drift response with $k_{friction}$ = 5 kips/in.

Table 5.5 provides a summary of the moment-drift response of the PreT-CB-ROCK system.

Table 5.5 Summary of moment-drift response.

Point of Interest	PreT-CB-ROCK	
	North Direction	South Direction
Maximum Moment (kip-in.)	-3628	+3802
Drift Ratio at Maximum Moment (%)	-10.31 (Set 10 – Cycle 2)	+10.33 (Set 10 – Cycle 2)
80% of Maximum Moment (kip-in.)	-2902	+3041
Drift Ratio at 80% of Maximum Moment (%)	N/A	N/A

The maximum base moment was measured during the maximum applied drift during the test, using separate measurements for drifts in the north and south direction. Failure of the specimens can be defined by the point at which the response moment degrades to 80% of its maximum (Davis et al., 2012); this did not occur during the PreT-CB-ROCK test. It should be noted that the peak moment for the south direction was approximately 5% larger than measured for the north direction. Two explanations are offered for the difference:

- The northwest, No. 4 reinforcing bar of the specimen did not fracture during the test. Because it was located on the north side of the connection, it likely had a larger, cross-sectional moment arm during the peak drift to the south, than during the following valley drift to the north.
- The strands progressively yielded during the test, most significantly during the final cycles (when the maximum column moments were measured). For those cycles, the north strands were first elongated to their highest strains during the peak displacement to the south, resulting in maximum yield stresses for those strands. When the column was subsequently "pushed" to the cycle's valley displacement, those north strands would have had lower stress (due to their previous yielding) than the corresponding south strands had during the initial pull to the peak drift. A detailed analysis of the strand behavior can be found in Section 6.7.

5.3 EFFECTIVE FORCE ACTING ON SPECIMENS

The effective lateral force acting at the top of the column was calculated by dividing the corrected base moment by h_1, the distance between the rocking interface and the application point of the horizontal load. The effective force was calculated with Equation 5.3.

$$F_{eff} = \frac{M}{h_1} \qquad \textbf{Equation 5.3}$$

The effective force versus displacement (noted as Δ_1 in Figure 5.1) is shown in Figure 5.6, and the response is summarized in Table 5.6. The effective force response is essentially a scaled version of the corrected moment-drift history.

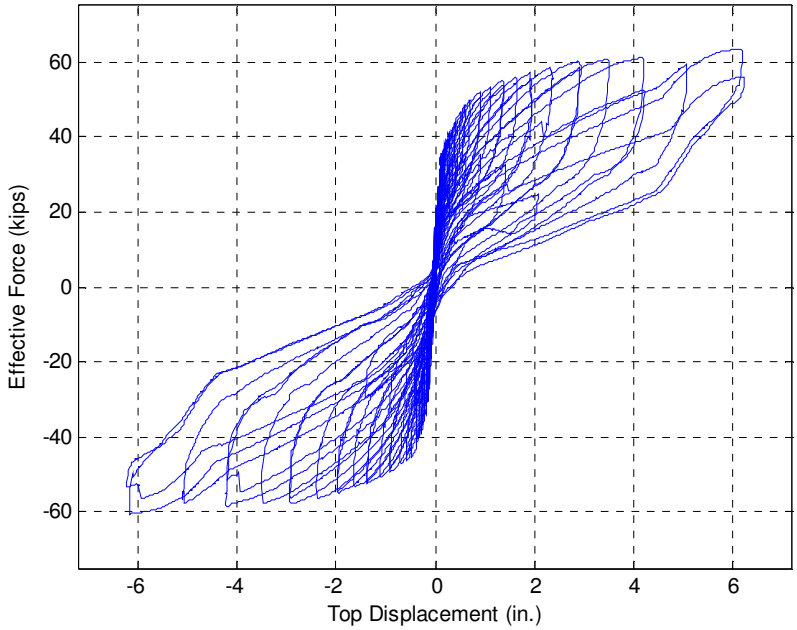

Figure 5.6 Effective force vs. displacement for PreT-CB-ROCK.

Table 5.6 Summary of measured effective forces.

Point of Interest	PreT-CB-ROCK	
	North Direction	South Direction
Maximum Effective Force (kips)	-60.7	+63.6
Displacement at Maximum Effective Force (in.)	-6.17 (Set 10 – Cycle 2)	+6.18 (Set 10 – Cycle 2)
80% of Maximum Effective Force (kips)	-48.5	+50.8
Displacement at 80% of Maximum Effective Force (in.)	N/A	N/A

5.4 COLUMN DISPLACED SHAPE

Displacements were monitored with string potentiometers attached to the column at various elevations, as described in Section 3.2.4. These displacements are plotted in Figure 5.7 and Figure 5.8 for several drift ratios. The curves in the two figures are essentially straight lines, and imply that nearly all of the column rotation was concentrated at the base of the column, and above the interface, the column body rotated almost as a rigid body, particularly at the larger displacements.

This instrumental evidence supported what was seen during the tests, and was in accordance with the planned behavior.

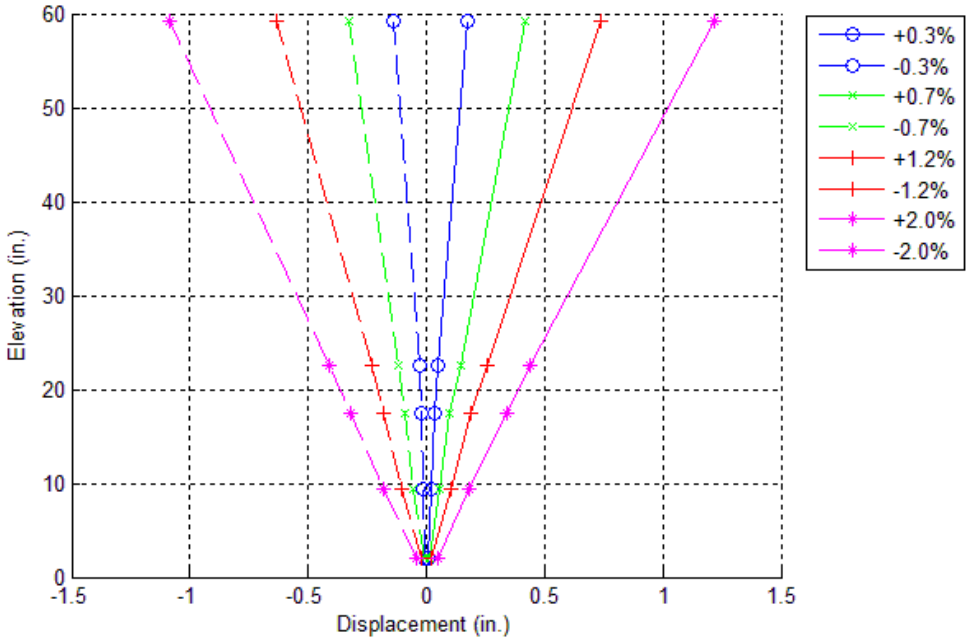

Figure 5.7 Displacement profile for drift ratios between ±0.3% and ±2.0% using string potentiometer data.

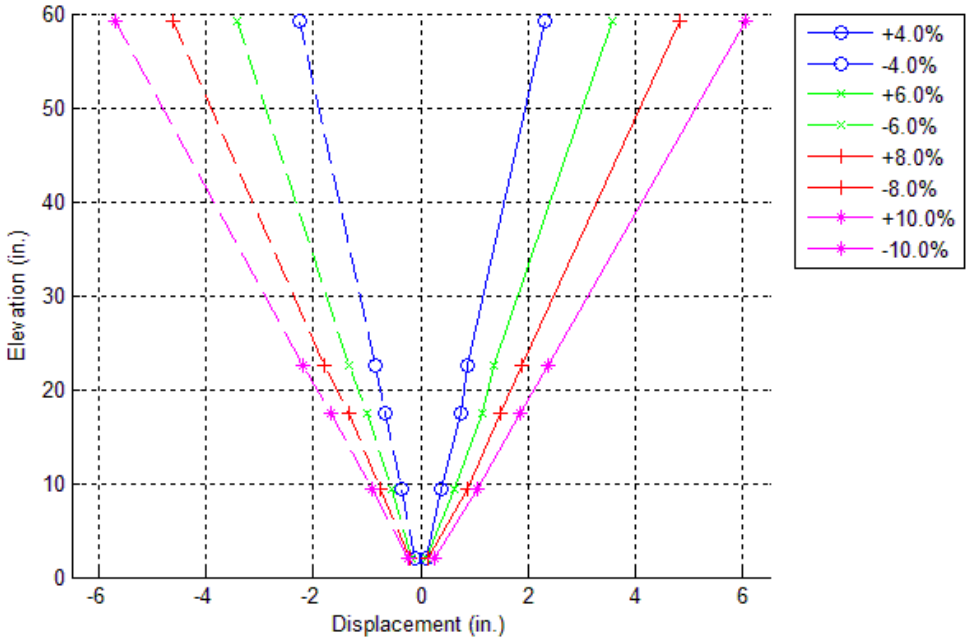

Figure 5.8 Displacement profile for drift ratios between ±4.0% and ±10.0% using string potentiometer data.

5.5 COLUMN ROTATIONS

Column rotations were calculated from data from three types of instruments: string potentiometers, inclinometers, and the Optotrak LED motion- capture system.

5.5.1 Column Rotations Using String Potentiometers

The average rotation between column elevations where string potentiometers were attached was calculated with Equation 5.4.

$$\theta_{i,string} = \frac{\Delta_{i+1} - \Delta_i}{h_{i+1} - h_i} \qquad \textbf{Equation 5.4}$$

In this equation, $\theta_{i,string}$ is the average rotation between a pair of successive instruments, the term "$\Delta_{i+1} - \Delta_i$" is the difference in displacement readings between the pair of string potentiometers, and the term "$h_{i+1} - h_i$" is the vertical distance between the pair of instruments. Essentially, this Equation 5.4 gives the secant slope between successive string potentiometers. Figure 5.9 and Figure 5.10 give the rotation profiles of the column, calculated with the string potentiometer data. These figures show that the rotation of the column was relatively constant above the connection, especially at the larger drift ratios.

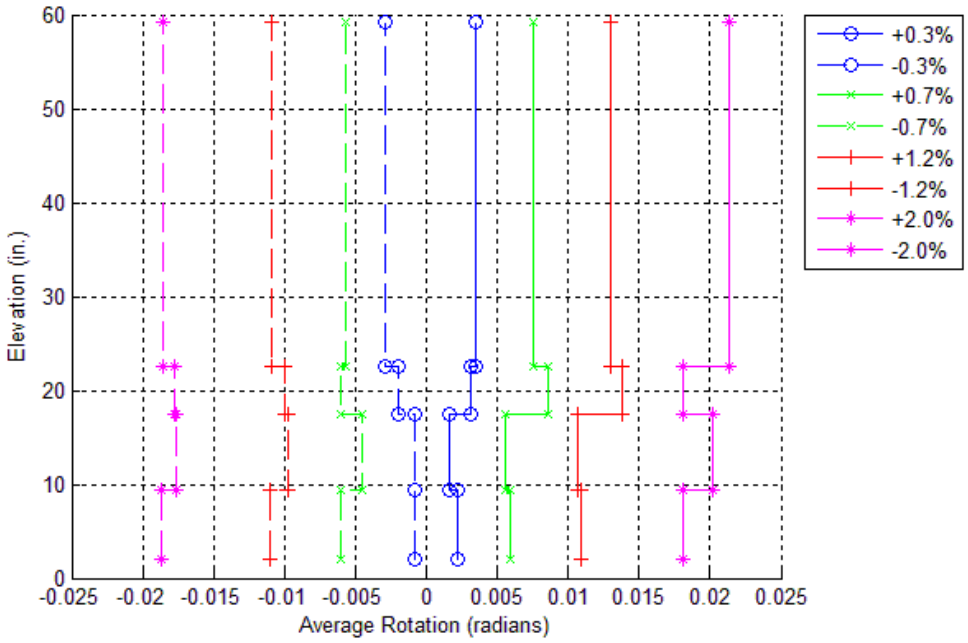

Figure 5.9 Rotation profile for drift ratios between ±0.3% and ±2.0% using string potentiometer data.

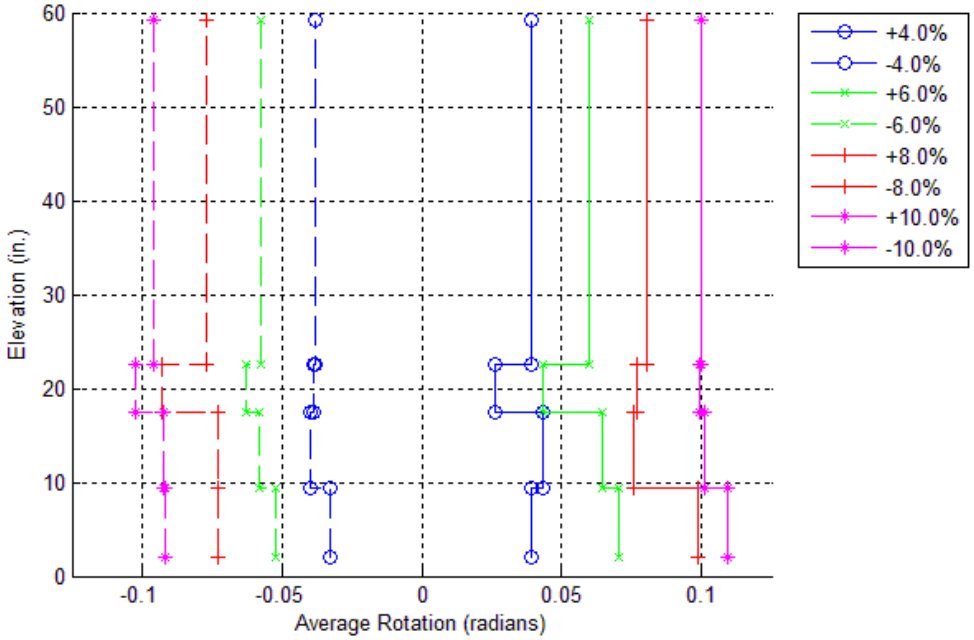

Figure 5.10 Rotation profile for drift ratios between ±4.0% and ±10.0% using string potentiometer data.

It is noted that the "jump" in the rotation profiles at column elevation of ~20 in. may be a result of instrumentation error. The string potentiometers used in this experiment had an at-best resolution of 0.01 in. (some potentiometers would only read intervals of 0.02 in. to 0.025 inches). If two successive potentiometers were "stuck" on resolution plateaus, then the relative error in reading between them would be "spread" over the distance between the potentiometers during the differentiation of the displacement data. This is most problematic for potentiometers placed close to each other, as was the case for the potentiometers at elevations of 11 ½" and 17 $^{3}/_{8}$". For example, if two successive potentiometers had a displacement reading error of 0.03 in. with respect to one another, it would result in a rotation error of 0.006 radians for potentiometers that were placed 5 in. apart, but 0.0015 radians for potentiometers placed 20 in. apart from one another.

5.5.2 Column Rotations Using Inclinometers

The inclinometers used in this experiment directly measured the column's rotation. The readings from these instruments are plotted in Figure 5.11 and Figure 5.12 for various levels of drift. They show the same pattern of essentially rigid body column rotation as displayed by the string potentiometer data.

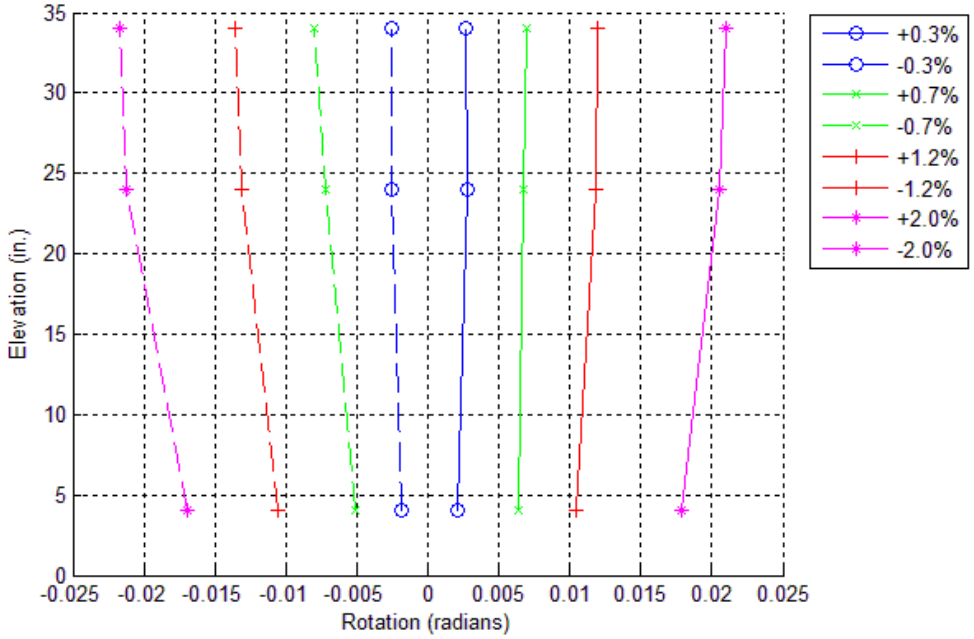

Figure 5.11 Rotation profile for drift ratios between ±0.3% and ±2.0% using inclinometer data.

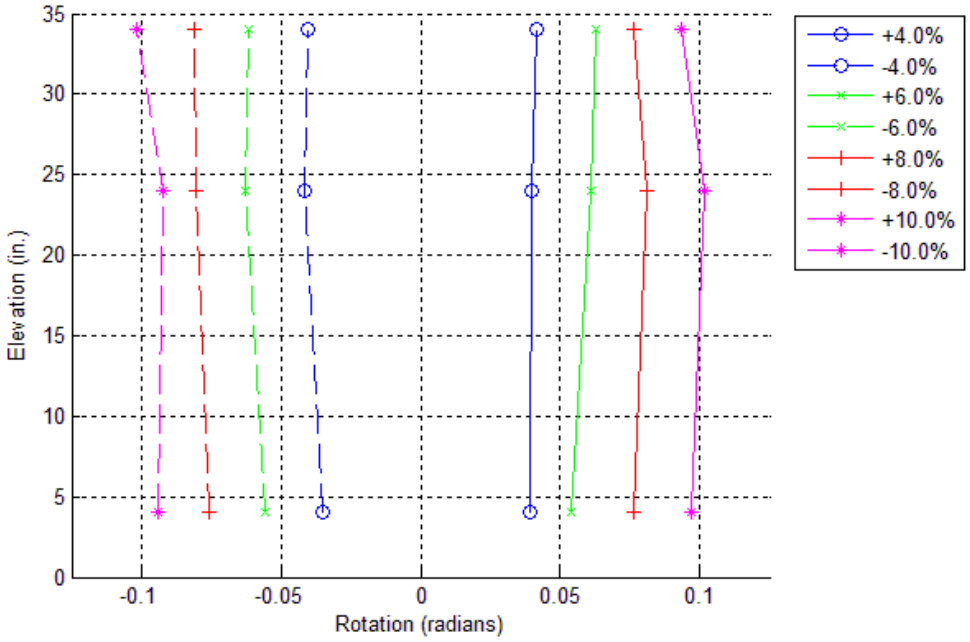

Figure 5.12 Rotation profile for drift ratios between ±4.0% and ±10.0% using inclinometer data.

5.5.3 Column Rotations Using Optotrak LED System

The inner product rule was used to determine column rotations from the LED targets of the Optotrak system. The rotation at a particular column elevation is given in Equation 5.5.

$$\theta_{opto} = \cos^{-1}\left(\frac{\boldsymbol{a}\cdot\boldsymbol{b}}{\|\boldsymbol{a}\|\|\boldsymbol{b}\|}\right) \qquad \textbf{Equation 5.5}$$

In this equation, θ_{opto} is the rotation at the elevation between a pair of rows of LED targets, $\boldsymbol{a}$ is the position vector established at the start of the test which joins the locations of the LED's in the pair, and $\boldsymbol{b}$ is a position vector joining the locations of the LED's at a specified drift; Figure 5.13 graphically defines the relevant variables.

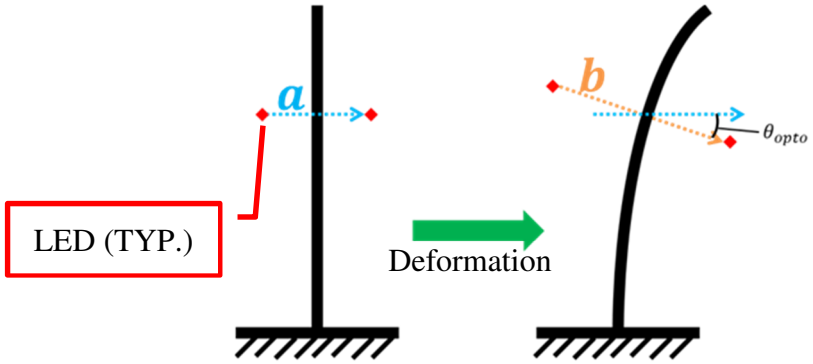

Figure 5.13 Graphical definition of variables for Optotrak rotation formulation.

Figure 5.14 and Figure 5.15 show the rotation profiles derived from the Optotrak data. It is noted that some data points are missing from these plots. This is due to the LED targets occasionally being obstructed from the view of the Optotrak cameras during the test.

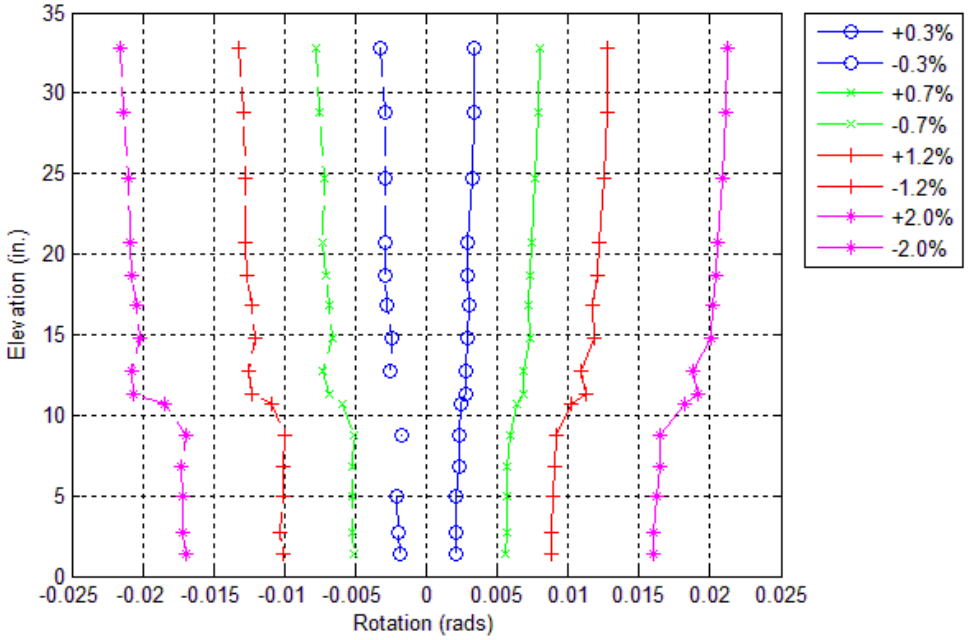

Figure 5.14 Rotation profile for drift ratios between ±0.3% and ±2.0% using Optotrak data.

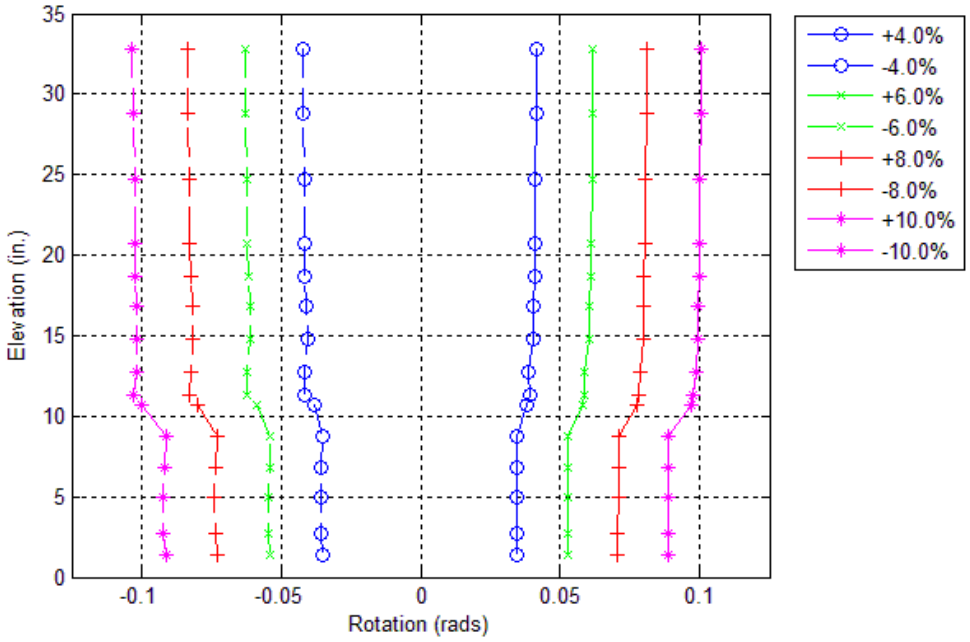

Figure 5.15 Rotation profile for drift ratios between ±4.0% and ±10.0% using Optotrak data.

5.5.4 Comparison of Rotation Measurements

The three methods for measuring column rotation are compared here. Figure 5.16 shows the calculated rotations for ±2.0% drift, and Figure 5.17 shows the results at ±10.0% drift for each of the three instrument systems.

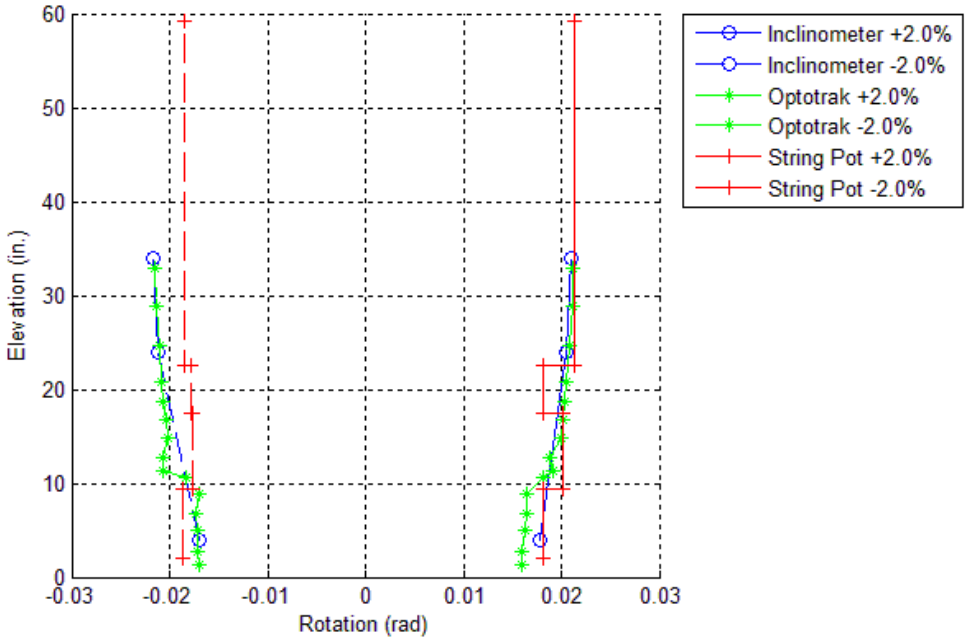

Figure 5.16 Rotation measurement comparison at ±2.0% drift.

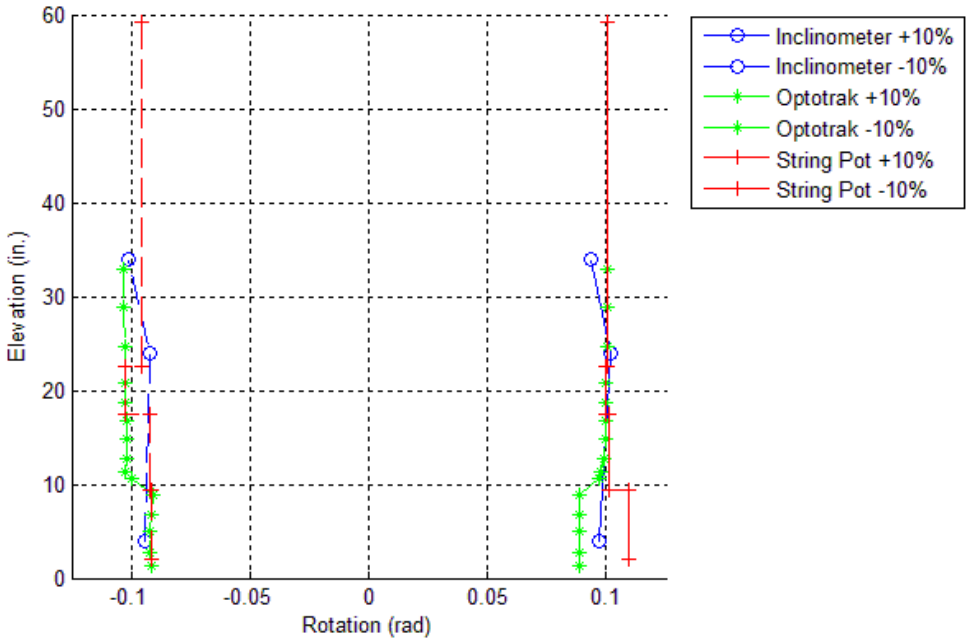

Figure 5.17 Rotation measurement comparison at ±10.0% drift.

The three methods for measuring column rotation provided similar results. In general, the inclinometers and Optotrak readings agreed very well with one another. It should be noted that the string potentiometers had an at-best resolution of 1/100th of an inch. This relatively coarse instrument resolution, combined with the differentiation of the experimental data to obtain rotation, suggests that the string potentiometer results were the least reliable of the three methods.

The Optotrak system gave the densest mesh of data. It agreed with the visual observations in that it showed essentially rigid body rotation in the tube region at the bottom and in the upper part of the column, where the moment was lowest and the cracking the least prevalent. It also showed a consistent jump at the interface between the tube and the concrete, 10" above the cap beam, and this is consistent with the presence there of the widest crack (0.4 mm) observed at any time during testing. For these reasons, the subsequent data analysis provided in this section relies on the Optotrak data more than on the other rotation measures.

5.6 COLUMN CURVATURE

The column curvatures were determined using the data from the inclinometers and the Optotrak LED system. The average curvature between successive instruments attached to the column was determined by dividing the change in the measured rotation by the distance between the instruments (the slope of a rotation profile line for a particular level of drift). The differentiation inherent in obtaining the curvatures reduces their accuracy, and, as expected, the values derived from the different instruments show significant differences.

5.6.1 Column Curvatures Using Inclinometers

Figure 5.18 and Figure 5.19 give the average curvature profile for the column at various drift levels.

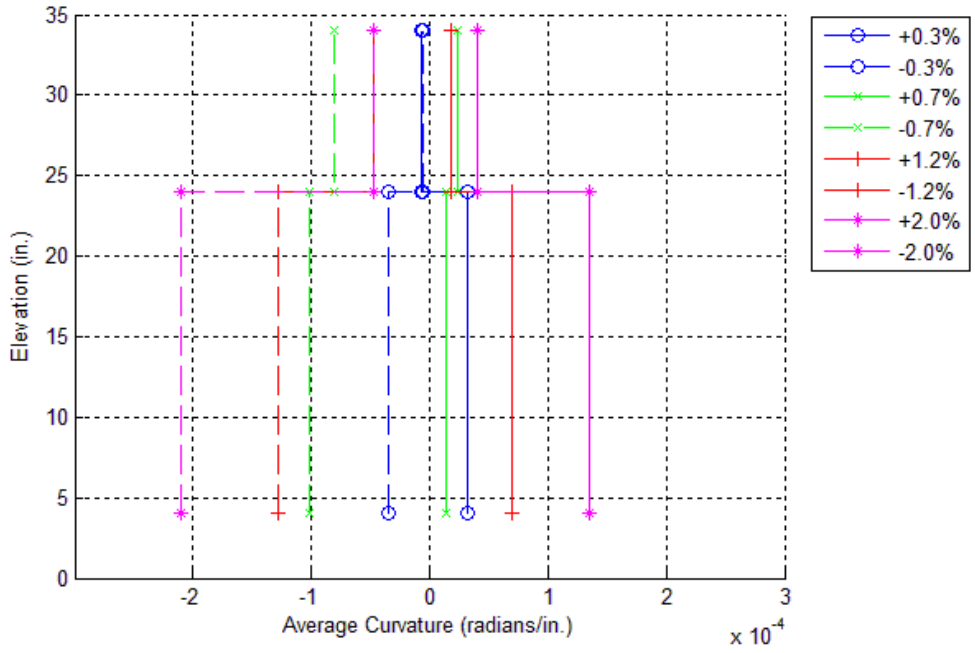

Figure 5.18 Curvature profile for drift ratios between ±0.3% and ±2.0% using inclinometer data.

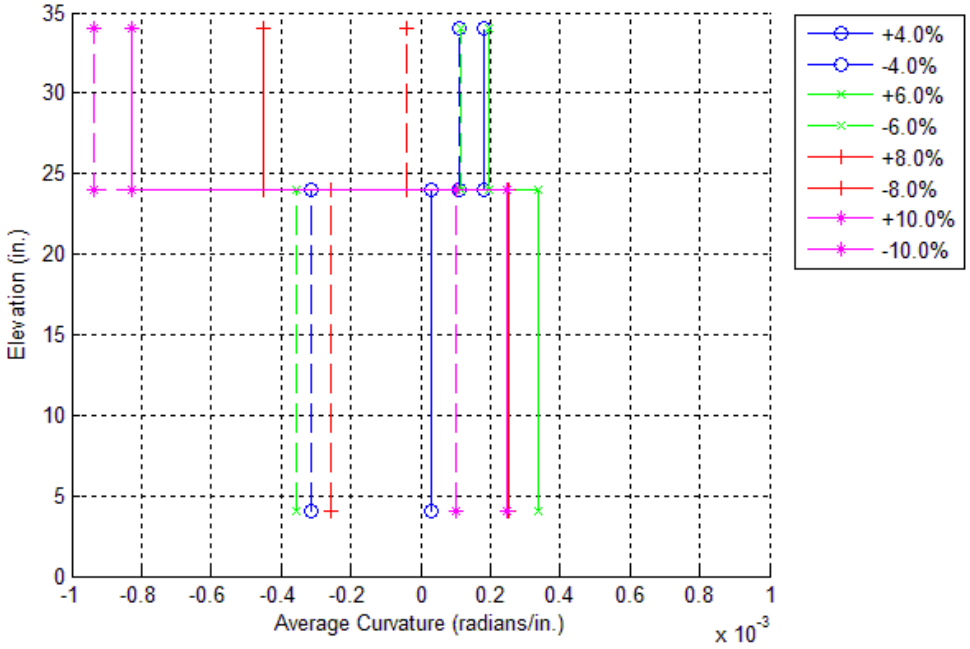

Figure 5.19 Curvature profile for drift ratios between ±4.0% and ±10.0% using inclinometer data.

5.6.2 Column Curvatures Using Optotrak LED System

Figure 5.20 and Figure 5.21 give the curvature profiles using Optotrak data.

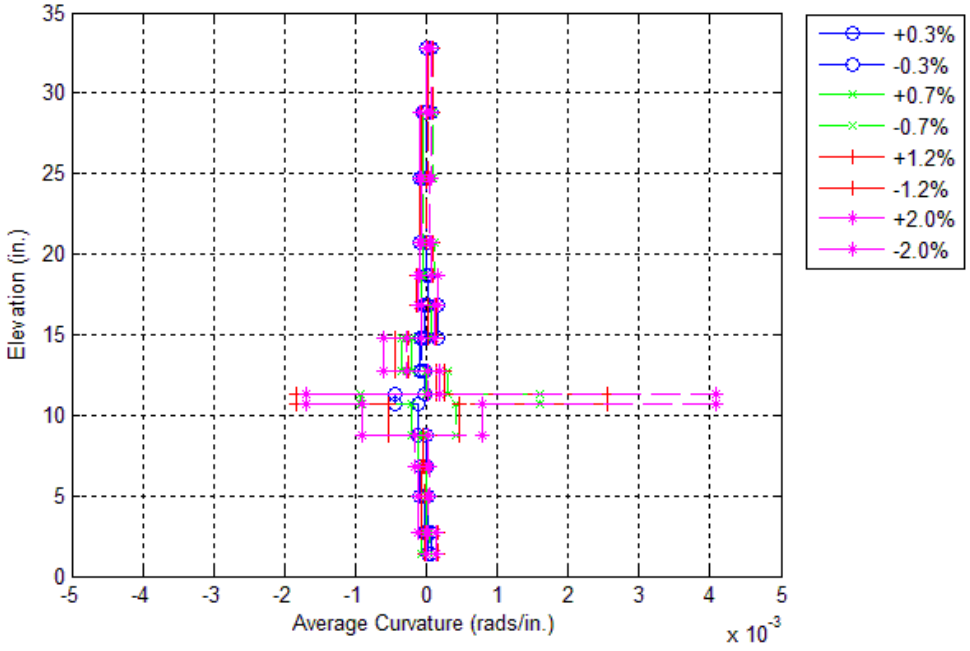

Figure 5.20 Curvature profile for drift ratios between ±0.3% and ±2.0% using Optotrak data.

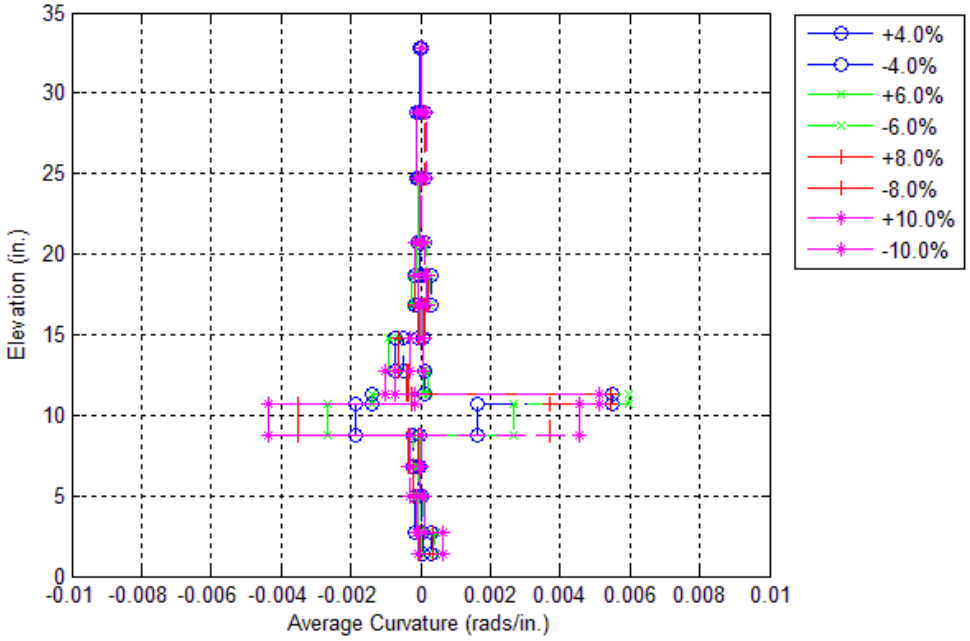

Figure 5.21 Curvature profile for drift ratios between ±4.0% and ±10.0% using Optotrak data.

The steel-tube length of the column (from an elevation of 0.5 to 10.5 inches) and the portion of the column above the tube (past an elevation of 12 inches) exhibited very little curvature. The primary sources of deformation were concentrated at an elevation of 10.5 inches (a large crack

developed at the interface between the tube and concrete) and the rocking interface with the cap beam. The concentration in curvature above the steel tube has been observed in other similar column testing (Schaefer et al., 2014a and Hewes and Priestley 2002).

All other sections of the column behaved in a relatively rigid manner. The Optotrak readings showed this trend clearly. The inclinometer readings were less useful because the spacing between the individual instruments was too great to precisely show the locations of concentrated curvature.

It is noted that analyzing the average curvature for a cracked medium is typically only meaningful if the cracks are numerous, uniform, and closely spaced. The PreT-CB-ROCK specimen did not crack in this manner; it "cracked" at the opening of the rocking interface and at the top of the steel confining tube. Therefore, the previous plots only serve to support the primary observation of the experiment: deformation was concentrated at the base and at the top of the tube.

5.7 STEEL TUBE LINEAR POTENTIOMETERS

Four linear potentiometers monitored the rocking behavior of the base of the column. These potentiometers were attached to the steel tube on the north, south, east, and west sides of the column. They measured the upward displacement of the base of the column as it lifted off of the grout pad during the drift cycles.

The south potentiometer output implausible results, and was believed to have malfunctioned during the test. The remaining three potentiometers were used to demonstrate the kinematics of the column's baseplate on the cap beam surface.

5.7.1 Drift versus Tube Displacement

The raw data from the linear potentiometers was plotted against the drift of the column. These plots are given in Figure 5.22 and Figure 5.23. The data for the displacement at the midsection of the tube was calculated by taking the average of the two linear potentiometers (one was attached to the east side of the tube and the other was attached to the west side).

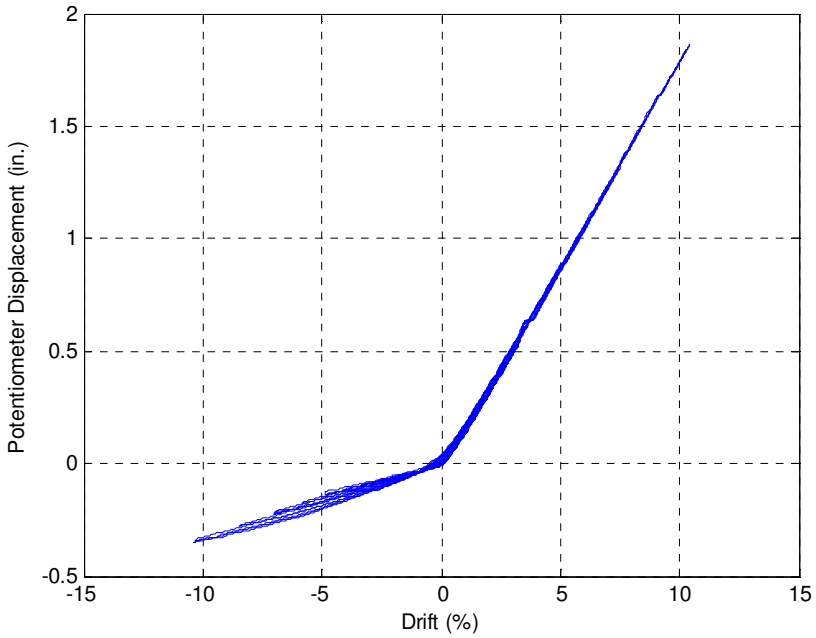

Figure 5.22 Displacement vs. drift for potentiometer on north side of tube.

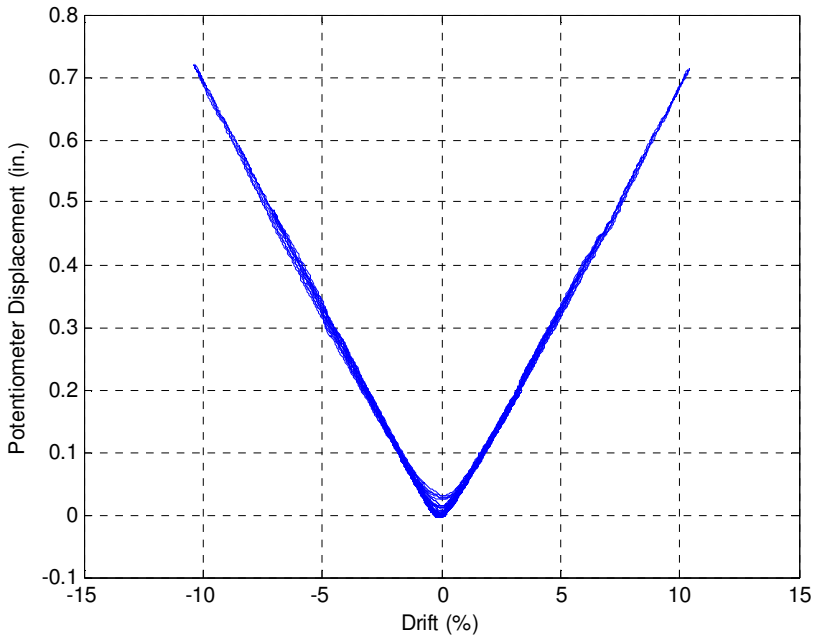

Figure 5.23 Displacement vs. drift for potentiometers on east/west sides of tube (the average of the two readings is plotted).

Both plots show a bilinear, V-shaped response that is very similar to the strain gauge results for the prestressing strands (see Section 5.12.1). This was expected as these linear potentiometers

essentially measured the vertical displacement of the rocking plate, which is directly proportional to the elongation of the unbonded strands (before the onset of slip).

For any given drift, the potentiometer measurement was likely a function of its distance to the baseplate's center of rotation and the baseplate's rotation angle. The assumed relation is given in Equation 5.6.

$$\Delta_{pot,measure} = e_{pot} * \theta_{baseplate} \qquad \textbf{Equation 5.6}$$

Where:

- $\Delta_{pot,measure}$ - The tube potentiometer measurement (in.)
- e_{pot} - The horizontal distance between the tube potentiometer and the baseplate's center of rotation (in.)
- $\theta_{baseplate}$ - The rotation angle of the baseplate (rad.), nearly equal to the drift ratio.

If Equation 5.6 is correct, then the bilinear responses of Figure 5.22 and Figure 5.23 suggest that the baseplate was rocking about single, constant, cross-sectional depths (one depth for each drift direction). That is, if the potentiometer measurement and the plate rotation angle (and therefore drift ratio) were linearly related, then e_{pot} must have been constant for drifts in one particular direction.

5.7.2 Drift Profiles

5.7.2.1 Tube Potentiometer Data Correction

The potentiometer data was first corrected in order to remove the contribution of the physical rotations of the instruments to their readings. A schematic is shown in Figure 5.24, and the calculation is given by Equation 5.7.

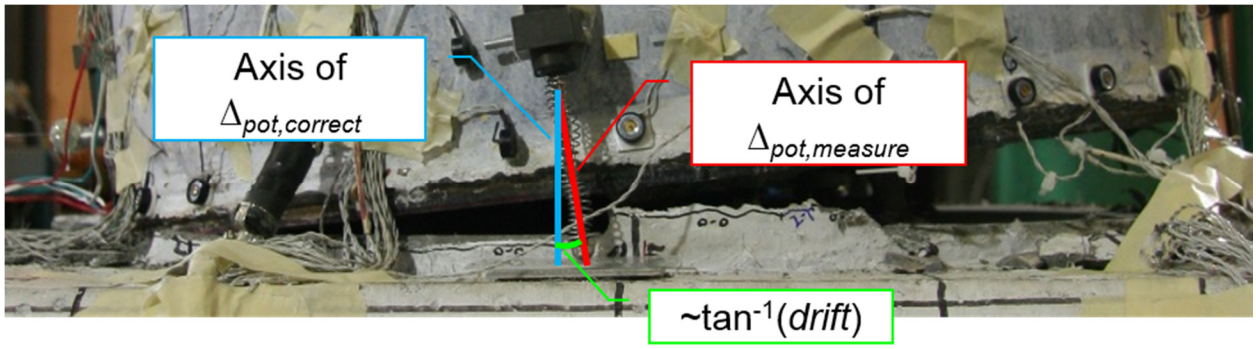

Figure 5.24 The actual potentiometer measurements included a contribution from the instrument's rotation.

$$\Delta_{pot,correct} = \cos[tan^{-1}(drift)] * \Delta_{pot,measure} \qquad \textbf{Equation 5.7}$$

In Equation 5.7, $tan^{-1}(drift)$ is the approximate angle of the potentiometer (with respect to "up"), $\Delta_{pot,measure}$ is the raw, uncorrected potentiometer reading, and $\Delta_{pot,correct}$ is the corrected potentiometer measurement. The corrected readings have been used here and in the following sections of this thesis.

5.7.2.2 Defining the Rocking Neutral Axis

The neutral axis of the rocking connection can be defined as the cross-sectional depth of zero net displacement (of the baseplate). This differs from the traditional, continuum mechanics concept of the neutral axis, which is the cross-sectional location of zero longitudinal strain due to bending.

Additionally, the proposed definition for the rocking neutral axis does not address the progressive rounding of the grout pad. That is, during a joint rotation, the base plate may actually not have been in contact with the underlying grout pad at the same location that the plate crossed its initial plane (due to the pad's plastic compression). The concept is schematically illustrated in Figure 5.25.

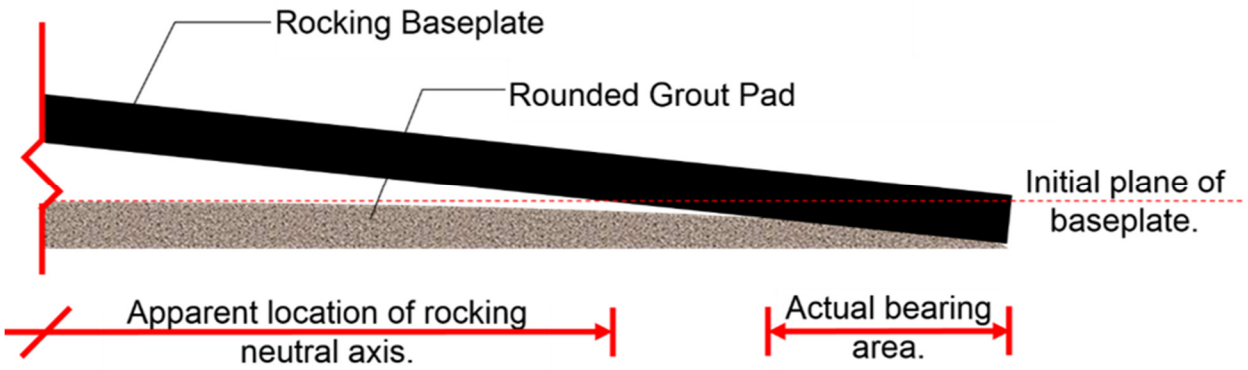

Figure 5.25 The measured location of the rocking neutral axis may not have matched the actual bearing area.

5.7.2.3 Profile Results

Figure 5.27 and Figure 5.28 plot the corrected output from these potentiometers. These figures were formed by taking the north-south position of the potentiometer on the cross-section of the column and plotting the corrected uplift at a particular level of drift – Figure 5.26 provides a conceptualization of the plots.

Because the south linear potentiometer did not give accurate results, data from the north, east, and west potentiometers were used to create each drift profile. This was done by changing the sign of the plotted instrument location for positive drifts (drifts in the southern direction); the actual data from the instruments were not altered. It should also be noted that the east and west potentiometers were not placed at the exact midsection of the column (due to conflict with other testing instrumentation), and therefore give the appearance of shifted or offset data points in the figures.

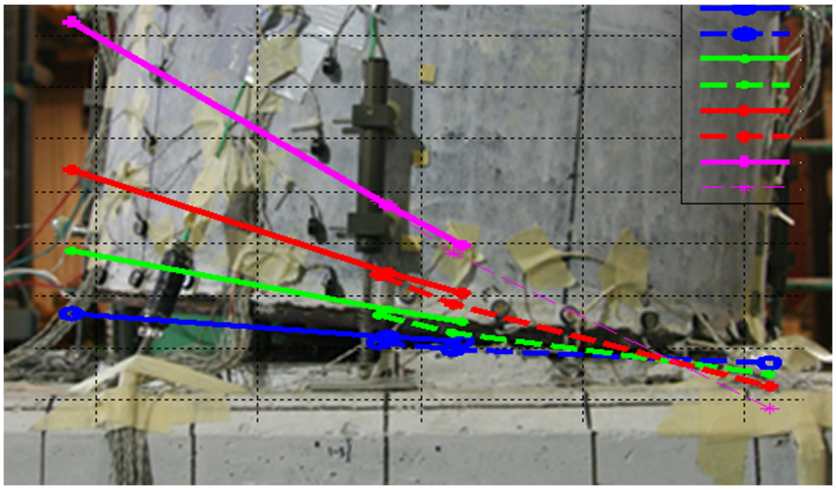

Figure 5.26 Conceptualization for plots in Figure 5.27 and Figure 5.28.

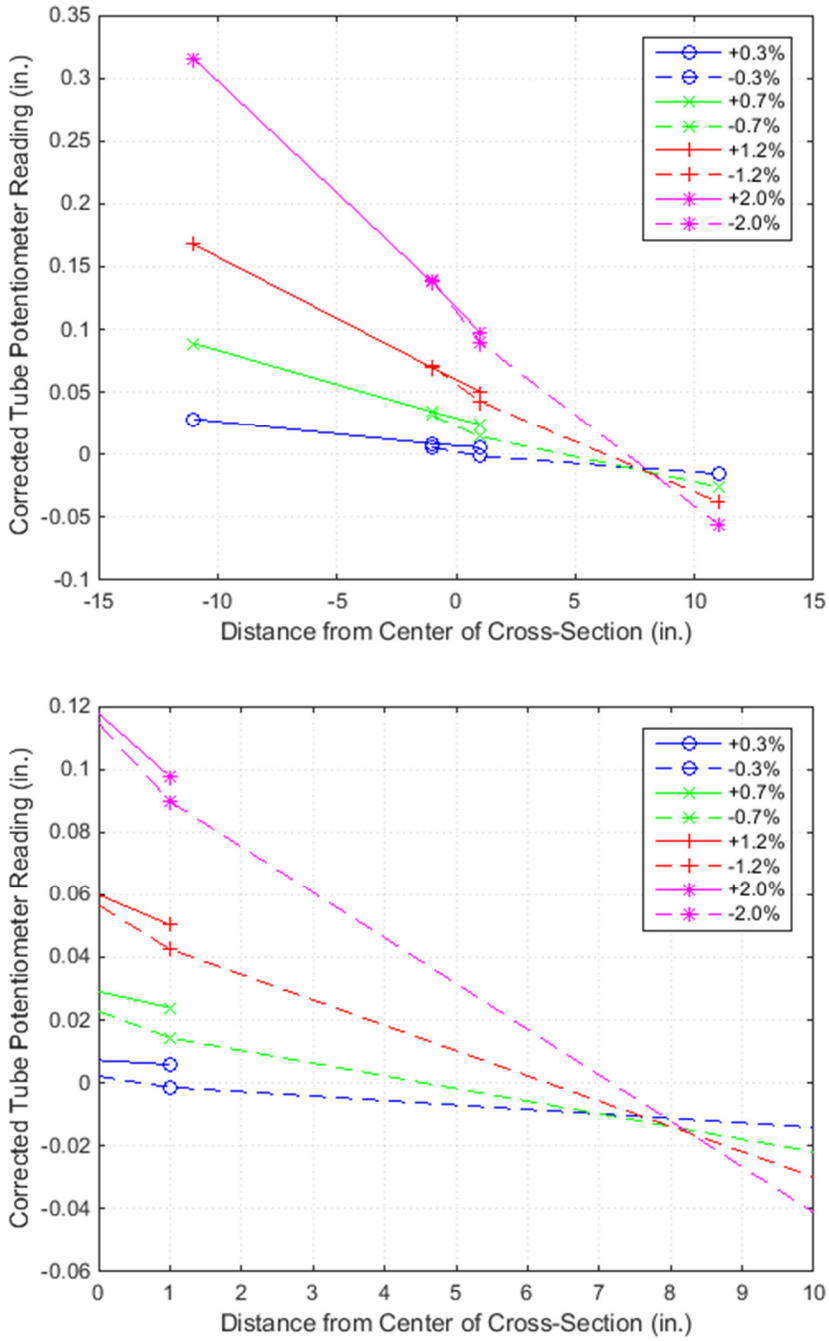

Figure 5.27 Corrected tube potentiometer readings for drift ratios between ±0.3% and ±2.0%: entire column shown on top, detail for compression side shown on bottom.

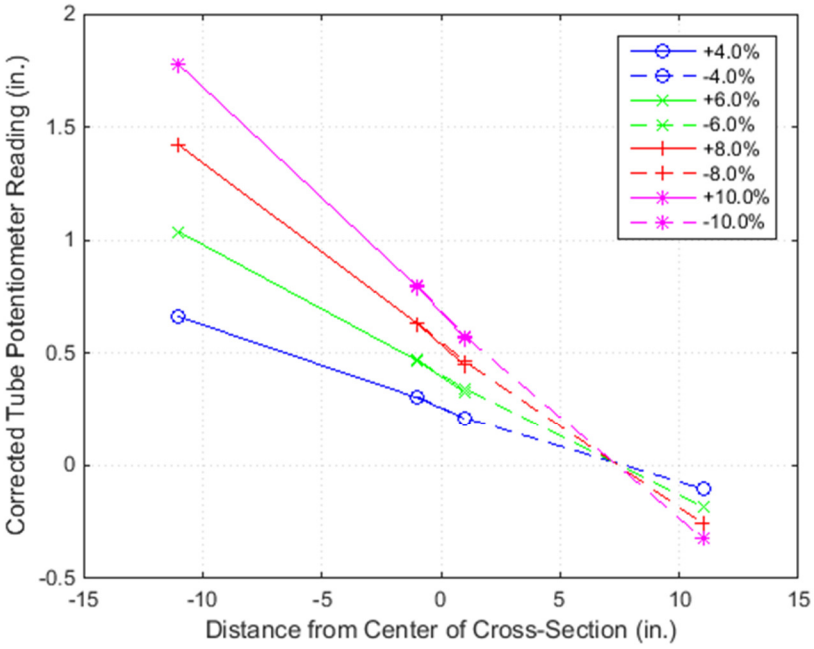

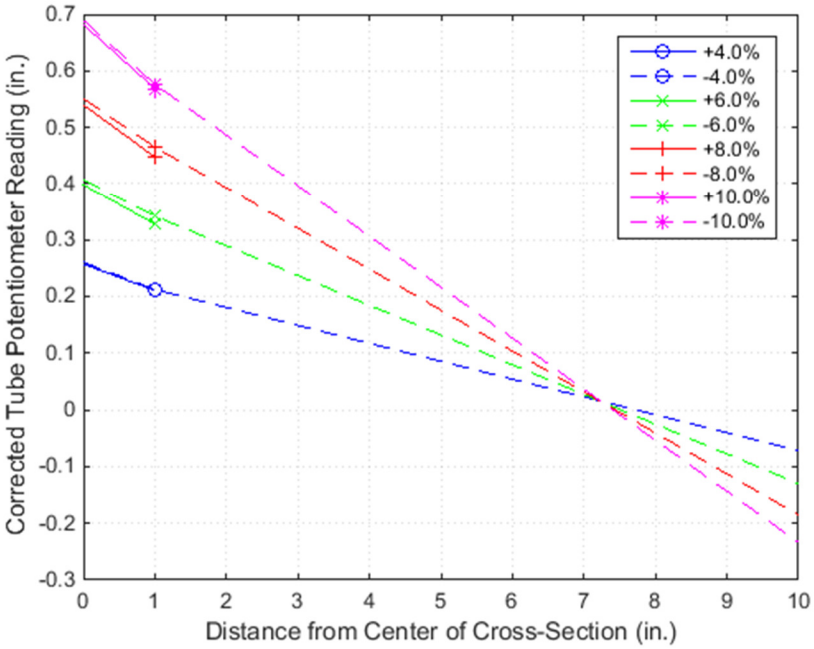

Figure 5.28 Corrected tube potentiometer readings for drift ratios between ±4.0% and ±10.0%: entire column shown on top, detail for compression side shown on bottom.

Figure 5.27 shows that, for drifts up to 1.2%, the neutral axis shifted from the near-center of the connection to 6.5 inches away from the center. Figure 5.28 shows that, for drifts greater than 2.0%, the neutral axis settled within a range of 7.5 to 8.0 in. away from the center of the connection (regardless of changes in drift ratio). This conclusion agrees with the observation of Section 5.7.1, that the neutral axis location was constant for much of the test's drift range. A thorough analysis of the neutral axis location can be found in Section 6.9.

5.8 STRAINS IN LONGITUDINAL REBARS

The three-wire strain gauges used on the steel reinforcing bars were improperly read by the data acquisition computer during the test. The results have not been shown in this section.

5.9 STRAINS IN SPIRAL

The three-wire strain gauges used on the spiral were improperly read by the data acquisition computer, or were incorrectly applied to begin with. However, Schaefer et al. (2014a) observed that the spiral strains within the steel-tube confined area of the column were very small. This suggested that the steel tube provided the majority of the confining force to the concrete, and is consistent with the respective volumetric ratios: $\rho_{vol} = 5.0\%$ for the tube and 0.85% for the spiral.

5.10 STRAINS IN STEEL TUBE

Before testing, strain-gauge rosettes were applied on the north face of the steel tube at elevations of two inches and six inches. These rosettes were composed of three, stacked, two-wire strain gauges oriented at 0°, 45°, and 90°. These two-wire strain gauges were properly recorded by the data acquisition system.

According to the experimental orientation, drifts to the north of the lab were identified as negative. Therefore, the north face of the column (where the rosettes were applied) was put into compression during negative drifts, and tension during positive drifts. Figure 5.29 and Figure 5.30 respectively show the hoop and longitudinal strains versus drift for the strain-gauge rosette placed at two inches above the top of the baseplate. The hoop strain is the reading from the strain gauge oriented at 0°, and the longitudinal strain is the reading from the stain gauge oriented at 90°.

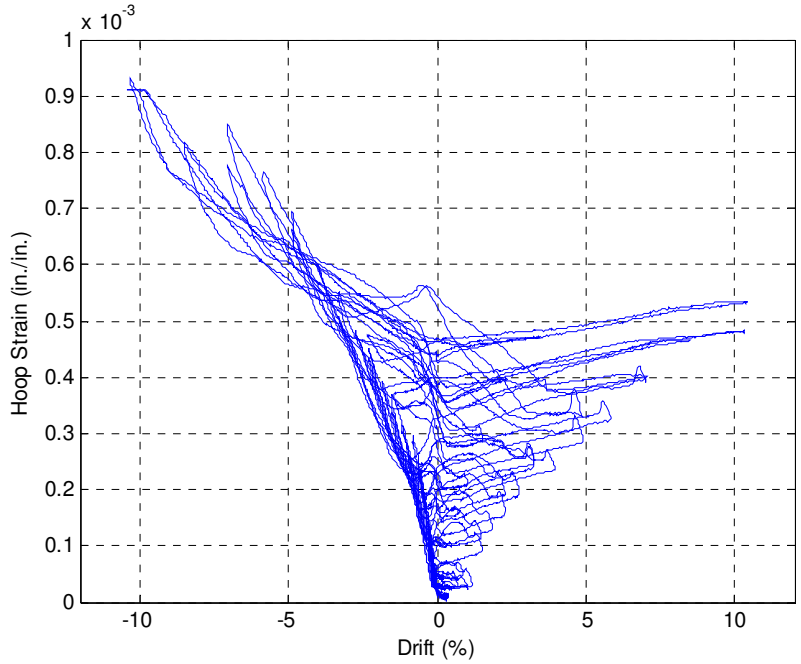

Figure 5.29 Hoop strain vs. drift at two inches above baseplate.

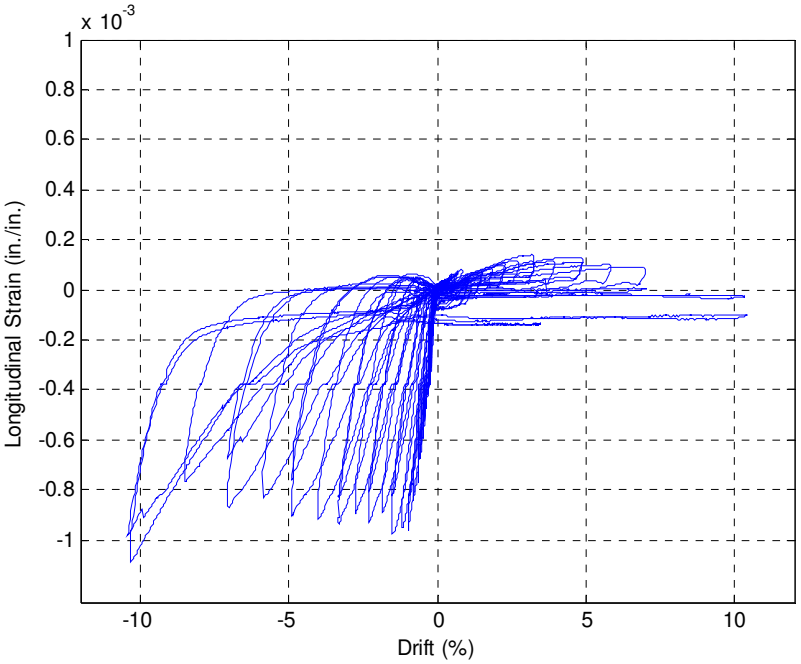

Figure 5.30 Longitudinal strain vs. drift at two inches above baseplate.

Figure 5.31 and Figure 5.32 respectively show the hoop and longitudinal strains versus drift for the strain-gauge rosette placed six inches above the baseplate. Again, the hoop strain is the reading from the strain gauge oriented at 0°, and the longitudinal strain is the reading from the stain gauge oriented at 90°.

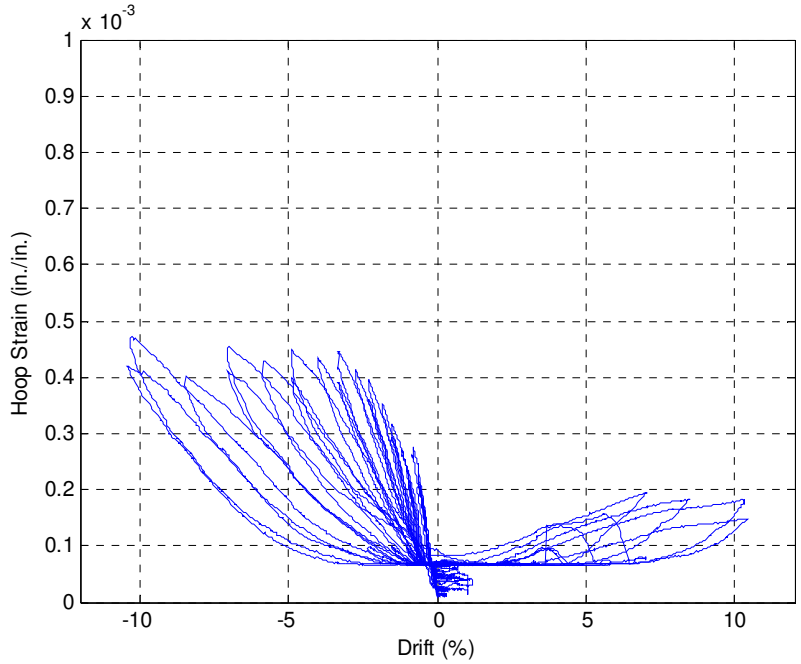

Figure 5.31 Hoop strain vs. drift at six inches above baseplate.

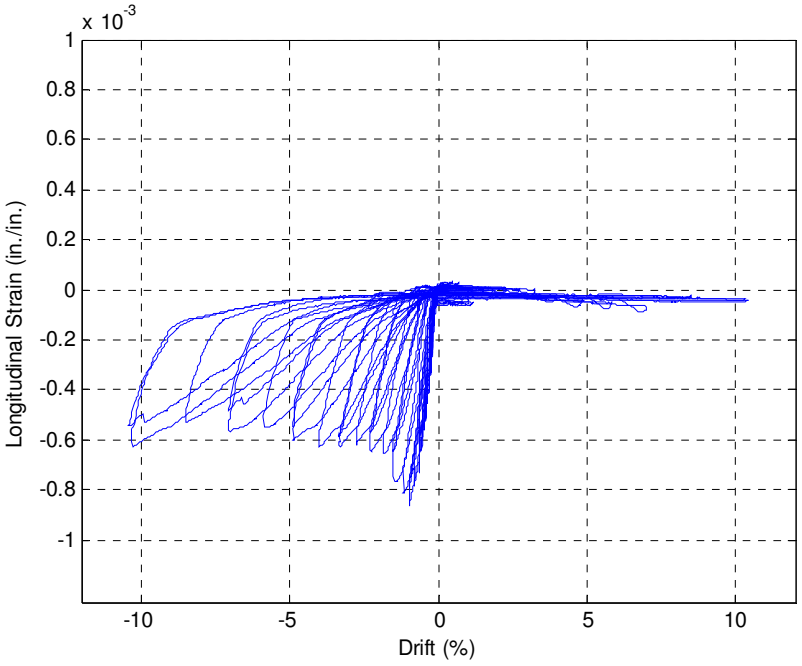

Figure 5.32 Longitudinal strain vs. drift at six inches above baseplate.

These results show that the longitudinal strains were compressive during negative drifts, with magnitudes up to about half of the yield strain, and tensile and significantly smaller during positive drifts. This behavior is as expected and suggests that some composite behavior was achieved between the tube and concrete for compression, but less so for tension. This behavior

was measured by both strain-gauge rosettes, but longitudinal strains were generally lower for the gauge at the 6 in. elevation.

The hoop strains were tensile for loading in both directions. They were larger (again up to about half of the yield strain) when the north side of the column, where the rosette was, was in compression. This is as expected. The strains were about half as large when the north column face was nominally in tension, which suggests that the entire circumference of the tube provided hoop confinement to the concrete.

Furthermore, the hoop strain versus drift plots for PreT-CB-ROCK had a shape similar to that of the spiral strain versus drift plots for PreT-CB-CONC (which did not have the confining tube detail). Figure 5.33 is a plot of the spiral strain on the north face of PreT-CB-CONC against drift ratio. The spiral strains were also generally tensile for both directions of loading, but much larger for drifts in the north direction (which put the north column face in compression). This comparison also suggests that the steel tube provided the confining force that is given by typical spiral reinforcement.

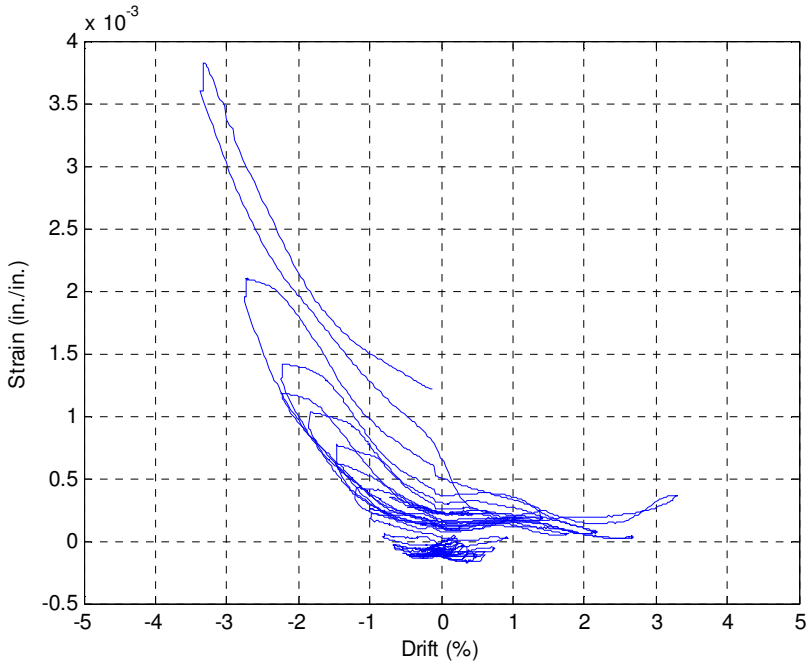

Figure 5.33 Spiral strain vs. drift for the north side of PreT-CB-CONC, at the column-cap beam interface (Davis et al., 2012).

A two-dimensional stress analysis, using the strain-gauge rosette results, is provided in the analysis section of this thesis (see Section 6.6).

5.11 STRAINS IN STEEL DOWEL BAR

Two-wire strain gauges were placed on the north and south faces of the steel dowel bar. These strains were properly recorded by the data acquisition system. The steel dowel bar was located at the rocking interface, and was intended to transfer shear forces from the column to the cap beam.

Figure 5.34 and Figure 5.35 respectively show the north and south strain gauge results plotted against the drift ratio of the column.

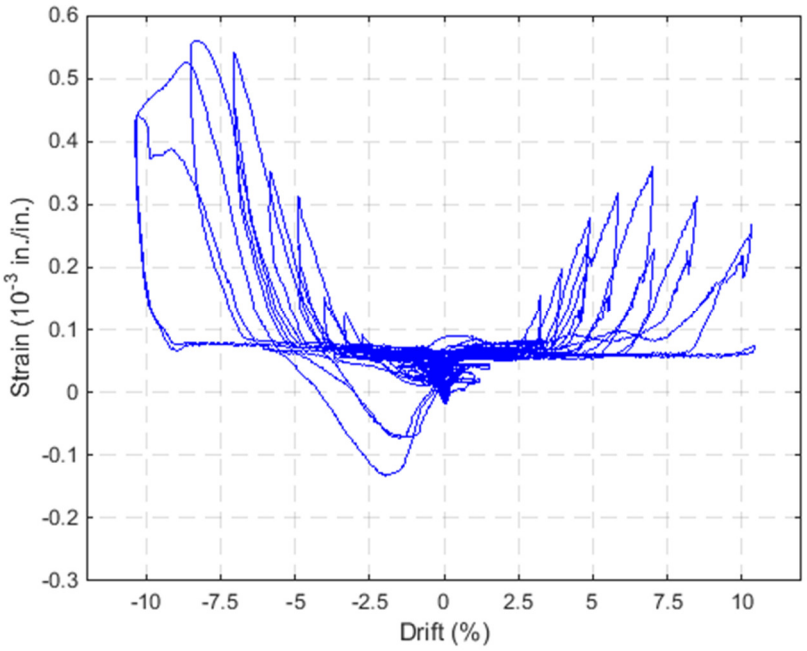

Figure 5.34 Strain vs. drift for north side of dowel bar.

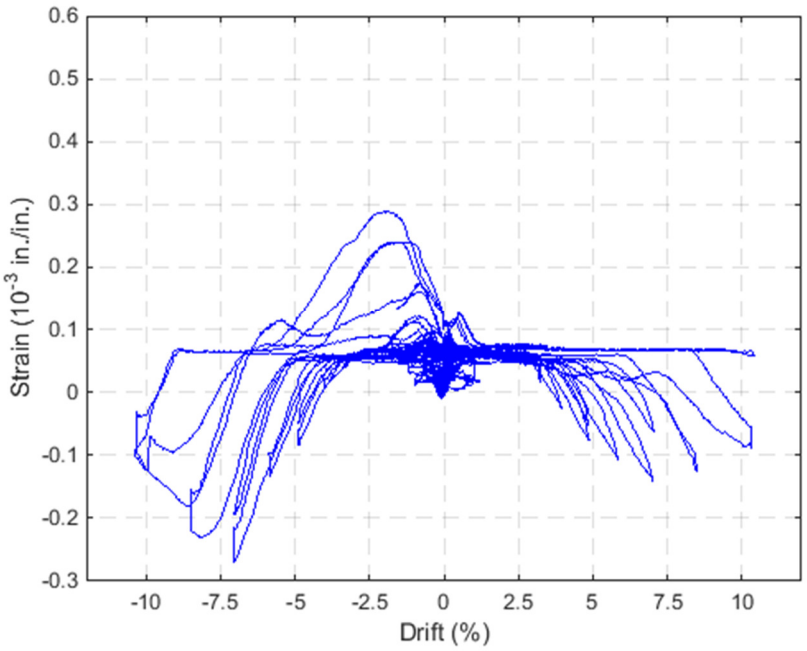

Figure 5.35 Strain vs. drift for south side of dowel bar.

These strain gauge results were not anticipated. The dowel bar was intended to effectively bend as a short cantilevered beam, as the dowel bar bore against the housing fixture placed in the

cap beam portion of the column. This described bending behavior would produce an odd function (equal and opposite responses for the two directions) for the strain versus drift plots. Furthermore, if the dowel bar was bending as expected, the plots for the north and south strain gauges would be mirror opposites of one another.

The net axial strain in the bar can be calculated by adding the output of the two gauges, and then dividing by two. The curvature in the bar can be calculated by subtracting the north gauge measurement from the south gauge, and then dividing by the bar diameter (2 in.). The net axial strain and curvature are shown in the left and right of Figure 5.36, respectively.

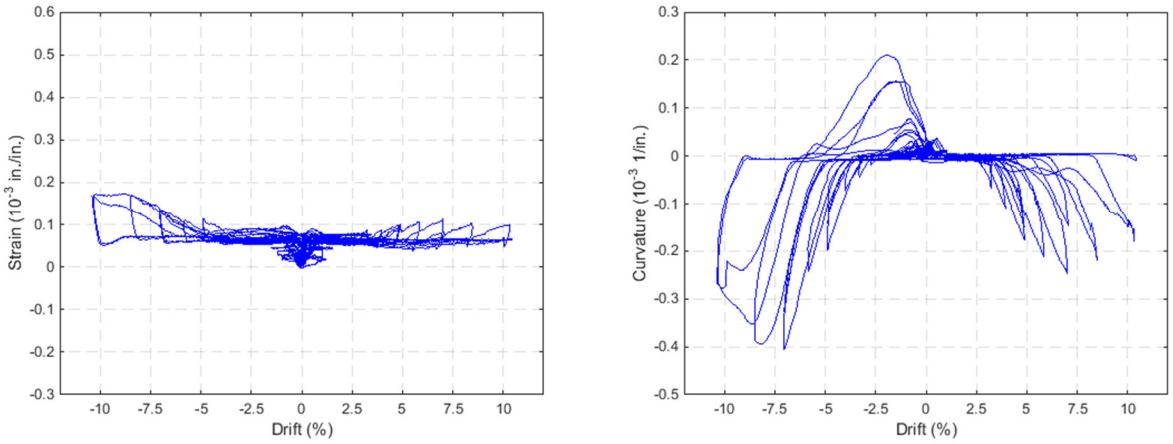

Figure 5.36 Net strain (left) and curvature (right) for the steel dowel bar.

A net axial strain of approximately 75με developed for much of the test. This could have been a result of the bar's friction with the hole in the annular plate of its housing.

5.12 STRAND RESPONSE

The behavior of the prestressing strands was measured with strain gauges and load cells, and is presented in this section. Further analysis of this data can be found in Section 6.7.

5.12.1 Strand Yielding and Buckling

5.12.1.1 Strain Gauge Data

The strands were instrumented with two-wire strain gauges, which were applied within the unbonded length of each strand (approximately 18 in. above the rocking interface). The strain results from these gauges were properly recorded by the data acquisition system.

The results from the strain gauges are shown in Figure 5.37 through Figure 5.39. A dashed, red line representing the nominal yield strain of 0.0087 in./in. (based on f_{py} = 250 ksi and E_p = 28600 ksi) has been included on these plots.

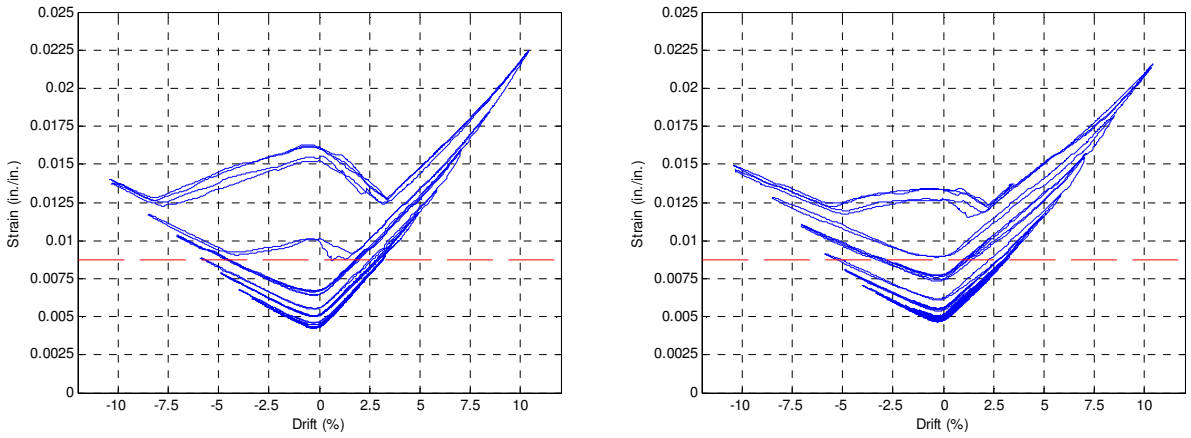

Figure 5.37 Strain vs. drift for NW strand (left) and NE strand (right); estimated yield line shown in dashed red.

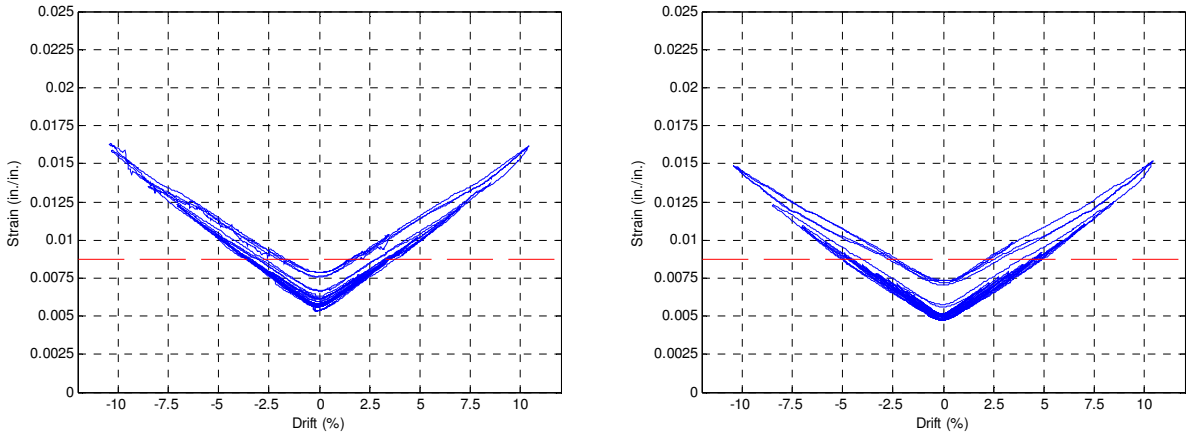

Figure 5.38 Strain vs. drift for W strand (left) and E strand (right); estimated yield line shown in dashed red.

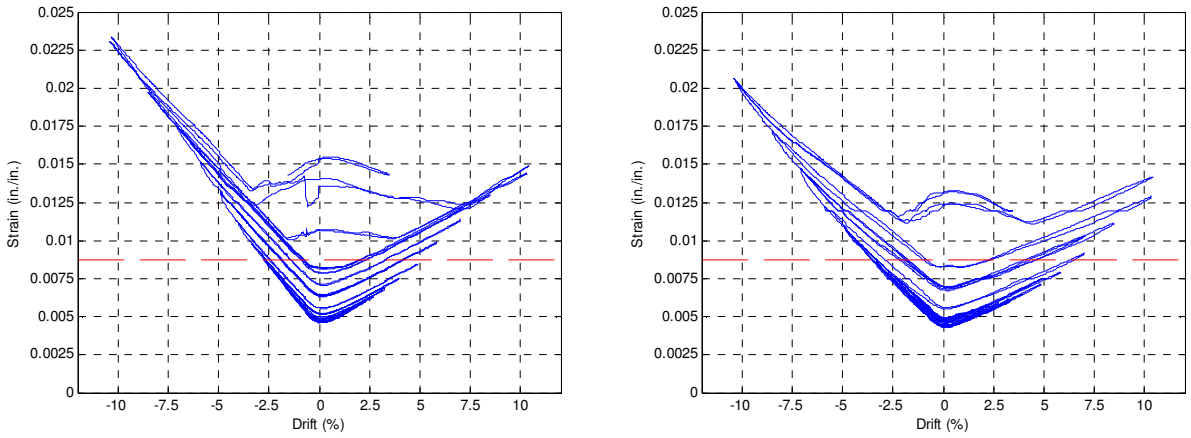

Figure 5.39 Strain vs. drift for SW strand (left) and SE strand (right); estimated yield line shown in dashed red.

The strains in each strand increased with increasing drift in each direction. Strains in the north strands displayed higher peaks when the column was displaced to positive drifts (pulled south) and the opposite was true for the south strands. The two central strands had a symmetric strain response. This response is as expected, based on the strand locations within the cross-section.

During the test, each strand exceeded the yield strain corresponding to the specified yield stress. The strands nearest the north and south face of the column reached their nominal yield strain at a drift of approximately 2.5%. The centrally located strands did not yield until drifts of 4-5%.

The strain gauge data presented this section is also used in Section 6.7.2 to approximate the stress of the strands during the test.

5.12.1.2 Possible Buckling of Unbonded Prestressing Strands

The strands located on the north and south sides of the cross-section exhibited unexpected behavior during the last two sets of the test. After reaching the maximum drifts of those cycles, the strains abruptly rose to a local peak as the column was returned to zero drift. This is in contrast to the response at smaller peak drifts, in which the strains returned smoothly to a well-defined "trough" at zero drift.

This behavior could have been caused by the buckling of the strands along their debonded lengths in the column. Figure 5.40 shows a sample time history of the two strain gauge results from the northeast strand (the first three cycles of set ten are plotted). The figure shows that the readings generally agreed with each other. However, after the column was displaced to approximately 10.33% drift, the gauge readings were almost identical near the peak drift in each direction, but differed at low drifts. This behavior (a strain gradient across the depth of the strand) suggests bending at low drifts, which in turn suggests buckling. This experimental analysis technique has been used to identify the buckling of longitudinal reinforcement in previous research (e.g., Rodriguez et al., 1999).

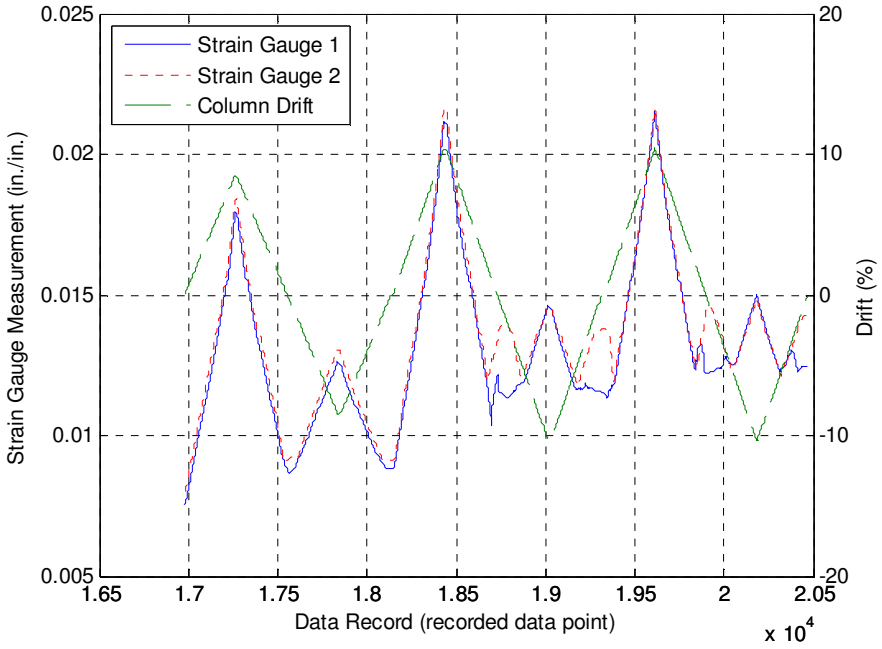

Figure 5.40 Time history of strain gauge readings on NE strand; drift shown for reference.

However, for a doubly-symmetric section undergoing pure bending, the strain reading from the compression face would negate the strain reading from the tension face if the two values were averaged. Conversely, during times of proposed strand buckling, the average strain gauge readings abruptly "spiked" in the positive (tensile) direction. Two explanations are offered:

1. The buckling behavior of the strands was not anticipated during the instrumentation phase of the specimen. For one particular strand, its pair of gauges were placed so that the gauges were applied on separate wires of the strand, at approximately the same longitudinal location (within ~4 in. of each other), and approximately on opposite faces of the strand. However, instrumenting the strand wires proved difficult, and the ideal placement was not always possible. The specific details of the final instrumentation were not recorded.

2. The buckling mechanism of the strands may not have followed traditional Euler modes. Rather, the strands may have locally buckled (by the stand wires unfurling and splaying away from the centerline of the strand) in addition to globally buckling in an Euler mode. These two possible buckling mechanisms are demonstrated in Figure 5.41. If the wires were indeed unfurling from the strand, the strain gauges would always record tensile strains, as they were placed on the outside of the strand wires.

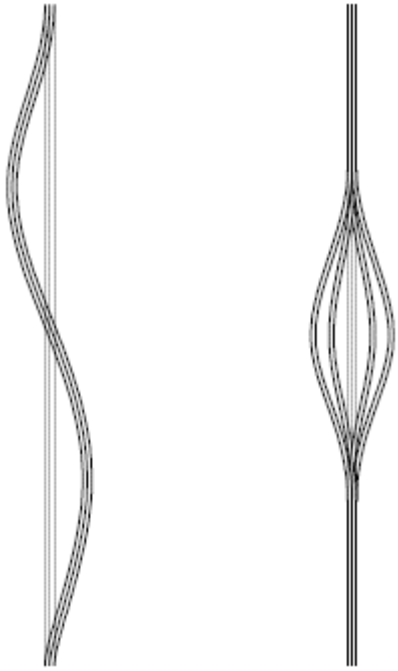

Figure 5.41 Possible buckling modes for prestressing strands: Euler buckling (left) and unfurling (right). The light gray line indicates the undeformed shape.

Additionally, the strands would have been laterally constrained by the PVC debonding tubes (not pictured in Figure 5.41), which further complicates the possible buckling behavior.

Assuming that this behavior resulted from strand buckling, Table 5.7 provides a summary of the onset of strand buckling during the test. The onset of buckling was defined as the point at which the pair of strain gauges on a particular strand began to differ from one another – which was qualitatively determined from examination of the strain gauge records. The north and south strands buckled during the same cycle of the test, and had similar levels of strain prior to the first occurrence of buckling.

Table 5.7 Summary of strains in prestressing strands.

Strand	Maximum Strand Strain	Max/Min Drift Prior to Buckling	Peak Strain Prior to Buckling	Strain at Onset of Buckling
Northeast	0.0216 in./in.	+10.33%	0.0214 in./in.	0.0119 in./in.
Northwest	0.0224 in./in.	+8.47%	0.0190 in./in.	0.0093 in./in.
East	0.0152 in./in.	N/A	N/A	N/A
West	0.0163 in./in.	N/A	N/A	N/A
Southeast	0.0206 in./in.	-10.32%	0.0207 in./in.	0.0117 in./in.
Southwest	0.0235 in./in.	-7.05%-	0.0174 in./in.	0.0084 in./in.

5.12.2 Strand Slipping

Slipping of the strands was detected with the use of load cells, which were placed between the screw thread device (STD) and anchor chuck of each strand at the top of the column (detailed in Section 2.9). These load cells and chucks were set during the re-stressing operation of the column. At that time, the strands had just been released, and were bonded to the concrete. The ends of the strands were then elongated, and the screw thread device on each strand was used to restrict the strand's elastic shortening after removal of the jack from the strand. This operation externally and mechanically anchored the strand at the top of the column. A load cell was placed between the strand chuck and the STD, which was put into compression as the chuck bore onto the load cell, which then bore onto the STD, which then bore onto the end of the column. Changes in the readings of these load cells would indicate slipping of the strands along their bonded length in the top of the column. It is noted that strand chucks were installed on both ends of the column, but load cells were only used at the top end of the column. This was done because the bonded length was 31.5 inches in the bottom of the column, but only 18 inches in the top. Therefore, if the strands were to lose bond with the concrete, slipping would most likely occur in the shorter bond length at the top.

Figure 5.42 through Figure 5.44 show the forces in the load cell on each strand for the test; it is noted that the plots follow the "compression-negative" sign convention. A change in the force, followed by a plateau in the load (as observed in the northwest strand), is believed to indicate partial slipping of the strand. The southwest strand appears to have maintained bond throughout the entire test (the load cell read the 6 kip anchorage force for the entire test). The four other strands (NE, W, E and SE) appear to have lost significant bond with the concrete.

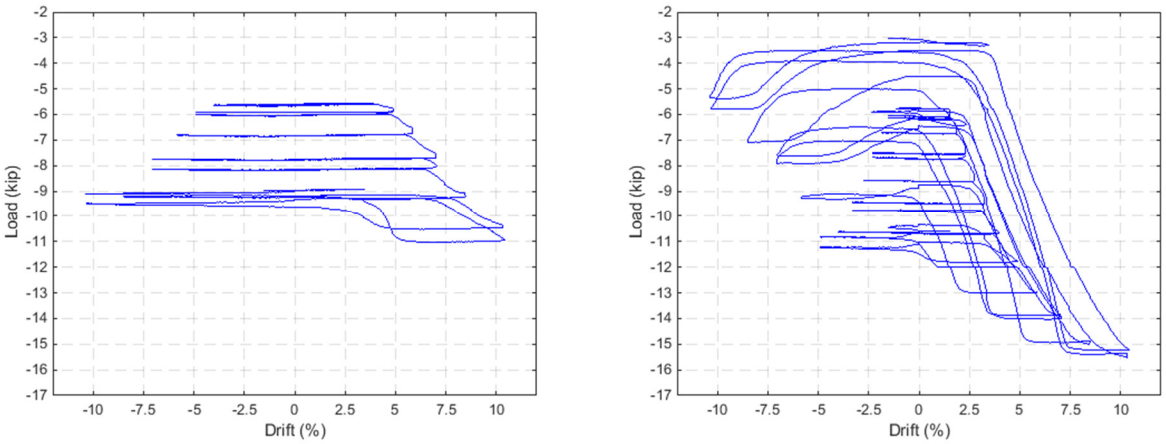

Figure 5.42 Drift vs. load in load cell for NW (left) and NE (right) strands.

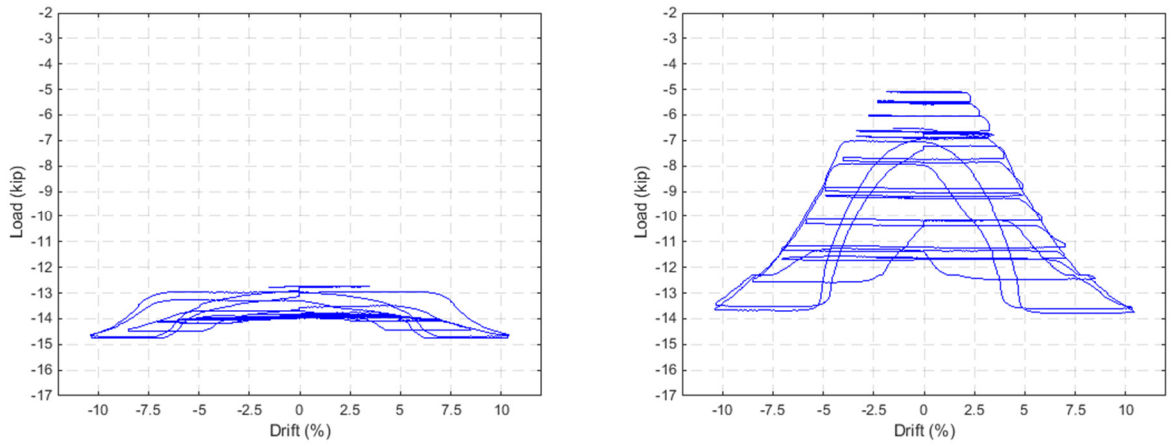

Figure 5.43 Drift vs. load in load cell for W (left) and E (right) strands.

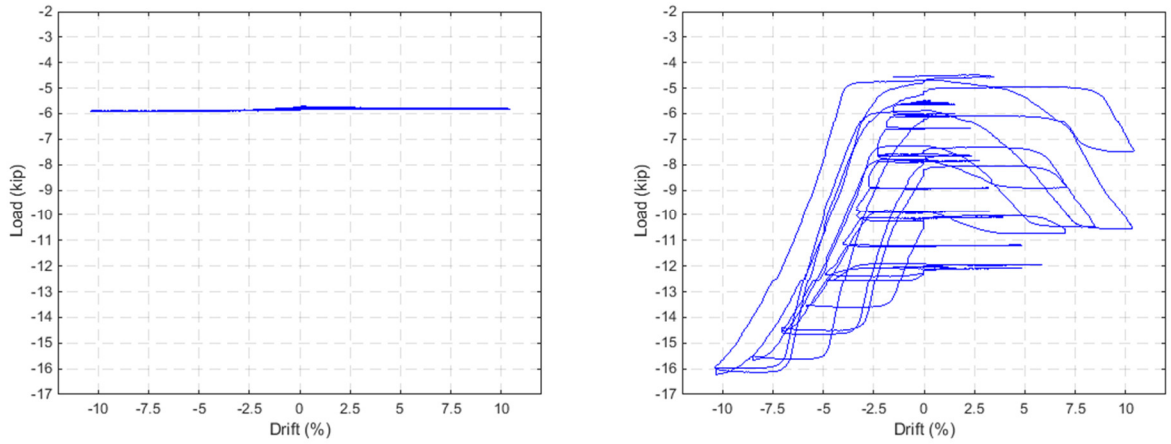

Figure 5.44 Drift vs. load in load cell for SW (left) and SE (right) strands.

The previous figures show that the strands on the west side of the column had less slip with respect to the strands on the east side. This could have resulted from the casting orientation of the specimen (the column was cast so that the east face was the top, finished surface of the concrete, see Section 2.9.1). The casting orientation resulted in more fresh concrete placed below the east strands (12.875" cast under the NE and SE strands versus 7.125" under the NW and SW strands). This may have reduced the concrete's available bond strength for those top-cast strands, often identified as the "top-bar effect". This phenomenon is considered in the development requirements of ACI 12.2.4 and Peterman (2007) extensively investigated the issue, for example.

Furthermore, the tendency for worse bond on top-cast strands also occurred in the prestressed columns tested by in Schaefer et al. (2014a) and Finnsson (2013). However, this specific conclusion was not realized in those reports, and differences in strand slipping were simply attributed to random variation in bond strength. Conversely, Davis et al. (2012) only measured slipping of one strand in his column tests. This could have been a result of superior concrete placement during the construction of his columns (the Davis columns were fabricated by a professional precaster).

Furthermore, this varying quality in the concrete bond may have affected the onset of strand buckling. Figure 5.37 and Figure 5.39 show that the west strands buckled during earlier cycles than the corresponding east strands (also summarized in Table 5.7). The better bond on the west strands could have induced more significant plastic straining at lower drift ratios. Conversely, when the east strands slipped prematurely, a strain loss likely resulted along their unbonded lengths. Furthermore, larger maximum strains were recorded for the west strands (again, with respect to the corresponding east strand).

Finally, it is noted that during construction, the west strand was believed to have slipped sometime during or after the release of the strands, but before the setting of the external, mechanical anchorages at the ends of the column (see Section 2.9.1.1). Therefore that strand was effectively post-tensioned to the design, effective prestress force (14.0 kip), which can be observed on the drift versus load cell data for that strand (on left in Figure 5.43).

The strand bond is further discussed and approximated in Section 6.7.3.

5.13 RESIDUAL DISPLACEMENT CYCLES

Following the main test, several displacement cycles were completed in order to investigate the residual properties of the column. Of particular interest were:

- the column's behavior without an applied vertical load,
- and the column's behavior after significant strand yielding.

This section provides some of the data that was collected during the residual cycles. Additional discussion of the setup for these cycles can be found in Section 3.3.2.

Figure 5.45 gives the effective force versus drift response. The effective force and drift were calculated in the same manner as described in Section 5.3, though it is noted that the effective force is essentially the reading of from the horizontal actuator, as these cycles were conducted with minimal axial load (the Baldwin loading head was used to stabilize the top of the column, resulting in a vertical load range of zero to 0.5 kips).

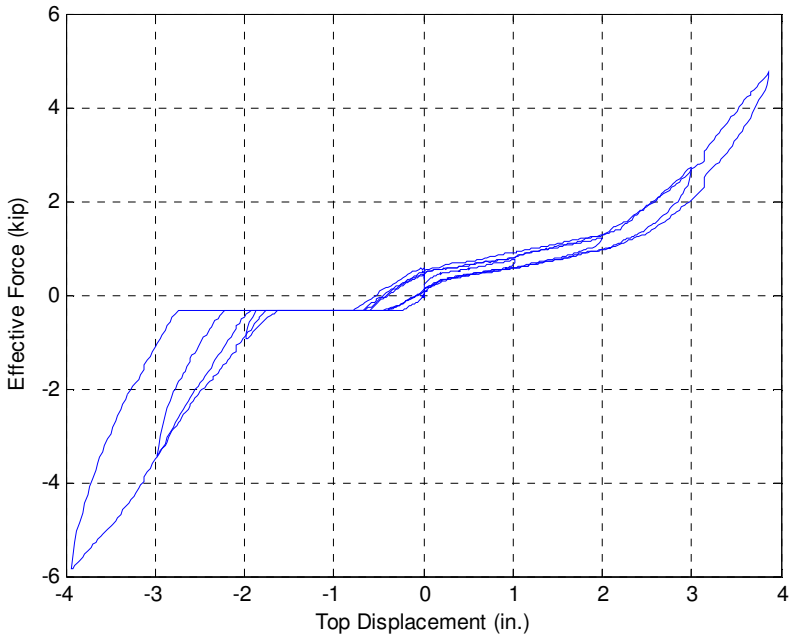

Figure 5.45 Effective force vs. top displacement for residual cycles.

It is noted that the "flat lining" portion of the effective force (appearing at a load of about -0.5 kips, on the negative displacement side of the graph) is representative of an error in the data acquisition for this experiment, which affected several potentiometer-type instruments, and all of the three-wire strain gauges (the gauges used on the reinforcing bars and spiral). This error appears to have produced erroneous ranges in data readings, which were unique to each instrument affected by the error. For measurement readings within these ranges, the data acquisition system would record the absolute lower bound of the range. For readings greater than the absolute maximum of the range, the data acquisition system would record the difference between the reading and absolute maximum, with an offset of the lower bound of the range. For example, if the erroneous range for the effective force were from -0.5 kips to -3.0 kips, then an actual force of -2.5 kips would be recorded as -0.5 kips (the reading is in the error range) and an actual force of -3.5 kips would be recorded as -1.0 kips (the reading is "past" the error range).

However, the positive load readings were not affected by this error, which offers potentially useful data concerning the behavior of the yielded, unbonded system.

The displacements measured by the linear potentiometers on the tube are plotted as a function of drift in Figure 5.46. The non-linearity of these responses may be a result of the residual rounding of the grout pad (following the primary 40 cycle test). It is noted that both of these potentiometers functioned properly during the residual cycles (in contrast to the defective potentiometer placed on the south side of the confining tube during the main 40 cycle test).

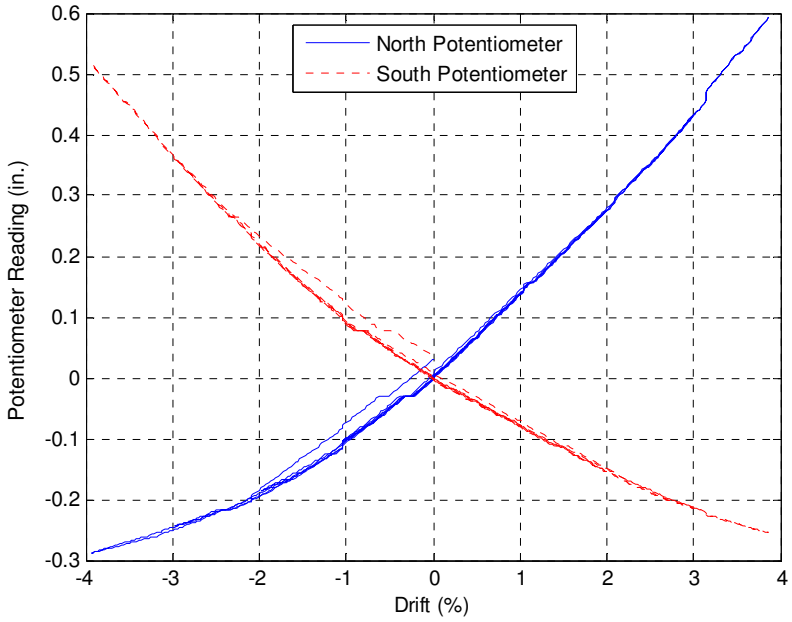

Figure 5.46 Tube potentiometer readings vs. drift for residual cycles.

6 Analysis and Comparison of Experimental Responses

The measured responses of the steel tube confined, column-cap beam test specimen (PreT-CB-ROCK) presented in Chapter 5 are compared with the responses of other related specimens in this chapter. The key properties and naming convention for the other specimens are provided in Chapter 1. Specifically, the responses are compared with those of:

- a column-cap beam test specimen (specimen PreT-CB-CONC from Davis et al., 2012),
- a steel tube confined, column-footing specimen (specimen PreT-SF-ROCK from Schaefer et al., 2014a),
- and a precast, non-prestressed, conventionally reinforced, column-to-footing connection (specimens PCC-SF-THK1 and -THK2 from Haraldsson et al., 2011b).

Table 6.1 summarizes the significant design differences between the three pre-tensioned specimens.

Table 6.1 Summary of geometric differences.

	Specimen		
Design Component	**PreT-CB-CONC**	**PreT-CB-ROCK**	**PreT-SF-ROCK**
Connection Detail	Not applicable	Steel tube and baseplate	Steel tube and baseplate
Socket Connection	Reduced diameter column extension and protruding No. 4 bars grouted into cap beam ducts	Reduced diameter column extension and protruding No. 4 bars grouted into cap beam ducts	Full width column cast into concrete footing
No. 4 Debonding Length	Not applicable	12 in.	8 in.
Strand Debonding Length	54 in.	54 in.	48 in.

6.1 MOMENT-DRIFT RESPONSES

The complete moment-drift cyclic responses of the top connection constructed with the rocking detail (PreT-CB-ROCK) and without the detail (PreT-CB-CONC) are compared in Figure 6.1. The responses of the top connection and bottom connection (PreT-SF-ROCK) are compared in Figure 6.2.

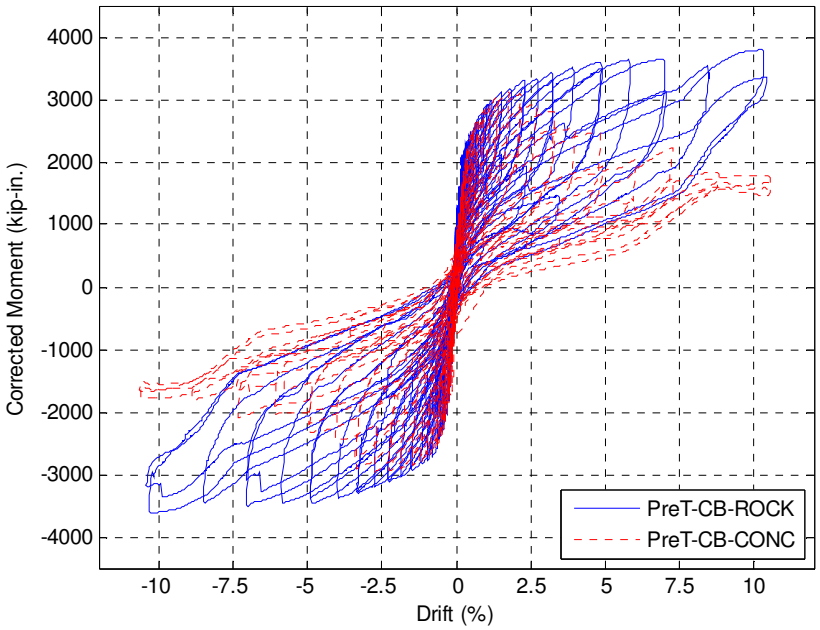

Figure 6.1 Comparison of PreT-CB-ROCK to PreT-CB-CONC.

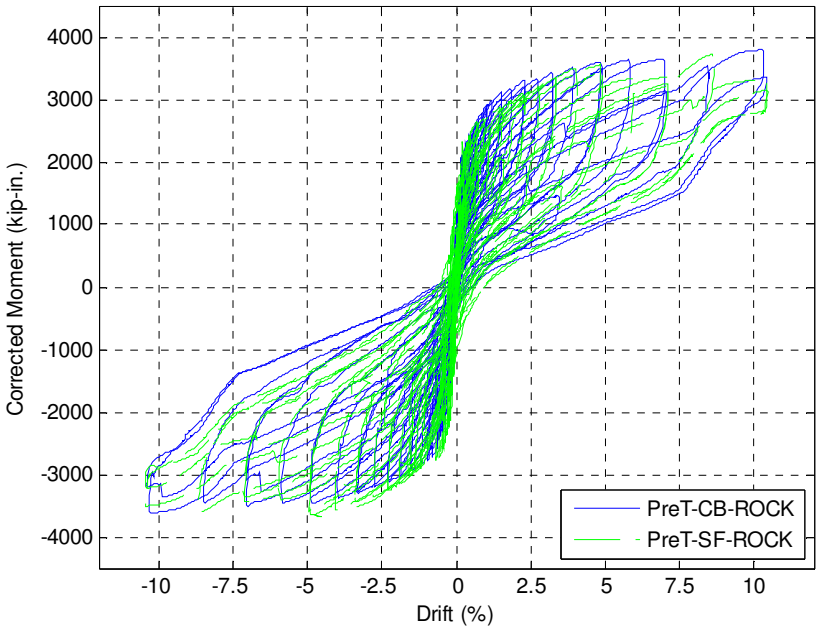

Figure 6.2 Comparison of PreT-CB-ROCK to PreT-SF-ROCK.

The strength of the PreT-CB-CONC specimen degraded throughout the test due to the progression of damage in that specimen. This damage was not observed in the PreT-CB-ROCK specimen; its measured moment-drift hysteresis shows a continually increasing strength up to a drift ratio of over 10%. The complete cyclic responses of the two rocking columns were very similar, but not identical. Both rocking systems had peak strengths at relatively large drift ratios,

maintained good ductility, re-centered well, and had similar bilinear stiffnesses. Table 6.2 summarizes the moment-drift responses. In the two -ROCK specimens, no value is given for the drift ratio at 80% of maximum moment because the available stroke of the horizontal actuator limited the applied drifts to ±10.65% (the maximum of the testing protocol). As shown in the corrected moment versus drift plot of Figure 5.5, the load appeared to still be increasing at a drift of 10%, despite the fact that most of the deformed bars had fractured by then.

Table 6.2 Summary comparison of moment-drift responses.

Point of Interest	PreT-CB-CONC		PreT-CB-ROCK		PreT-SF-ROCK	
	North Direction	South Direction	North Direction	South Direction	North Direction	South Direction
Maximum Moment (kip-in.)	-2948	+3114	-3628	+3802	-3690	+3725
Drift Ratio at Maximum Moment (%)	-2.73	+1.77	-10.31	+10.33	-4.49	+8.61
80% of Maximum Moment (kip-in.)	-2358	+2491	-2902	+3041	-2952	2980
Drift Ratio at 80% of Maximum Moment (%)	-4.93	4.84	N/A	N/A	N/A	N/A

6.2 FORCE-DRIFT ENVELOPES

The envelopes of effective force versus drift ratio for several test specimens (PreT-CB-ROCK, PreT-CB-CONC, and PreT-SF-ROCK) are shown in Figure 6.3. The corresponding normalized versions of the envelopes are shown in Figure 6.4. The normalization was performed by dividing a specimen's south-drift response by its maximum effective force in that direction, and the north-drift response by its maximum effective force in that direction. For clarity, only the peak and valley results from the second cycle of each set are shown.

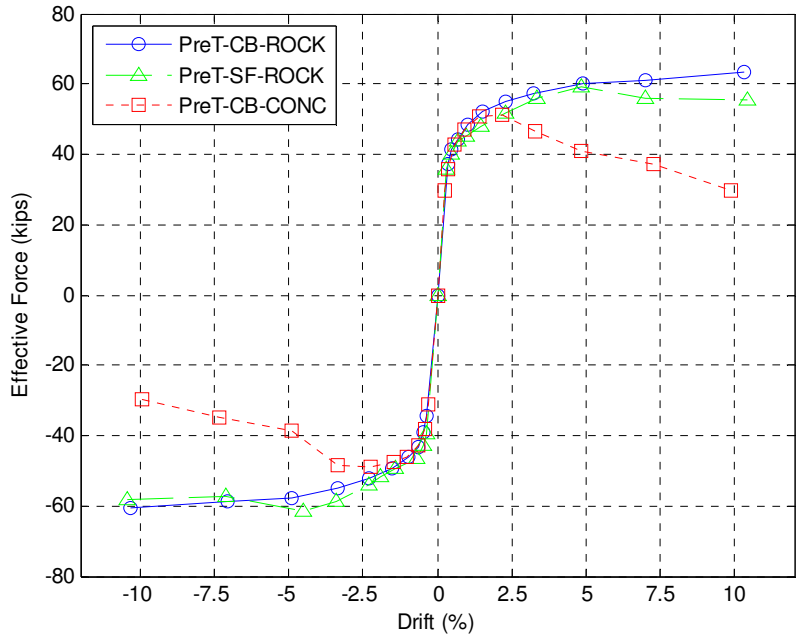

Figure 6.3 Effective force vs. drift ratio envelopes.

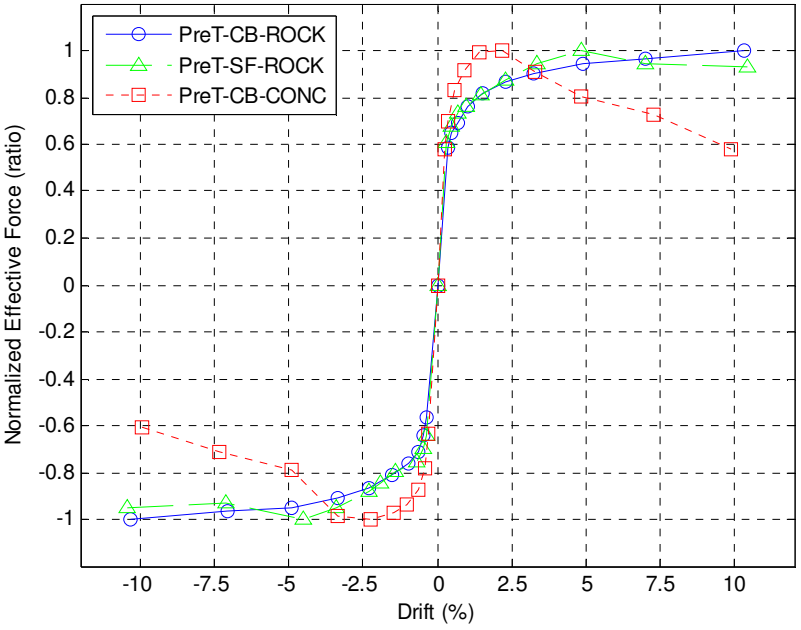

Figure 6.4 Normalized strength envelopes.

The strength envelopes for the three specimens were nearly identical up to a drift ratio of approximately +/-2.5%. At that drift ratio, the PreT-CB-CONC specimen began to lose strength due to concrete spalling within the plastic-hinge region of the column. The two rocking specimens (PreT-CB-ROCK and PreT-SF-ROCK), whose ends were confined by the steel tube, exhibited similar strengths up to drift ratios of approximately +/-5%. At this level of drift, the reinforcing

bars in the spread footing specimen (PreT-SF-ROCK) began to fracture, leading to a slight degradation in strength. The cap-beam specimen (PreT-CB-ROCK) maintained strength in both directions for the entire test, and exhibited peak strengths during the final set of the test (drift level of approximately +/-10.5%). This difference in behavior is attributed to the longer debonded length for the steel reinforcing bars in that specimen, which allowed elongations to be distributed over longer lengths of the reinforcing bar, which delayed bar fracture.

The normalized strength plot graphically demonstrates the early peak and subsequent strength degradation of PreT-CB-CONC, the maintaining of strength of PreT-SF-ROCK after bar fracture, and the continual strength gain of PreT-CB-ROCK to the maximum applied drift levels of the test.

Bridge columns are typically expected to experience drift ratios of approximately 1.5% to 2% in the design basis earthquakes (DBE). A maximum considered earthquake (MCE) may result in drift ratios of 3% to 4%. Peak flexural strengths occurred at drift levels greater than 5% for both the steel tube confined specimens. The performance of both specimens can therefore be judged to be more than adequate to resist the cyclic loading of seismic events.

6.3 ENERGY DISSIPATION

The energy dissipated by each specimen was calculated by integrating (using the trapezoid rule) the area of the effective force versus displacement loops for each test cycle.

6.3.1 Comparison of Unbonded, Pre-Tensioned Specimens

The energy dissipated per cycle during the PreT-CB-ROCK test is shown in Figure 6.5; Figure 6.6 shows the corresponding cumulative energy dissipated during that test. Both figures show that the dissipated energy correlated closely with the imposed drift ratio, as expected.

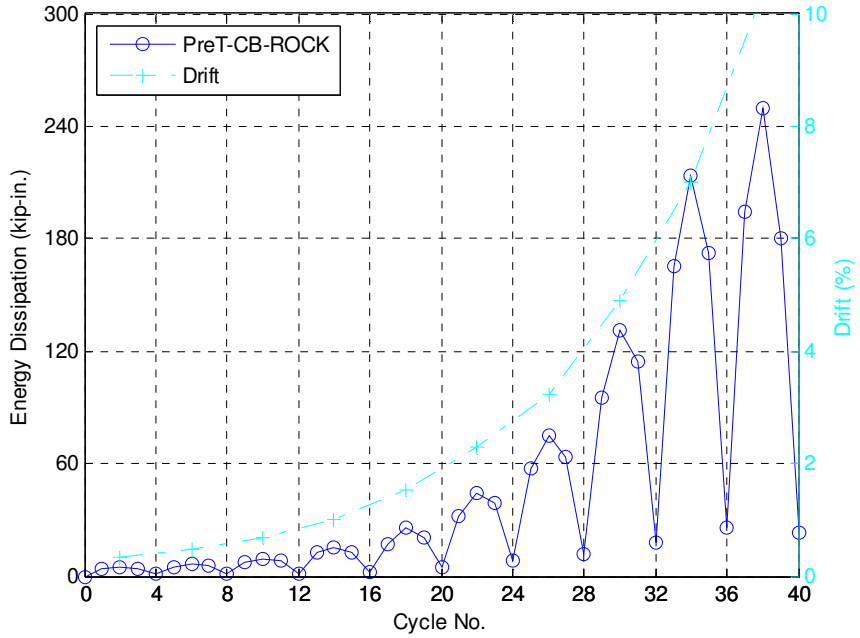

Figure 6.5 Energy dissipated per cycle for PreT-CB-ROCK.

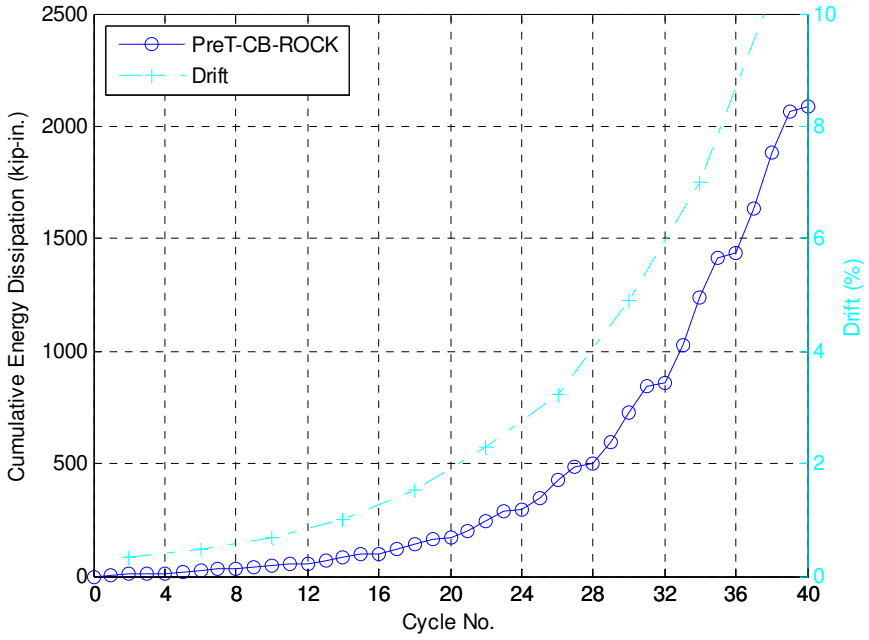

Figure 6.6 Cumulative energy dissipated for PreT-CB-ROCK.

Figure 6.7 and Figure 6.8 show the energy dissipation for the three unbonded, pre-tensioned bridge column specimens. The energy dissipation for the steel tube confined columns, PreT-CB-ROCK and PreT-SF-ROCK, were similar until the sixth cycle set (Cycle 21), corresponding to a drift ratio of approximately 2%. This difference was attributed to the longer debonded length for the reinforcing bars in the PreT-CB-ROCK specimen, which spread axial

elongations of the bars over longer lengths and delayed the onset of fracture in the reinforcing steel. The PreT-CB-CONC specimen, which did not have the steel tube assembly, exhibited similar levels of energy dissipation compared to the rocking systems until Set 7-Cycle 25, at a drift ratio of about 2.5%. At that point in the test, significant spalling had occurred in the column along with subsequent reinforcing bar buckling and fracture.

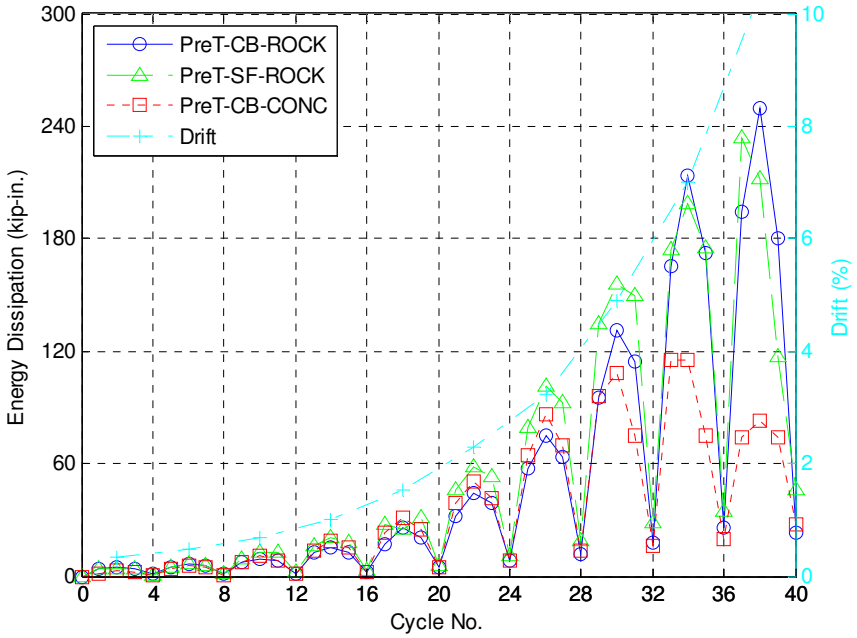

Figure 6.7 Comparison of energy dissipation per cycle.

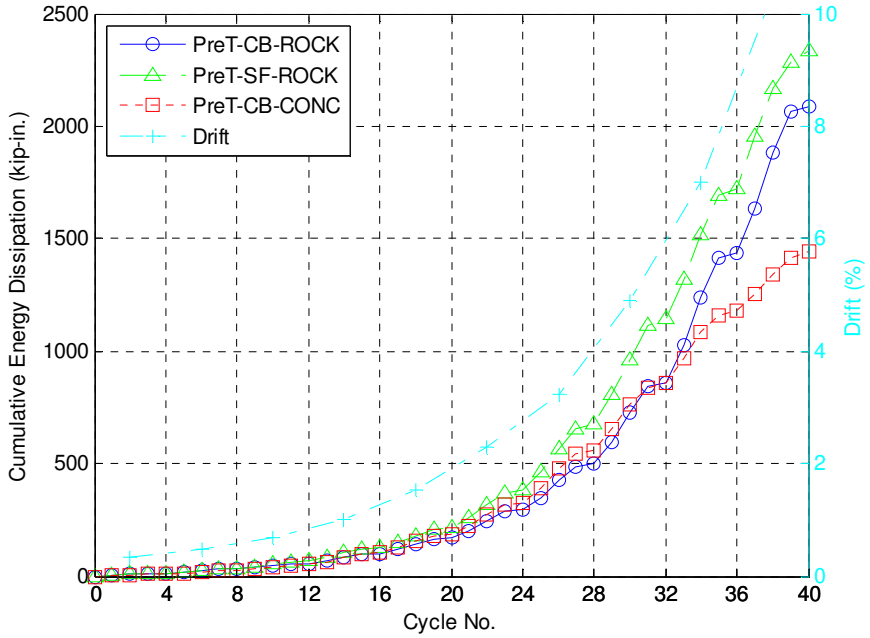

Figure 6.8 Comparison of cumulative energy dissipation.

To facilitate comparison among a variety of test specimens, the energy dissipation of these tests was normalized. This normalization was completed by dividing the area of each cycle's force-displacement loop ($A_{loop(i)}$) by the area of a rectangle defined by the maximum and minimum effective forces observed during the entire test (F_{max} and F_{min}), and the maximum and minimum displacements of the respective cycle ($\Delta_{max(i)}$ and $\Delta_{min(i)}$). Figure 6.9 graphically illustrates the formulation for the normalization.

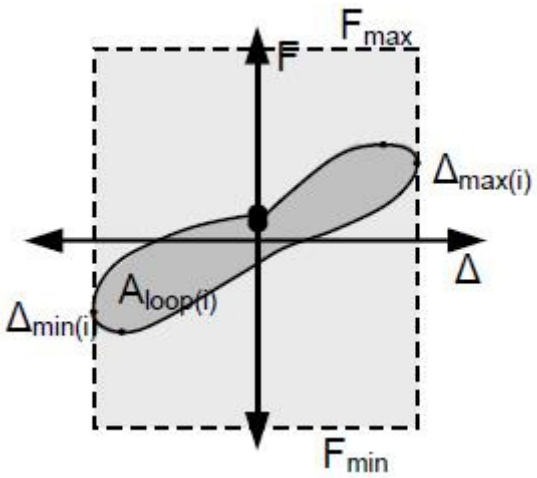

Figure 6.9 Normalization method for energy dissipation (Pang et al., 2008).

Figure 6.10 provides a plot of the cumulative normalized energy dissipation for the three pre-tensioned specimens (over the course of the test), and Figure 6.11 provides a plot of the cumulative normalized energy dissipation against column drift.

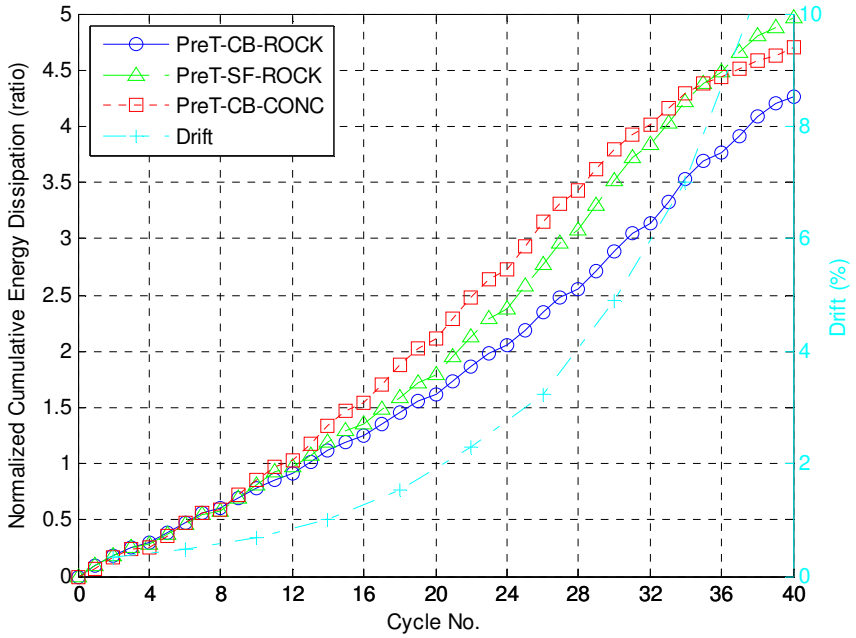

Figure 6.10 Comparison of normalized cumulative energy dissipation for entire test.

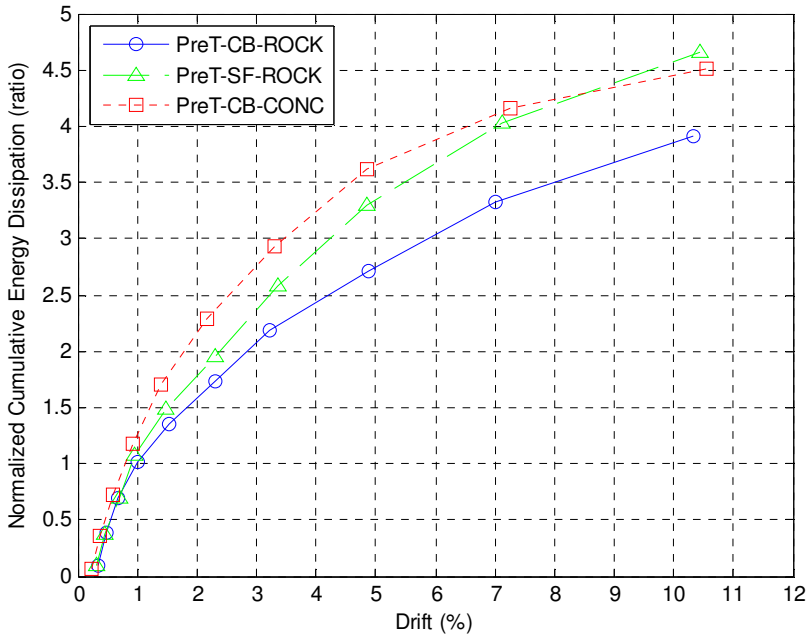

Figure 6.11 Comparison of normalized cumulative energy dissipation against drift ratio.

However, a slightly different method of normalization was used by Davis, Finnsson, and Schaefer. In those reports, the cumulative energy dissipated was normalized by dividing the energy dissipated in each cycle by the area of a box defined by F_{max}, F_{min}, Δ_{max}, and Δ_{min}: the peak and valley forces and displacements of the entire test. Figure 6.12 shows this normalization for the PreT- systems, for the sake of comparison to previous research.

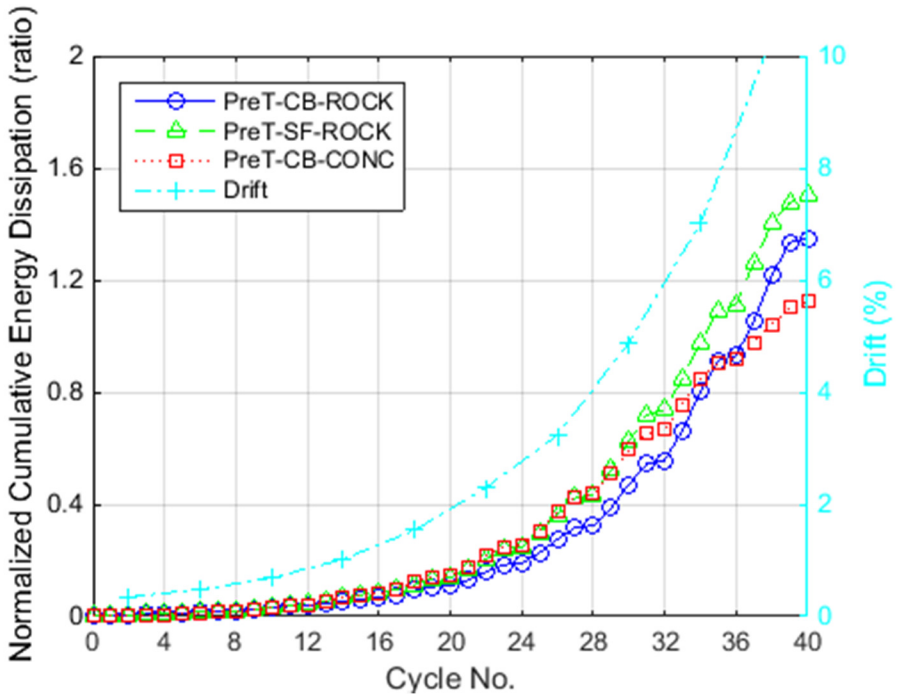

Figure 6.12 Comparison of normalized cumulative energy dissipation for entire test, using Davis's formulation.

6.3.2 Comparison with Non-Prestressed Specimens

The energy dissipation capacities of PreT-CB-ROCK were compared to those of two other specimens that were similar but not prestressed (specimens PCC-SF-THK1 and -THK2 from Haraldsson et al., 2011b). Such a comparison offers an evaluation of performance differences between the unbonded, rocking, prestressed structure tested in this project and more conventional reinforced concrete systems. Figure 6.13 shows the energy dissipation of each specimen; Figure 6.14 gives the cumulative energy dissipation observed during the course of each test.

These figures demonstrate the significantly larger degree of energy dissipation observed in the non-prestressed specimens. This is an expected result because the prestressing strands were designed to provide approximately 60% the flexural strength, and they did not cyclically yield in tension and compression. The energy dissipated per cycle in a re-centering column with unbonded pre-tensioning is thus inevitably lower, particularly in the later cycles, when some of the rebars had fractured. Up to about Cycle 22 (~2.5% drift) the ratio of energy dissipations (PreT/PCC) is about 1.0, but at higher drift it drops to about 2/3.

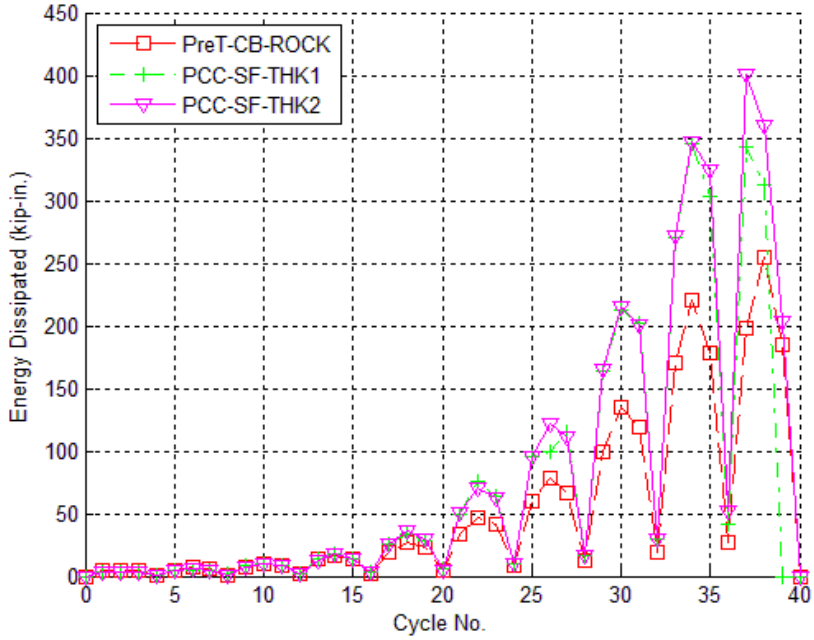

Figure 6.13 Energy dissipation per cycle compared to non-prestressed systems.

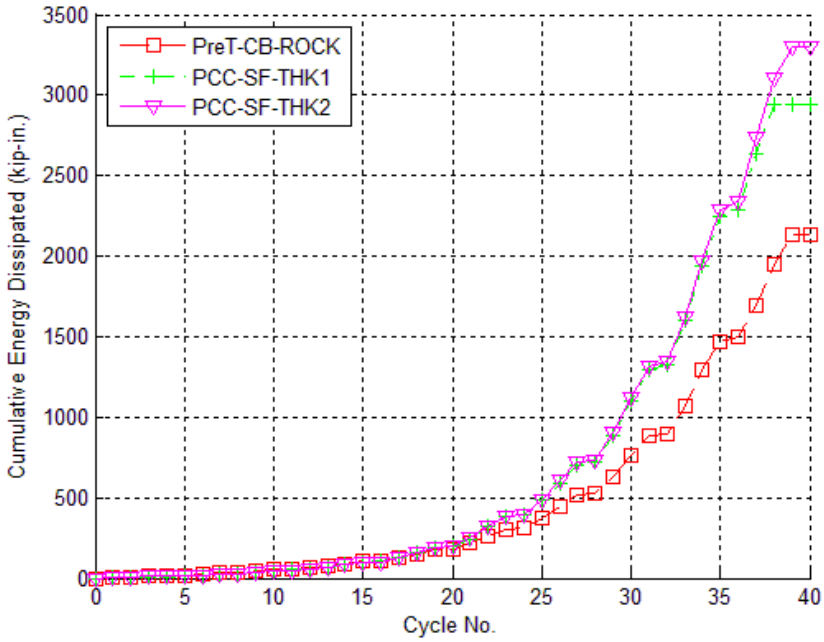

Figure 6.14 Cumulative energy dissipation compared to non-prestressed systems.

The energy dissipation of these non-prestressed systems was also normalized in order to ease comparison between specimens. This normalization followed Davis's method, as described in Section 6.3.1. Figure 6.15 provides a plot of the normalized cumulative energy dissipations for the specimens examined within this section. The plot shows that the conventional reinforced

concrete systems continued to dissipate energy for the entire test. The later cycles appeared to be contributing the most to the specimen's energy dissipation (similar with the rocking systems).

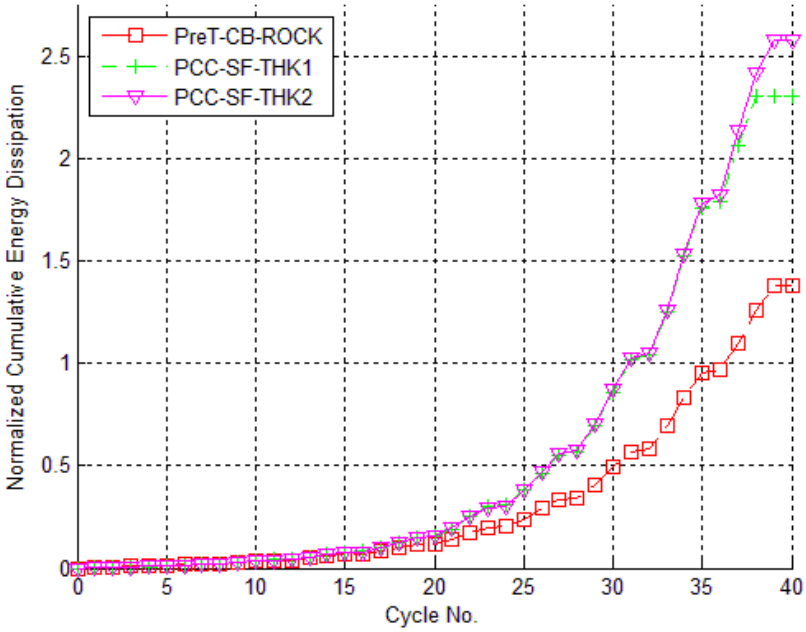

Figure 6.15 Normalized cumulative energy dissipation compared to non-prestressed systems.

6.4 EQUIVALENT VISCOUS DAMPING

The equivalent viscous damping (EVD) of the PreT-CB-ROCK specimen was determined from the energy dissipation properties, using Equation 6.1 (e.g., Chopra, 2007).

$$\zeta_i = \frac{2}{\pi} \cdot \frac{A_{loop(i)}}{A_{box(i)}} \qquad \textbf{Equation 6.1}$$

where $A_{loop(i)}$ is the area enclosed by a particular loop of the specimen's force-displacement history, and $A_{box(i)}$ is the area of the rectangle that encloses the loop (with limits of $F_{max(i)}$, $F_{min(i)}$, $\Delta_{min(i)}$, and $\Delta_{max(i)}$ for the loop in question). This geometry is slightly different from the definitions used in the normalized energy dissipation, and is graphically shown in Figure 6.16.

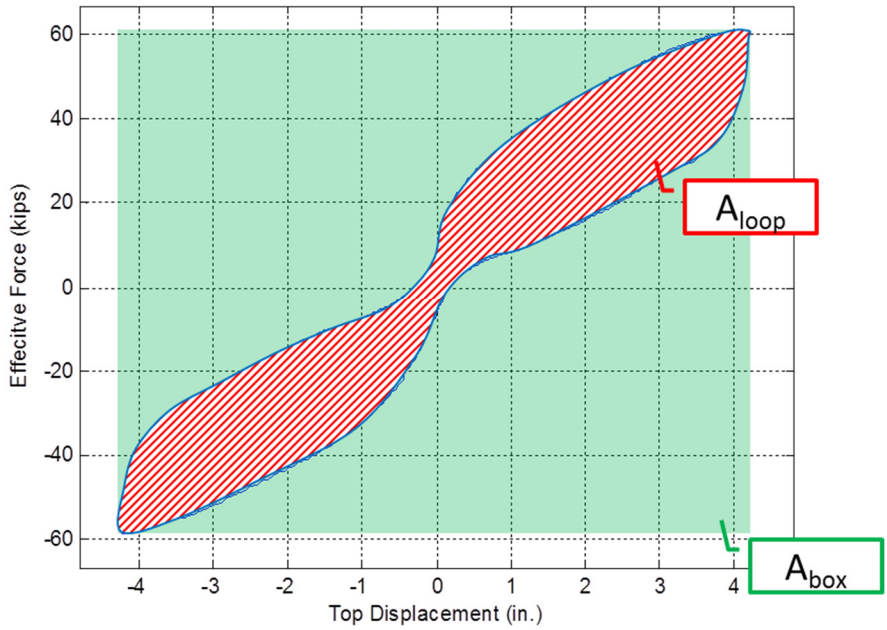

Figure 6.16 Graphical definition of variables in the equivalent viscous damping formulation.

Figure 6.17 shows the equivalent viscous damping for the prestressed specimens referenced in this section. PreT-SF-ROCK and PreT-CB-CONC resulted in similar ranges of equivalent viscous damping (10% to 15% EVD for drift ratios up to 6%). Up to a drift ratio of 6%, specimen PreT-CB-ROCK displayed lower damping ratios than the others, which again is attributable to the longer debonded length of the steel reinforcing bars for that column.

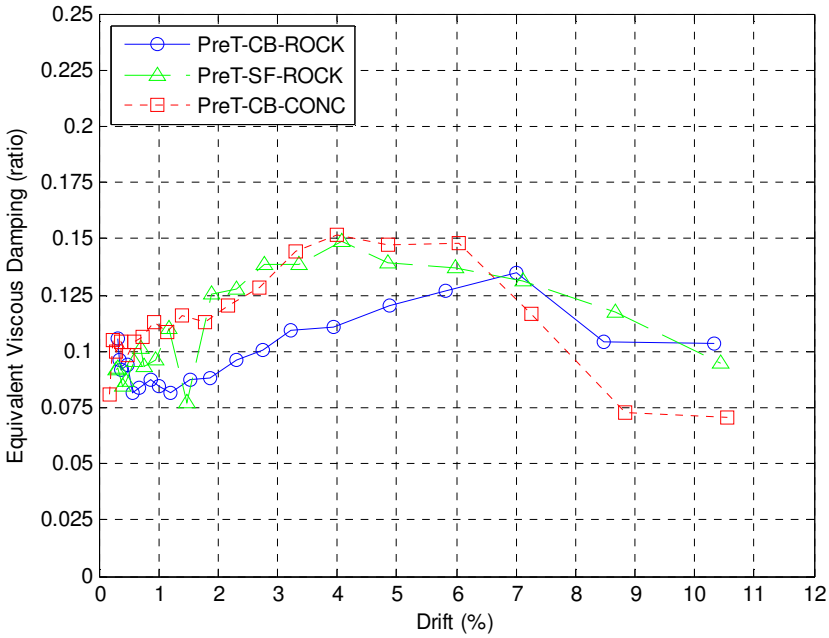

Figure 6.17 Equivalent viscous damping for prestressed specimens.

Figure 6.18 shows the equivalent viscous damping results for a non-prestressed, precast bridge column specimen (PCC-SF-THK2), along with the pre-tensioned specimens. Specimen PCC-SF-THK2 exhibited larger equivalent viscous damping coefficients than the prestressed specimens after a drift ratio of approximately 1.5%. In linear-dynamic analyses for single degree-of-freedom systems, maximum displacements tend to be inversely related to damping ratio. Therefore, it is possible that the unbonded, pre-tensioned, hybrid structures that are examined in this chapter would have relatively larger peak displacements during seismic events. A discussion of this topic can be found in Section 7.6.

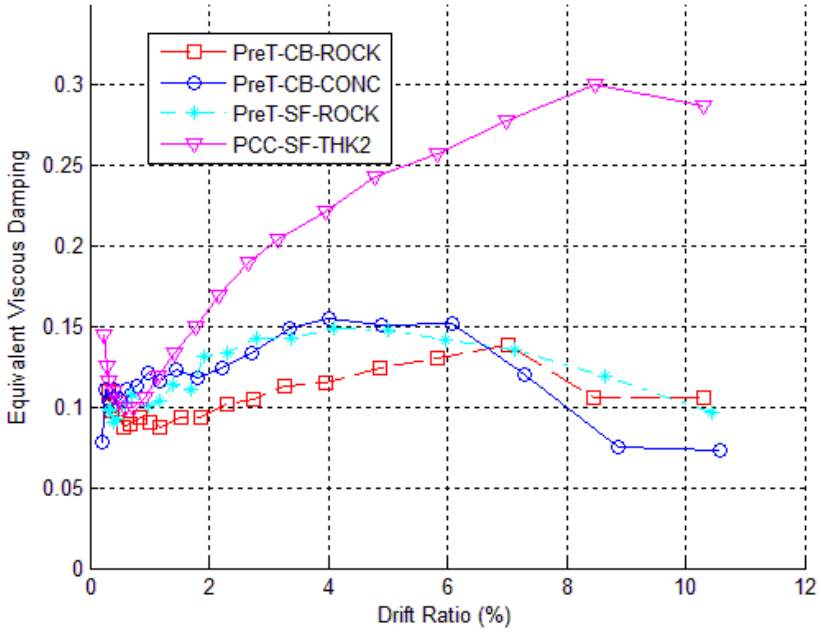

Figure 6.18 Comparison of equivalent viscous damping for prestressed and non-prestressed specimens.

6.5 COLUMN RE-CENTERING

The limiting of residual displacements following a seismic event was a key design goal for the rocking system. From a qualitative assessment of the effective force-displacement response (Figure 5.6), PreT-CB-ROCK re-centered well. That is, when the top of the column was returned to its initial, "zero" displacement, the applied load measured by the MTS actuator was very small.

The re-centering behavior can be quantitatively assessed with a parameter called the normalized crossover displacement (Haraldsson et al., 2011b). The crossover displacements were originally intended to be the displacements at which the resistance drops to zero after unloading from a peak value. They may be different for the positive and negative directions. Haraldsson modified that definition so that the force was $0.1F_y$, rather than zero, because the stiffness near the crossover point was low in their non-prestressed specimens. His modification was intended to reduce the scatter in the analysis results, and is illustrated in Figure 6.19.

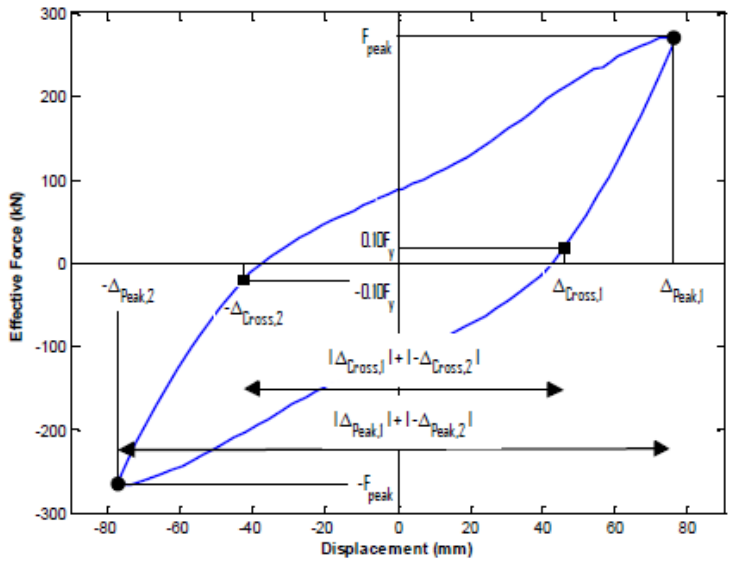

Figure 6.19 Normalized crossover displacement, as used by Haraldsson et al. (2011b).

However, for the analysis presented here, the relatively intuitive, "unmodified" formulation was used to quantify the re-centering. Figure 6.20 graphically identifies the relevant parameters of the normalized crossover displacement used in this analysis.

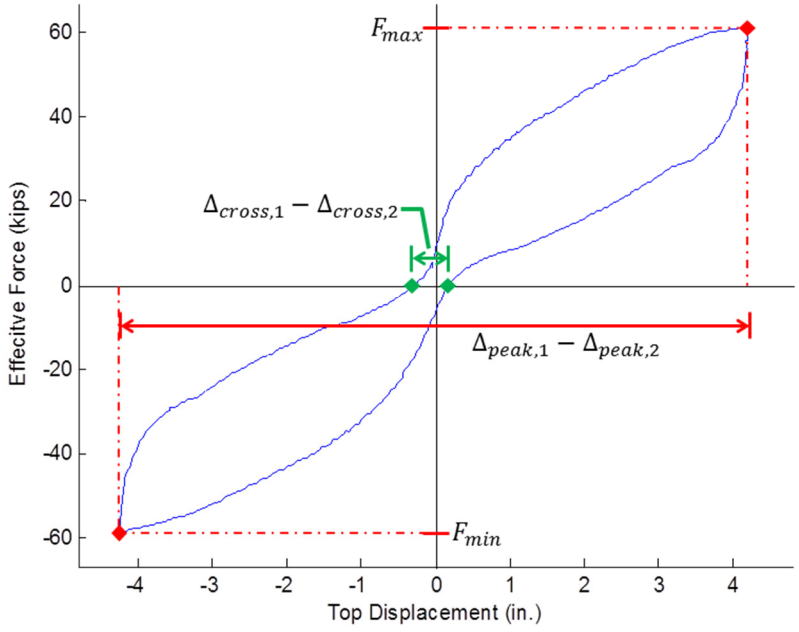

Figure 6.20 Definition of normalized crossover displacement and applied to Set 9-Cycle 2.

For any particular cycle, the crossover displacements were identified as the displacements at which zero effective force was measured after unloading from a maximum or minimum displacement. Then, the difference between the two crossover displacements was divided by the peak-to-valley displacement range for that cycle. The resulting value ranges from 0.0 to 1.0, with

0.0 representing perfect re-centering and 1.0 representing no re-centering at all. The normalized crossover displacement was calculated with Equation 6.2.

$$Normalized\ Crossover\ Displacement = \frac{\Delta_{cross,1} - \Delta_{cross,2}}{\Delta_{peak,1} - \Delta_{peak,2}} \qquad \textbf{Equation 6.2}$$

The normalized crossover displacements for the prestressed specimens analyzed in this section are shown in Figure 6.21, and ranged from nearly zero to 0.15 for drift ratios between 1% and 10%.

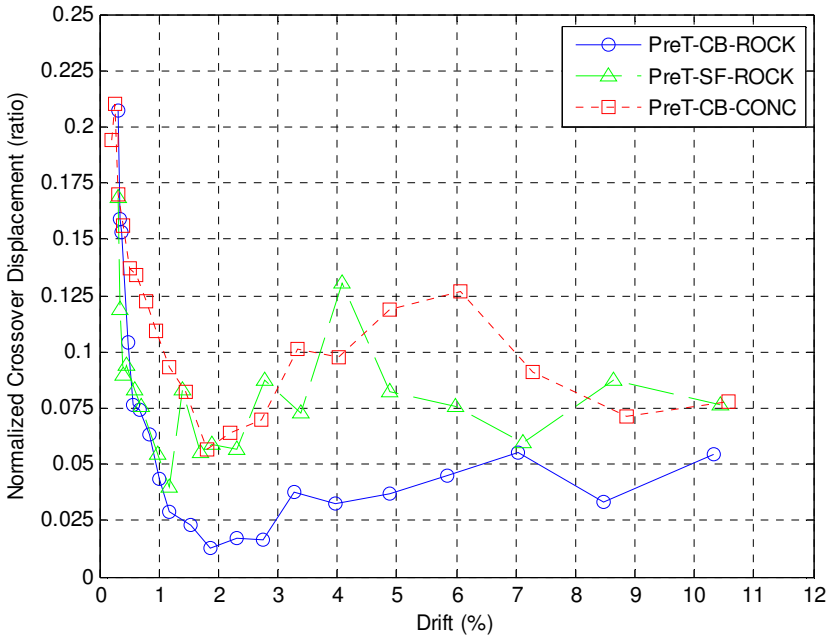

Figure 6.21 Normalized crossover displacements for prestressed specimens.

Normalized crossover displacement values at lower drift levels (less than 1%) are likely to be unreliable because of the frictional resistance within the loading channel at the top of the column. That frictional resistance is likely to be approximately the same for all load cycles, so it represents a larger proportion of the total resistance at low applied loads. Furthermore, the re-centering capabilities of the specimen are less relevant for lower levels of drift, as the peak and residual displacements would be correspondingly small.

Figure 6.22 provides a comparison between the prestressed specimens and two non-prestressed, precast, reinforced concrete specimens. It shows that the normalized crossover displacements for prestressed specimens are always smaller than for the non-prestressed specimens and, for drifts greater than 2%, they are smaller by at least an order of magnitude. This suggests that the pre-tensioned columns re-centered much better than their non-prestressed counterparts.

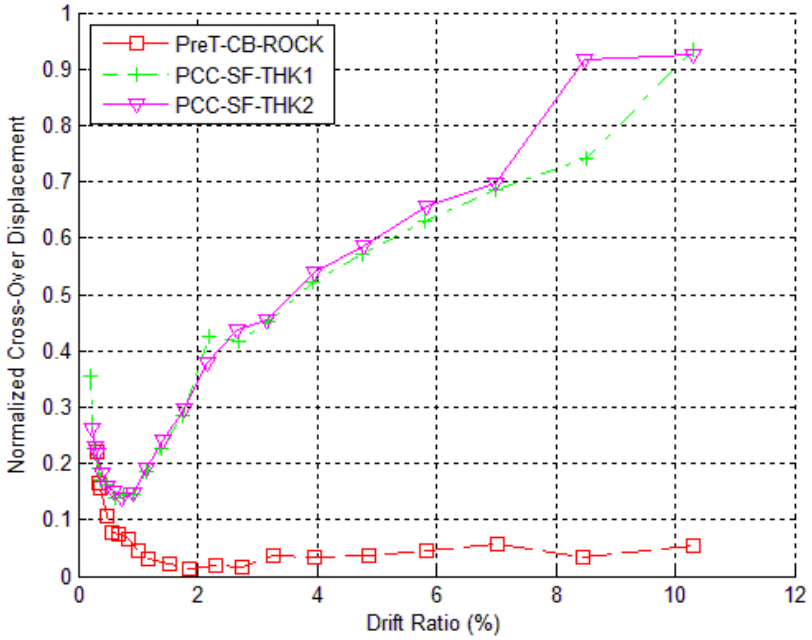

Figure 6.22 Comparison between prestressed and non-prestressed specimens for normalized crossover displacements.

6.6 STRESS ANALYSIS OF STEEL TUBE

The strain-gauge rosette results were used to calculate stresses in the steel tube; the raw readings from these gauges (hoop and longitudinal strains) can be found in Section 5.10. These were stacked, 45°-rectangular rosettes (two-wire strain gauges oriented at 0°, 45°, and 90°), and were put at elevations of 2 in. and 6 in., both on the north face of the column. According to the frame of reference of the experiment, drifts in the north direction of the structures lab were considered negative. Such drifts put the north face of the column into compression.

Plane stress was assumed at the location of the gauge, and Equation 6.3 through Equation 6.12 were used to perform a stress analysis of the tube in the elastic range. They are typical plane stress equations for two-dimensional elasticity (e.g., Riley et al., 2002).

$$\gamma_{xy} = \frac{(\varepsilon_{45} - \varepsilon_0 * cos_{45}^2 - \varepsilon_{90} * sin_{45}^2)}{sin_{45} cos_{45}} \qquad \textbf{Equation 6.3}$$

$$(\epsilon_{p1}, \epsilon_{p2}) = \frac{\varepsilon_0 + \varepsilon_{90}}{2} \pm \sqrt{\left(\frac{\varepsilon_0 + \varepsilon_{90}}{2}\right)^2 + \left(\frac{\gamma_{xy}}{2}\right)^2} \qquad \textbf{Equation 6.4}$$

$$\epsilon_{p3} = \epsilon_z = -\frac{\nu}{1-\nu}(\varepsilon_0 + \varepsilon_{90}) \qquad \textbf{Equation 6.5}$$

$$\gamma_p = \max[(\epsilon_{p1} - \epsilon_{p2}), (\epsilon_{p1} - \epsilon_{p3}), (\epsilon_{p3} - \epsilon_{p2})] \qquad \textbf{Equation 6.6}$$

$$\theta_p = \tan^{-1}\left(\frac{\gamma_{xy}}{\varepsilon_0 - \varepsilon_{90}}\right)$$ **Equation 6.7**

$$\sigma_x = \frac{E_s}{1-\nu^2}(\varepsilon_0 + \nu * \varepsilon_{90})$$ **Equation 6.8**

$$\sigma_y = \frac{E_s}{1-\nu^2}(\varepsilon_{90} + \nu * \varepsilon_0)$$ **Equation 6.9**

$$\sigma_{p1} = \frac{E_s}{1-\nu^2}(\varepsilon_{p1} + \nu * \varepsilon_{p2})$$ **Equation 6.10**

$$\sigma_{p2} = \frac{E_s}{1-\nu^2}(\varepsilon_{p2} + \nu * \varepsilon_{p1})$$ **Equation 6.11**

$$\tau_{max} = \frac{\sigma_{p1} - \sigma_{p2}}{2}$$ **Equation 6.12**

Figure 6.23 and Figure 6.24 provide plots of the calculated first principal and second principal stresses versus drift for both strain-gauge rosettes. The second principal stress is oriented close to the vertical.

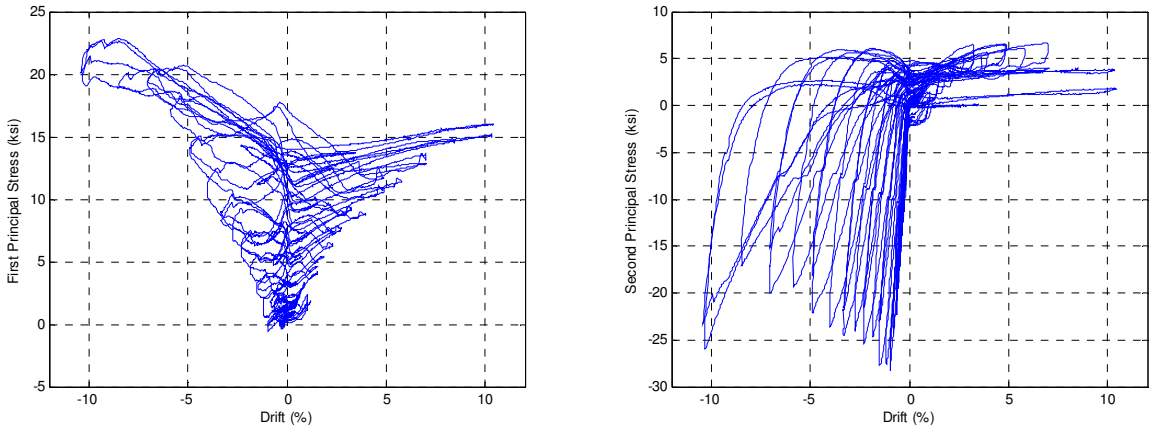

Figure 6.23 First principal (left) and second principal (right) at 2 in. elevation.

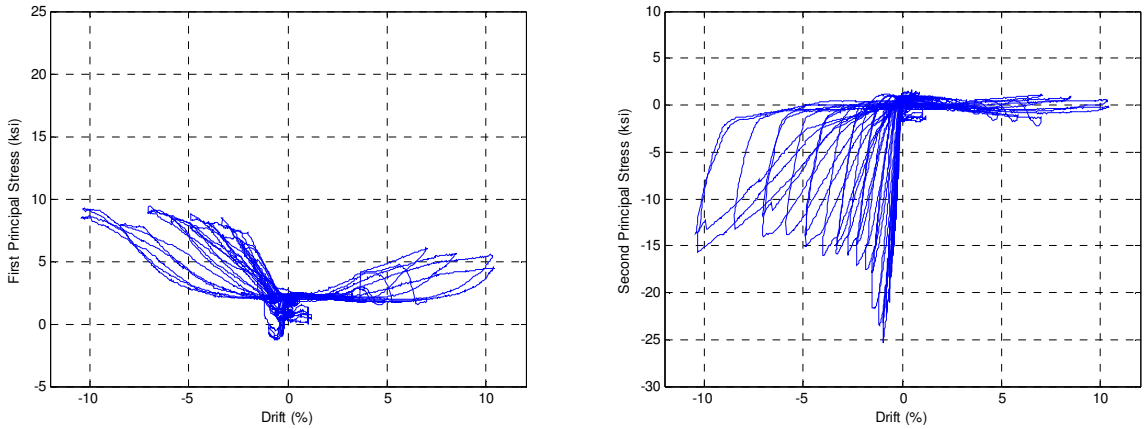

Figure 6.24 First principal (left) and second principal (right) at 6 in. elevation.

Both plots show tendencies that are similar in principle but the amplitudes were different. The second principal stress is approximately the vertical stress, and can be seen to be close to zero when the column lifts off. It is negative (i.e., compressive) for negative drifts when that column face is in compression. That finding is as expected, and is particularly true for the upper gauge. The compressive stress was slightly higher in the gauge at 2 in. from the interface.

The first principal stress is approximately the hoop stress. In both gauges, that stress is tensile regardless of the direction of the drift. The hoop stress is larger when the drift is negative, as might be expected, but is still significant even when the opposite side of the column is in compression. The hoop stress is significantly higher in the gauge at 2 in. from the interface.

6.6.1 Evaluation of Yield Criteria

The stress state was evaluated against the Tresca and von Mises two-dimensional yield criteria. Figure 6.25 gives the maximum shear stresses versus drift.

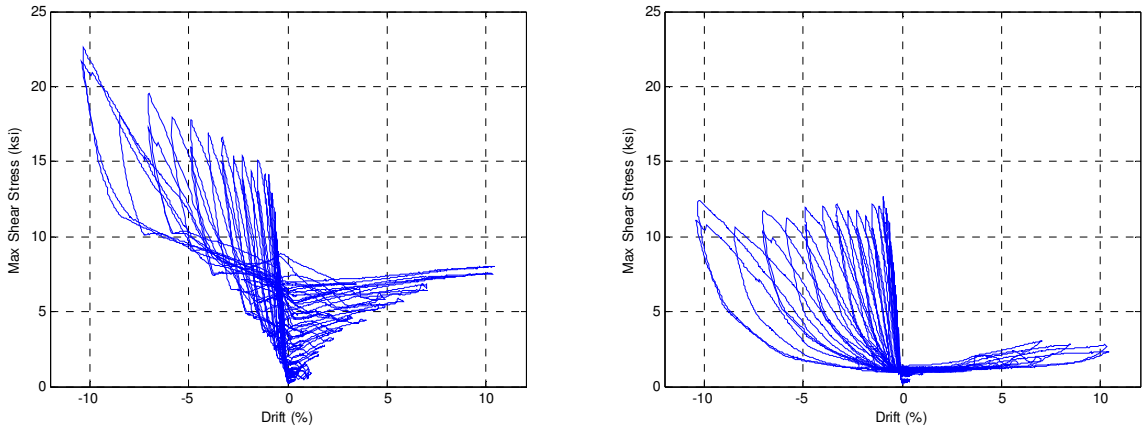

Figure 6.25 Maximum shear stress vs. drift at 2 in. elevation (left) and 6 in. elevation (right).

The shear stress was largest under negative drifts. This is as expected because at that time the vertical stress is compressive and the hoop stress is tensile. The largest shear stress, of 22.5 ksi, was calculated from the lower elevation strain gauge. The specified yield strength of the tube was 49 ksi. The maximum shear stress (Tresca) failure criterion would therefore predict yielding when the shear stress reached $\frac{1}{2}f_{y,tube}$, or 24.5 ksi. Thus the data implied that the steel tube just remained elastic throughout the test, at least at the elevations of the gauges.

Furthermore, Figure 6.26 plots the envelope of the stress state (as ordered pairs of hoop and longitudinal stresses for the first and second cycles of each set) against the tube steel's Tresca and von Mises yield envelopes. Both gauges indicated that for north drifts, the tube was active in hoop tension and longitudinal compression (but larger in magnitude at the 2 in. elevation). For south drifts, the gauge at 2 in. suggested that the tube was at similar hoop stresses as for the north direction, but that longitudinal stresses were tensile and smaller in magnitude. The gauge at 6 in., however, indicated that both stresses were very low for south drifts. Finally the graphical assessment of the yield envelopes also suggested that the tube just remained within the Tresca envelope, but was well within the von Mises criterion for the entire test.

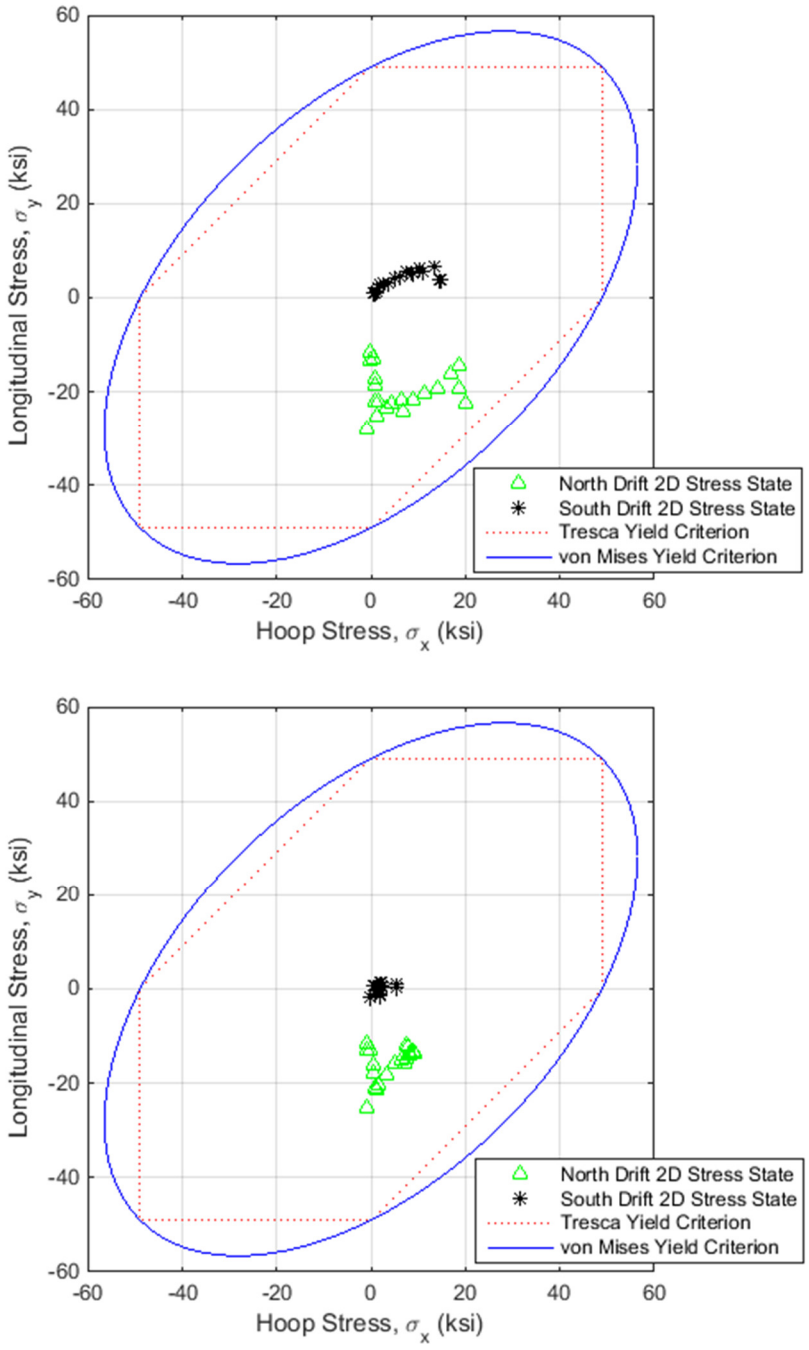

Figure 6.26 Stress state and two-dimensional yield envelopes at 2 in. elevation (top) and 6 in. elevation (bottom).

6.7 STRAND BEHAVIOR

6.7.1 Cyclic Constitutive Model

6.7.1.1 Menegotto-Pinto Backbone

The prestressing constitutive behavior was approximated with a Menegotto-Pinto curve (e.g., Naaman, 2012). The model is defined by Equation 6.13, and is shown in Figure 6.27.

$$f_p(\varepsilon_p) = E_p * \varepsilon_p \left[Q + \frac{1-Q}{\left(1 + \left(\frac{E_p * \varepsilon_p}{K * f_{py}}\right)^N\right)^{1/N}} \right] \qquad \textbf{Equation 6.13}$$

The variables in Equation 6.13 are defined as:

f_p	-	strand stress
ε_p	-	strand strain
E_p	-	strand modulus of elasticity (32000 ksi – taken from materials testing)
f_{py}	-	strand yield stress (242.5 ksi - assumed)
Q	-	model parameter (0.028)
N	-	model parameter (9)
K	-	model parameter (1.09)

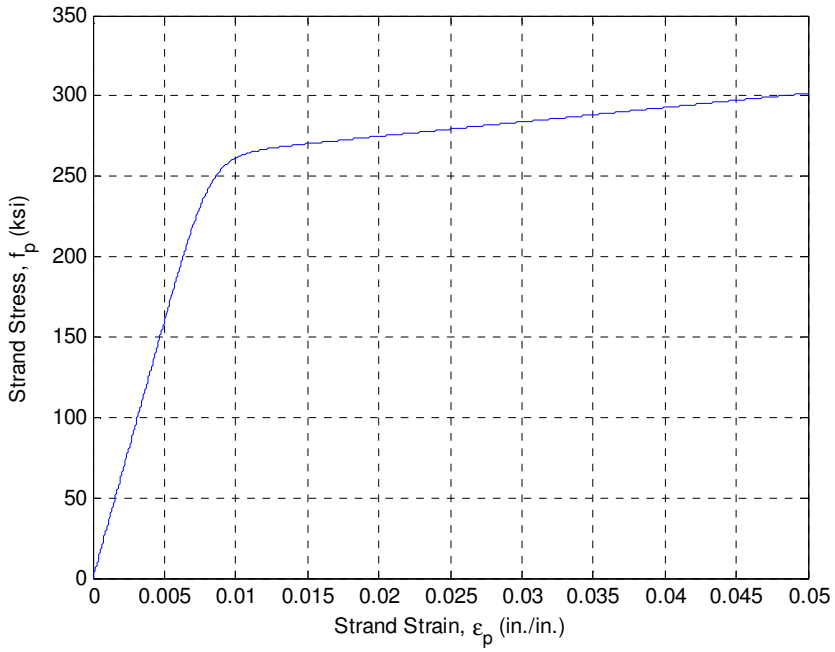

Figure 6.27 Stress vs. strain model for prestressing strand.

The model parameters were selected to fit the materials testing results from the cyclic, chuck-anchored strand test (see Figure A.9 in Appendix A: Materials Testing). In those tests, two-wire strain gauges were applied to individual strand wires in order to measure strain. The gauges were aligned with the strand wires, as opposed to the longitudinal axis of the strand. This was the same instrumentation detail used for the strands of the experimental specimen.

6.7.1.2 Cyclic Yielding in Tension

Cyclic loading for the strands was estimated with the Menegotto-Pinto model of Equation 6.13. The cyclic loading model (for a given strain record) is described in the flowchart of Figure 6.28 and the typical unloading/reloading stress-strain path is shown in Figure 6.29.

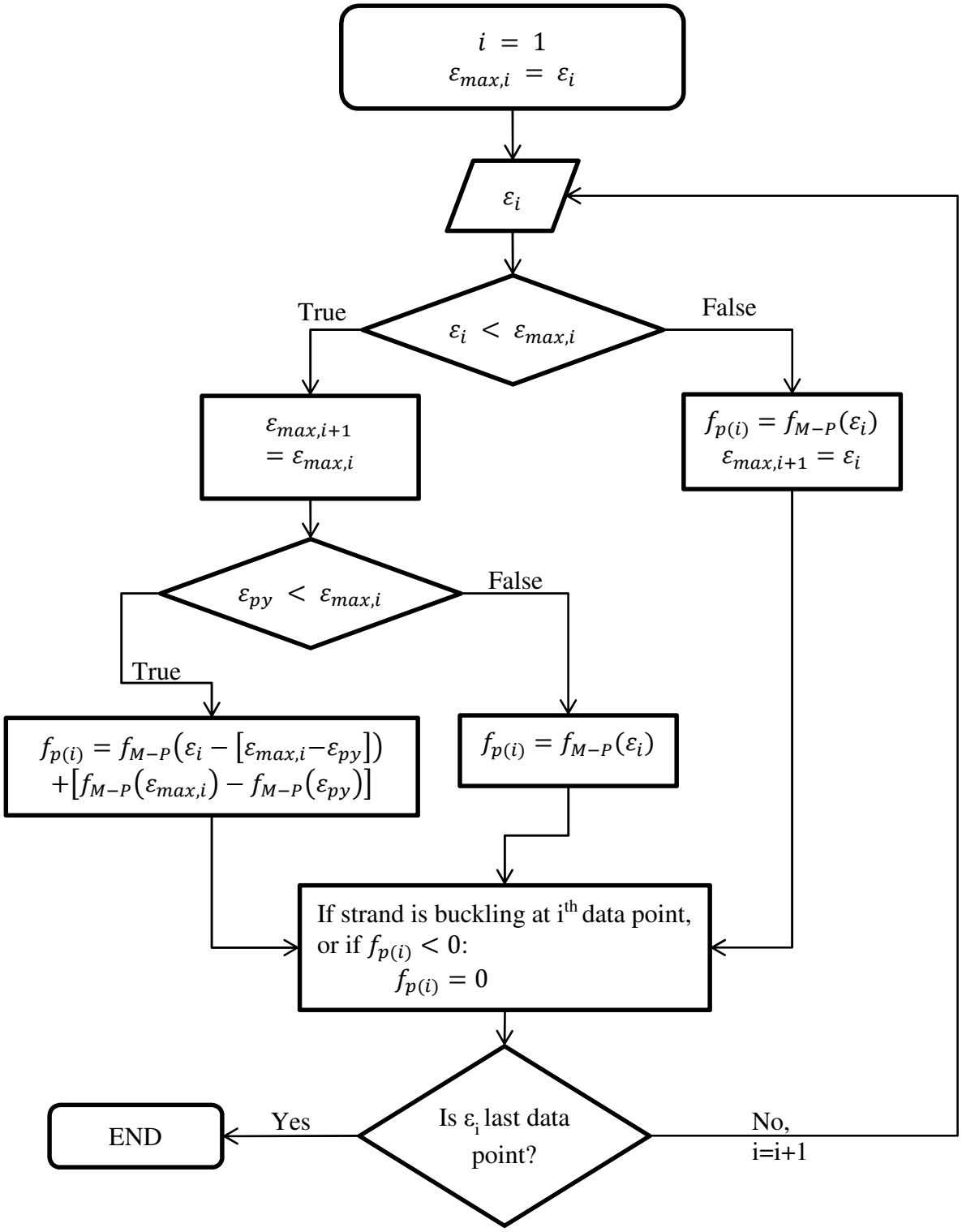

Figure 6.28 Flowchart for strand cyclic loading.

The variables in Figure 6.28 are defined as:

i - index for ith data point

ε_i - strand strain for i^{th} data point

$\varepsilon_{max,i}$ - previous maximum strain, up to i^{th} strain reading

$f_{p(i)}$ - strand stress for i^{th} data point

$f_{M\text{-}P}(x)$ - Menegotto-Pinto function of Equation 6.13, with "x" as input

ε_{py} - strand yield strain (assumed as 0.0087 in./in.)

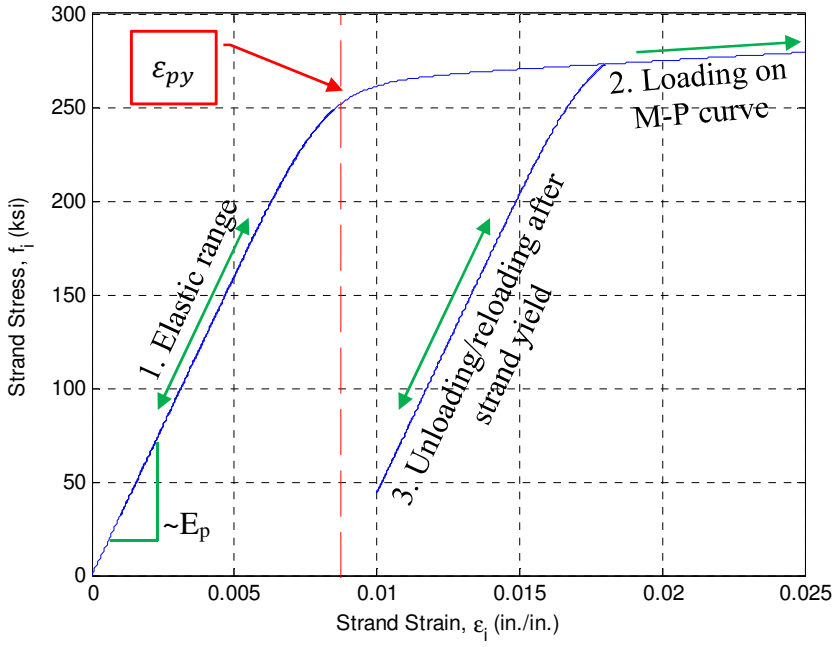

Figure 6.29 Stress vs. strain model for cyclic loading (assumed yield strain shown with dashed, red line).

Essentially, the model has four conditions, which are identified in Figure 6.29:

1. An elastic portion which the function follows so long as the strand has not been yielded ($\varepsilon_{i,max} \leq \varepsilon_{py}$).
2. The backbone of the Menegotto-Pinto function if the strand is being strained past yield ($\varepsilon_{py} < \varepsilon_{i,max} \leq \varepsilon_i$).
3. A post-yield, unloading/reloading path ($\varepsilon_{py} \leq \varepsilon_i < \varepsilon_{i,max}$), which is the elastic portion of the Menegotto-Pinto function with the upper limit shifted from ε_{py} to $\varepsilon_{i,max}$.
4. A correction of setting $f_{p(i)}$ = 0 ksi during times the strand was buckling (qualitatively determined from inspection of the strain gauge history – see Figure 5.40, for example), or if the previous conditions output a compressive stress (condition not shown on Figure 6.29).

For reference, the NE strand's predicted stress-strain history is shown in Figure 6.30. This plot was formed with the NE strand's full strain gauge data history as the input for the cyclic model.

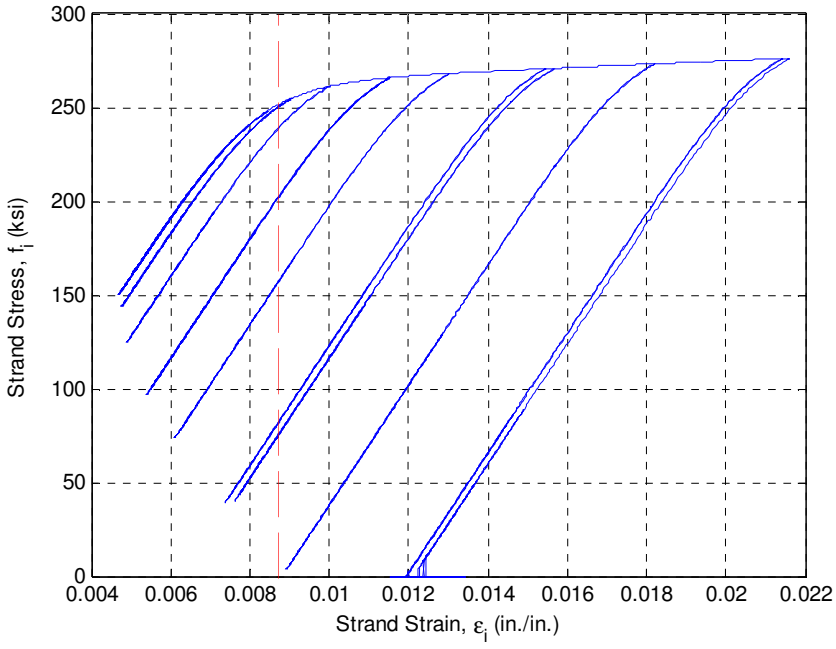

Figure 6.30 Cyclic stress vs. strain plot for NE strand (assumed yield strain shown with dashed, red line).

Figure 6.31 demonstrates the correction for strand buckling or compressive stress (the application of condition 4) for the NE strand (predicted strand stress is plotted against drift ratio). In the plots of Figure 6.31, it can be observed that the cyclic stress-strain model did a fair job at predicting a stress-reversal at the onset of strand buckling.

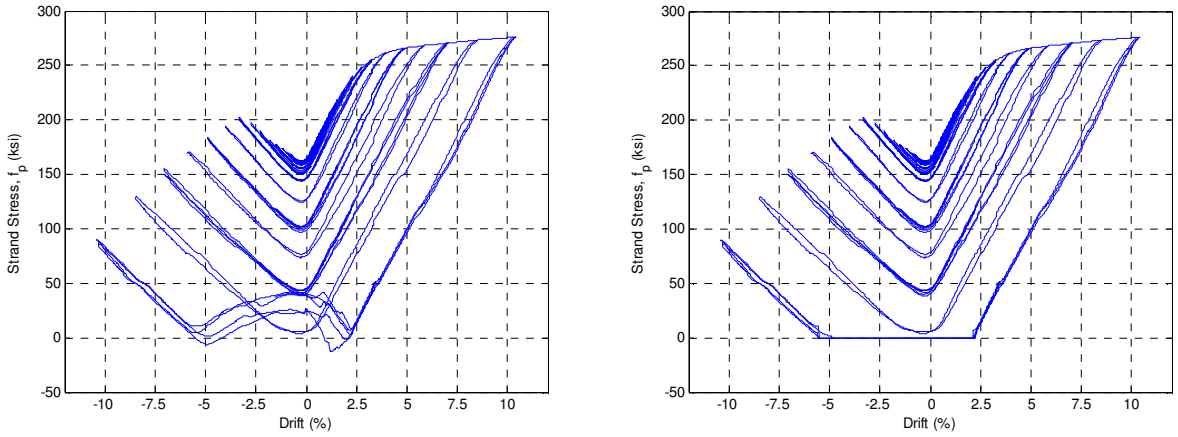

Figure 6.31 Cyclic stress vs. drift without the condition 4 correction (left), and with the condition applied (right) for the NE strand.

6.7.1.3 Model Simplifications

6.7.1.3.1 Strand Slip

The cyclic model described by Figure 6.28 does not include the effects of strand slip, even though slip was indicated by the strand load cell data examined in Section 5.12.2. This simplification was taken because the model was developed to analyze the experimental strain gauge data, not for structural modeling.

It was assumed that, as an individual strand slipped, any deviations in the strain response would be properly recorded by the strand strain gauges. That is, as a strand slipped along its bonded length at the top or bottom of the column, it likely led to a decremental strain in the strand, which would be measured by the strain gauges on the strand. It has been assumed that the strain measurement could then be directly related to strand stress through the model, regardless of the occurrence of slip.

6.7.1.3.2 Strand Buckling

Additionally, the cyclic model described by Figure 6.28 does not include a compressive response. The following discussion provides the rational for the simplification.

During the final cycles, when the column was displaced to the highest drift levels of the test, the strand strain gauge data suggested that the some of the strands began buckling as the specimen was returned to zero drift (see Section 5.12.1.2). The exact buckling behavior was unknown, but was likely to be very complicated. The possible mechanisms may have included: traditional elastic buckling, unfurling and untwisting of the wires, and laterally constrained buckling due to the strand debonding tubes. Some of these modes are schematically depicted in Figure 5.41.

The strands' elastic, Euler buckling load can be calculated with Equation 6.14 (e.g., Riley et al., 2002). Such a calculation provides an indication of the compressive capacity of the unbonded stand, even though it does not address the post-buckling behavior. That is, some form of buckling likely initiated at or before this compressive load, and the result has been considered a lower bound for the initial buckling load.

$$P_{crit} = \frac{n^2 * \pi^2 * E_p * I_{strand}}{(k * l_{strand})^2} \qquad \textbf{Equation 6.14}$$

The variables defined in Equation 6.14 are:

P_{crit}	-	elastic buckling load
n	-	modal factor (1.0 for first mode)
E_p	-	strand modulus of elasticity (29000 ksi - assumed)
I_{strand}	-	strand moment of inertia ($6.404e10^{-4}$ in.^{4})
k	-	effective length factor (0.5 for fixed-fixed element)
l_{strand}	-	strand unbraced length (54 in.)

For a single strand, the calculated, elastic, first mode, Euler buckling load was 251 pounds. This correlates to 2.95 ksi, and an incremental compressive strain of 102με. This lower limit for the critical buckling stress was just 1.22% of the nominal yield stress of 242.5 ksi. Therefore, it was assumed that including a compressive response for the strand would not provide significant insight into the strand behavior, and zero stress was set as the lower bound (compression) capacity.

Furthermore, the strand strain gauges did not record compressive strains. During the periods of suspected buckling, the strain gauge measurements always abruptly "spiked" in the positive (tensile) direction (discussed in Section 5.12.1.2). Therefore, if the cyclic model did include buckling behavior, it could not be applied to this analysis, as it relies on the strain gauge recordings.

6.7.2 Strand Stress during Testing

The strand strain gauge data was analyzed with the cyclic model described in Section 6.7.1. Strand stress versus drift is plotted in Figure 6.32 through Figure 6.34.

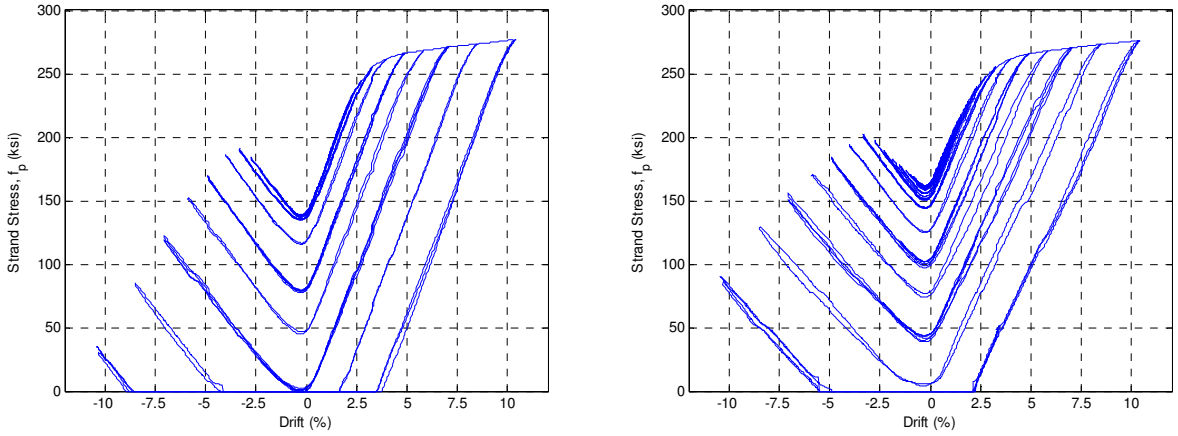

Figure 6.32 Stress vs. drift for NW strand (left) and NE strand (right).

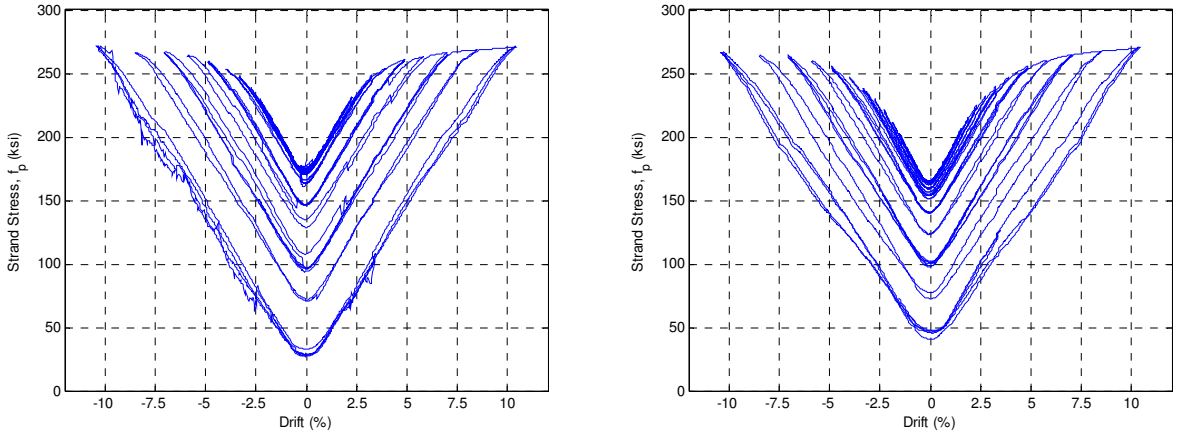

Figure 6.33 Stress vs. drift for W strand (left) and E strand (right).

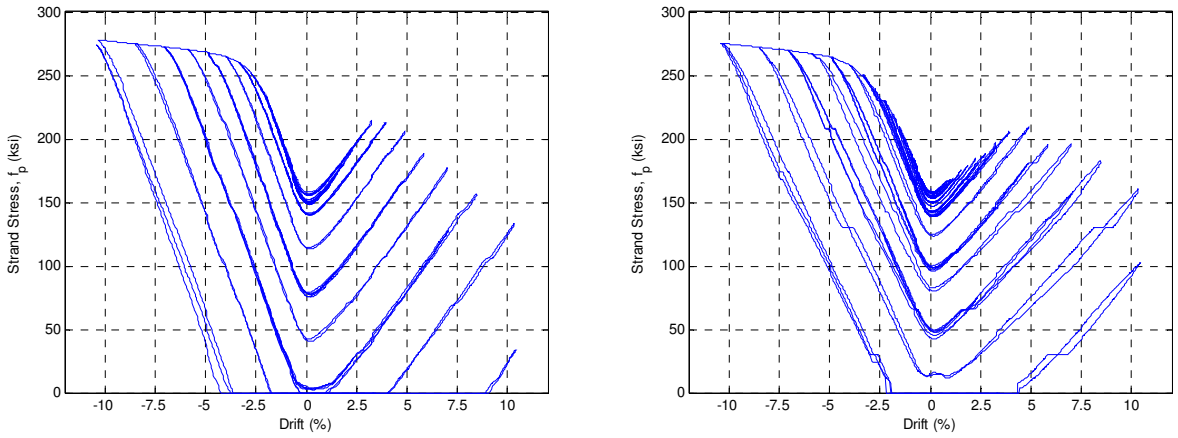

Figure 6.34 Stress vs. drift for SW strand (left) and SE strand (right).

The previous figures suggest:

- the centrally located west and east strands (Figure 6.33) maintained tension and provided a re-centering force for the entire test,
- the northeast and southeast strands (Figure 6.32-right and Figure 6.34-right) buckled during the final ±10.33% drift cycles during the last set of the test, and
- the northwest and southwest strands (Figure 6.32–left and Figure 6.34-left) buckled during the ±8.47% drift cycles in the final set.

Examination of the measured strand load cell data indicated that the northwest and southwest strands had better bond than the northeast and southeast strands (see Section 5.12.2). This difference in bond strength could have affected the onset of strand buckling. That is, for a prematurely slipped strand, elongations would be spread over a longer unbonded length, and significant plastic straining of the strand would be delayed (which may have contributed to the onset of buckling).

6.7.3 Bond Force at Top of Column

6.7.3.1 Calculated Bond Force

The bond force with the concrete at the top of the column was calculated for each strand with Equation 6.15.

$$F_{bond} = F_{strand} - F_{LC} \qquad \textbf{Equation 6.15}$$

The variables in Equation 6.15 are graphically identified in Figure 6.35, and are defined as:

F_{bond}	-	bond force of the concrete at the top of the column
F_{strand}	-	the strand tensile force, calculated by multiplying strand's stress by its nominal area (0.085 in^2)

F_{LC} - the force reading from the load cell at the top of the column, see Section 5.12.2. It is noted that this data followed the compression-negative sign convention, which was corrected for the analysis of this section (the sign of the data was flipped to follow an "upwards-positive" convention).

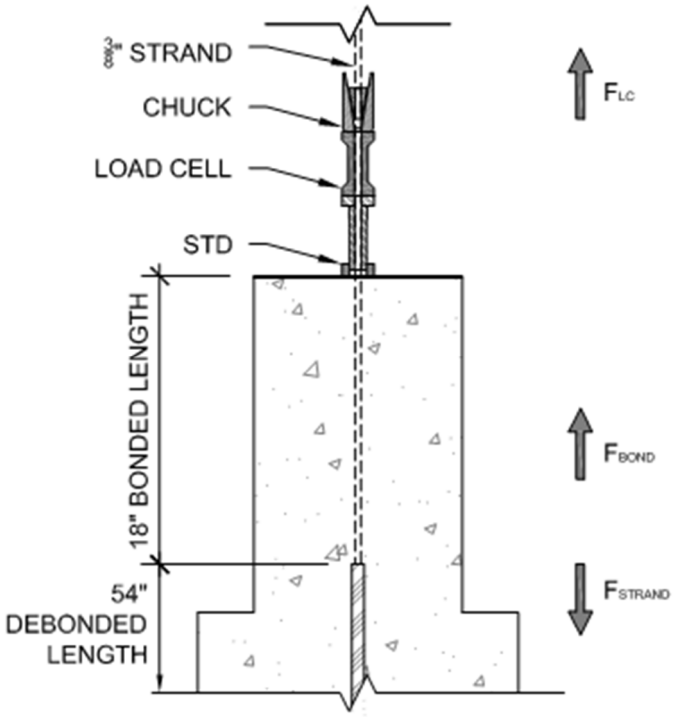

Figure 6.35 Idealized, net force diagram at the top of the column for one strand (from east elevation).

Figure 6.36 through Figure 6.38 show the net bond force (between the top of the PVC debonding sleeve and the load cell) as a function of column drift.

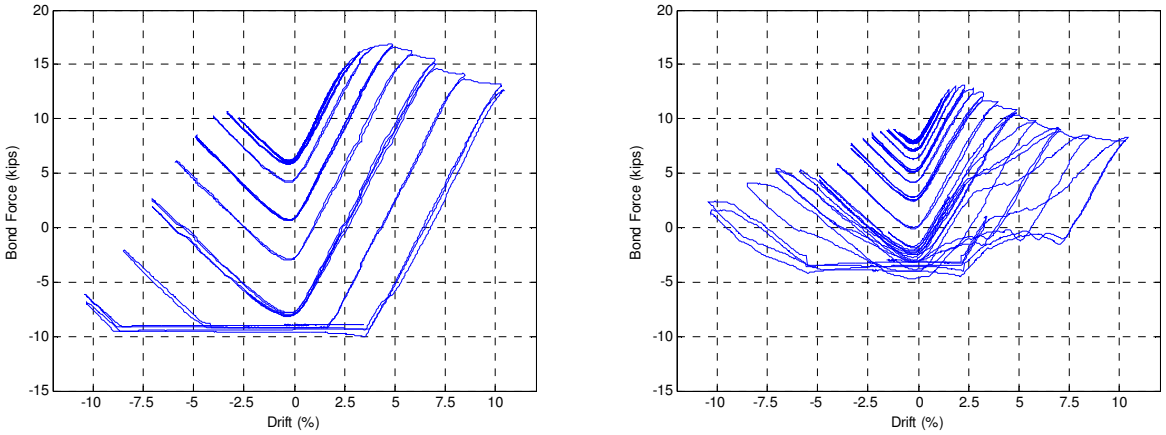

Figure 6.36 Bond force vs. drift for NW strand (left) and NE strand (right).

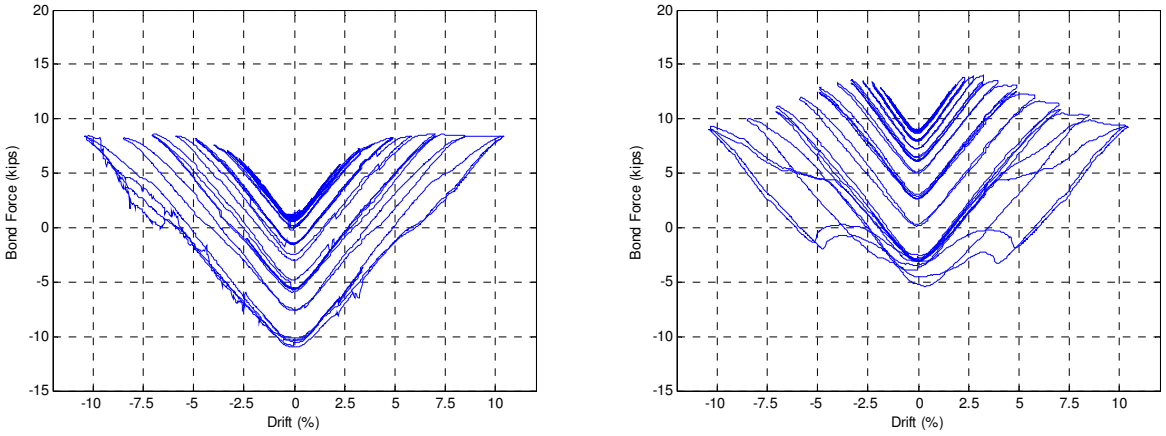

Figure 6.37 Bond force vs. drift for W strand (left) and E strand (right).

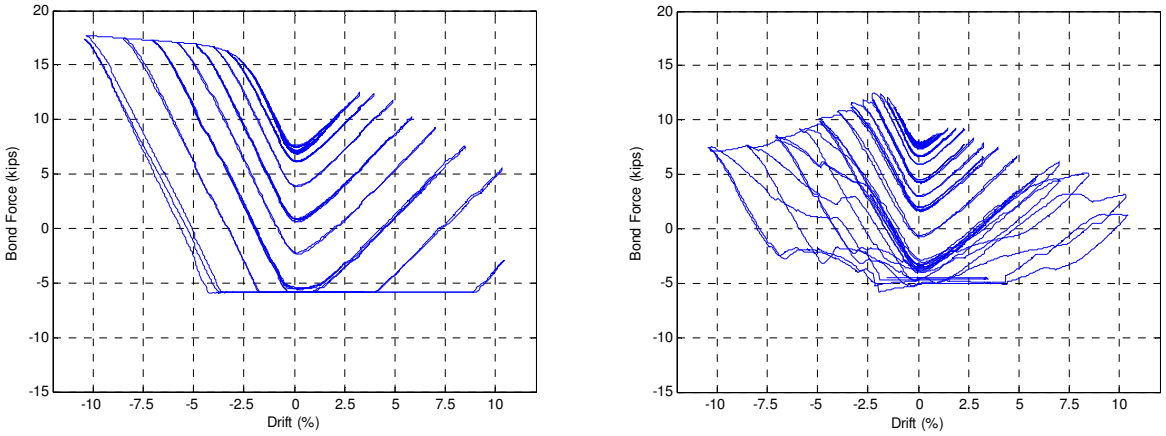

Figure 6.38 Bond force vs. drift for SW strand (left) and SE strand (right).

The previous plots show the progressive slipping of several of the strands (demonstrated by the lower magnitude bond force at successive peak/valley drifts). It is noted the plots do not give the strand force, but the direction and magnitude of the net bond force between the concrete and strand at the top of the column. Therefore, when a negative force is shown on the bond force plots, it suggests that the net concrete bond had reversed direction (from upwards to downwards) in order to resist the external anchorage force at the STD and load cell assembly.

6.7.3.2 Bond Force as a Result of Casting Orientation

Finally, the bond forces can be considered with respect to casting orientation. Table 6.3 provides a summary of the strands' maximum bond forces (which are assumed to be proportional to bond strength). The reader is reminded that the column was cast such that the eastern face of the column was the top, finished surface of the specimen. Therefore, the eastern strands had the most fresh concrete placed underneath them: 12.875 in. under the NE and SE versus 7.125 in. under the NW and SW strands.

Table 6.3 Bond force correlated to strand casting orientation.

Strand	Strand Casting Orientation	Maximum Bond Force (kips)
Northwest	Bottom	16.9
Northeast	Top	13.1
Southwest	Bottom	17.7
Southeast	Top	12.5

Results from the east and west strands were not considered here because of the slipping of the west strand during the prestressing release.

If the average maximum bond force of the bottom-cast, west strands (17.3 kips) is divided by the average maximum bond force of the top-cast, east strands (12.8 kips), the result is 1.35. This suggests that the bond strength of the bottom-cast strands was 35% better than that of the top-cast strands. This result roughly coincides with the top-bar factor given in the development provisions of *ACI 318-11*: $\psi_t = 1.3$. This ACI factor implies that the ratio between the bond strengths of bottom-cast and top-cast bars is 1.3.

Peterman (2007) investigated the effects of casting depth and concrete fluidity on strand bond. He too found that "top-cast" strands have weaker bond and require longer development lengths. In his tests, the ratio between bottom-cast and top-cast bond strengths ranged from 1.2 to 2.2, depending on concrete mix design. However, he concluded that the bond strength was actually more strongly correlated with the amount of concrete placed above top-cast strands (weaker bond resulted when less concrete was placed above a top strand).

Furthermore, Peterman was initially investigating the effect of self-consolidating concrete (SCC) on strand bond. At the time of the study, the engineering community suspected that SCC may result in weaker bond strengths because the material is not vibrated during the casting process. In this regard, Peterman found that weaker bond resulted for more fluid SCC mixtures. While the concrete used to cast PreT-CB-ROCK may not qualify as a true SCC, it did contain significant proportions of water reducing admixture and high-range water reducer, and was more fluid (slump of 8.75 in.) than traditional concrete mix designs. Therefore, this material selection may have had an effect on the strand bond for the specimen. However, the concrete used in this experiment was internally vibrated during placement, in contrast to the SCC's used by Peterman.

6.8 MEASURED COLUMN STIFFNESS

In this section, the stiffness is considered with respect to the following system properties:

- joint decompression of the column-to-cap beam connection, and
- the yield drift of the column.

6.8.1 Joint Decompression

The force-displacement responses of the rocking columns (shown in Figure 6.2) were very similar to the idealized, bilinear stiffness model for an unbonded, pre-tensioned system (see Figure 1.2). Therefore, the decompression of the joint may have had more effect on the stiffness transition than the first yield of rebar.

6.8.1.1 Decompression Moment

The following equations were used in order to determine the joint decompression moment:

$$M_{decomp} = \pm\left(f_{t,joint} - \frac{P_{col}}{A_{plate}}\right)S_{plate} \qquad \textbf{Equation 6.16}$$

$$S_{plate} = \frac{\pi\left(r_{plate}\right)^3}{4} \qquad \textbf{Equation 6.17}$$

Where:

$f_{t,joint}$	-	tensile strength of the connection (assumed to be zero)
M_{decomp}	-	decompression moment for the joint
S_{plate}	-	section modulus of the baseplate (r_{plate} = 10 in., S_{plate} = 785.4 in.^{3})
P_{col}	-	vertical load applied by the Baldwin (-159 kips)
A_{plate}	-	area of the annular baseplate (r_{plate} = 10 in., A_{circ} = 314.2 in.^{2})

The resulting decompression moment was calculated as ±397.5 kip-inches, which corresponds to an effective force of ±6.646 kips (for h_1 = 59.813 in.). It is noted that Equation 6.16 does not include the axial force due to the prestressing, P_{pt}. This was done because the strands were bonded within the reduced diameter extension of the column, before the socket connection had been completed. Therefore, it was assumed that before the joint opened, the prestressing force did not contribute to compressive stress between the baseplate and grout pad. Additionally, the self-weight of the column has been neglected for simplicity.

PreT-SF-ROCK had a nearly identical column design and geometry as PreT-CB-ROCK. However, that specimen had a wet-socket connection into a footing. For that detail, the strands were bonded in a full width, 20 in. diameter, octagonal segment below the baseplate (as opposed to the reduced diameter extension). This full width segment can be seen in Figure 6.39. Therefore, for the footing connection, the axial force of the prestressing strands would contribute to the initial compressive stress between the baseplate and the underlying concrete. When the effective prestressing force was included with P_{col} in Equation 6.16, the resulting decompression moment

was calculated as ±607.9 kip-inches, which corresponds to an effective force of ±10.13 kips for the PreT-SF-ROCK specimen.

Figure 6.39 Bottom, 20 in. wide octagonal section of PreT-SF-ROCK (Schaefer et al., 2014a).

6.8.1.2 Primary, Pre-Decompression Stiffness

The calculated decompression moments and the respective effective force versus displacement data were used to determine initial system stiffnesses for the two rocking columns. A first-order line was fitted to the ordered pairs of force-displacement data points, which are shown in Figure 6.40 and Figure 6.41.

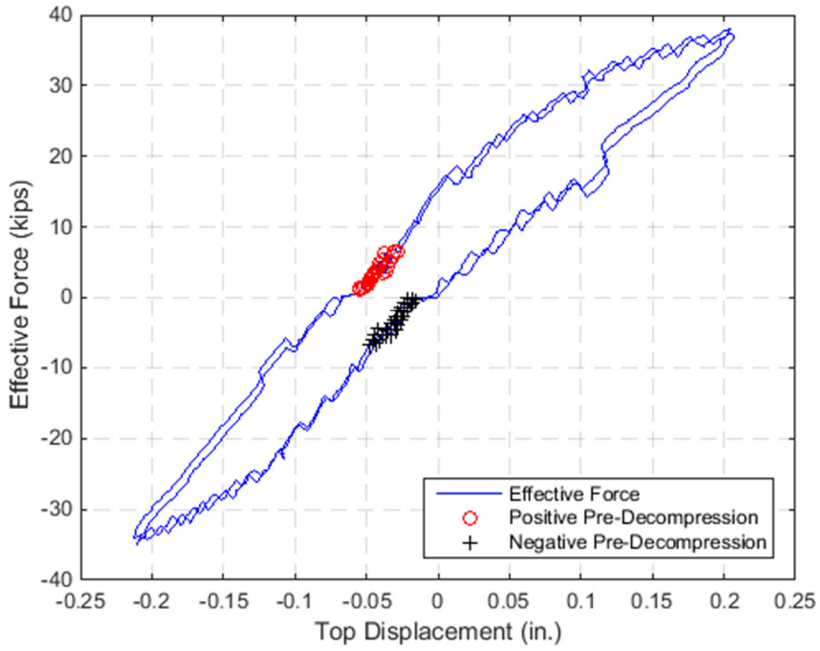

Figure 6.40 The second and third cycles of PreT-CB-ROCK's effective force versus displacement response.

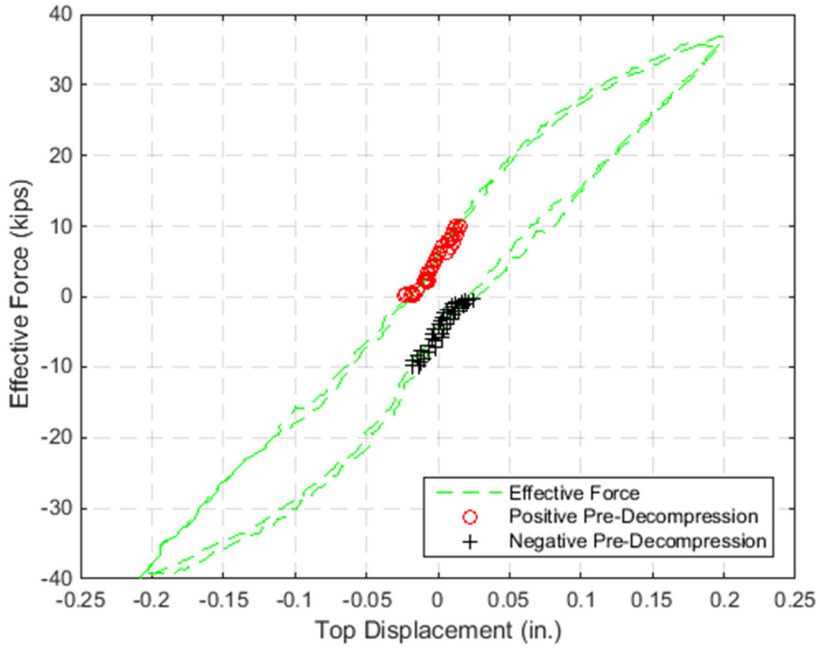

Figure 6.41 The second and third cycles of PreT-SF-ROCK's effective force versus displacement response.

In the preceding figures, the relevant data points from south drifts are circled in red, and the data from north drifts are marked with black plus signs. Only the data between zero effective force and the ±decompression force was used for the line fitting. The second and third cycles of the test were used for this analysis, as the first set had the smallest drifts and were expected to be within the specimens' elastic ranges. The very first test cycle was not used because the response was somewhat erratic as the specimen "settled" into a re-centering trend (for example, PreT-CB-ROCK's response was noticeably shifted in the "negative" displacement direction for the early cycles). However, the figures show that, for both specimens, the calculated decompression moments were exceeded within the first set. Therefore, the response of the first set was certainly non-linear, and may have induced inelastic deformations within the specimens' materials.

For a particular specimen, the slopes of the fitted lines represented the system's average primary stiffnesses, $k_{pre\text{-}decomp}$. The stiffnesses were not necessarily the same for the north and south directions. Table 6.4 gives the results for this initial stiffness analysis.

Table 6.4 Summary of primary stiffness to joint decompression moment, $k_{pre\text{-}decomp}$.

Specimen	North Direction Stiffness (kip/in.)	South Direction Stiffness (kip/in.)	Average Stiffness (kip/in.)
PreT-CB-ROCK	213	206	210
PreT-SF-ROCK	255	289	272

When the north/south stiffnesses are compared against each other for one specimen, there was good consistency. However, the PreT-SF-ROCK specimen had significantly higher measured stiffnesses than the cap beam connection (an average of 1.30 times higher). The following explanations are offered for this difference:

- PreT-SF-ROCK was cast from stiffer concrete, giving that column a calculated uncracked stiffness that was 1.11 times greater than –CB-ROCK (see Section 7.1.1). Essentially, the analysis of this section is an assessment of the columns' uncracked properties, as the columns were likely uncracked prior to joint decompression (the calculated cracking moments were 2.11 and 3.84 times the calculated joint decompression moments for –SF-ROCK and -CB-ROCK, respectively).
- The grout pad between the baseplate and the cap beam may have had an axial flexibility through its thickness, providing a rotational flexibility to the baseplate. This was probably not the case for PreT-SF-ROCK, as it had highly confined concrete directly under its baseplate.
- The joint stiffness may degrade after successive opening and closing. PreT-CB-ROCK's connection was likely opened when the horizontal MTS actuator was attached to the top of the column, and again during the preliminary cycle (see Section 4.3: Initial Damage). This may have prematurely degraded the rotational stiffness of the column-to-cap beam joint. Furthermore, for both experiments, every cycle began with a forced displacement to the south direction, followed by one to the north. The pre-decompression stiffness for PreT-SF-ROCK was 13.6% higher for the initial south direction, which supports the theory of stiffness degradation for the connection.
- The two specimens had different bases, which had different gross dimensions. The footing was far larger, and had length x width x height dimensions of 76 in. x 68 in. x 35.25 inches (Schaefer et al., 2014a); the cap beam, on the other hand, had dimensions of 78 in. 28 in. x 31.5 inches (see Figure B.21). In this thesis and in Schaefer's report, it has been assumed that both bases were absolutely rigid, and that all of the applied displacement at the top of the column was accommodated by bending deformation of the column and the concentrated rotation of the column-base connection. However, the footing and cap beam bases must have deformed to some degree, which would have been most proportionally significant at the lower column drifts prior to joint decompression. At higher drifts, on the other hand, the measured response indicated that nearly all of the deformation came from the rocking of the joint. Because of the footing's much larger size, it would have had a much larger bending stiffness than the cap beam. It is noted that the rotations of the bases were not directly measured with experimental instrumentation.
- During the footing pour of PreT-SF-ROCK, the top of the footing concrete was not placed at the exact same elevation as the bottom of the baseplate, as indicated in Figure 6.42. Schaefer et al., (2014a) described this element as a ½-inch tall "fillet" or cusp which broke off at a relatively low drift level. Because it surrounded the entire circumference of the plate, it could have "locked" the plate into the footing, especially for low deformations. Therefore, this minor placement defect may have provided additional resistance to the initial opening of the footing connection. It is

noted that a similar cusp of grout was formed around the PreT-CB-ROCK baseplate (see Figure 2.25). However, it was far thinner than the one around the footing connection, and it was cracked during the attachment of the horizontal actuator (see Figure 4.3). Therefore, it probably did not affect the measured structural response of the column-to-cap beam specimen.

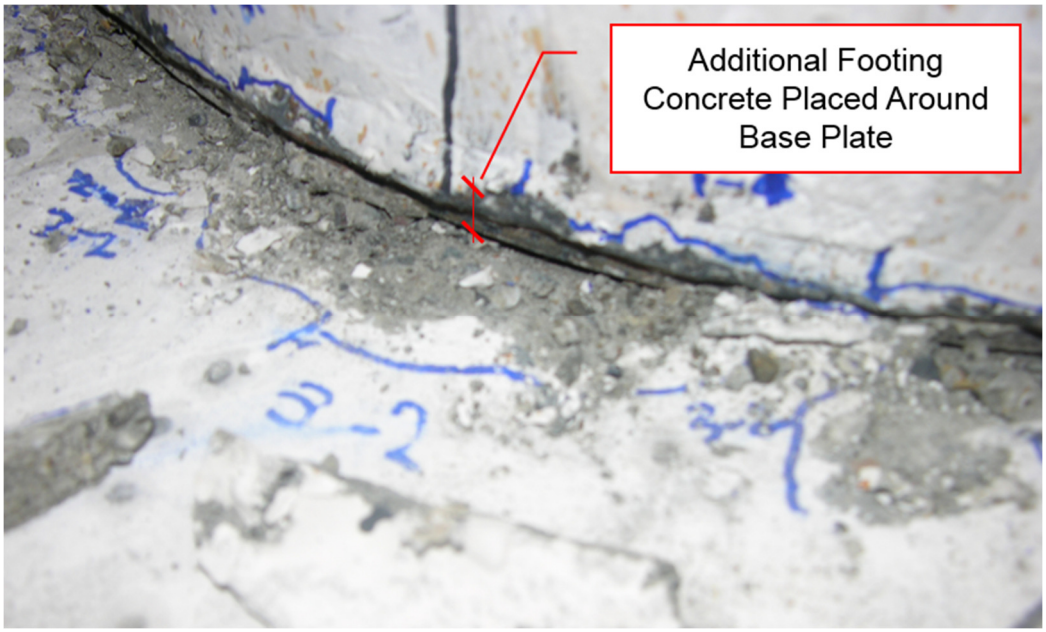

Figure 6.42 Additional footing concrete that had been placed around the baseplate of PreT-SF-ROCK; photo taken after the concrete had broken off (adapted from Schaefer et al., 2014a).

It is worth noting that PreT-SF-ROCK's shorter debonding lengths for the strands (48 in. versus 54 in.) and No. 4 rebars (8 in. versus 12 in.) should not have affected the relative, *pre-decompression* behaviors. Because these reinforcing elements were unbonded across the connection, they did not maintain strain compatibility with the concrete at the joint, and should not have contributed to its rotational stiffness. That is, strain increases in the longitudinal reinforcement would only be affected by the overall geometric deformation of the column due to bending, which was assumed to be negligible at low drifts. However, the shorter debonding lengths would affect the *post-decompression* behavior. After the joint opened, reinforcement elongations due to the rocking would be distributed over shorter lengths for PreT-SF-ROCK, resulting in greater increases to the tensile forces across its joint at smaller rotations.

Furthermore, PreT-SF-ROCK's effective prestressing force contributed to the initial, compressive, contact stress between the baseplate and underlying column concrete (as previously discussed). However, this geometry likely did not affect the pre-decompression stiffness of the joint. Before joint decompression, the applied stresses were likely low and within the linear-elastic material ranges for both specimens. Therefore, the additional prestressing force would have only increased the footing joint's decompression moment; thereby maintaining that connection's initial stiffness properties for slightly larger column drifts.

6.8.1.3 Secondary, Post-Decompression Stiffness

Unbonded structures are also characterized by the secondary system stiffness following joint decompression. These post-decompression stiffnesses were calculated by fitting a first-order line to the secondary response.

The first and second cycles of each set were exclusively considered for this method. For these cycles, the forced column displacement was greater than the previous maximum, and therefore gave a positive stiffness to the envelope. Therefore, these data points were assumed to be representative of the specimens' monotonic push-over responses.

More specifically, the first cycle was selected as the cycle at which the response appeared to fully transition from the primary to secondary stiffness (qualitatively assessed). The final cycle was selected as the last cycle in which all six No. 4 bars were still intact. The secondary stiffness was determined as the slope of a first-order line that was fitted to these specific data points.

The fitted lines, along with the selected ordered pairs and hysteretic force-displacement responses, are shown in Figure 6.43 and Figure 6.44 for the rocking specimens; Table 6.5 summarizes the results.

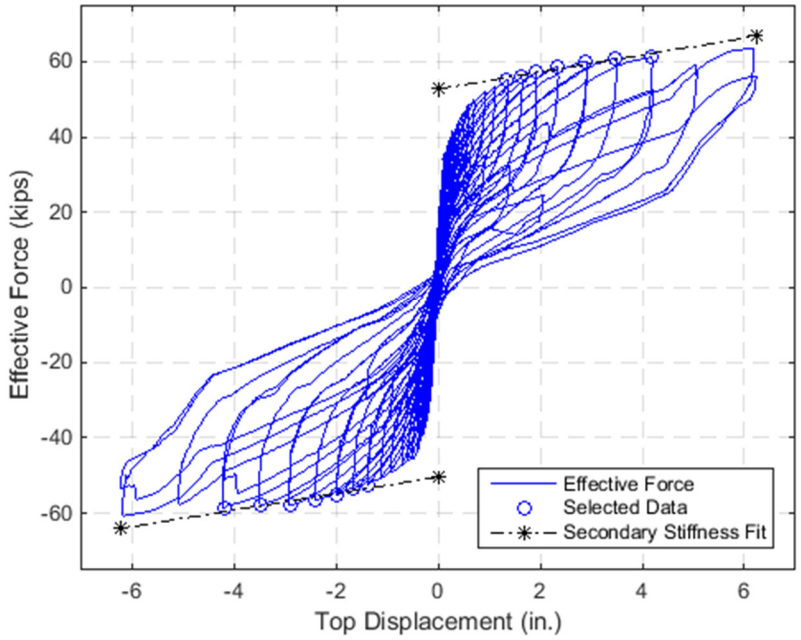

Figure 6.43 Secondary, post-decompression stiffness for PreT-CB-ROCK.

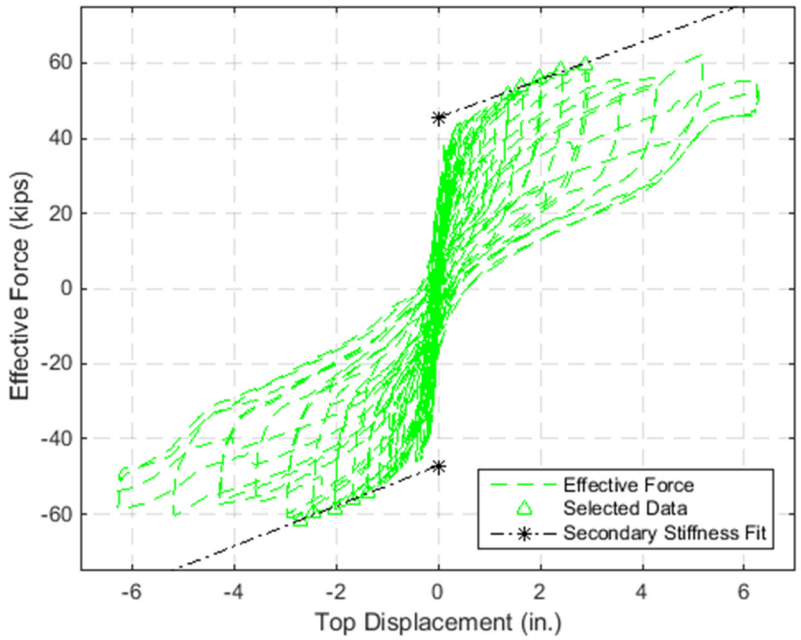

Figure 6.44 Secondary, post-decompression stiffness for PreT-SF-ROCK.

Table 6.5 Summary of secondary stiffness following joint decompression, $k_{post\text{-}decomp}$.

Specimen	First Cycle Used for Fit	Last Cycle Used for Fit	North Direction Stiffness (kip/in.)	South Direction Stiffness (kip/in.)	Average Stiffness (kip/in.)
PreT-CB-ROCK	Set 6 – Cycle 2	Set 9 Cycle 2	2.56	2.53	2.54
PreT-SF-ROCK	Set 6 – Cycle 2	Set 8 – Cycle 2	5.35	5.03	5.19

The results were very similar in both directions, for both specimens. This was expected because both specimens had similar strength responses in both directions, and the applied displacements were large enough that deviations due to physical offsets would have been insignificant in the calculation.

However, the stiffness for the footing connection was again higher than for the cap beam specimen (2.04 times higher on average). In all likelihood, this was most affected by the shorter debonding lengths used for PreT-SF-ROCK than for –CB-ROCK. The footing connection had debonding lengths of 8 and 48 in. for its No. 4 bars and strands, respectively. Conversely, the cap beam connection had the corresponding debonding lengths of 12 and 54 inches. Generally speaking, axial stiffness is inversely proportional to element length, and 12/8= 1.5, 54/48 = 1.125, and 1.5*1.125 = 1.67. Therefore, the general relation between the specimens' post-decompression stiffnesses can be largely explained by the differences in debonding lengths. The two specimens had essentially identical reinforcing areas and material properties.

Otherwise, PreT-SF-ROCK has been generally observed to be stiffer, and the previously proposed reasons for this tendency may have affected the secondary stiffness.

6.8.1.4 Complete Bilinear Model

The average primary and secondary stiffnesses were combined in order to form a bilinear model for the rocking specimens. The bilinear models and force-displacement responses are plotted in Figure 6.45 and Figure 6.46.

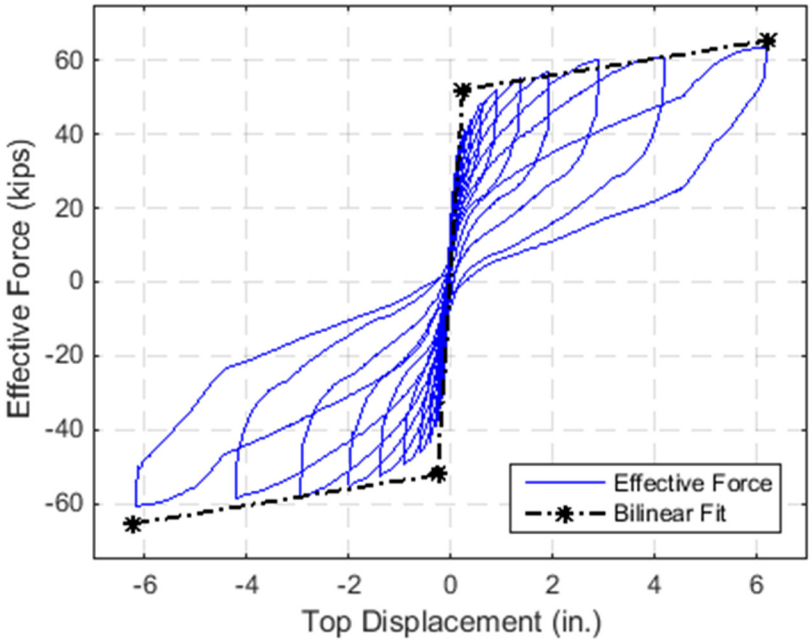

Figure 6.45 The bilinear fit for PreT-CB-ROCK, along with its second cycle hysteresis.

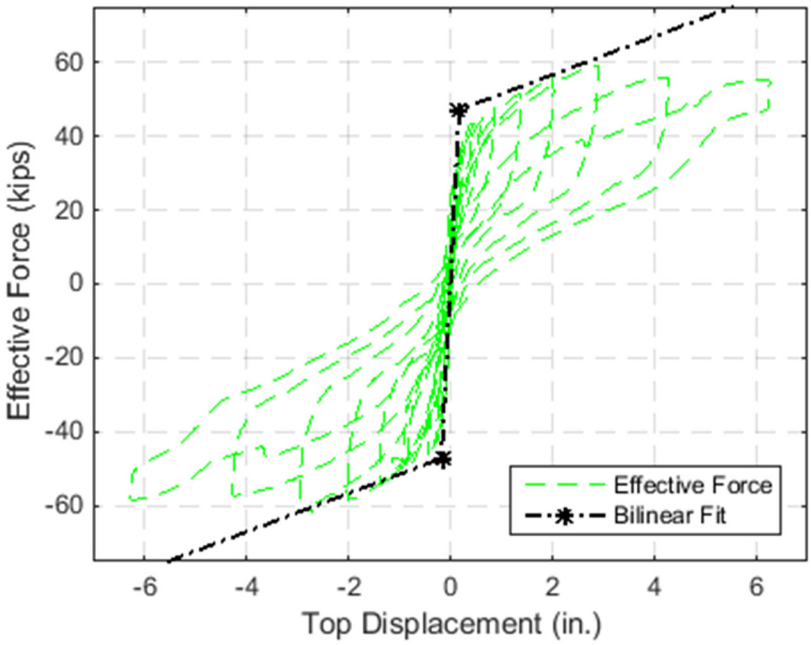

Figure 6.46 The bilinear fit for PreT-SF-ROCK, along with its second cycle hysteresis.

For clarity, only the second cycle of each set was plotted in the preceding figures. Table 6.6 provides the parameters for these models.

Table 6.6 Bilinear model parameters for rocking specimens.

Specimen	Primary Stiffness (kip/in.)	Secondary Stiffness (kip/in.)	Ratio (secondary: primary)	Displacement Intersection (in.)	Force Intersection (kip)
PreT-CB-ROCK	210	2.54	0.0121	±0.248	±52.1
PreT-SF-ROCK	272	5.19	0.0191	±0.173	±47.1

6.8.2 Effective Stiffness to First Yield

Previous researchers have used a column's yield displacement and the corresponding force at that displacement to generate an initial system stiffness (Paulay and Priestley, 1992). Traditionally, the yield point was identified as the deformation which first causes a longitudinal rebar to yield or the concrete to reach a strain of 0.002 (e.g., Elwood and Eberhard, 2009). Unfortunately, this exact formulation was unavailable for the analysis of PreT-CB-ROCK due to the improperly acquired strain gauge data from the rebars.

6.8.2.1 Determination of Yield Moment

In lieu of rebar strain data, an alternative method for determining the yield drift has been proposed here. This method makes use of the linear potentiometers that measured the tube kinematics (see Section 3.2.6). The formulation was similar to the process for designing the debonded length in

Section 2.5. If rigid body motion of the baseplate is assumed, then a yield drift for the connection can be determined with:

- section geometry (where rebars are located),
- the baseplate motion (readings from the linear potentiometers),
- yield strain for the steel rebar (from materials testing), and
- the unbonded length of the rebar (from intentional debonding and assumed bar slip).

The No. 4 longitudinal rebars were intentionally debonded for 12 in., and likely debonded another 0.5 in. ($^1/_2$ d_b at the top and bottom of the bar). Therefore, the column drift causing the first yield elongation of the rebar (along this unbonded length) can be readily determined. The following geometric and constitutive relations were used:

$$\Delta_{y,bar} = \varepsilon_y * l_{No.4} \qquad \textbf{Equation 6.18}$$

$$\varepsilon_y = \frac{f_y}{E_s} \qquad \textbf{Equation 6.19}$$

$$\Delta_{bar} = \Delta_{pot,E/W} + \frac{d - {}^{D}/_{2}}{{}^{D}/_{2} + 1}(\Delta_{pot,N} - \Delta_{pot,E/W}) \qquad \textbf{Equation 6.20}$$

Where:

$\Delta_{y,bar}$ - yield elongation of the north-most rebar (0.0295 in.)
ε_y - yield strain of the steel (0.00236 in./in.)
$l_{No.4}$ - unbonded length of the No. 4 bars, plus ½ in. to account for bond slip (12.5 in.)
f_y - yield stress of the steel, determined from materials testing (73.1 ksi)
E_s - modulus of elasticity of the steel, determined from materials testing (31000 ksi)
$\Delta_{pot,E/W}$ - average of corrected readings from east and west potentiometers
$\Delta_{pot,N}$ - corrected reading from north potentiometer
d - section depth to rebar (1.375 in. for south bar and 18.625 in. for north bar)
D - column diameter (20 in.)

Equation 6.20 was derived from an assumption of similar triangles with respect to the potentiometer measurements and the instruments' physical locations on the specimen. The assumed geometry of the behavior is shown in Figure 6.47.

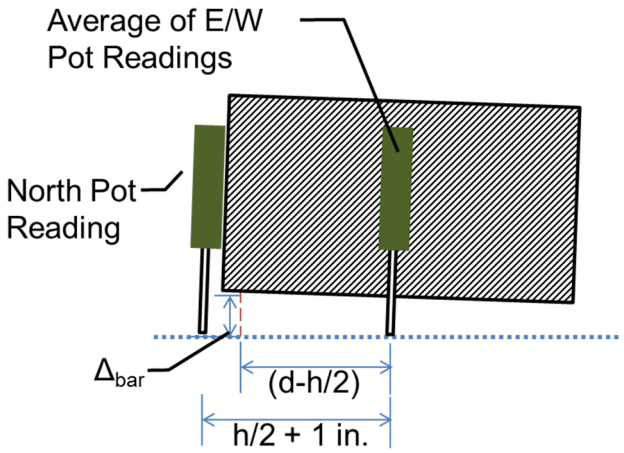

Figure 6.47 Assumed geometry of rocking behavior.

Figure 6.48 shows the calculated elongation of the north-most rebar as a function of drift; Figure 6.49 shows the calculated elongation for the south-most rebar.

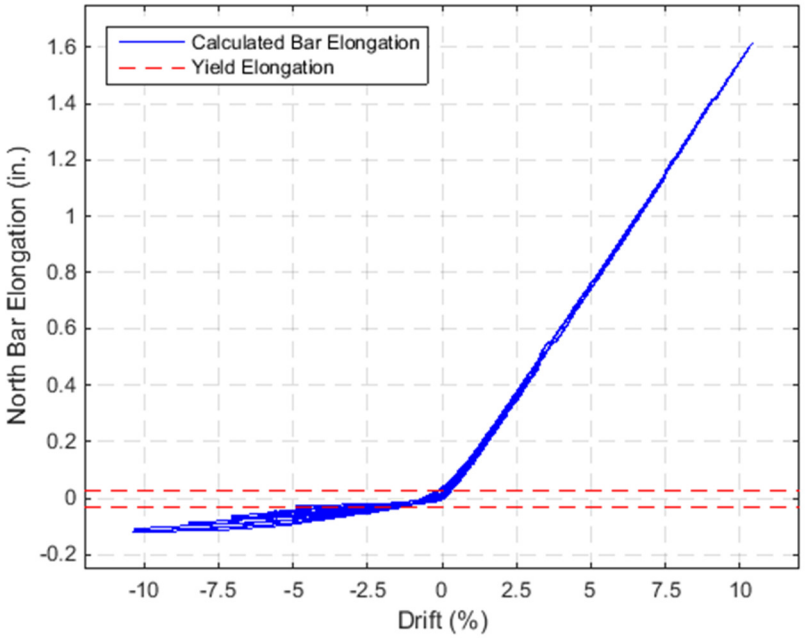

Figure 6.48 Elongation of north No. 4 rebar with yield elongation shown in dashed red (negative elongation indicates shortening).

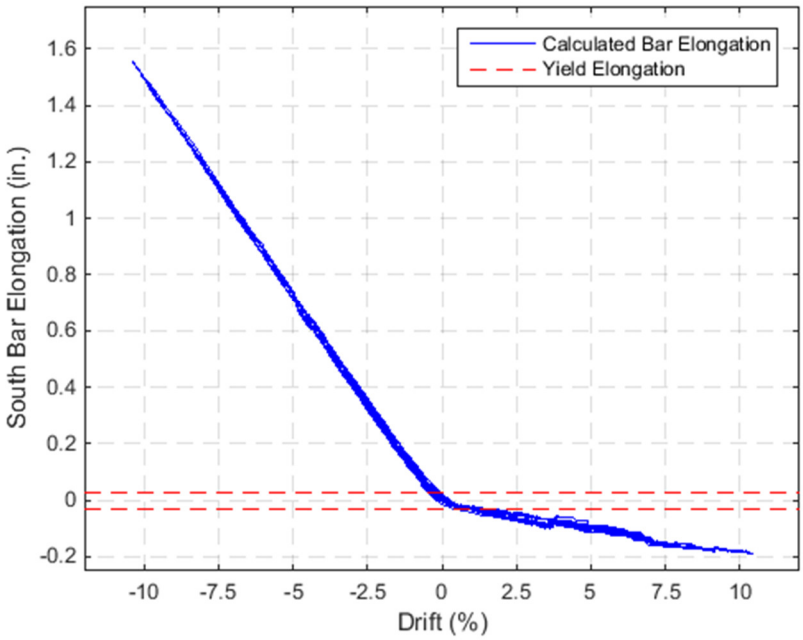

Figure 6.49 Elongation of south No. 4 rebar with yield elongation shown in dashed red (negative elongation indicates shortening).

The previous plots suggest that while compressive deformations were low, the top of the bar was displaced to both compression and tension yielding elongations. It can also be observed that the results were strongly bilinear, which was similarly observed in the tube potentiometer data of Section 5.7.1 and the strand strain gauge data of Section 5.12.1.1. It should be noted, however, that the outer-most bars fractured during the 7.40% drift cycle, so the data is meaningless for the higher drifts.

An examination of strain gauge measurements from PreT-SF-ROCK can provide a qualitative assessment of this formulation's validity. The test of the footing connection was not afflicted by systematic strain gauge misreadings; "direct" strain measurements were therefore available for that test. Figure 6.50 compares the *calculated* strain of the south-most bar of PreT-CB-ROCK (using Equation 6.20 and an assumed unbonded length of 12.5 inches) to the *measured* strain of the south-most bar of PreT-SF-ROCK.

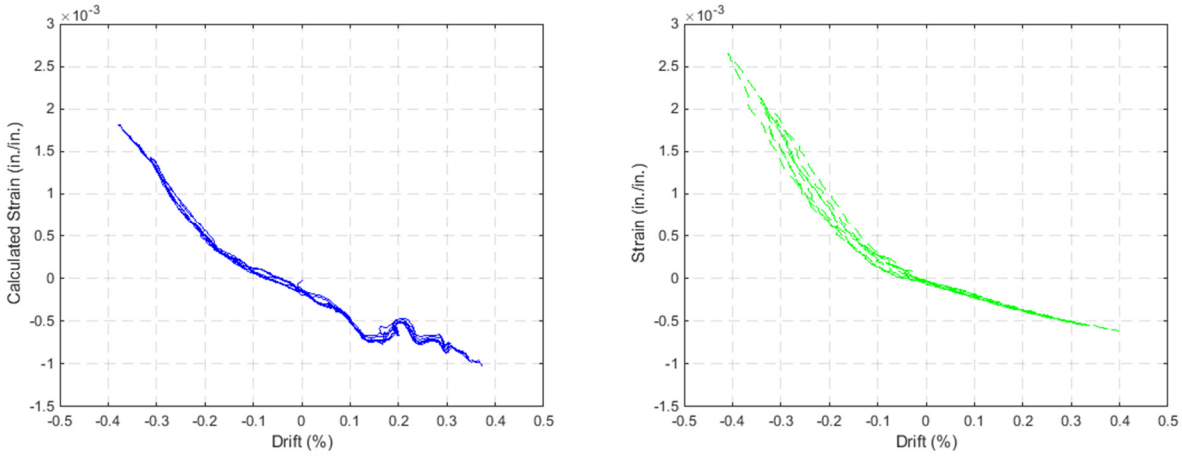

Figure 6.50 Calculated strain of PreT-CB-ROCK's south-most No. 4 bar (left) and measured strain of PreT-SF-ROCK's south-most No. 4 bar (right).

In Figure 6.50, the responses were very similar. It is noted that after the fifth cycle, the gauge from PreT-SF-ROCK began recording significant and sudden tensile yield strains. After that began to happen, the bilinear shape of the strain-to-drift relationship was disrupted. Therefore, it was assumed that the analysis of this section (of determining bar strain from the tube potentiometers), was valid at least up to the first tensile yield of the rebars.

6.8.2.2 Traditional Effective Stiffness to Yield Moment

After the applied drift causing first No. 4 rebar yield was determined, an initial stiffness was calculated with Equation 6.21; results are summarized for the pre-tensioned specimens in Table 6.7.

$$k_{eff,y} = \frac{F_{eff,y}}{\Delta_{y,top}} \qquad \textbf{Equation 6.21}$$

Table 6.7 Results for initial stiffness to first yield of No. 4 rebar.

Parameter	PreT-CB-ROCK		PreT-SF-ROCK		PreT-CB-CONC	
	North Direction (negative drift)	**South Direction (positive drift)**	**North Direction (negative drift)**	**South Direction (positive drift)**	**North Direction (negative drift)**	**South Direction (positive drift)**
Calculated yield elongation, $\Delta_{y,bar}$	0.0295 in.	0.0295 in.	N/A*	N/A*	N/A*	N/A*
Test cycle at first yield	Set 2 – Cycle 2 (sixth test cycle)	Set 1 – Cycle 2 (second test cycle)	Set 2 – Cycle 1 (fourth test cycle)	Set 1 – Cycle 3 (third test cycle)	Set 2 – Cycle 1 (fourth test cycle)	Set 2 – Cycle 2 (fifth test cycle)
Drift at first yield	-0.447%	+0.342%	-0.371%	+0.331%	-0.317%	+0.308%
Measured displacement at first yield, $\Delta_{y,top}$	-0.267 in.	+0.205 in.	-.222 in.	+0.198 in.	-0.190 in.	+0.185 in.
Corrected moment at first yield	-2300 kip-in.	+2240 kip-in.	-2450 kip-in.	+2210 kip-in.	-2020 kip–in.	+2030 kip-in.
Effective force at first yield, $F_{eff,y}$	-38.4 kip	+37.4 kip	-40.8 kip	+36.9 kip	-33.6 kip	+33.8 kip
Initial stiffness, $k_{eff,y}$, according to Equation 6.21	144 kip/in.	183 kip/in.	184 kip/in.	186 kip/in.	177 kip/in.	183 kip/in.

*Direct strain gauge data was available for rebars, and therefore, the bar elongation calculation of Equation 6.20 was not required.

It is noted that the "North Direction" results used the calculated elongation or measured strain of the south-most bar, and vice versa for the "South Direction" results.

The north/south forces causing first yield were consistent with one another, for both specimens. However, the measured displacements at first yield were different by 30.2% for PreT-CB-ROCK. The results could be significantly influenced by the "offset" characteristic of the early drift cycles. For example, the early force-displacement response (shown in Figure 6.40, for example) seems to be offset by approximately -0.04 in. (or graphically speaking, the response is "shifted" to the left on the plot). On the other hand, the early test cycles of PreT-SF-ROCK (Figure

6.41) were fairly symmetric about both axes, so Equation 6.21 provided consistent results between directions for that specimen.

However, the stiffness calculation of Equation 6.21 implies that the specimen's force-displacement curve starts at the origin – which would be true for a monotonic pushover test or for a perfectly re-centering column, but not for the cyclic testing of these experiments. This may not be as significant for tests of traditionally reinforced concrete specimens. For conventionally reinforced concrete columns (with bonded bars), the displacement at first yield may be relatively larger, and any small, initial displacement offsets would not greatly affect the stiffness calculation. For the rocking, pre-tensioned design, however, first yield occurs at a somewhat low column displacement, and an offset of ±0.01 in. can greatly affect calculation results.

Furthermore, for rocking columns, non-linearity is initiated by joint decompression, not rebar yielding or concrete cracking. This is another reason that Equation 6.21 may not be the best quantifier of such a system's behavior.

6.8.2.3 Modified Effective Stiffness to Yield Moment

Because of the sensitivity of Equation 6.21 to the early yielding of the pre-tensioned columns, a modification has been used to determine the secant stiffness to the first yield drift. The modification is given by Equation 6.22, and simply uses the preceding cross-over displacement as the "origin" for the stiffness calculation.

$$k_{eff,mod,y} = \frac{F_{eff,y} - 0\ kips}{\Delta_{y,top} - \Delta_{y,cross}} \qquad \textbf{Equation 6.22}$$

Figure 6.51 graphically shows the modified initial stiffness results for PreT-CB-ROCK's first yielding cycles; Figure 6.52 is for PreT-SF-ROCK and Figure 6.53 is for PreT-CB-CONC. Numerical results are given in Table 6.8.

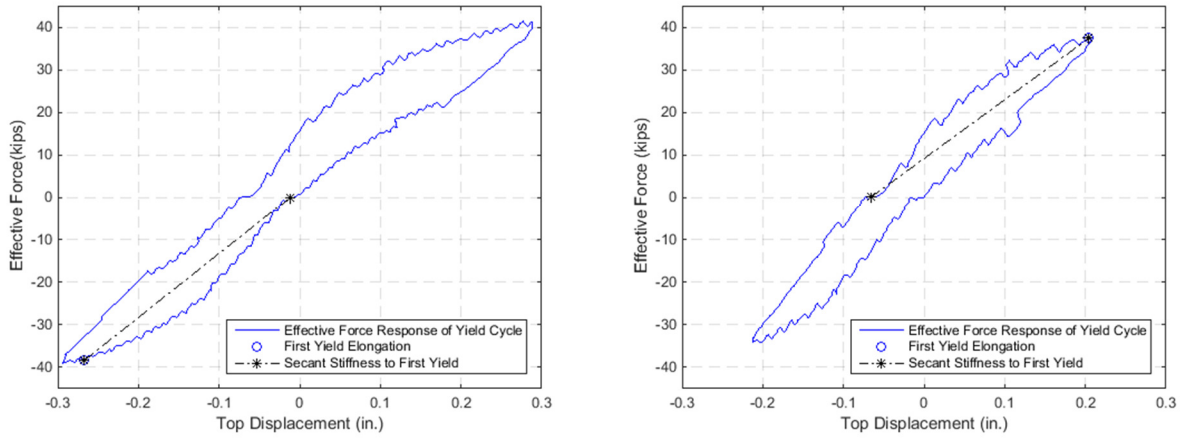

Figure 6.51 The first yielding cycle in the north direction (left) and in the south direction (right) for PreT-CB-ROCK.

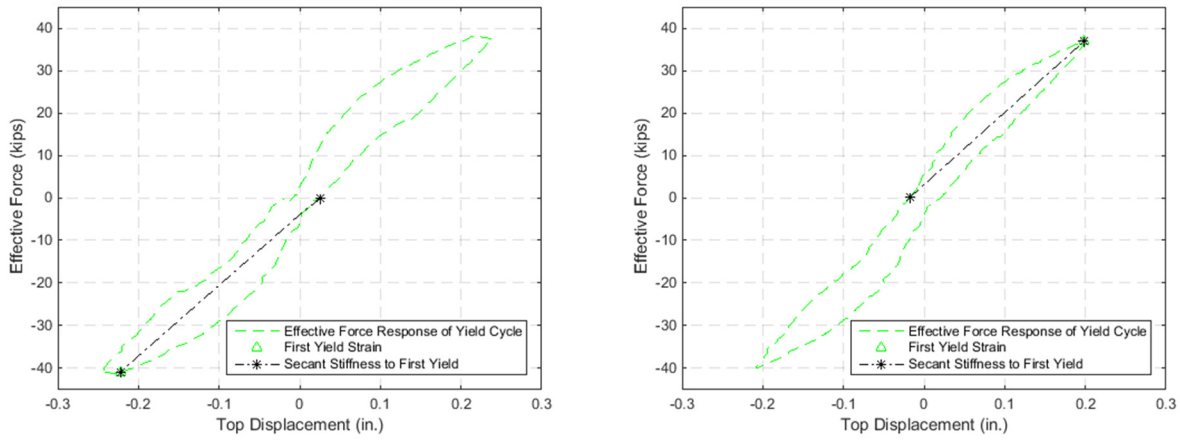

Figure 6.52 The first yielding cycle in the north direction (left) and in the south direction (right) for PreT-SF-ROCK.

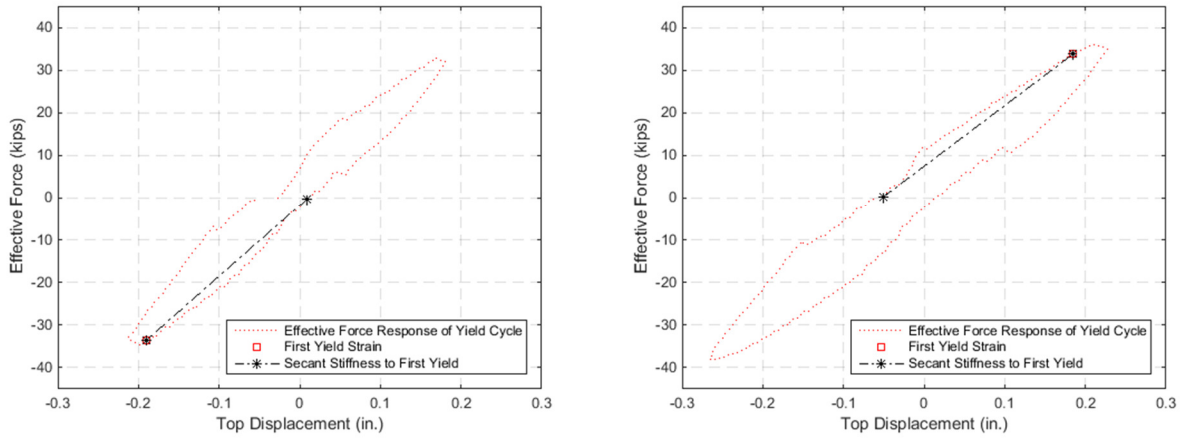

Figure 6.53 The first yielding cycle in the north direction (left) and in the south direction (right) for PreT-CB-CONC.

Table 6.8 Results of modified effective stiffness to yield moment, $k_{eff,mod,y}$.

Specimen	Stiffness in North Direction (kip/in.)	Stiffness in South Direction (kip/in.)	Average (kip/in.)
PreT-CB-ROCK	150	138	144
PreT-SF-ROCK	165	170	168
PreT-CB-CONC	167	142	155

Several conclusions can be drawn from the results:

- The pre-yield, force-displacement response of the "non-rocking" PreT-CB-CONC (shown in Figure 6.53), was mostly linear and followed the secant response (shown with a dashed black line in the figures).

- However, the responses of the rocking systems were already non-linear before first rebar yield, which was likely due to the transition from the primary, pre-decompression stiffness to the secondary, post-decompression stiffness.
- The modified secant stiffness calculation given by Equation 6.22 always gave more flexible results. However, it also gave more consistent results on whole.
- The rocking connection with the footing was, on average, 1.16 times stiffer than the cap beam connection. This was probably due to the shorter debonded lengths (for the rebars and strands) for the column-to-footing specimen. Additionally, the concrete used for PreT-SF-ROCK was stiffer than that for the cap beam specimen, giving a larger, uncracked, elastic stiffness (see Section 7.1.1 for the predicted, uncracked system properties). Finally, the footing likely had a higher bending stiffness than the cap beam, which would have had a more significant contribution to the overall system stiffness for low column drifts.
- Despite differences in detailing, the pre-tensioned systems exhibited similar yield moments, yield drifts, and effective stiffnesses. This was graphically observed in the various figures of Section 6: the three specimens had nearly-identical responses for the earlier, lower drift cycles.
- The lower stiffness in the south direction could have been influenced by the varying grout pad thickness (see Section 2.9.3.3). If the axial stiffness of the pad was inversely proportional to its thickness, then the thicker pad on the south side of the connection would be more flexible through its thickness than the north, which would affect the overall rotational stiffness of the baseplate.

6.9 DETERMINATION OF NEUTRAL AXIS LOCATION

The neutral axis of the rocking connection, defined as the cross-sectional location of zero net displacement of the baseplate, was calculated with the measurements of the tube potentiometers. It is noted that this is not the traditional definition of a neutral axis, which is the cross-sectional depth at zero longitudinal bending strain. The instruments are discussed in Section 3.2.6, and the data, including drift profiles, can be found in Section 5.7.

Figure 6.54 schematically illustrates the assumed rocking geometry, which forms the basis of this analysis. Equation 6.23 gives the equation for the neutral axis calculation, c. The reader is reminded that the potentiometer on the south face of the steel tube gave erratic results, and was assumed to have malfunctioned. Therefore, Equation 6.23 only uses the measurements of the north, east, and west potentiometers.

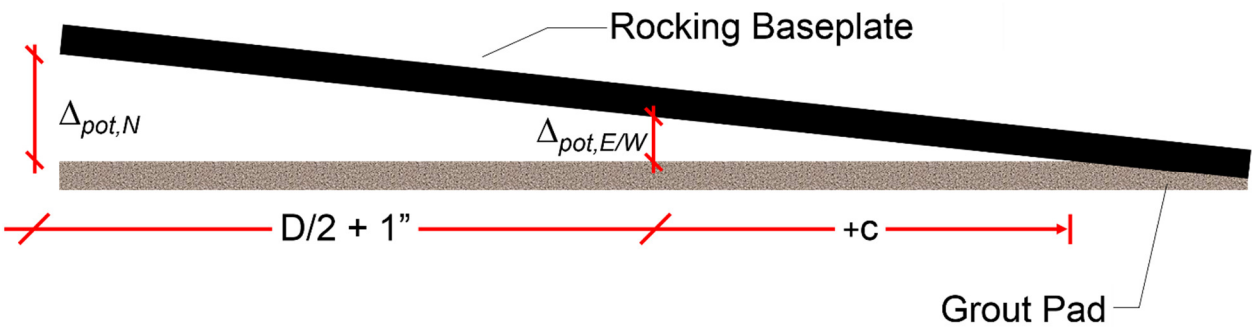

Figure 6.54 Identification of relevant variables for assumed rocking geometry (rounding of the pad has not been depicted in the figure).

$$c = \frac{D/_2 + 1"}{\frac{\Delta_{pot,N}}{\Delta_{pot,E/W}} - 1}$$ **Equation 6.23**

Where:

c - location of the neutral axis of the rocking connection, measured from the section's mid-height, with the south direction being positive

$\Delta_{pot,E/W}$ - average of corrected readings from east and west potentiometers

$\Delta_{pot,N}$ - corrected reading from north potentiometer

D - column diameter (20 in.)

The results of Equation 6.23 have been plotted against drift for the entire test in Figure 6.55. For reference and clarity, the results for Set 10-Cycle 2 (the first ±10.65% drift cycle) were isolated in Figure 6.56.

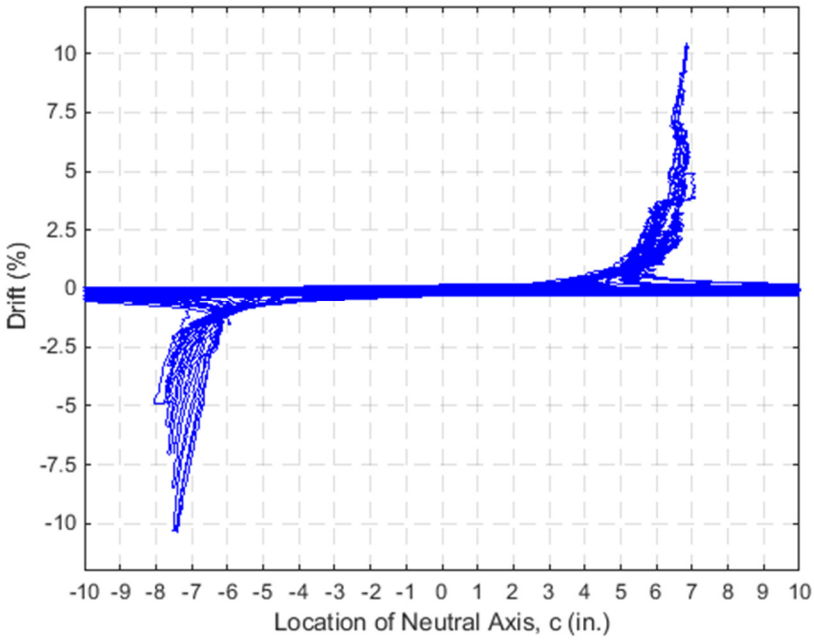

Figure 6.55 Location of rocking neutral axis, measured from the center of the steel baseplate (i.e., +10 in. is the south face and -10 in. is the north face).

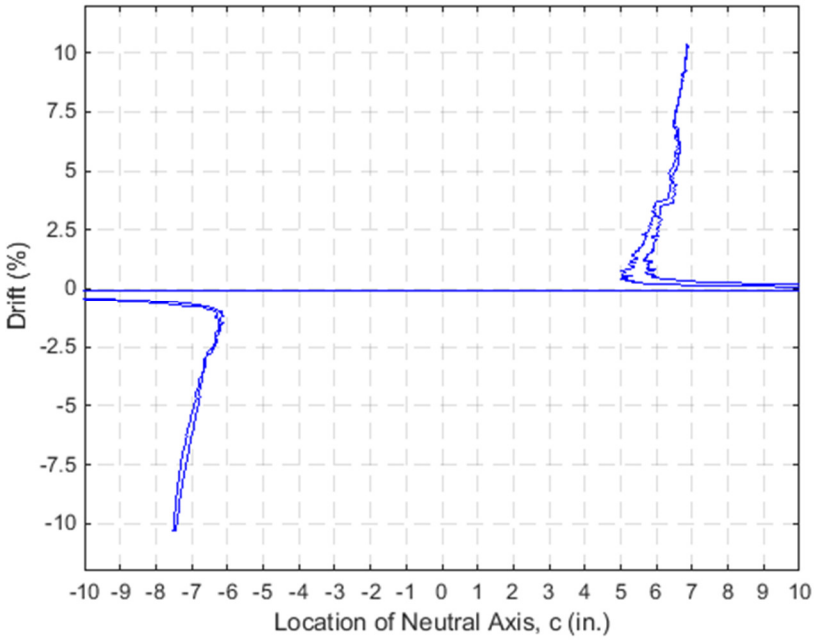

Figure 6.56 Location of rocking neutral axis for Set 10-Cycle 2.

Figure 6.57 gives the envelope for the neutral axis location; it was formed by plotting the calculation result at the peak and valley drifts for the first and second cycles of each set. For reference, Figure 6.58 shows the north/south envelopes on the same plot quadrant; the figure was formed by changing the sign of the ordered pairs from the unmodified, north direction envelope.

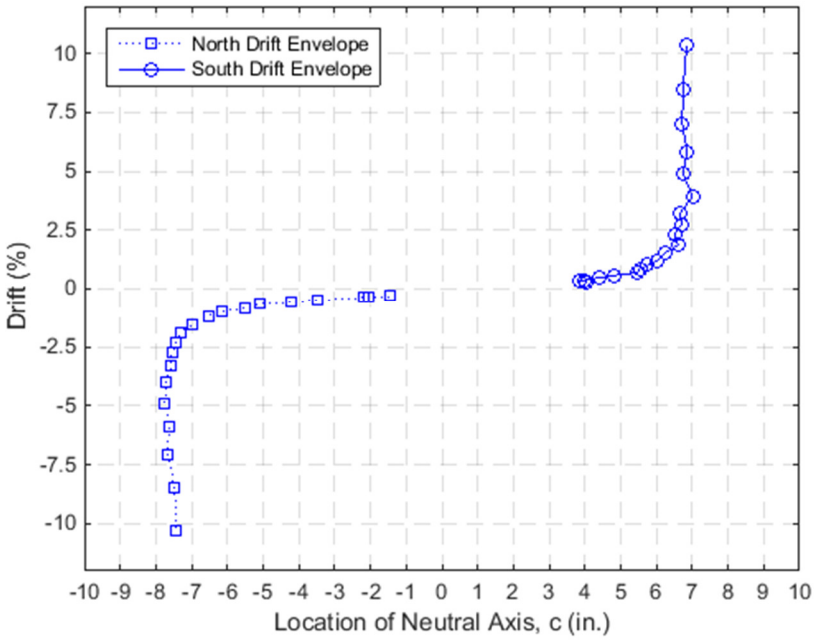

Figure 6.57 Envelope of neutral axis locations – peak and valley drifts of the second cycle of each set of have been plotted.

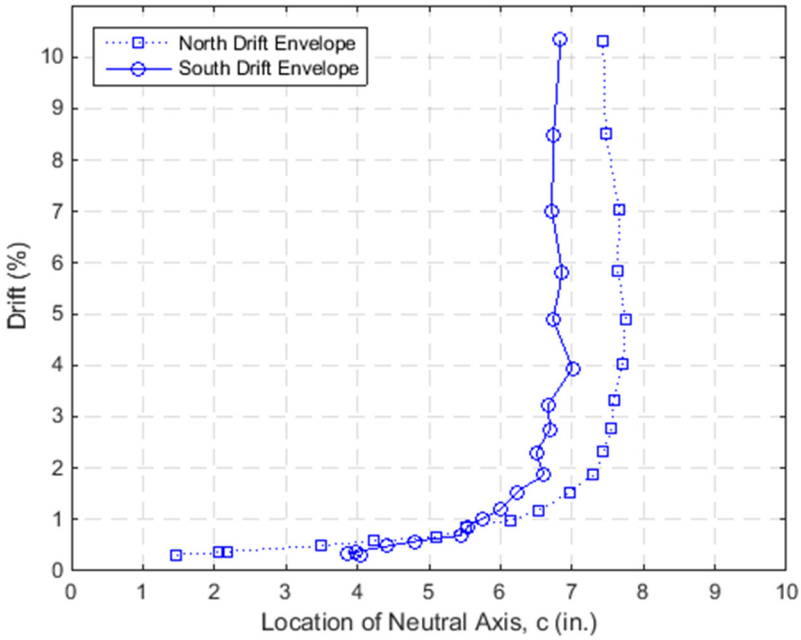

Figure 6.58 Envelopes of rocking neutral axis.

Several interesting trends can be observed in the previous plots:

- The calculated neutral axis approaches positive infinity when transitioning from zero to positive drifts, and negative infinity for the

transition from zero to negative drift. This trend corresponds to no rocking neutral axis at the transition between positive and negative drift (i.e., pure compression and no baseplate rotation).

- The envelopes show that, during the transition from 0% to 1% drift, the neutral axis location abruptly shifted from the near-center to a constant value of about 7 inches.
- The neutral axis location was not the same for both directions. It settled on +6.75 in. for positive drifts, and -7.5 in. for negative drifts (which correspond to depths of 3.25 in. and 2.5 in. when measured inward from the exterior faces of the column). The smaller bearing area for negative drifts could have been a result of the progressive yielding of the reinforcement. That is, for any particular cycle, the northern reinforcement would have been "maximally" yielded during the initial displacement in the south (positive) direction, and then that reinforcement would generate a reduced tensile force during the following displacement to the north (negative) direction. Alternatively, the difference in bearing depth could be due to variances with the grout pad placement. The pad was thicker on the south side, which may have resulted in a reduced axial stiffness through its thickness there. Or, the placed grout pad may have simply been stronger on the north side, and therefore required less bearing area for the same compressive force.
- Other than the tending toward ±infinity at zero drift, the response appears to be doubly-asymptotic in nature.
- For the north (negative) direction, the backbone of the neutral axis depth seems to drop for drifts greater than 5%. This could have been the result of the increased tensile force across the cross-section for larger drift cycles, which would require a larger bearing area for a constant compressive strength.

It is worth considering the somewhat erratic results for positive drifts. This was likely due to the use of the north and east/west potentiometers for the neutral axis calculation, regardless of its location. That is, when the neutral axis was on the north side of the connection, it was between the available instruments and the location was *interpolated* between the readings. When the neutral axis was on the south side of the connection, however, the instruments were being used to effectively *extrapolate* "outward" toward the neutral axis result.

Finally, it is worth noting that Equation 6.23 does not consider the permanent compression, or rounding, of the grout pad. This was observed starting with the seventh set, but was most significant during the ninth and tenth sets (see Section 4.6.2). Therefore, the calculated neutral axis may not have perfectly aligned with the actual depth of bearing during those drift ratios (schematically demonstrated in Figure 5.25).

6.10 EFFECTIVE FORCE ON STEEL DOWEL

The 2 in. diameter dowel bar was instrumented with one strain gauge on its south side, and one strain gauge on the north side. The pair of gauges were applied approximately ½ in. above the

annular plate of the housing fixture (shown in Figure 2.11). The strain gauge data from the dowel bar was used to estimate the force on the bar.

By subtracting the north gauge output from the south gauge readings, and dividing the result by the 2 in. diameter, curvature was calculated for the bar (presented in Figure 5.36). The resulting sign convention implied that moments producing a tensile strain on the south side of the bar were positive (or by vector convention, moments in the "down-cross-north" direction were positive). If the bar behaved as a cantilever beam across the joint (as intended), a concentrated force in the north direction would produce positive moment in the bar, and vice versa for forces to the south.

According to Euler-Bernoulli beam theory, the bending moment can be calculated with the product of the bar curvature, the steel's elastic modulus (assumed to be 29000 ksi), and the moment of inertia (0.785 $in.^4$ for the 2 in. diameter bar). The resulting moment is plotted against drift in Figure 6.59.

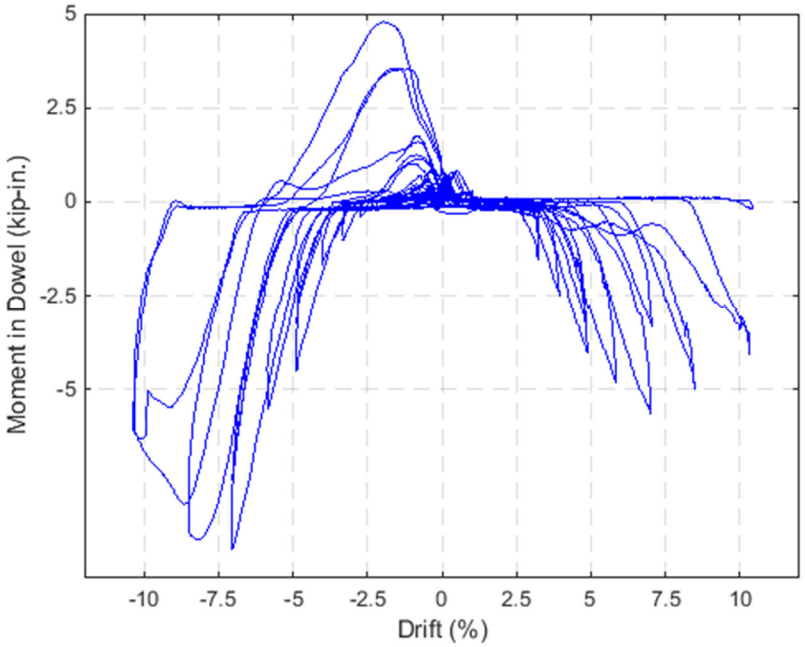

Figure 6.59 Moment in dowel, assuming Euler-Bernoulli beam theory.

If the bar behaved as a cantilevered beam, the effective force on the bar can be approximated by dividing the moment by the average of the east and west tube potentiometer readings. That measured displacement would have corresponded to the pull-out distance of the bar from the housing fixture. The resulting calculation for the force on the bar is plotted against drift in Figure 6.60 (a half inch offset was added to the pull-out distance in order to account for the gauge placement on the bar).

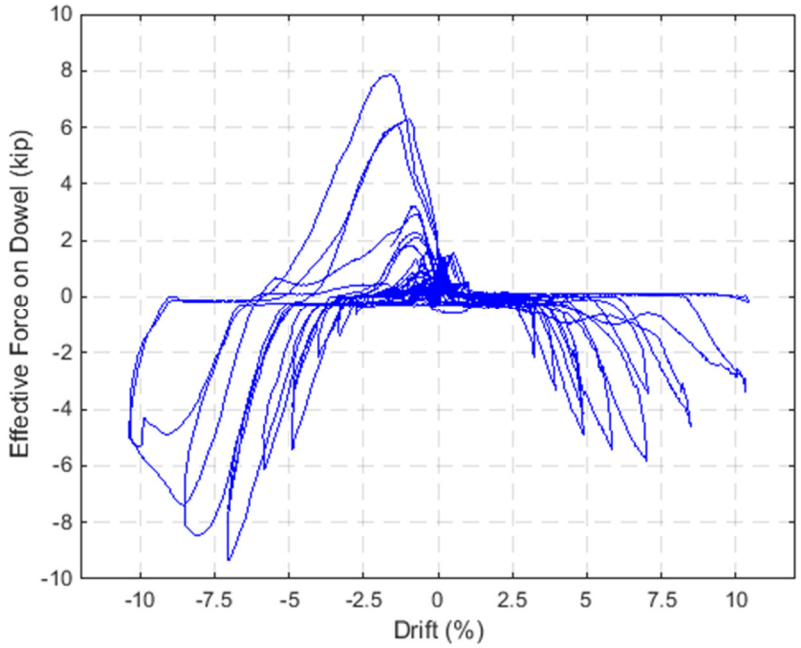

Figure 6.60 Effective force on dowel, assuming it behaved as a cantilever beam.

However, the resulting moment and effective force plots were not anticipated. They suggested that, for both positive and negative drifts, a force in the south direction would be generated on the bar (according to the previously established sign convention). For clarity, the second cycle envelope is shown in Figure 6.61.

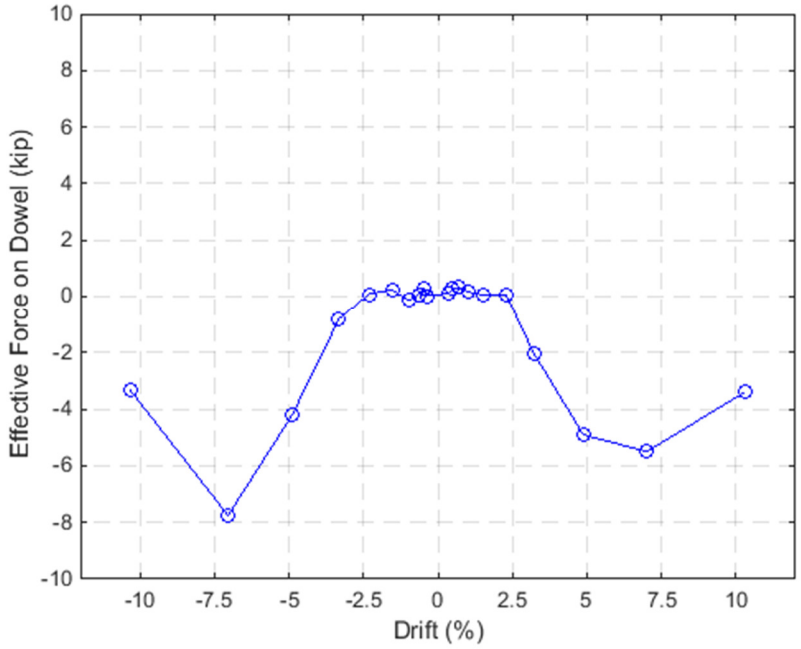

Figure 6.61 Envelope of effective force on dowel bar.

The results suggested that for low drifts, there was no force in the bar. But for higher drifts, the bar was always subjected to a force in the south direction (at least at peak and valley drifts). Therefore, it has been concluded that the bar probably did not behave as intended. In all likelihood, it did not fully engage the rim of the annular housing for low drifts. At near-zero drifts, contact between the dowel and housing would only result from shear slip of the baseplate on the grout pad, which was not indicated by the measured response. At higher drifts, as the bar began to rotate within the housing assembly, the bar's end and sides likely came into contact with the housing components at multiple locations, which would have produced an end moment on the bar, as opposed to a concentrated force. This may explain the irregular response of the bar.

However, it is noted that this analysis was derived with simple, engineering beam theory, which is probably not appropriate for the dowel bar structure (its maximum cantilever span length would have been ~2 in., compared to the bar diameter of 2 in.).

Regardless, the small strains (less than 10% of yield) from the strain gauges suggested that the bar was not significantly loaded during the test, and that the applied shear force was transferred from the column to the cap beam through friction between the baseplate and grout pad. Furthermore, the peak, calculated force in the bar was only ~9 kips in the south direction, and ~8 kips in the north direction. Considering the maximum effective force of ±60 kips, it has been assumed that the dowel bar was not required for the connection.

6.11 ESTIMATION OF MOMENT STRENGTH CONTRIBUTIONS

The estimated strand stress, known axial force, and estimated neutral axis location were used to determine the internal, resistive moment contributions to the rocking joint.

6.11.1 Analysis Formulation

6.11.1.1 Forces and Geometry

By taking the moment of each force about the compressive resultant, the strength contribution of the forces on the cross-section were individually determined. The relevant geometry for this analysis is pictured in Figure 6.62, and the moment contribution of each element is given by Equation 6.24.

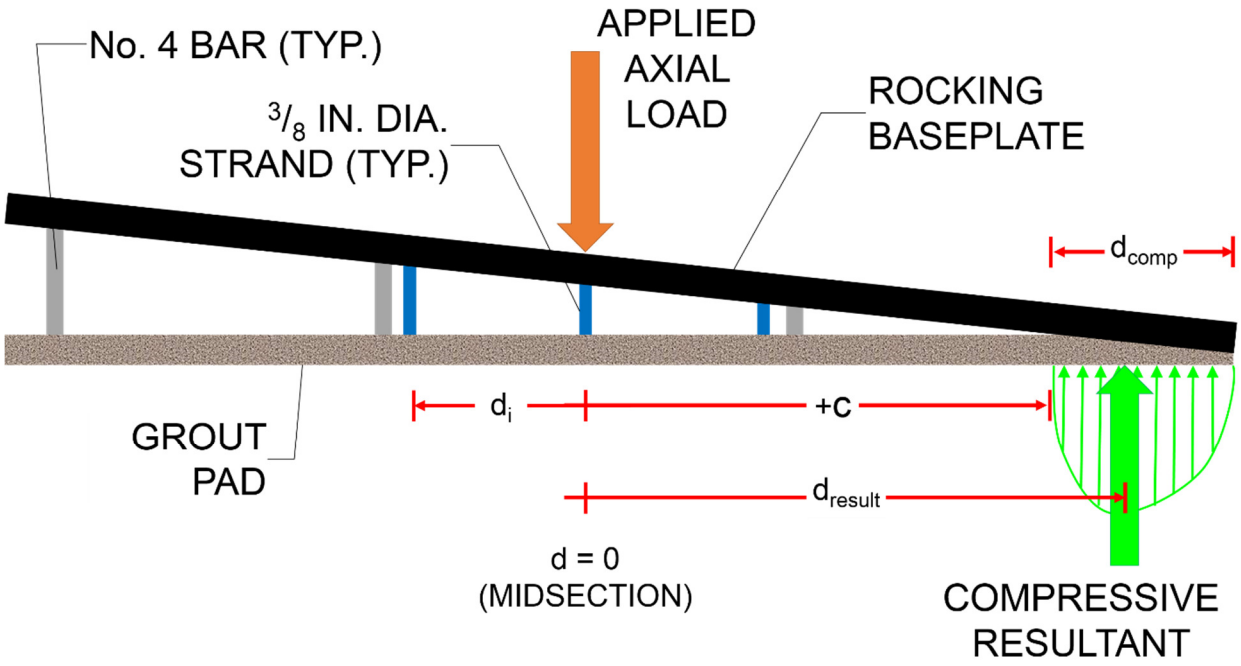

Figure 6.62 Relevant section geometry and forces for the analysis of this section.

$$M_i = (d_{result} - d_i)F_i \qquad \textbf{Equation 6.24}$$

Where M_i is the moment contribution of element i, d_{result} is the north-south distance of the compressive resultant to the midsection, d_i is the distance from the midsection to the i^{th} element, and F_i is the axial force for the i^{th} element.

For the entire test, the axial load was directly measured from the Baldwin output, and the individual strand stresses were later estimated with the cyclic model of Section 6.7.1. The individual rebar forces, on the other hand, were unknown. However, the strength contribution due to all of the bonded, mild steel reinforcement was eventually estimated by subtracting the strength contributions of the strands and axial load from the total, applied moment.

6.11.1.2 Estimating the Location of the Compressive Resultant

The exact location of the compressive resultant, and therefore the lever arm of each cross-sectional force, was not known. The neutral axis location (and therefore the depth of the compressive zone) was determined from the tube potentiometers in Section 6.9. However, this did not give the location of the compressive resultant, as it was a function of the grout material's constitutive properties in addition to the circle segmental bearing area on the pad. Therefore, a more helpful relation would be the one given in Equation 6.25.

$$M_i = \left(\left(c + \eta * d_{comp}\right) - d_i\right) F_i \qquad \textbf{Equation 6.25}$$

Where η is a factor relating the resultant location to the total depth of compression, d_{comp} – measured relative to the neutral axis location, c. This factor was similar to the k_2 factor described in most texts (e.g., Wight and MacGregor), but has been modified here for sign convention (the factor becomes smaller as the resultant gets closer to the neutral axis).

For PreT-CB-ROCK's rocking joint, the factor was numerically approximated with a fiber element model that was used to predict the flexural strength of the connection (see Section 7.4.1.6.3). That analysis assumed a Mander confinement model for the grout (derived from the measured response), and used the circular geometry of the joint cross-section. The calculated factor was plotted against drift, and the statistical toolbox of MATLAB 2014b was used to fit a power equation to the ordered pairs. This function is given by Equation 6.26, and it is plotted in Figure 6.63 (the moment-rotation results are not shown here).

$$\eta = 0.07911 * |drift\_[\%]|^{-0.5415} + 0.3917 \leq 0.589 \qquad \textbf{Equation 6.26}$$

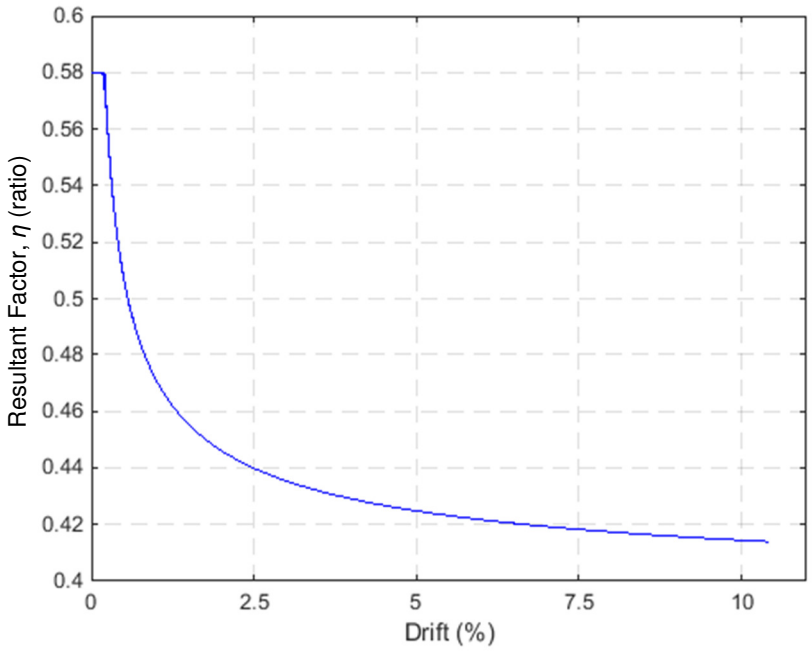

Figure 6.63 The fitted line for the resultant factor.

The upper limit of 0.589 corresponds to the compressive resultant location for the neutral axis at the midsection, and a linear constitutive response from the grout pad (i.e., the compressive resultant is 5.89 in. away from the midsection for linear-elastic bending of a 20 in. diameter, circular cross-section).

Two functions were then fit to the north/south envelope of the neutral axis data in order to develop continuous relationships between the applied drift ratio and the neutral axis location. The fitting was also done with the statistical toolbox of MATLAB 2014b. The two equations are given in Equation 6.27 and Equation 6.28, and the fitted functions are plotted against the full envelope in Figure 6.64.

$$c_{fit,south} = 4.592 * \tan^{-1}(3.29 * drift\_[\%]) * e^{-0.003882 * drift\_[\%]} \quad \textbf{Equation 6.27}$$

$$c_{fit,north} = 6.441 * \tan^{-1}(1.288 * drift\_[\%]) * e^{0.02895 * drift\_[\%]} \quad \textbf{Equation 6.28}$$

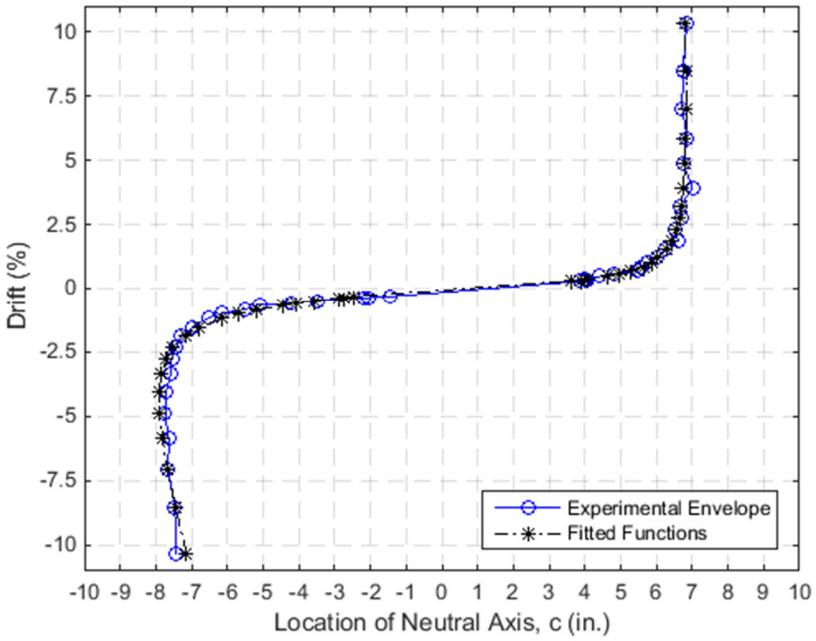

Figure 6.64 Continuous functions fitted to the neutral axis location vs. drift envelope.

Using the fitted data, Figure 6.65 shows the estimated location of the compressive force resultant, along with the neutral axis location, as functions of drift.

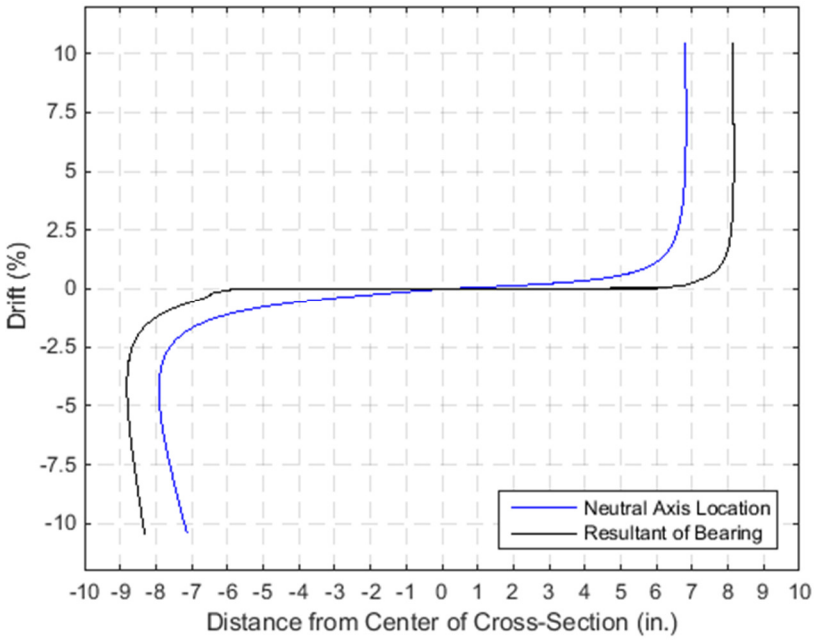

Figure 6.65 The approximated locations of the neutral axis and compressive resultant, for positive and negative drifts.

6.11.2 Results

6.11.2.1 Moment Contributions of Components

The axial load was assumed to act at the midpoint of the cross-section. The internal moment due to the axial load is plotted in Figure 6.66.

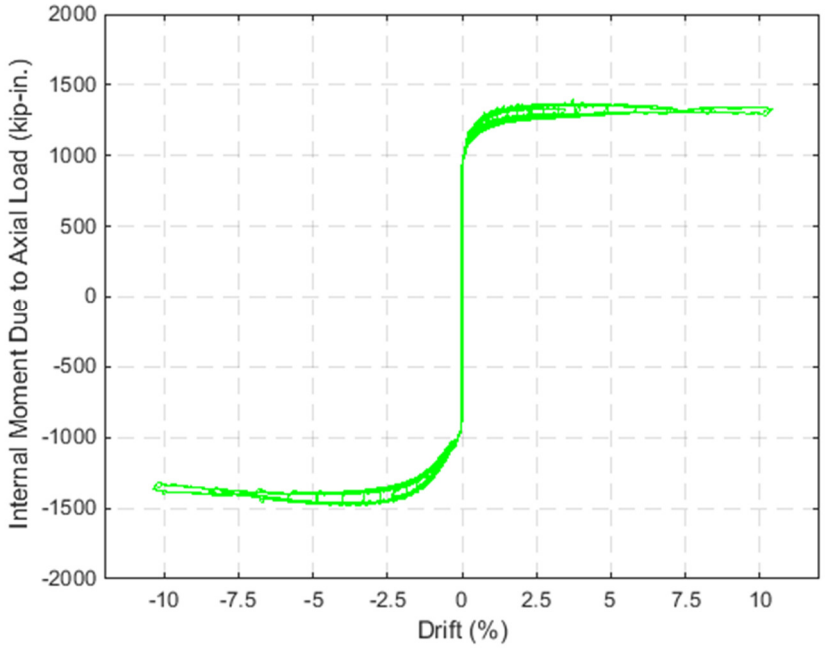

Figure 6.66 Resistive moment contribution of the axial load.

By taking the approximated, cyclic stress of each strand, the nominal strand area, and the distance of each strand from the compressive resultant, the moment contributions of the individual strands were calculated. Figure 6.67 shows the total moment from the prestressing, which was the sum of all six strands at each point during the test.

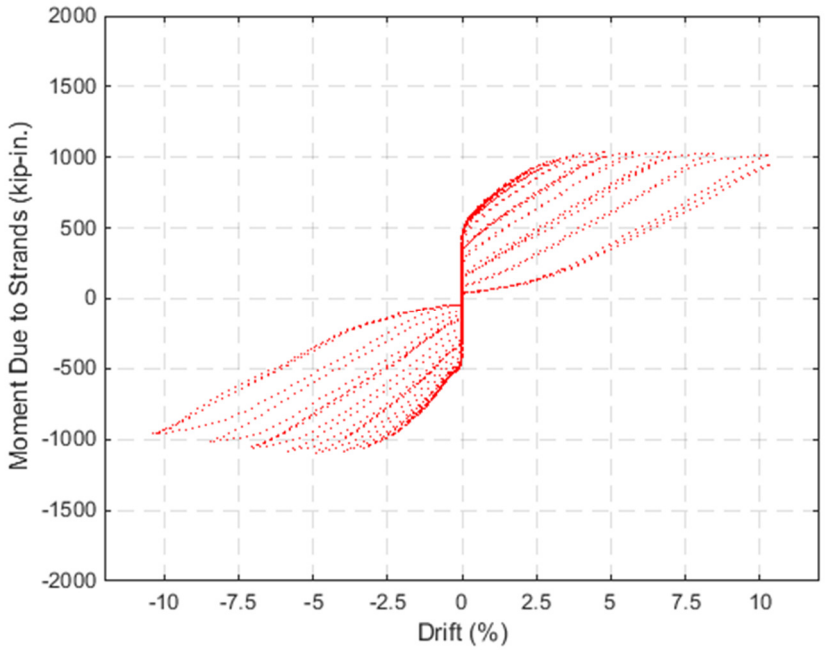

Figure 6.67 Moment contribution of all the prestressing strands.

Finally, the contribution from all of the bonded reinforcement was estimated by subtracting the axial load and prestressing moments from the total applied moment. Figure 6.68 plots the rebar moment contribution versus drift.

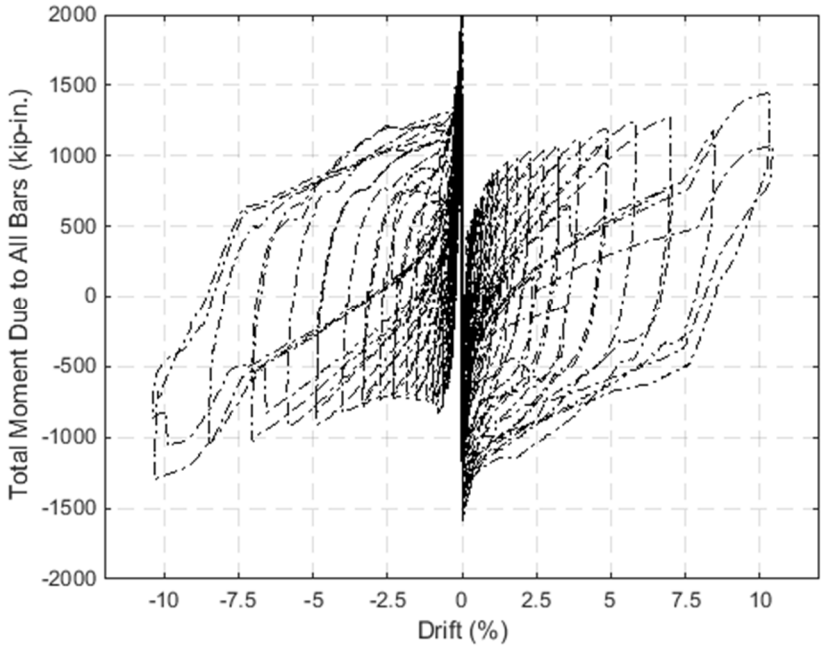

Figure 6.68 Estimated moment contribution from the bonded, No. 4 reinforcing bars.

6.11.2.2 Total Moment and Comparison

Figure 6.69 plots the full response of the axial load, strands, and rebars versus drift, along with the total measured response. Figure 6.70 gives the envelope of each component against drift (first and second cycles have been plotted). Finally, Figure 6.71 plots the percent contribution each resisting moment to the total applied moment; the first/second cycle envelope was used for that plot.

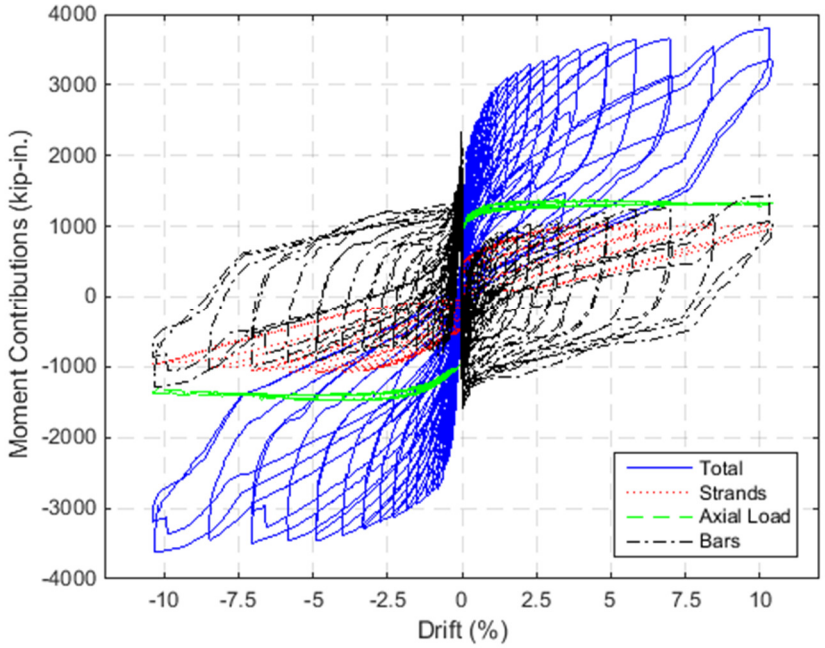

Figure 6.69 The total, applied moment versus the internal, resistive moments.

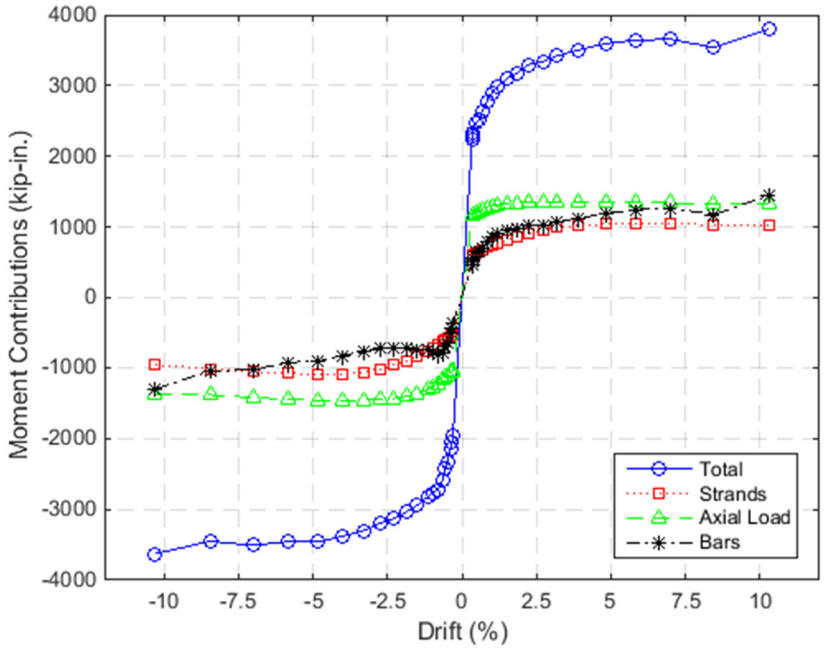

Figure 6.70 The envelope of the applied and resisting moments.

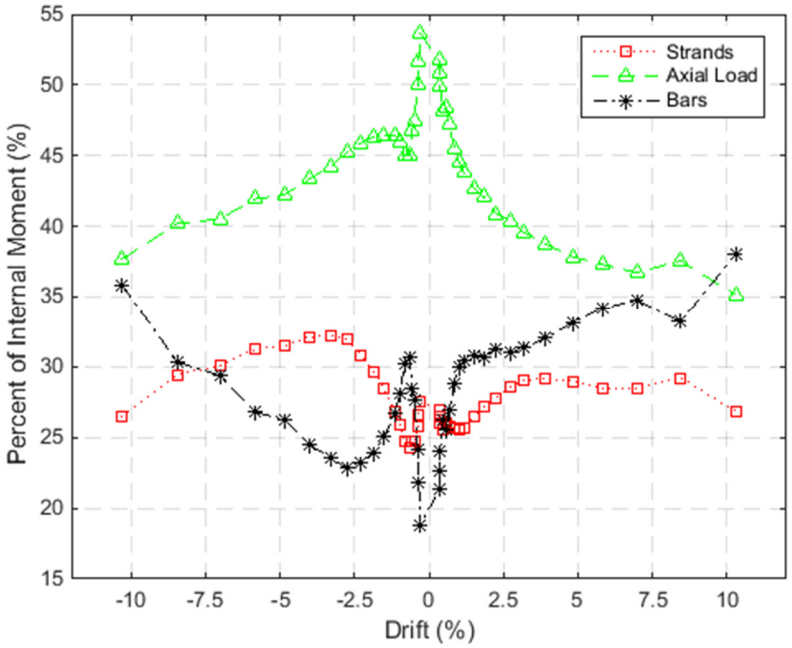

Figure 6.71 The contribution of each resistive component, as a percentage of the total joint strength.

The previous plots show that, for low drift, right as the joint was decompressing, the axial load was the largest contributor to the resistance of the base plate rotation. This was a reasonable result as the rebars were unbonded across the joint, and therefore would not produce a large force at low drifts. The strands, on the other hand, were prestressed, and therefore produced a resistive force to the opening of the joint (albeit lower in magnitude than the applied vertical load).

As the neutral axis shifted and settled to a value of ~±7.5 in., the relative contribution of the axial load diminished, as the moment magnitude of that component was constant. The strands also had a fairly constant moment contribution for higher drifts. That was likely due to the low secondary stiffness of prestressing steel. The rebars, on the other hand, were able to strain harden, and their cumulative contribution to the internal moment was much larger at higher drifts. It is also interesting to note the reduction in the rebar's moment contribution for negative displacements between -1% to -7% drift. For a particular cycle, this was likely due to the bars being yielded in tension during the first pull to the south, and then transitioning to a compressive stress (in a tension elongation) during the subsequent push to the north. At the valley drift for the particular cycle, the bars would not be at the same tension stress as for the initial peak drift.

Davis et al., (2012) had originally developed the PreT- design so that about 40% of the reinforcing strength came from the bonded bars, and 60% from the strands. This analysis suggested that the strength contributions were more even between the two reinforcement types, at least for the PreT-CB-ROCK specimen. However, the nominal, ultimate stress of the bars used for this specimen was 107.3 ksi, and Davis likely assumed a lower bar strength for his initial design.

Finally, the contributions of the strands and rebars, which are the components of a hybrid system, can be qualitatively compared to the theoretical responses of such systems on their own; Figure 6.72 provides such a comparisons.

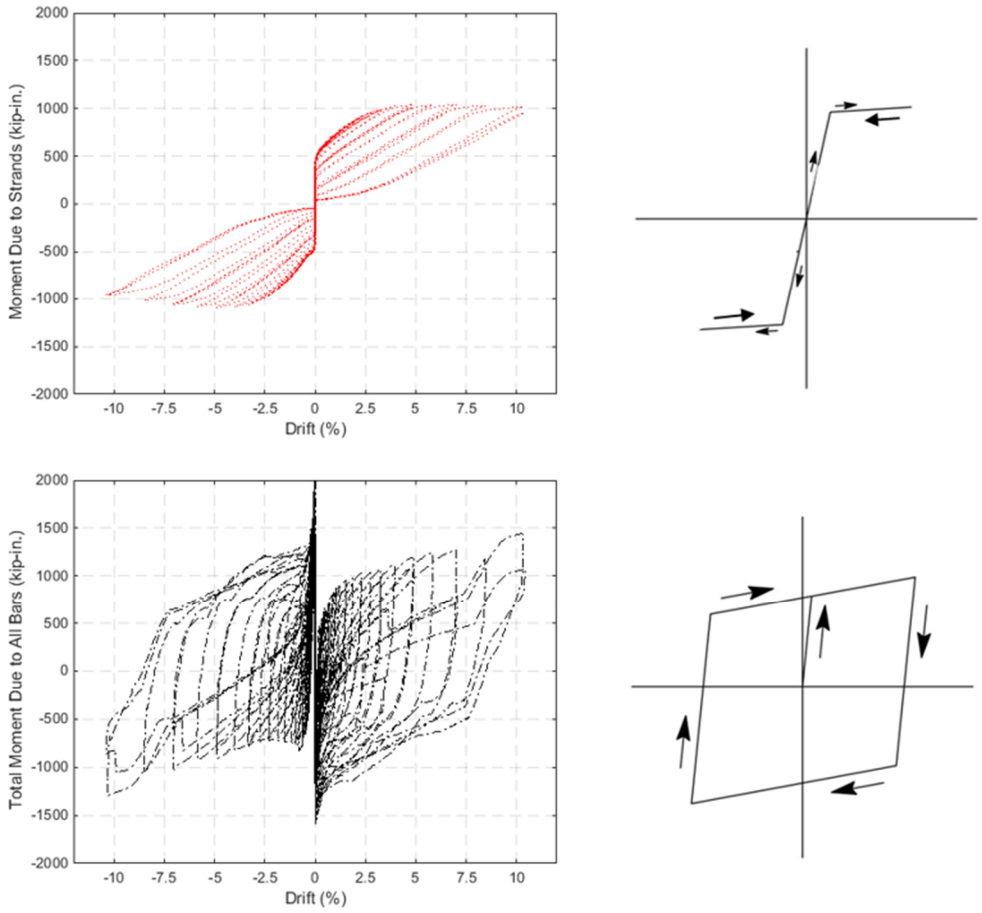

Figure 6.72 Comparison of the component moment responses to the theoretical concept of bonded/unbonded hybrid connection design (adapted from Stanton et al., 1997).

The strands' pre-yield behavior was very similar to the theoretical, bilinear response for an unbonded system. However, the strand response becomes somewhat tri-linear after they yield. The moment contribution of the rebars had a very similar shape as the typical hysteresis of a traditionally reinforced concrete system.

6.11.2.3 Discussion of Discrepancies and Validity

It is noted that this analysis did not close. That is, the calculated moment contribution for the rebars was disproportionately large for Set 10-Cycle 3, even though five of the six bars had broken by the peak/valley of that cycle. Furthermore, the isolated rebar hysteresis does not form an even parallelogram (i.e., the north and south responses do not perfectly align). The following explanations are offered:

- The northwest bar never fractured during the test. Using its cross-sectional location, and assumed resultant locations of ±8.0 in., that bar's moment contribution at its ultimate strength would have been -103 kip-in. in the north direction, and +240 kip-in. in the south direction.
- The resultant location was related to drift by assuming a constitutive response for the grout pad, and modeling the tension loads of the

reinforcement. In reality, the compressive resultant was also a function of the rounding of the grout pad. That is, when the grout pad was significantly rounded during the final test cycles, the actual bearing area would have been smaller than that indicated by the neutral axis data (see Figure 5.25). Therefore, the lever arms for the strands and axial loads could have been larger for the final cycles, giving those elements a greater contribution to the total moment. Because the rebar moment was determined by subtracting the strand and axial load from the total, the calculated moment attributed to the bonded reinforcing would have been proportionally less.

- The strand stresses/forces were approximated with a cyclic stress-strain model, which was not perfect in itself, and used strain gauge data from plastically elongated elements as its input.
- The measured force-displacement response was first corrected with a frictional model to remove the effects of the sliding/rotating bearing assemblies. That model was not absolutely accurate.

Finally, the pre-decompression behavior did not appear to be well captured by this analysis. However, the decompression analysis showed that the decompression moment was exceeded in the first set (and was only ~10% of the peak strength). Therefore, this was assumed to be insignificant when considering the response envelopes.

7 Comparison with Modeling

7.1 PREDICTED COLUMN STIFFNESS

The measured stiffness of the systems can be compared against the theoretical, uncracked stiffness and a predictive stiffness degradation models.

7.1.1 Theoretical Uncracked Stiffness

Hairline cracking in the PreT-CB-ROCK column was observed in the preliminary, trial cycle and in the first cycle of the actual test. Therefore, it would be difficult to correlate the observed and measured responses to the calculated, uncracked system properties, and they are presented here in order to serve as a baseline for the stiffnesses of the specimens.

The cantilever portion of the column had several distinct cross-sections:

- an over-reinforced, 13 in. deep segment (8.5 in. long),
- a 20 in. wide octagon that was reinforced with six No. 4 bars (7.5 in. long),
- a 20 in. wide octagon that was reinforced with six No. 4 bars and six No. 6 bars (34 in. long), and
- a 20 in. diameter, steel tube confined section that was reinforced with six No. 4 bars and six No. 6 bars (10 in. long).

The majority of the column had the 20 in. wide, octagonal cross-section that was reinforced both with No. 4 and No. 6 bars; it is shown in Figure B.12. Therefore, it was used for the elastic system properties considered in this section. The transformed area and transformed moment of inertia were calculated as 351.7 in.^{2} and 9530 in.^{4}, respectively (see Appendix E: Calculations for calculation spreadsheet). The unbonded strands were assumed to provide no contribution to the bending stiffness of the section. The calculation used the axial stiffnesses that were determined from materials testing (see Appendix A: Materials Testing).

Using the cross-section's transformed moment of inertia and the specimen's material properties, the column's cracking moment, M_{cr}, and uncracked bending stiffness, $k_{uncracked}$, can be determined with Equation 7.1 and Equation 7.2, respectively (e.g., Wight and MacGregor, 2011). Table 7.1 provides variable explanations and parameter inputs for these equations.

$$M_{cr} = \pm\left(f_r - \frac{P_{total}}{A_t}\right)\frac{I_t}{y} \qquad \textbf{Equation 7.1}$$

$$k_{uncracked} = \frac{3 * E_c * I_t}{{h_1}^3} \qquad \textbf{Equation 7.2}$$

Table 7.1 Variable explanations, inputs, and results for Equation 7.1 and Equation 7.2.

Variable Symbol	Variable Note	PreT-CB-ROCK	PreT-SF-ROCK	PreT-CB-CONC
f_r	rupture strength of concrete	0.909 ksi*	0.709 ksi‡	0.628 ksi‡
P_{total}	total axial load on the column, from Baldwin and effective prestressing	-243.2 kips	-243.2 kips	-243.2 kips
A_t	section transformed area†	351.7 $in.^2$	347.4 $in.^2$	337.5 $in.^2$
I_t	transformed moment of inertia†	9530 $in.^4$	9367 $in.^4$	8943 $in.^4$
y	distance from neutral axis to maximum bending stress	assumed D/2 = 10 in.	assumed D/2 = 10 in.	assumed D/2 = 10 in.
E_c	concrete modulus of elasticity	4930 ksi*	5620 ksi*	4776 ksi‡
h_1	cantilever length of the column	59.813 in.	60.0 in.	60.0 in.
M_{cr}	cracking moment of column, Equation 7.1	±1525 kip-in.	±1368 kip-in.	±1206 kip-in.
M_{decomp}	decompression moment of rocking joint (see Section 6.8.1.1)	±397.5 kip-in.	±607.9 kip-in.	N/A
$k_{uncracked}$	the theoretical stiffness of the uncracked, cantilever length of the column, Equation 7.2	659 kips/inch	731 kips/inch	593 kips/inch
$k_{pre\text{-}decomp}$	the measured initial stiffness to the decompression moment, taken as average from Table 6.4	210 kips/inch	272 kips/inch	N/A

*Material property taken from respective report: Appendix A: Materials Testing of this thesis for PreT-CB-ROCK, Schaefer et al. (2014b),
†Section property calculations can be found in Appendix E: Calculations.
‡Assumed from *ACI 318 11* relations, reproduced in Equation 7.3 and Equation 7.4.

$$f_r\,[\_psi] = 7 * \sqrt{f_c\,[\_psi]} \qquad \textbf{Equation 7.3}$$

$$E_c\,[\_psi] = 57000 * \sqrt{f_c\,[\_psi]} \qquad \textbf{Equation 7.4}$$

The calculated, uncracked column stiffnesses were far higher than the rocking columns' measured, pre-decompression stiffnesses. The following explanations are offered:

- The measured stiffness could have been affected by shear deformations, which were not considered in the uncracked stiffness calculation.
- The bases of the specimens (either footing or cap beam), must have deformed to some degree, and therefore lent a flexibility to the overall system stiffnesses. Such base deformations (either bending or rigid body) would have been be most significant at low column drifts.
- Neither column was an absolute continuum, the stiffest section was selected for the uncracked properties.
- The underlying grout pad between the baseplate and cap beam of CB-ROCK may have reduced that column's apparent stiffness.
- The frictional model used to correct the force-displacement response was not absolutely perfect, and would have had a more proportionally significant affect at lower applied forces and displacements.

7.1.2 Predicted Stiffness Degradation

From continuum mechanics (e.g., Riley et al., 2002), the specimens' effective bending stiffnesses can be calculated with the Equation 7.5:

$$\left(EI_{eff,eqv}\right)_{meas} = \left(k_{eff,mod,y}\right)\frac{{h_1}^3}{3} \qquad \textbf{Equation 7.5}$$

Where $k_{eff,mod,y}$ is the secant stiffness to yield (see Equation 6.22), and h_1 is the cantilever column height. It is noted that Equation 7.5 comes from linear-elastic, continuum beam mechanics, which are not valid for the non-linear, inelastic response of a rocking column. Therefore, the bending rigidity calculated with Equation 7.5 was considered an equivalent, beam bending stiffness for the columns.

The equivalent bending rigidity can be compared to the column section's initial, uncracked, gross bending rigidity: E_cI_g. Such a parameter makes use of the concrete's modulus of elasticity, E_c, and the cross-section's gross moment of inertia, I_g. When possible, the modulus of elasticity should be determined from materials testing, and I_g can be determined from a section property calculation. For the columns considered in this thesis, I_g was calculated as 8760 in.^{4} for the 20 in. diameter, octagonal cross-section. It is noted that these specimens were not prismatic, and the 20 in. wide octagonal section represented the most "common" section for the columns.

The results of Equation 7.5 were then compared to a model that predicts the degradation in bending stiffness for a cast-in-place, traditionally reinforced, non-prestressed concrete column. It was developed by Elwood and Eberhard (2009), and is given in Equation 7.6.

$$\left(\frac{EI_{eff}}{E_c I_g}\right)_{calc} = \frac{0.45 + 2.5 \cdot \frac{P_{total}}{A_g \cdot f_c}}{1 + 110 \cdot \frac{d_b}{D} \cdot \frac{D}{h_1}}$$ **Equation 7.6**

In this equation, P_{total} is the total axial load on the column (including the force from the effective prestress), A_g is the gross area of the column, f_c is the compressive strength of the concrete, d_b is the bar diameter (the No. 4 diameter of ½ in. was used), h_1 is the cantilever length of the column (distance from connection to applied lateral load), and D is the column diameter.

The axial force on the concrete due to the column's effective prestressing force was added to the vertical load applied by the Baldwin. While not constant, increases to the prestressing force were assumed to remain small near the transition from gross to effective stiffness. Table 7.2 provides a detailed summary for several pre-tensioned specimens.

Table 7.2 Unique inputs, results, and comparisons for the bending stiffness calculations of Equation 7.5 and Equation 7.6.

Specimen	f_c (ksi)	E_c (ksi)	$k_{eff,mod,y}$ (kip/in), Table 6.8	$(EI_{eff,eqv})_{meas}$ (x10^4 kip-in.^{2})	E_cI_g (x10^4 kip-in.^{2})	$(EI_{eff,eqv})_{meas}$ / E_cI_g	$(EI_{eff}/E_cI_g)_{calc}$	Ratio (meas : calc)
PreT-CB-ROCK	9.03 †	4930 †	144*	1027	4319	**0.238**	**0.340**	**0.699**
PreT-SF-ROCK	10.27 †	5620 †	168*	1206	4923	**0.245**	**0.328**	**0.747**
PreT-CB-CONC	7.02 †	4780 ‡	155*	1112	4184	**0.266**	**0.371**	**0.716**

†Engineering property from materials testing of respective project; either Appendix A: Materials Testing of this thesis, or Davis et al., (2012), or Schaefer et al., (2014b).

‡Estimated using the *ACI 318 11* relation between concrete compressive strength, f_c, and axial stiffness, E_c (reproduced in Equation 7.4). Actual materials test data was not available.

The model of Equation 7.6 generally under predicted the stiffness degradation of the pre-tensioned systems. That is, the $(EI_{eff}/E_cI_g)_{calc}$ factors are higher than the measured values, and would predict higher effective stiffnesses for equivalent columns. This is likely due to the nature of the rocking connection: the stiffness to the yield moment is greatly influenced by the transition from the primary, pre-decompression stiffness to the secondary, post-decompression stiffness (see Section 6.8.1.4). The model, on the other hand, uses the reduction in cross-sectional contact area (due to concrete cracking) and bar slip to estimate the stiffness loss.

However, the model results agreed with the general magnitude of the measured results. Furthermore, the pre-tensioned specimens all had similar, measured reductions in stiffness, which produced similar "meas:calc" ratios when compared to the model. Therefore, the conceptual framework of the Elwood and Eberhard model was probably still valid, but the model would need to be refined and calibrated for the pre-tensioned systems.

7.1.3 Summary and Comparison of Stiffnesses

A summary of all the calculated and measured stiffnesses is provided in Table 7.3. It includes results for both rocking connections, two "non-rocking" pre-tensioned specimens, and a conventionally reinforced column that had a similar geometry (PCC-SF-THK2).

Table 7.3 Summary of stiffnesses (all values given in kips/inch).

Specimen	Measured Primary Pre-Decomp, $k_{pre\text{-}decomp}$ (Table 6.4)	Measured Secondary Post-Decomp, $k_{post\text{-}decomp}$ (Table 6.5)	Measured Effective Stiffness to Yield, $k_{eff,mod,y}$ or $k_{eff,,y}$ (Table 6.8)	Calculated Uncracked Concrete, $k_{uncracked}$ (Table 7.1)	Predicted Effective Stiffness to Yield, $k'_{eff,,y}$ (calculated from Table 7.2 results)
PreT-CB-ROCK	210	2.54	144♦	656	206
PreT-SF-ROCK	272	5.19	168♦	731	224
PreT-CB-CONC	N/A*	N/A*	155♦, 180	593 ‡	215
PreT-SF-CONC	N/A*	N/A*	178[+]	448 ‡	170[+]
PCC-SF-THK2	N/A*	N/A*	138[+]	461 ‡	132[+]

*Parameter not applicable to specimen design.
‡Calculation made with assumed material relations of *ACI 318 11*.
[+]Result taken from respective report: Davis et al., (2012) or Haraldsson et al., (2011b).
♦Modified effective stiffness to yield (Section 6.8.2.3).

Several trends can be observed from Table 7.3:

- The specimens were more flexible than the theoretical, uncracked, column stiffness suggested.
- The footing specimens were stiffer than the corresponding cap beam specimens. It is noted that while the traditional effective stiffness results for the two "non-rocking" systems were roughly equal, the footing specimen had a 6 in. taller column.
- The pre-tensioned specimens had higher effective stiffnesses than the conventionally reinforced SF-THK2 specimen.

Furthermore, the previous calculations show that the calculated decompression moments were just 26.1% and 44.4% of the column cracking moments (see Section 6.8.1.1 for pre-decompression analysis). Therefore, the systems' connections likely decompressed and opened at far lower lateral loads than that causing column cracking. The measured responses indicated that the post-decompression stiffness reduced to just 1-2% of the pre-decompression stiffnesses (see Section 6.8.1.4). On the other hand, the measured effective stiffness degradation was 24% of the calculated gross stiffness (see Table 7.2). This supports the measured response observations of

Section 5.6: system deformation primarily resulted from joint rotation, as opposed to cumulative curvature caused by distributed flexural cracking and elastic bending.

7.2 COLUMN RE-CENTERING

The limiting of residual displacements following a seismic event was a key design goal for the rocking system. A method to predict and design the re-centering behavior of a reinforced concrete column was developed by Hieber et al. (2005). The method relies on the "re-centering ratio", which is a ratio of the nominal re-centering forces acting on a column (prestressing forces and axial load), to the resisting forces (from the bonded longitudinal reinforcing steel). These forces are shown schematically in Figure 7.1. It is noted that the re-centering ratio is a design property, and not a measured one. A column with a re-centering ratio greater than 1.0 should be expected to re-center.

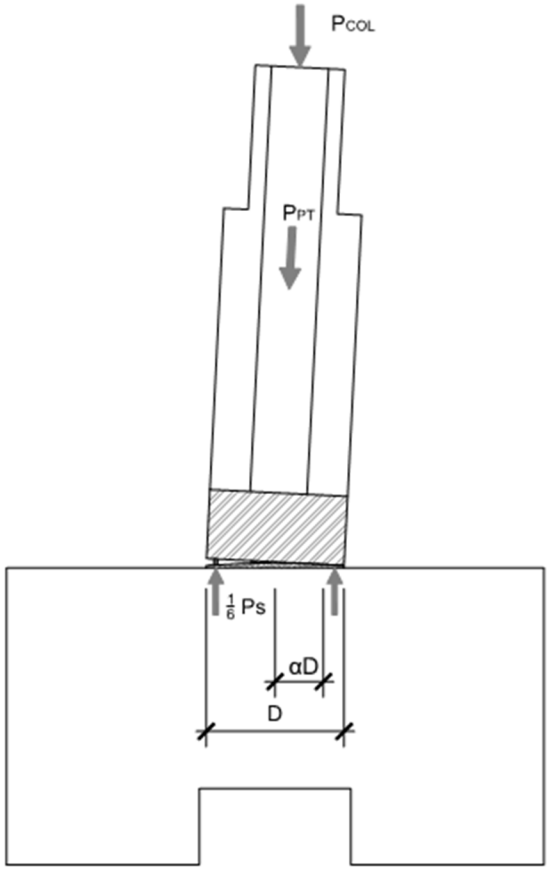

Figure 7.1 Forces used to calculate the re-centering ratio.

The re-centering ratio is determined by first summing restoring and resisting moments about the centroid of the compression zone of the column's cross-section. The moments at zero drift are approximated by Equation 7.7 and Equation 7.8.

$$M_{re-center} = \left(P_{col} + P_{pt}\right) \cdot \alpha D = \left(P_{col} + A_p \cdot f_{pe}\right) \cdot \alpha D \qquad \textbf{Equation 7.7}$$

$$M_{resisting} = P_s \cdot \alpha D = (A_s \cdot f_y) \cdot \alpha D$$ **Equation 7.8**

In the preceding equations, P_{col} is the axial load on the column, P_{pt} is the column's prestressing force, P_s is the force in the longitudinal steel (assuming that all steel is yielding in compression), and αD is the distance between the center of the column cross-section and the center of the compression block. The re-centering moment is then divided by the resisting moment to generate the re-centering ratio, λ_{re}, as defined by Equation 7.9.

$$\lambda_{re} = \frac{M_{re-center}}{M_{resisting}} = \frac{(P_{col} + P_{pt})}{P_s} = \frac{P_{col} + A_p \cdot f_{pe}}{A_s \cdot f_y}$$ **Equation 7.9**

The prestressed specimens considered in Section 6 all had the same axial load, prestressing force, and reinforcing steel (only considering longitudinal rebar crossing the rocking interface of the column). The properties of these specimens result in an initial re-centering ratio of approximately 3.4. It is noted that this calculation was done by assuming a rebar yield stress, f_y = 60 ksi and the design, effective prestressing stress, f_{pe} = 165 ksi. Furthermore, the re-centering ratio likely loses its validity at larger column drifts, when the stabilizing effect of the vertical load diminishes.

The greater-than-one re-centering ratio agrees with the measured behavior of the PreT- specimens. The effective force-displacement responses of those specimens indicated good re-centering. Furthermore, the PreT- specimens had very small normalized crossover displacements (Section 6.5), especially when compared to similar, non-prestressed columns.

7.3 SHEAR STRENGTH

7.3.1 Column

The shear capacity of the column was calculated with two methods: equations provided by *ACI 318-11* and a set of shear equations proposed by Priestley et al. (1994). Equation 7.10 to Equation 7.12 were taken from *ACI 318-11*.

$$V_c = 2 \cdot \left(1 + \frac{P_{total}}{2000 \cdot A_g}\right) \cdot \sqrt{f_c} \cdot D \cdot d$$ **Equation 7.10**

$$V_s = \frac{A_v \cdot f_{yt} \cdot d}{s}$$ **Equation 7.11**

$$V_n = V_c + V_s$$ **Equation 7.12**

The variables in these shear equations are defined as:

- V_n - the nominal shear strength of the member
- V_c - the concrete contribution to the shear capacity of the member
- V_s - the contribution to the shear strength that is provided by shear reinforcement
- P_{total} - the total axial load for columns (the yield prestressing force was added to this because the maximum effective force was observed at large drifts, when the strands were likely to undergo yield straining – 159 kips from the applied load plus 242.5 ksi*0.85 in.^{2}*6 strands = 283.7 kips).

A_g - the gross, cross-sectional area of the member (331.4 in.^{2} for the 20 in. diameter section and 78.8 in.^{2} for the reduced diameter extension.)
f_c - compressive strength of the concrete (9030 psi on test day)
D - width of section (20 in. for main section, 9.75 in. for reduced diameter extension)
d - section depth (18.625 in. for octagonal section, 7.75 in. for reduced diameter section)
A_v - area of shear reinforcement (0.0413 in.^{2})
f_{yt} - yield stress of the transverse reinforcement (86.3 ksi)
s - spacing of shear reinforcement (1.25 in. for both sections)

The calculated ACI strengths for the 20 in. diameter, octagonal section were:

V_c = 70.8 kips
V_s = 53.1 kips
V_n = 123.9 kips

The calculated ACI strengths for the 9.75 in. diameter, reduced diameter extension were:

V_c = 14.4 kips
V_s = 22.1 kips
V_n = 36.5 kips

The shear strength of the column was also calculated with a method developed by Priestley et al., (1994), which defines concrete shear strength as a function of the displacement ductility. Equation 7.13 to Equation 7.16 were used for the method.

$$V_n = V_c + V_p + V_s \quad \textbf{Equation 7.13}$$

$$V_c = k_{ductility} \cdot \sqrt{f_c} \cdot A_{cracked} \quad \textbf{Equation 7.14}$$

$$V_p = \frac{D-c}{2h_1} \cdot P_{col} \quad \textbf{Equation 7.15}$$

$$V_s = \frac{\pi}{2} \cdot \frac{A_v \cdot f_{yt} \cdot D'}{s} \cdot cot\, 30° \quad \textbf{Equation 7.16}$$

The variables in these shear equations are defined as:

V_n - nominal shear capacity
V_c - component from concrete
V_p - component from axial load
V_s - component from shear steel
$k_{ductility}$ - displacement ductility parameter for member ($1.2 \leq k_{ductility} \leq 3.5$)
f_c - specified concrete strength (measured at 9030 psi on test day)
$A_{cracked}$ - taken as 80% of the gross cross-sectional area (264.8 in.^{2})
D - section diameter (20 in.)
c - depth to the neutral axis (estimated as 3 in., from measured results)
h_1 - length of the cantilever (59.813 in.)
P_{col} - axial load (159 kip)
A_v - area of spiral (0.04133 in.^{2})
D' - center-to-center diameter of spiral (18.125 in.)

f_{yt} - yield stress of the transverse reinforcement (86.3 ksi, from materials testing)
s - spacing of shear reinforcement (1.25-in. pitch)

For the assumed parameters above, the nominal shear capacity of the 20 in. diameter, octagonal section, V_n, ranged from 193.4 kips to 251.3 kips (according to the prescribed range in ductility factor). The concrete component, V_c, was 30.2 kip to 88.1 kip. The axial load component, V_p, was 22.5 kip. The shear steel component, V_s, was 140.7 kip.

Shear damage was not observed during the tests; all cracks were from flexure, none of which resulted in significant damage. This performance was consistent with PreT-SF-ROCK and other pre-tensioned specimens at the University of Washington.

This absence of shear damage was expected as the calculated, nominal shear capacity of the column using the ACI model was much greater than the maximum effective force during the test (V_n/V_u = 123.9 / 63.6 = 1.95). The shear equations developed by Priestley et al., predicted an even greater nominal shear capacity for the column (V_n / V_u = 3.04 to 3.95). In this test and in two previous rocking tests, strain gauge readings from the spiral were consistently low. This suggested that the concrete alone provided the shear resistance to the load. If this were the case, it is possible that the amount of spiral could be reduced for the column without risk of shear damage.

Furthermore, Hewes and Priestley (2002) also observed a complete lack of shear damage for their unbonded, jacketed columns. For their unbonded system, a diagonal strut developed from the bearing area to the applied load point at the top of the column. The horizontal component of that strut was assumed to carry the full column shear. While the PreT- columns had a combined bonded/unbonded hybrid design, the percentage of mild steel reinforcement was relatively low. Therefore, the shear behavior of the PreT- columns may have been similar to the theoretical, unbonded system.

7.3.2 Rocking Connection

Slip was not observed at the rocking interface. Because the dowel bar was inactive for most of the test, or behaved in an unanticipated manner, it has been assumed that the shear force was transferred through the connection entirely by friction between the pad and baseplate. Hewes and Priestley (2002) also observed this behavior for their post-tensioned, jacketed, segmental columns. However, they suggested that shear keys be considered for squat columns or for bridge columns with relatively low axial loads.

Otherwise, the actual shear capacity of the column-to-cap beam interface was not predicted.

7.4 MODELING FLEXURAL STRENGTH OF SPECIMEN

The PreT-CB-ROCK specimen was modeled with a moment-rotation program and with a finite element analysis.

7.4.1 Moment-Rotation Fiber Model

A moment-rotation program was developed in MATLAB 2014b in order to predict PreT-CB-ROCK's moment-drift response. It was similar to a discretized moment-curvature analysis. However, because the strands and rebars were unbonded at the joint (and therefore did not maintain strain compatibility with the concrete), such a model would not be appropriate.

The moment-rotation model was two-dimensional in nature, and only push-over in one direction was considered. The basic flow was:

- input a joint rotation for the baseplate,
- iterate a value for the neutral axis depth until axial force equilibrium was achieved,
- calculate element elongations, forces, and sum the resulting element moments about the neutral axis location, and then
- estimate drift as a function of the inputted joint rotation and bending deformation resulting from the calculated moment.

It included the non-linear constitutive response of the materials, but did not include geometric non-linearity or cyclic loading. The details of the model are described in this section.

7.4.1.1 Model Geometry

The model was formulated as a two-dimensional pushover analysis. Joint rotations about the east-west axis were inputted, and the resulting moment about that axis and column drift were outputted. The cross-section geometry was first discretized and projected onto a two-dimensional plane, as shown in Figure 7.2.

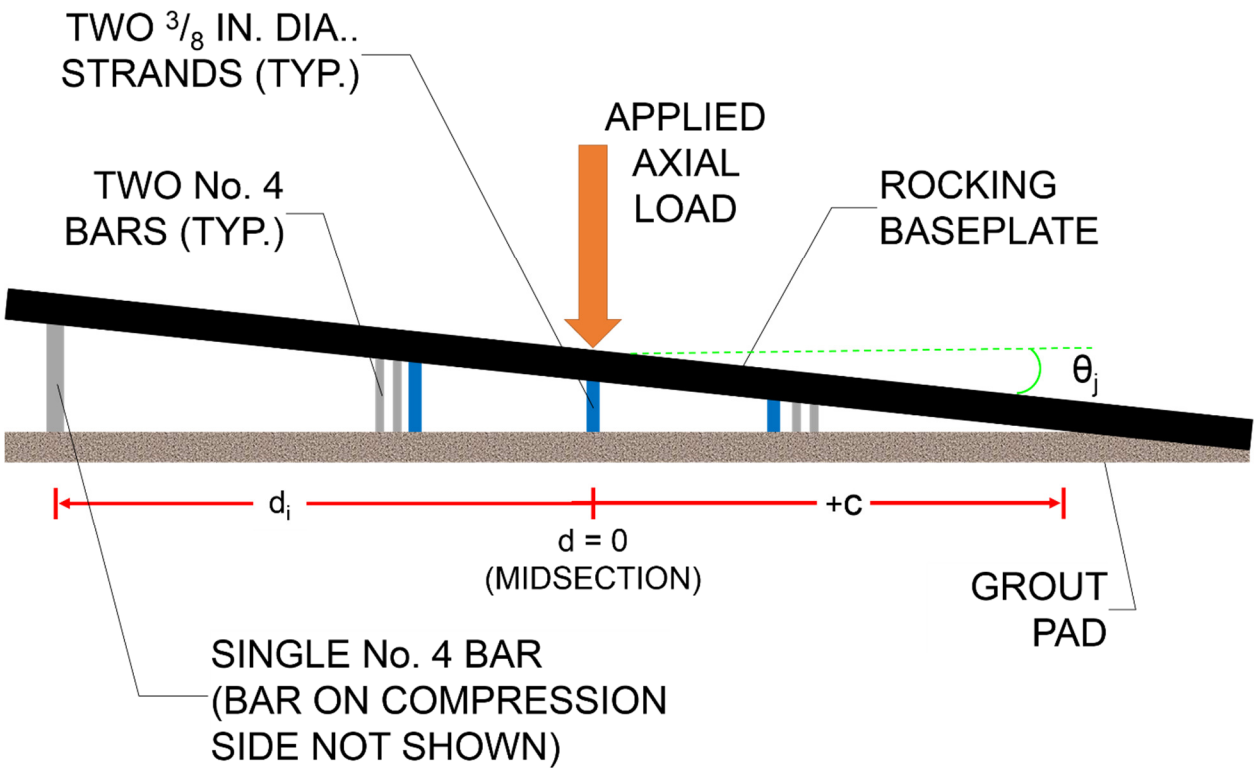

Figure 7.2 Two-dimensional geometry of moment-rotation model.

In the figure, d_i refers to the distance of an element to the joint midsection, with the sign convention of distances to the right being positive. The inputted neutral axis location, c, and joint rotation angle, θ_j, are also marked in the figure.

Only the structural elements which crossed the plane of the rocking connection were included in the program. The following specimen details were not considered in any way:

- the steel confining tube,
- the discontinuous No. 6 bars (that were welded to the baseplate),
- the dowel bar and housing fixture, and
- the cap beam base.

The reinforced concrete column above the connection was considered by approximating its bending deflection due to the calculated moment, and then adding that deflection to the final drift output.

7.4.1.1.1 Reinforcement

Only the No. 4 bars and prestressing strands were included in the model, as they were the only reinforcing elements that were bonded on either side of the rocking joint. The "d_i" locations of the reinforcing bars and prestressing strands were set as their north-south distances to the midpoint of the cross-section. Specific dimensions are given in Figure B.12. Nominal areas of both strands and rebars were used, and it is noted that the "inner" reinforcing elements of Figure 7.2 each represent two bars or strands.

The unbonded lengths of the No. 4 bars and the prestressing strands were set to the design lengths of 12 in. and 54 in., respectively. Slip was not considered for either element type.

7.4.1.1.2 Axial Load

The axial load was assumed to act at the mid-section of the joint.

7.4.1.1.3 Grout Pad

Only the half of the grout pad that laid on the compression side of the joint was included in the model. The resulting, 10 in. "long" pad was then discretized into 1000 slices of equal in-plane thickness (10 in. / 1000 layers = 0.01 in. per slice). The out-of-plane width for each slice was calculated based on its distance from the center of the joint by Equation 7.5; that is, it was simply a function of the circular geometry of the joint.

$$w_{pad,i} = 2 * \sqrt{10^2 - {d_{pad,i}}^2} \qquad \textbf{Equation 7.17}$$

The area for each grout pad element was then calculated by multiplying the in-plane thickness (0.01 in.) by the out-of-plane width. For simplicity, the grout pad area was not corrected by removing the areas that overlapped the reinforcement.

The thickness of each pad layer was uniformly set as the design thickness of 0.5 inches. This may not have been accurate to the test specimen, as the placed grout pad varied from extremes of ~$^{7}/_{16}$ in. on the north side to ~$^{12}/_{16}$ in. on the south side (see Section 2.9.3.3).

7.4.1.2 Material Constitutive Models

7.4.1.2.1 Rebar

A complete curve was used to model the stress versus strain relationship for the rebar (e.g., Park and Paulay, 1975). It consisted of a linear elastic portion, a yield plateau, a non-linear strain hardening segment, and a linear segment for the strain softening. The model parameters were selected to fit the materials test results for the No. 4 rebar (see Appendix A: Materials Testing). The model is defined by Equation 7.18 through Equation 7.21, and is shown in Figure 7.3.

$$f_s(\varepsilon_s) = \begin{cases} E_s * \varepsilon_s & \varepsilon_s \le \varepsilon_y \\ f_y & \varepsilon_y < \varepsilon_s \le \varepsilon_{SH} \\ f_y \left[\dfrac{m * \Delta\varepsilon_s + 2}{60 * \Delta\varepsilon_s + 2} + \dfrac{\Delta\varepsilon_s (60 - m)}{2(30r + 1)^2} \right] & \varepsilon_{SH} < \varepsilon_s \le \varepsilon_u \\ f_u + (\varepsilon_s - \varepsilon_u) \dfrac{f_r - f_u}{\varepsilon_r - \varepsilon_u} & \varepsilon_u < \varepsilon_s \le \varepsilon_r \\ 0 & \varepsilon_r < \varepsilon_s \end{cases} \qquad \textbf{Equation 7.18}$$

$$\Delta\varepsilon_s = \quad \varepsilon_s - \varepsilon_{SH} \qquad \textbf{Equation 7.19}$$

$$m = \quad \frac{\frac{f_u}{f_y}(30r+1)^2 - 60r - 1}{15r^2} \qquad \textbf{Equation 7.20}$$

$$r = \quad \varepsilon_u - \varepsilon_{SH} \qquad \textbf{Equation 7.21}$$

The variables in Equation 7.18 are defined as:

f_s	-	steel stress (input)
ε_s	-	steel strain (output)
E_s	-	steel Modulus of Elasticity (31000 ksi)
f_y	-	steel yield stress (73.1 ksi)
f_u	-	steel ultimate stress (107.3 ksi)
f_r	-	steel rupture stress (100.0 ksi)
ε_y	-	steel yield strain (0.00236 in./in.)
ε_{SH}	-	steel strain hardening strain (0.00921 in./in.)
ε_u	-	steel strain at ultimate stress (0.1024 in./in.)
ε_r	-	steel rupture strain (0.14 in./in.)
$\Delta\varepsilon_s$	-	difference between inputted steel strain and strain hardening strain
m	-	model parameter, calculated with Equation 7.20
r	-	model parameter, calculated with Equation 7.21

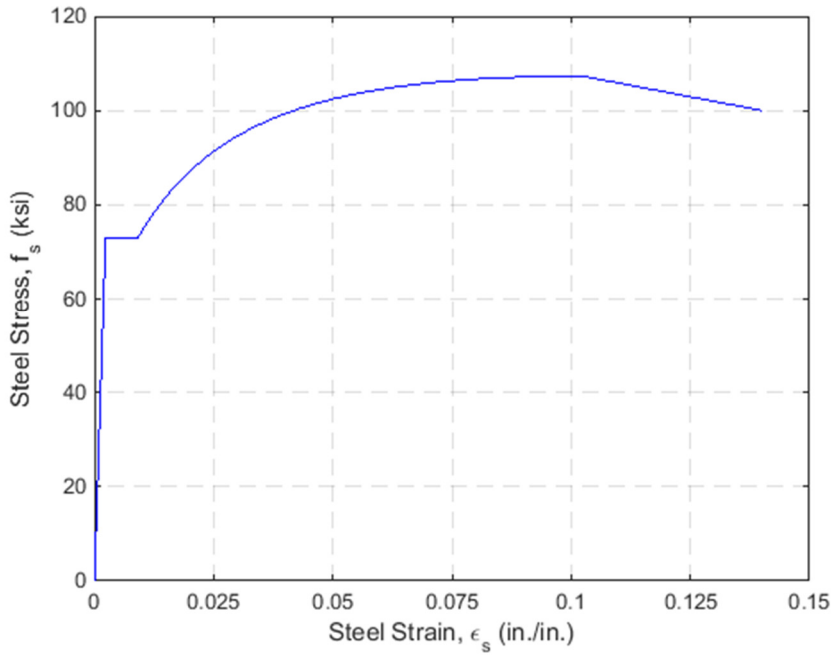

Figure 7.3 Stress vs. strain model for rebar.

It is noted that the modulus of elasticity used in the model disagrees with the conventionally accepted value for the property (31000 ksi versus 29000 ksi). This came from rebar testing, and was likely a result of the delivered bar area having a greater-than-nominal area, which would give a relatively larger, measured axial stiffness for the bar, with respect to nominal, specified properties. However, the modulus was still directly derived from materials testing, and was therefore assumed to be appropriate for the moment-rotation model (i.e., the total force of the bar would be correct, so long as the nominal area was used).

7.4.1.2.2 Prestressing Strand

The prestressing constitution was approximated with the Menegotto-Pinto curve introduced in Section 6.7, which was given by Equation 6.13. However, that model was calibrated against strain gauge data, which may have resulted in a spuriously high initial axial stiffness, E_p. For the flexural modeling of this section, the initial stiffness for the strands was set to 29000 ksi; all other parameters were the same as given in Equation 6.13. The modified stress-strain relation is shown in Figure 7.4. No strands fractured during the test, and therefore a rupture strain was not specified.

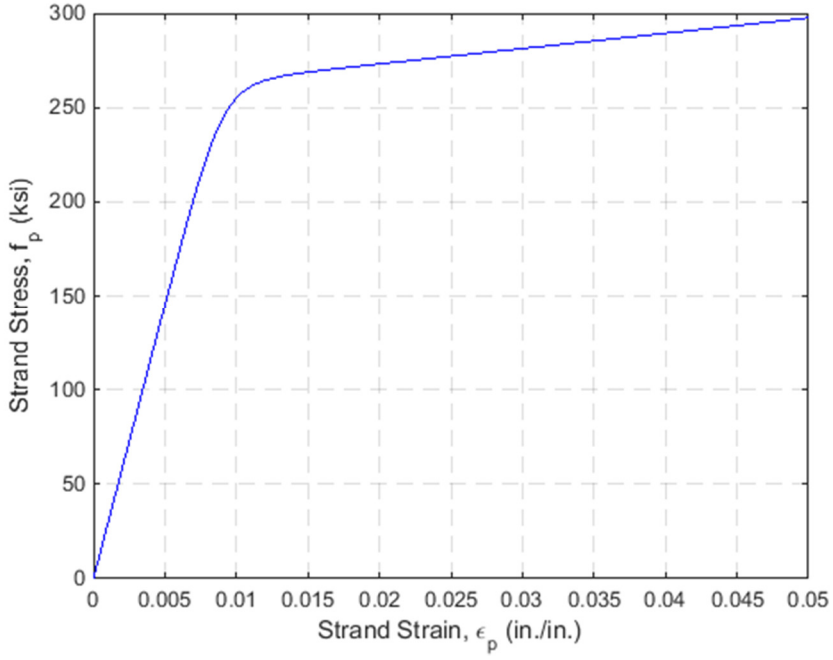

Figure 7.4 Menegotto-Pinto model used in the moment-rotation model for the strand constitution.

7.4.1.2.3 Grout Pad

The exact engineering properties of the fiber-reinforced grout were unknown. Compressive testing of 2 in. mortar cubes on test day suggested that the grout strength was 6875 psi. However, previous testing at 7, 14, and 28 day intervals all gave higher results than the measured strength on test day (at a grout age of 31 days). Those previous tests indicated that the grout strength was approaching 10 ksi (see Table A.1). Furthermore, the grout manufacturer gives 10 ksi as the 28 day strength for the flowable consistency of the unmodified material (Dayton Superior, 2011). Finally, elastic stiffness tests were not conducted on the grout.

To further complicate the issue, the friction from the steel baseplate probably provided extreme levels of confinement to the grout pad. Therefore, traditional, uniaxial materials testing may not have been entirely relevant, regardless.

In lieu of accurate materials data and a thorough understanding of the confined behavior of the pad, Mander's model for confined concrete (Mander et al., 1988) was used to approximate the stress-strain response of the fiber-reinforced grout pad. The exact parameters for the confinement model were selected with knowledge of the measured response of the rocking joint, and from engineering judgment. Therefore, this portion of the moment-rotation model is not strictly predictive, but it led to good moment-drift results and reasonable neutral axis results.

The Mander model has been reproduced in Equation 7.22 to Equation 7.25; the initial modulus of elasticity (E_c) was calculated from the *ACI 318-11* relation of Equation 7.26. The full response is shown in Figure 7.5.

$$f_c(\varepsilon_c) = \begin{cases} 0 & 0 \le \varepsilon_c \\ \dfrac{f'_{cc} * x * r_{Mander}}{(r_{Mander} - 1 + x^{r_{Mander}})} & \varepsilon_{cc} \le \varepsilon_c < 0 \\ f'_{cc} & \varepsilon_c < \varepsilon_{cc} \end{cases} \quad \textbf{Equation 7.22}$$

$$x = \frac{\varepsilon_c}{\varepsilon_{cc}} \quad \textbf{Equation 7.23}$$

$$r_{Mander} = \frac{E_c}{(E_c - E_{sec})} \quad \textbf{Equation 7.24}$$

$$E_{sec} = \frac{f'_{cc}}{\varepsilon_{cc}} \quad \textbf{Equation 7.25}$$

$$E_c = w_c^{1.5} 33 \sqrt{f_c} \quad \textbf{Equation 7.26}$$

The variables in preceding equations are defined as:

- f_c - grout stress (output)
- ε_c - grout strain (input)
- f'_{cc} - peak compressive strength of confined grout (estimated as 16730 *psi*)
- ε_{cc} - corresponding strain at peak confined strength (estimated as 0.5325 in./in.)
- E_c - initial modulus of elasticity (4484 ksi per *ACI 318-11* of Equation 7.26)
- w_c - measured unit weight of the grout (139 pcf)
- f_c - measured, unconfined compressive strength of the grout on the specimen test day (6875 psi)

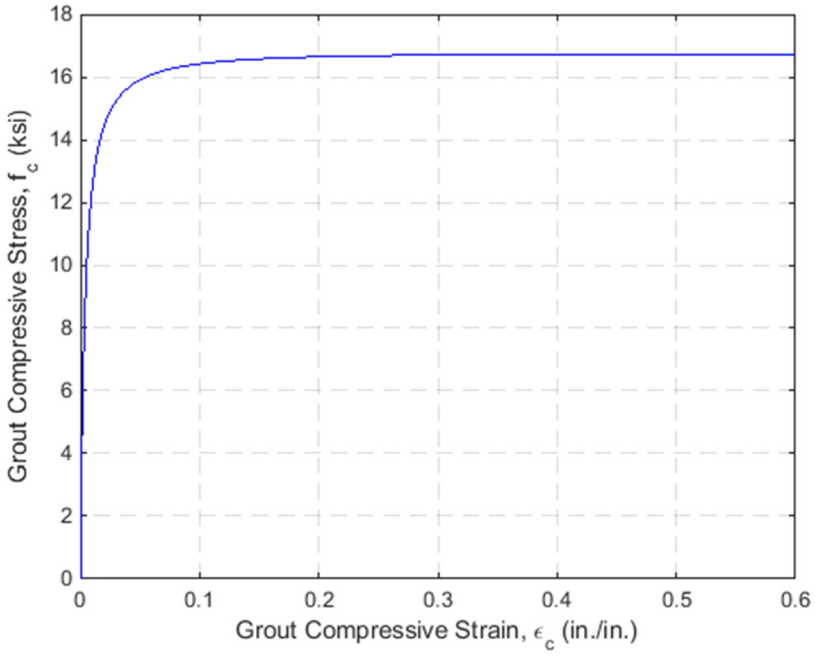

Figure 7.5 Stress vs. strain model for fiber-reinforced grout pad.

As previously stated, the parameters of the Mander model were selected from the measured responses of the test, and from the reinforcement materials data. The tube potentiometers indicated that, at the highest drifts near the end of the test, the neutral axis location settled at ~7.5 in. away from the center of the cross-section (see Section 6.9). Ignoring any effects of the rounding of the grout pad, this corresponds to a compressive area of 22.67 in.^{2} for the circular cross-section of the baseplate.

The peak strength, f'_{cc}, was selected by considering the required, maximum, compressive force on the cross-section. The materials testing of the prestressing strands indicated that the secondary, linear response began at ~265 ksi, and had an upper limit of >300 ksi. The ultimate strength of the rebars was 107.3 ksi and the yield strength was 73.1 ksi. If, at the highest drifts of the tests, all six strands were assumed to be at 275 ksi, one rebar at ultimate, and four rebars at yield, the resulting tension force would have been 220 kips (using nominal reinforcement areas). When this tension force is added to the applied axial load of 159 kips, the required compressive force to maintain axial equilibrium would have been 379 kips. Dividing 379 kips by 22.67 in.^{2} gives 16.73 ksi. At very large stains (>0.05 in.), the Mander model resulted in stresses close to the specified peak stress. Therefore, at large drifts, it was assumed that the entire bearing area exhibited the near peak confined strength, and 16.73 ksi was selected for the property in the moment-rotation model, which corresponded to 2.433 times the measured fiber-reinforce grout strength on test day.

The corresponding strain at peak stress, ε_{cc}, was also selected by considering the measured neutral axis location of 7.5 inches. If the peak, exhibited strength occurred at the maximum 10.65% drift ratio, the most extreme fiber of the pad would have been compressed by approximately 0.26625 in., if calculated by Equation 7.27 and assuming that the joint rotation angle equaled the drift ratio. This displacement corresponded to an axial strain of 0.5325 in./in. for the pad thickness of 0.5 inches. Therefore, 0.5325 in./in. was specified for the stain at peak stress.

Finally, the post-peak response was simply set to the peak confined strength (i.e., a crushing strain was not used). This was specified because very little grout pad crushing was observed during the test, and it appeared to primarily result from crushing of the grout that was erroneously placed underneath the weld between the tube and the baseplate (this also resulted in the "cusp" of the pad, see Figure 2.25). In this sense, Mander's model was modified for this analysis (he included a post-peak degradation in strength).

7.4.1.3 Element Displacements and Strains

For a specified neutral axis location and joint rotation angle, the rebar, strand, and grout pad layer strains were determined by first calculating their elongations/shortenings. These were calculated with the following equation:

$$\Delta_i = \theta_j (d_i - c) \qquad \textbf{Equation 7.27}$$

Where the element elongation/shortening, Δ_i, is a function of the inputted joint rotation angle, θ_j, the element's distance from the midpoint of the joint, d_i, and the inputted neutral axis depth, c. Therefore, this assumption is analogous to the plane-sections-remain-plane assumption of moment-curvature analysis. That is, deformations (as opposed to strains) vary linearly with distance from the neutral axis location.

Element strains were then determined by dividing the displacement by the respective element length: 12 in. for the bars, 54 in. for the strands, and 0.5 in. for the grout pad. Using constant values for the bar and strand debonded lengths implied no slip of the reinforcement during loading. Finally, the design prestressing strain (165 ksi / E_s = 0.00569 in./in.) was added to each strand strain.

The moment-rotation model of this section was similar to previous efforts to model rocking connections. For example, Tobolski (2010) developed a model for rocking, post-tensioned, concrete filled tubes. However, he assumed that the entire bearing area of the connection would act at an average, uniform compressive strain equal to the joint rotation angle (in radians), as prescribed by Stanton et al. (2002). The basis of this assumption is that the shortening of the compressed concrete is spread over a length equal to the neutral axis distance, c, which is schematically shown in Figure 7.6.

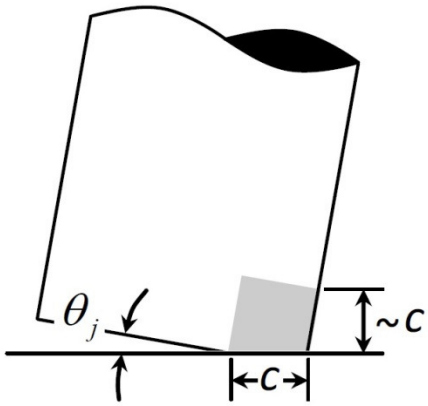

Figure 7.6 Schematic of CFT rocking behavior for Tobolski's moment-rotation model (2010).

For the analysis of PreT-CB-ROCK, however, the grout pad was a discrete element, with a discrete thickness. The pad was also assumed to be far more axially flexible than the confining tube portion of the column base. Therefore, compressive strains for the grout pad elements were assumed to be calculable in the same manner as for the reinforcing elements.

7.4.1.4 Component Forces

For a given neutral axis location and joint rotation angle, the axial stress was calculated for each element (rebars, strands, and grout pad slices). For a particular element, the stress was a function of its strain (calculated with Equation 7.27) and respective constitutive model.

The nominal cross-sectional areas of the rebar/strands were used to determine their force contributions on the cross-section, and the areas of the discretized grout pad slices were used. The force of each element was simply calculated as the element stress times its area.

The axial load was set at a constant 159 kips.

7.4.1.5 Model Formulation and Output

For a specified joint rotation, the value for the neutral axis location, c, was iterated until axial force equilibrium was achieved. The bisection method was used to numerically determine c, with a tolerance in axial force set to 0.5 kips.

Moment was then calculated about c for each element and the axial load. The sum of the moments, M_{out}, was then outputted as a result of the program. The displacement at the top of the column, Δ_1, was calculated with Equation 7.36 through Equation 7.38.

$$\Delta_1 = \Delta_{joint} + \Delta_{bending} \quad \textbf{Equation 7.28}$$

$$\Delta_{joint} = \theta_j * h_1 \quad \textbf{Equation 7.29}$$

$$\Delta_{bending} = \frac{M_{out}}{h_1} * \frac{1}{k'_{eff,y}} \quad \textbf{Equation 7.30}$$

Where Δ_{joint} was the top displacement due to the joint rotation, and $\Delta_{bending}$ was the deflection contribution due to bending of the column. The bending deflection was estimated from the outputted moment (which corresponded to an effective force) and the linear, effective stiffness, $k'_{eff,y}$, that was predicted by the Elwood and Eberhard model (206 kips/in.). Finally, drift was calculated as the total displacement at the top of the column divided by the column height, h_1 (59.813 in.).

Additionally, two points were added for the total response: 0 kip-in. at 0% drift, and the calculated cracking moment at the corresponding displacement (using the uncracked column stiffness).

7.4.1.6 Results

7.4.1.6.1 Moment-Drift Envelope

Figure 7.7 shows the moment-drift results of this model, plotted against the experimental envelope of PreT-CB-ROCK. The experimental envelope is the average between the north and south drifts

and moments for the second cycle of each set. It is noted that the individual points on the moment-rotation curve do not specifically correspond to the experimental moment-drift points. Additional model results were added to the plot in order to increase the resolution of the curve.

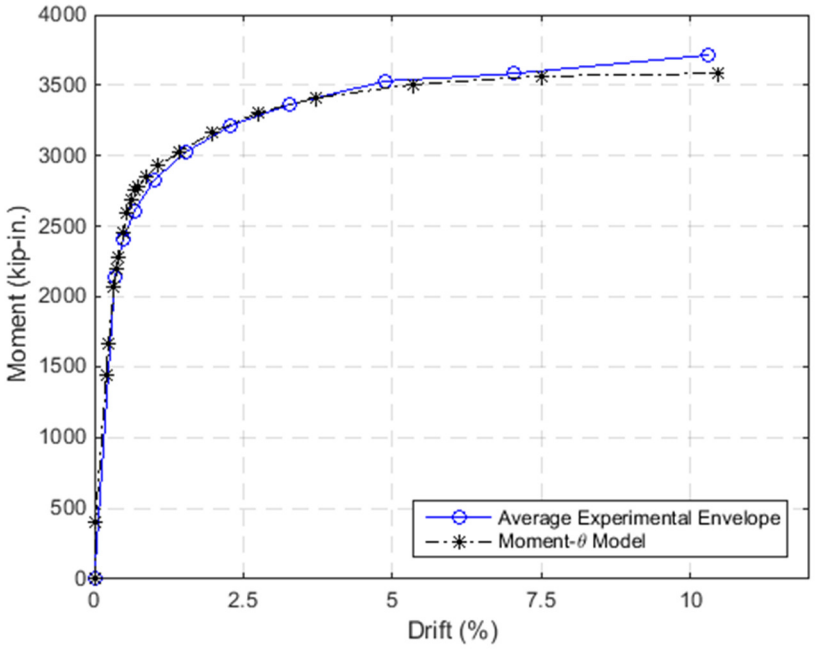

Figure 7.7 Comparison of moment-rotation model to experimental strength envelope.

The model produced a good fit to the experimental envelope. It closely followed the initial system stiffness, transition, and post-decompression stiffness. The model predicted a peak moment of 3585 kip-in., whereas an average of 3715 kip-in. was measured during the experiment. A full summary of the modeled strength results can be found in Table 7.5.

However, the model output a stiffer response during the transition from pre- to post-decompression stiffness. That is, the model predicted a sharper "knee" between the linear responses. This could be due to several reasons:

- Bar/strand slip was not considered in the model, which would have made the joint more flexible.
- The Mander model maintained a relatively high stiffness on the path to the peak compressive strength. If a model with a lower transitional stiffness on the way to peak strength had been used, then the required bearing area would be increased during the transition, and moment contributions decreased (because the neutral axis would be nearer to the center of the cross-section).
- The stiffness used to predict bending deformation, $k'_{eff,y}$, could have been too large (this was concluded in Section 7.1.2).

Furthermore, it is noted that at the peak moment/drift result, no bars had broken in the moment-rotation model. Conversely, the peak, experimental strength occurred after the north-

most bar had fractured. This was probably because cyclic loading effects were not considered in the moment-drift program.

7.4.1.6.2 Neutral Axis Location

The neutral axis location, *c*, is plotted against the experimental envelope in Figure 7.8. The model also produced good results here, and showed that the neutral axis shifted from near the center of the cross-section at low drifts, to about 2.5 in. at higher drifts. However, the grout pad's Mander parameters were selected in order to give this result, so such a conclusion would be circular.

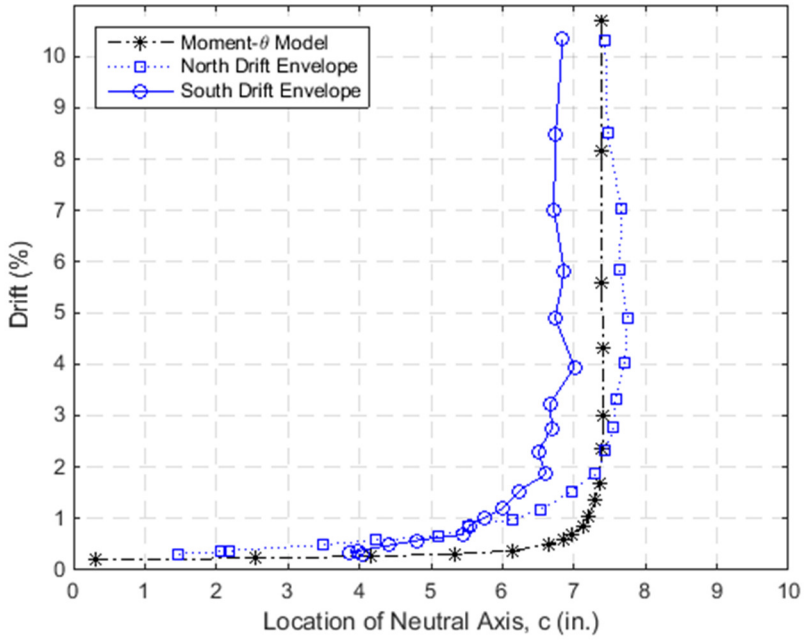

Figure 7.8 Comparison between the moment-rotation model and the experimental response for the neutral axis location.

However, these results also showed too sharp a transition between the primary and secondary responses. It can be observed that the moment-rotation model's relation between neutral axis location and drift had a very similar shape as the Mander model used in this analysis. Therefore, if a confined concrete model with a lower transitional stiffness to peak compressive stress had been used, the moment-rotation program may have given better results for the transition between low and high drifts.

7.4.1.6.3 Resultant Factor, η

The location of the compressive resultant force was also determined from the moment-rotation program. This quantity was not measured during the test, but the results that are presented here were used in the data analysis of Section 6.11.

In order to complete that analysis, a factor relating the location of the compressive resultant to the depth of the compression zone was required. It was similar to the k_2 parameter given in other texts (e.g., Wight and MacGregor), but was instead defined by the resultant's distance to the neutral axis, as opposed to the compression face.

The factor was numerically determined from the moment-rotation model with Equation 7.31, which is essentially a center-of-mass calculation. Figure 7.9 shows the moment-rotation program's output for the relevant compressive parameters.

$$\eta = \frac{\sum F_i(d_i - c) \Big/ \sum F_i}{(10 - c)}$$ **Equation 7.31**

Where:

η	-	factor relating the location of the compressive resultant to the depth of the compression zone (10 in. - c)
F_i	-	the force of an individual grout pad slice.
$(d_i - c)$	-	the lever arm of a discretized grout pad slice to the neutral axis depth
$(10 - c)$	-	the depth of the compression zone for the 10 in. radius grout pad

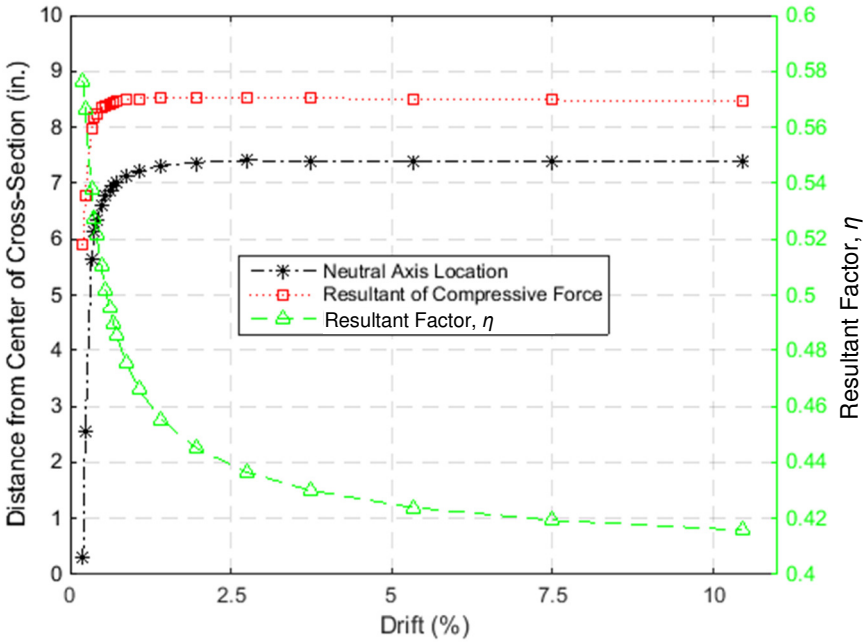

Figure 7.9 The modeled neutral axis location, compressive resultant location, and factor relating the two, as a function of drift.

7.4.1.6.4 Element Moment Contributions

The forces of the reinforcing elements and the axial load were then multiplied by their distances to the compressive resultant. This operation isolated the moment contribution of the individual elements. This procedure was used to approximate the moment contributions of the experimental test results (see Section 6.11); the results from the moment-rotation program are presented here.

Figure 7.10 gives the total moment of each element type (strands, bars, or axial load), and Figure 7.11 gives the percentage contribution of each element to the total moment of the joint.

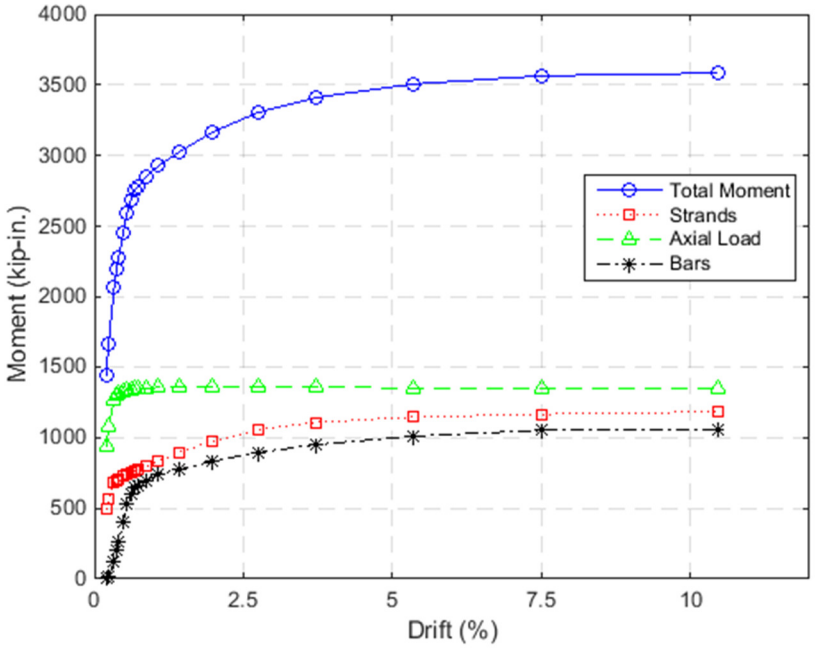

Figure 7.10 The total, internal moments of the reinforcing elements and axial load, as a function of drift.

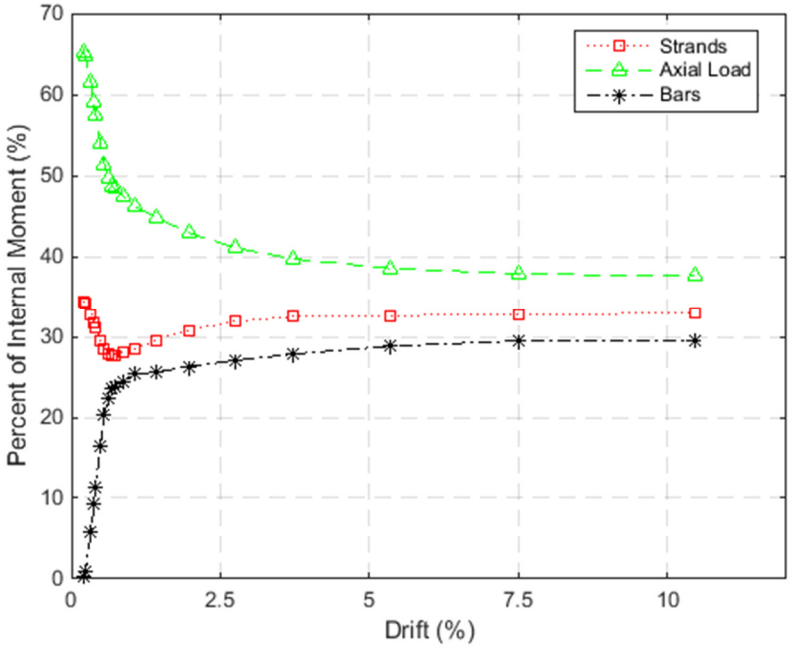

Figure 7.11 The percentage contribution to the total moment, as a function of drift.

The modeling results can be readily explained. When the rocking joint first opened at low drifts, the rebars would not be activated because of their 12 in. debonding (that is, the gap needed to open before the rebars became significantly stressed). The strands, on the other hand, were prestressed and therefore immediately produced a resistive moment to small rotations of the

baseplate. And at lower drifts, the applied axial load was the largest force on the cross-section (1.89 times the effective prestressing force), and it had a similar moment arm as the other elements. Therefore, the applied load made the largest resisting moment at low drifts.

As the specimen response transitioned to higher drifts, however, the relative contributions changed. The axial load was constant, and once the neutral axis settled on ~7.5 in. away from the midsection, the resistive moment due to the axial load became relatively constant. Similarly, the strands approached a near-constant moment contribution, as they had a relatively flat yield plateau in their constitutive response. However, once the rocking gap opened, the rebars became elongated and strain hardened; and gave a larger proportion of the resistive moment for higher drifts.

Davis initially developed the PreT- design so that ~40% of the reinforcing strength came from the bars, and ~60% came from the strands. However, the moment-rotation program indicated that the reinforcing strengths were nearly the same for higher drifts (each at ~30% of the total); but for lower column displacements (<0.75% drift), the rebars did not contribute to the strength. The difference for low drifts was a result of the intentional debonding of the bars at the connection, which was first done by Schaefer et al., (2014a) for the PreT- design. Furthermore, the No. 4 bars used for PreT-CB-ROCK had a nominal, ultimate strength of 107.3 ksi. Davis probably assumed a lower ultimate rebar strength for his design, which explains the difference between the design and modeled ratio in reinforcement strengths.

For comparison, the results of Section 6.11 (the experimental analysis of the moment contributions) have been reproduced in Figure 7.12. The positive envelope (the first and second cycles of each set in the south direction) is shown in the figure.

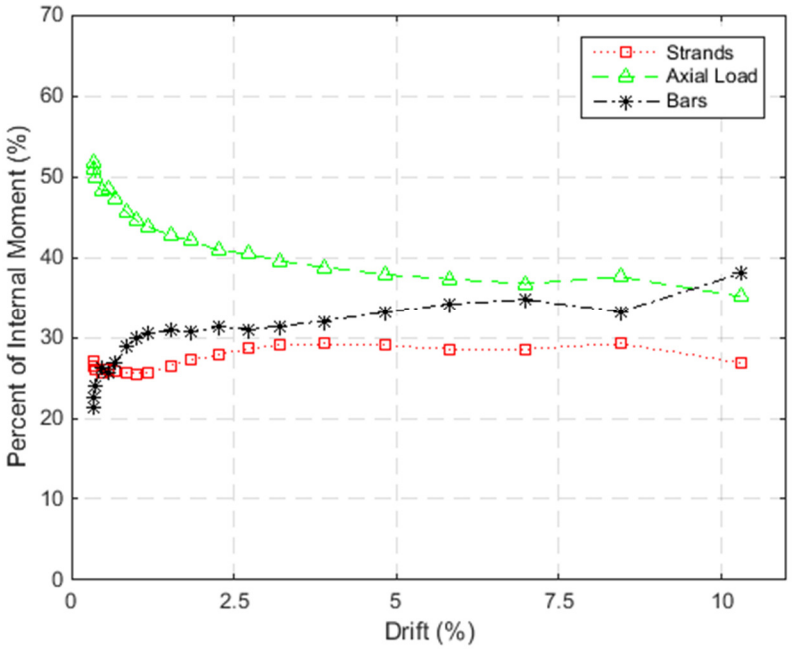

Figure 7.12 The moment contributions resulting from the experimental analysis, reproduced here for comparison to the moment-rotation results.

Similar trends resulted from the experimental envelope:

- At low drifts, the axial load is the largest contributor to the resistive moment, while the rebars appear to have given a relatively low contribution to the strength.
- At higher drifts, the strength contributions approached constant values; the rebars and strands gave roughly equal percentages of the internal, resistive moment.

7.4.2 Two-Dimensional Finite Element Analysis

A finite element analysis was completed in the commercial software program Abaqus CAE 6.13-4 in order to model PreT-CB-ROCK's response. The model was simplified in order to produce results for the full drift spectrum of the test.

The entire model, with gross dimensions, is shown in Figure 7.13. A detail of the rocking connection is shown in Figure 7.14. Table 7.4 gives the numerical coding for these figures. The model geometry was also a two-dimensional projection of the specimen, in the same manner as the previously discussed moment-rotation model. The components and geometry followed the design specimen, but the following elements were not considered:

- the dowel bar and housing fixture,
- the cap beam base,
- and the No. 6 discontinuous bars.

More detailed descriptions of the parts, sections, meshing, and assembly of the model follow.

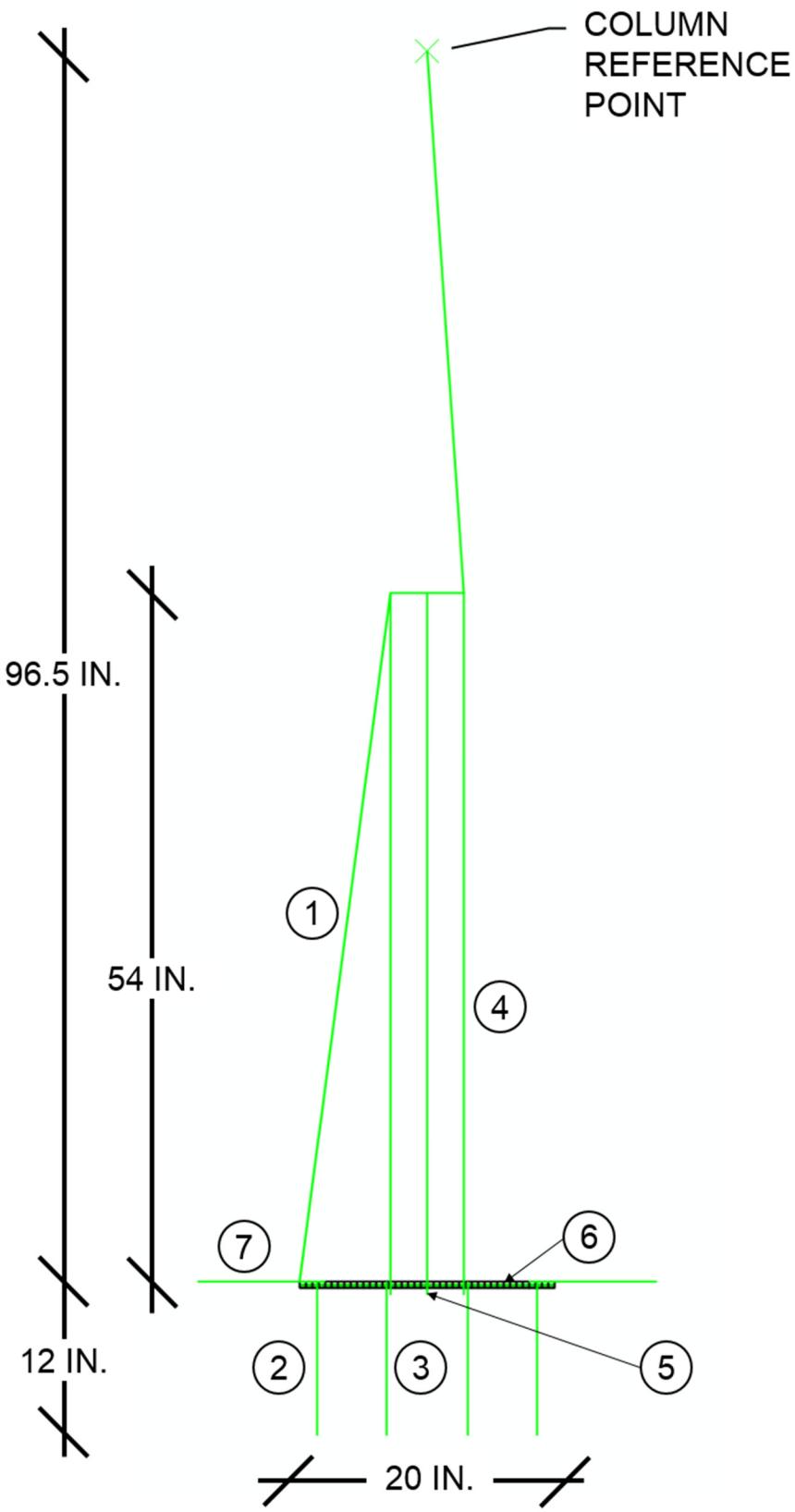

Figure 7.13 The entire two-dimensional assembly used in the finite element model.

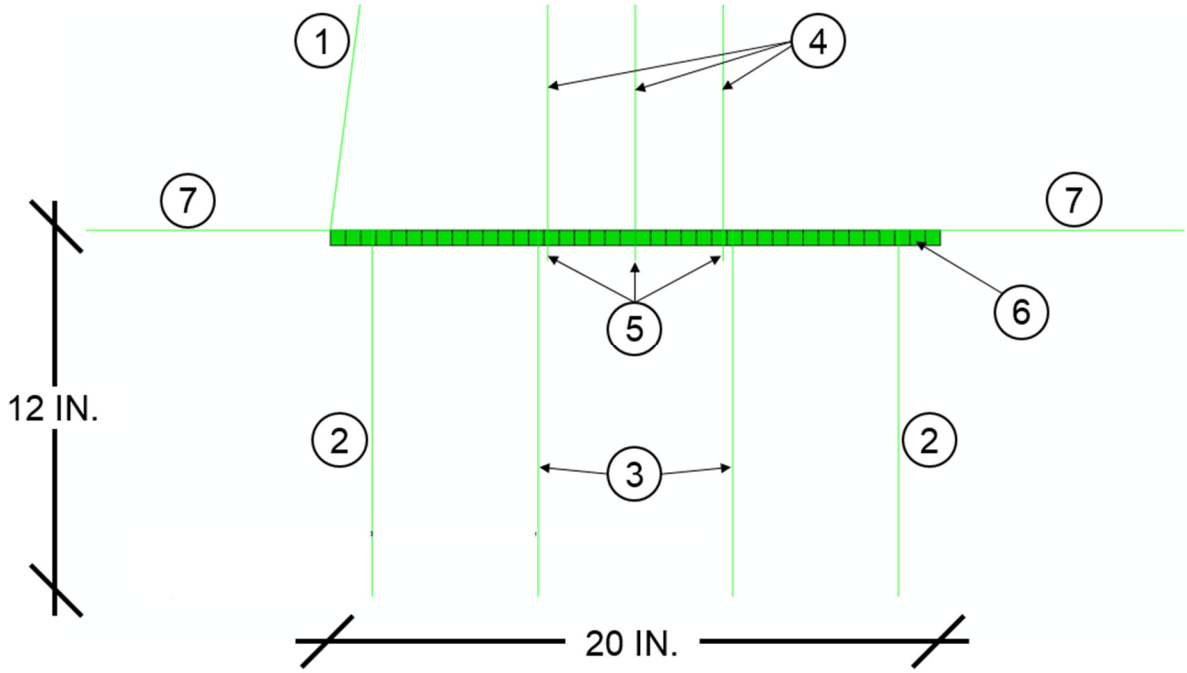

Figure 7.14 Detail of rocking connection elements in finite element model.

Table 7.4 Number coding of elements in the assembly figures.

Number in Figure 7.13 and Figure 7.14	Specimen Component	Modeled As	Number Used in finite element model.
1	Top bearing fixture, pre-tensioned column, and rocking detail (confining tube and baseplate)	Analytical rigid, 2D wire element	1
2	North-most and south-most No. 4 reinforcing bars	12 in. long truss elements	2
3	The NE/NW and SE/SW pairs of No. 4 reinforcing bars	12 in. long truss elements	2
4	The NE/NW, E/W, and SE/SW pairs of 3/8 in. diameter prestressing strands	54 in. long truss elements	3
5	"Fuse" elements introduced to prevent compressive stresses from developing in the strands	1 in. long, "no compression" truss elements	3
6	Fiber-reinforced grout pad	½ in. wide by ½ in. tall, 2D plane stress elements with out-of-plane thicknesses corresponding to their distance from the midsection	20
7	Elements introduced to generate the horizontal reaction at the joint, which simplified the contact algorithm used between the grout pad and column elements	10 in. long, "no tension" elements	2

7.4.2.1 Model Components

7.4.2.1.1 Column

Every specimen component above the rocking interface was effectively modeled with a single, analytical rigid, 2D wire element. The coordinates of this wire corresponded with the other elements of the model. That is, the "base" of the element was a 20 in. long, horizontal segment to represent the baseplate, it then made a horizontal plateau 54 in. above the base in order to anchor the tops of the strands, and it then terminated 96.5 in. above the base, which was the elevation of the vertical load from the Baldwin during the experimental testing.

Being a ridged, non-deformable body, this element did not require material definition.

The element was not directly assigned boundary conditions. The truss elements that connected to the column produced the reaction forces for the analysis. Finally, the top of this element served as the reference point for the entire model. The vertical load and horizontal cyclic

displacements were applied there, and force and displacement were recorded at the node in order to generate moment-drift responses.

7.4.2.1.2 Rebars

The rebars were modeled with single, 12 in. long, truss elements. The elements were assigned either 0.2 in.^{2} or 0.4 in.^{2} areas, depending on if they represented a single rebar on the cross-section or a pair of bars.

The elastic and plasticity settings of Abaqus were used to define the material response of the rebar. One hundred ordered pairs of stress versus strain were generated with the constitutive model used for the moment-rotation analysis (see Section 7.4.1.2); the post-yield material response was then isolated in order to define the steel's plasticity. However, Abaqus CAE uses true stress and true strain for input/output (as opposed to nominal or engineering values). Therefore, the plastic response was input as ordered pairs of true stress and plastic true strain, calculated by Equation 7.32 through Equation 7.34 (e.g., Dassault, 2012). The elastic modulus was defined with Equation 7.35, and the Poisson's ratio was set to 0.30.

$$\varepsilon_{true} = \ln(1 + \varepsilon_{nom}) \quad \textbf{Equation 7.32}$$

$$\varepsilon_{plastic,true} = \varepsilon_{y,true} - \varepsilon_{true} \quad \textbf{Equation 7.33}$$

$$\sigma_{true} = \sigma_{nom} * (1 + \varepsilon_{nom}) \quad \textbf{Equation 7.34}$$

$$E_{true} = {}^{\sigma_{y,true}}/_{\varepsilon_{y,true}} \quad \textbf{Equation 7.35}$$

The bottom nodes of the rebar elements were set as pins, and the top nodes were connected to the column element with tie constraints.

7.4.2.1.3 Strands and Fuses

The measured response and the data analysis indicated that the strands buckled during the cyclic loading of the column. Such behavior (tensile plasticity and zero compression capacity) is not readily modeled in Abaqus CAE. The program's material plasticity feature and no-compression/tension settings cannot be used together. Therefore, a scheme was developed to model the tensile yielding/compression buckling response of the strands. For a particular strand, one 54 in. long element was used to model the full tension response. This element was connected to a 1 in. long "fuse" to prevent the strand from going into compression.

The elastic-plastic response for the 54 in. long segments was defined in the same manner as prescribed for the rebar. However, the no-compression setting cannot be used with the plasticity setting in Abaqus CAE. Therefore, the fuse element was set to a no-compression, elastic material with a modulus of 10000 ksi. Both materials were assigned a Poisson's ratio of 0.30.

The 54 in. long elements were each assigned a cross-sectional area of 0.17 in.^{2} (which corresponded to two strands). The fuses were assigned areas of 10 in.^{2}, which made them effectively rigid when compared to the strands.

Tie constraints were used to connect the tops of the strands to the plateau formed by the rigid column element. The node that connected each strand portion with its fuse was assigned a

horizontal reaction in order to keep the node stable. The bottom node of the fuse was given vertical and horizontal reactions.

With this approach, a tensile force could be transmitted from the reaction node to the 54 in. long element, but not compressive forces. It is possible that the fuse elements could have been further calibrated to model the slip of the strands.

7.4.2.1.4 Horizontal Reaction Elements

The reaction elements at the base of the column were introduced in order to simplify the contact algorithm between the pad and the baseplate. Instead of the horizontal reaction being accommodated through friction between the pad and column, discrete forces went through these elements to reaction nodes. This simplified the contact algorithm between the pad and column, and improved the efficiency of the analysis.

The elements were 10 in. long and assigned cross-sectional areas of 2 $in.^2$.

The modulus of elasticity was set to 6000 ksi, and the Poisson's ratio to 0.30. Coupled with their 10 in. lengths and 2 $in.^2$ cross-sectional areas, the reaction elements had an axial stiffness of 1200 kip/inch. For the maximum measured effective force of ~60 kips, this would produce an equivalent contact "slip" of 0.05 in., which was judged to be appropriate. Furthermore, the reaction material was set to "no-tension". With this setting, a particular reaction element only became activated when the column rocked on its side of the connection.

Finally, the outer node of each reaction element was pinned (to provide the horizontal reaction for the joint), and the inner node was connected to the base of the rigid column element with a tie constraint. The tie nodes were set 2 in. inside the north/south edges of the rigid element, which was the estimated center of contact area between the pad and baseplate.

7.4.2.1.5 Grout Pad

The grout pad was discretized into twenty parts, which were assigned out-of-plane thicknesses that corresponded to their distance from the center of the cross-section. This was the nearly same discretization scheme that was used for the moment-rotation analysis (see Section 7.4.2.1.5). Here, however, there were only ten slices in either direction (as opposed to 1000). Therefore, the each part was assigned an out-of-plane thicknesses gave the equal, segmental bearing area for the respective one inch width on the circular cross-section.

The twenty parts were then meshed as ½ in. wide by ½ in. tall, 2D, plane stress elements (forty in total).

The material for the grout pad was defined in the same manner as used for the reinforcing steel, as opposed to a concrete damaged plasticity model. Therefore, the grout material in the analysis was technically a ductile material with equal compressive and tension responses. This was done to simplify the model, and it was assumed that it would have no effect on the results (i.e., tension stresses within the pad were assumed to be small). A Poisson's ratio of 0.20 was assigned to the grout material. Finally, the Abaqus defaults were selected for the transformation of the inputted uniaxial stress-strain data to a biaxial material response for the plane stress grout pad elements.

The bottom nodes of the grout pad elements were assigned pin boundary conditions. Interaction between the column and pad was modeled with frictionless, hard contact, with separation allowed. The column was set to the master surface, as it was the more rigid element.

7.4.2.2 Loads and Steps

7.4.2.2.1 Prestressing

In the first step of the analysis, the bottom nodes of the strand fuse elements were displaced downward so that the effective prestressing tension of 165 ksi would be produced in each strand.

The non-linear geometry setting was activated for this step, and remained on for the duration of the analysis.

7.4.2.2.2 Axial Load

A 159 kip, downward force was then applied to the top reference point of the column.

7.4.2.2.3 Forced Displacements

The top reference point was cyclically displaced in the horizontal direction in order to model the applied drift spectrum of the test. Only the second cycle of each set was used for this finite element analysis.

The vertical displacement of the top reference point was not constrained. Such a boundary condition may have been more representative of the actual test setup. However, because the column in the assembly was set as a rigid element, and therefore had no axial flexibility, it would have deformed the grout pad elements to near-zero and negative volumes.

7.4.2.3 Results

The analysis failed during the Set 10-Cycle 2 return from peak drift. That is, the analysis failed to converge as the column was being returned from +10.65% drift to 0% drift. However, the analysis otherwise produced good results, and seemed to capture the observed rocking behavior of the specimen, as shown in Figure 7.15.

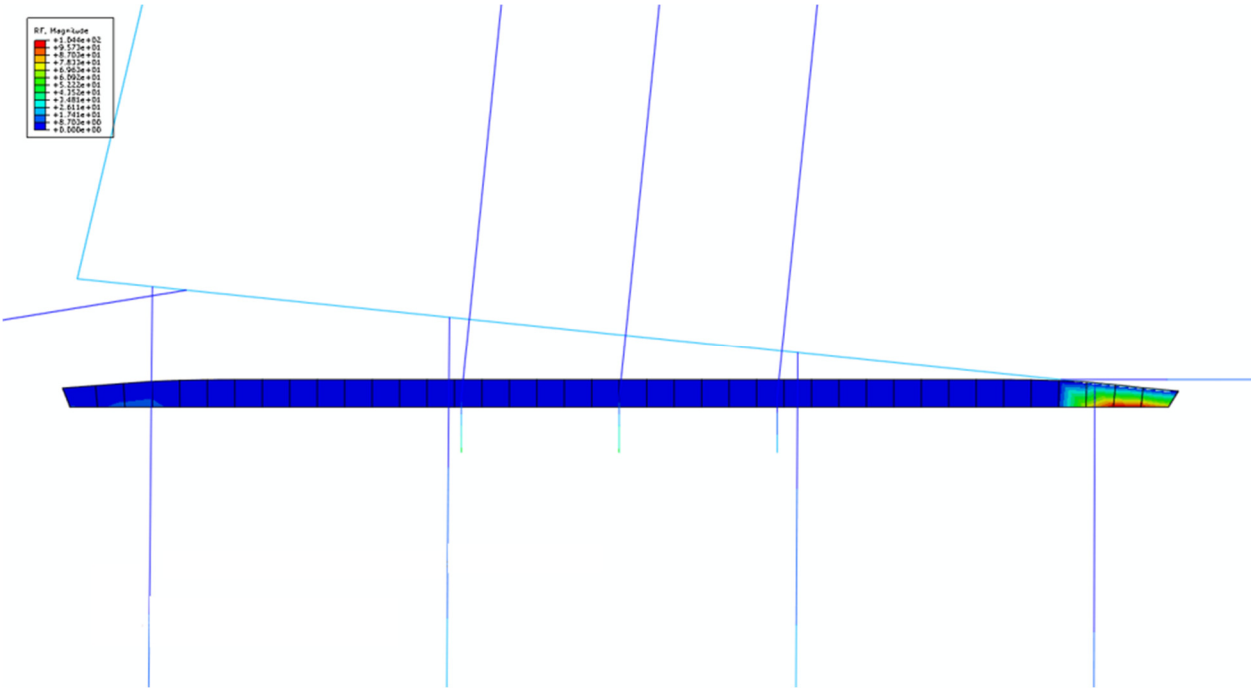

Figure 7.15 The assembly behaved in a rocking manner. The figure shows the connection at +10.65% drift; the reaction magnitude was selected in the output viewer.

7.4.2.3.1 Moment Strength Hysteresis

The model gave similar strength results to the measured moment-drift response. The applied moment was calculated in the same manner as for the experimental response, described in Section 5.2. However, the model's h_1 height was 96.5 in., as opposed to 60 inches. The full finite element analysis results are plotted against the second cycles of the experimental response in Figure 7.16.

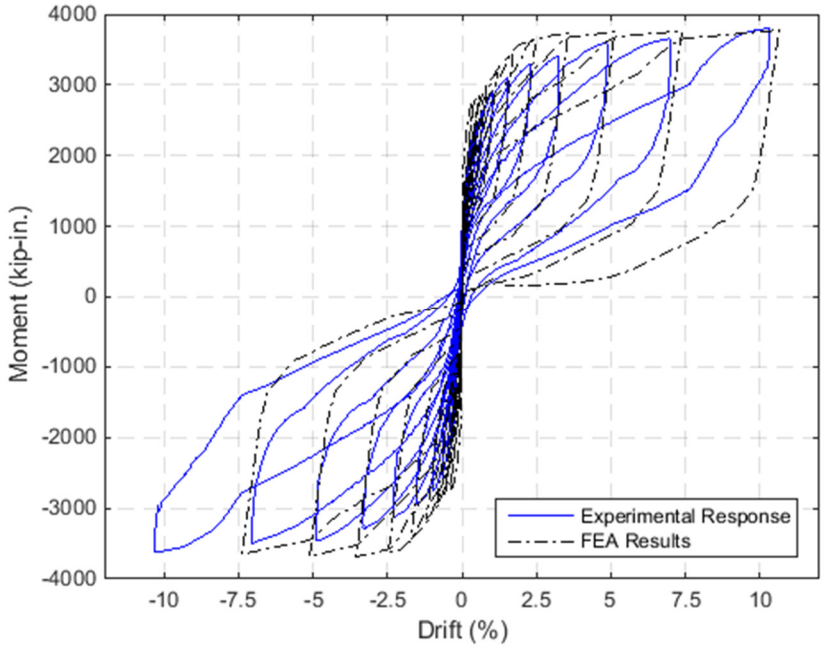

Figure 7.16 Moment vs. drift for the experimental response and the finite element analysis, the second cycles of each set are plotted from the measured response.

The modeled column exhibited essentially perfect re-centering, which was similar to the experimental column. For higher drifts, the finite element analysis gave a similar strength envelope and post-decompression stiffness.

However, the individual flags of the modeled response had far larger areas than for the measured one. Only the second cycle of each set was used for the analysis, which probably led to this discrepancy in energy dissipation. That is, the specimen had been pushed to four cycles in each set, thereby degrading the rebars more quickly than for the analysis.

Additionally, the analysis output far stiffer results than what was measured. The following explanations are offered:

- The FEA column was modeled as a rigid element, and therefore had no bending deformation.
- Bar/strand slip was not considered in the analysis, which could have decreased the transitional stiffness of the joint.
- The material selection for the grout pad may have been too stiff, which was also indicated in the moment-rotation model.
- The cap beam base was not included in the analysis, which may have lent a flexibility to the overall system, which would have been most significant at lower column drifts.

Furthermore, it is noted that element deletion was not included in the finite element model, and that all six rebars were intact for the entire analysis.

7.4.2.3.2 Neutral Axis Location

The neutral axis location was calculated in the same manner as Section 6.9. Here, however, the displacements of the north/south edges of the column base were used directly, as opposed to the offset tube potentiometers on the north, east, and west faces of the column. Figure 7.17 shows the results from the finite element analysis, plotted against the experimental envelope values for the neutral axis.

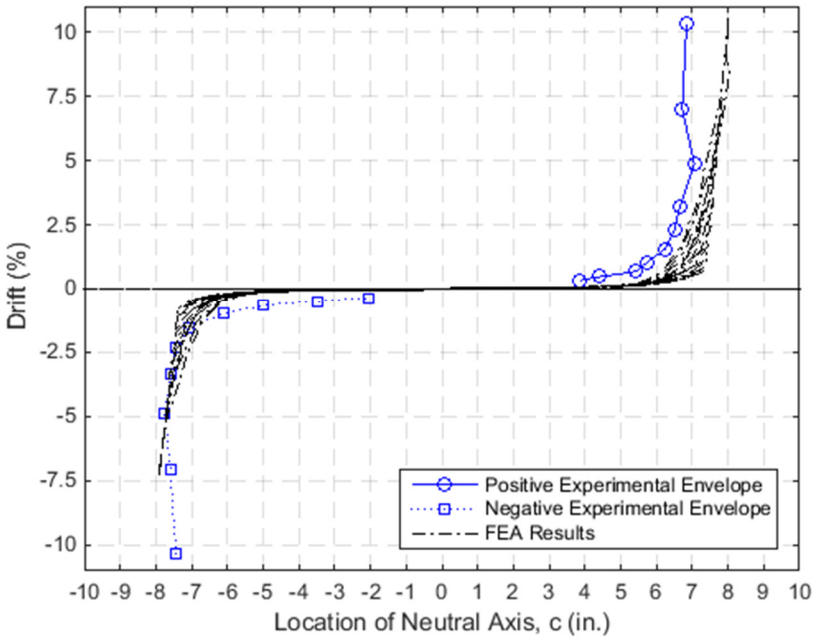

Figure 7.17 The neutral axis location vs. drift for the finite element analysis.

The modeled response was similar to the measured one. However, the neutral axis appears to have shifted too quickly to the constant neutral axis location of ±7.5-8.0 inches. This may have resulted from bar slip not being considered in the FEA. Or, the Mander model may have been too stiff during its transition from small to large axial strains (that is, it approached the peak strength at strains <1/10th specified).

7.4.2.3.3 Strand Response

The stress and strain results for the NE/NW strand element have been shown here to assess the model and for comparison to the experimental response. Figure 7.18 shows the element's strain versus drift; an assumed yield strain is shown with a dashed red line (0.0091 in./in. for the Abaqus material model); the strain gauge measurements from the NW strand are also shown for comparison. Figure 7.19 shows the NE/NW strand element's stress versus drift; the cyclic stress analysis for the NW strand is also shown for comparison.

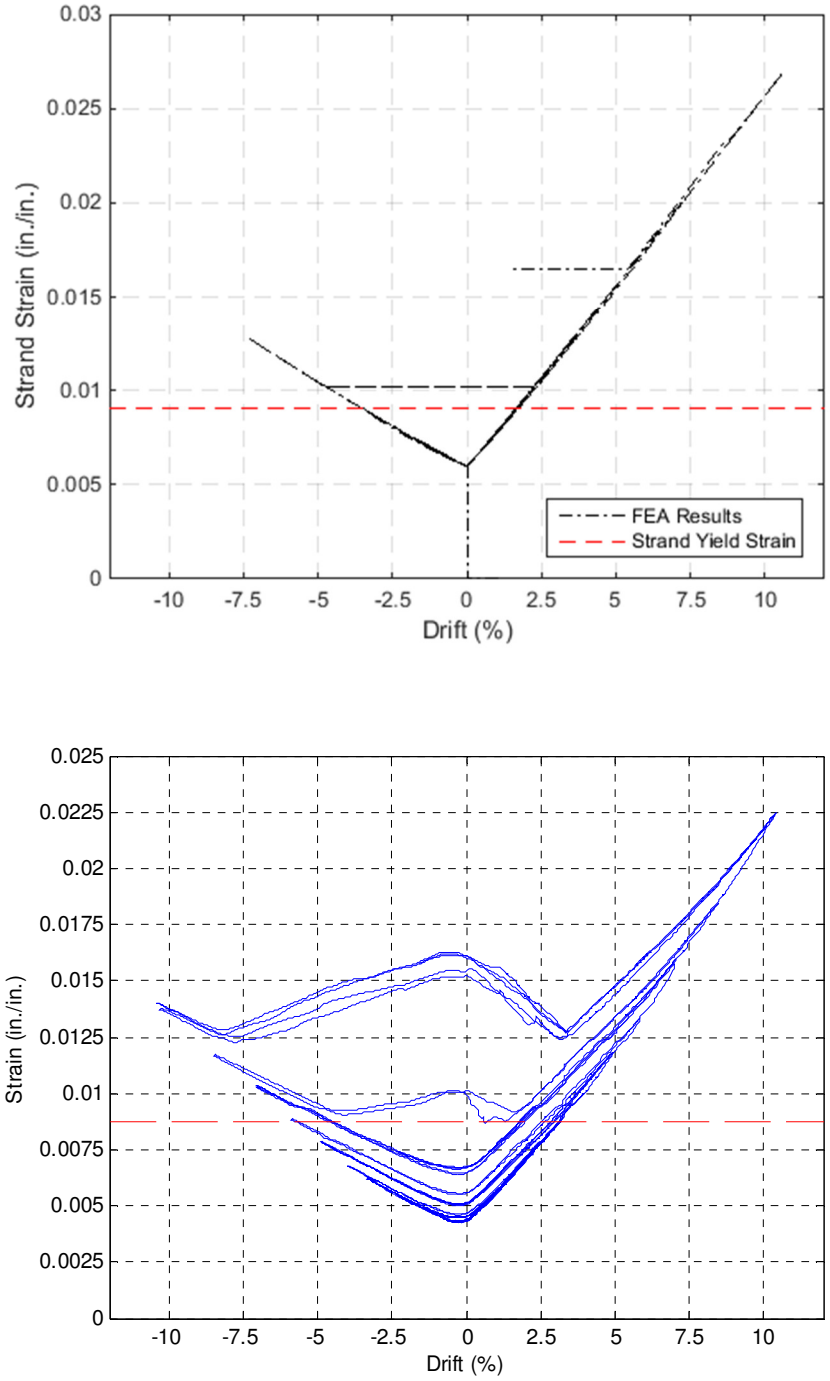

Figure 7.18 The strain vs. drift response for the NE/NW strand of the FEA model (top), and the experimental measurements of the NW strand (bottom).

The modeled strain response had a similar bilinear shape as the experimental ones examined in Section 5.12.1.1. However, the corresponding specimen strands did not yield until ~2.5% drift, but the FEA model predicted yield at ~1.5% drift. Furthermore, the peak modeled strain was 0.0270 in./in., whereas the experimental maxes for the NE/NW strands were ~0.022 in./in.. These differences were likely due to the slip of the strands in the specimen, which was not

considered for the FEA model. That is, as the strands slipped during the cyclic testing, they presumably lost prestressing strain. Therefore, the experimental strand strains would have been lower than for a perfectly bonded strand.

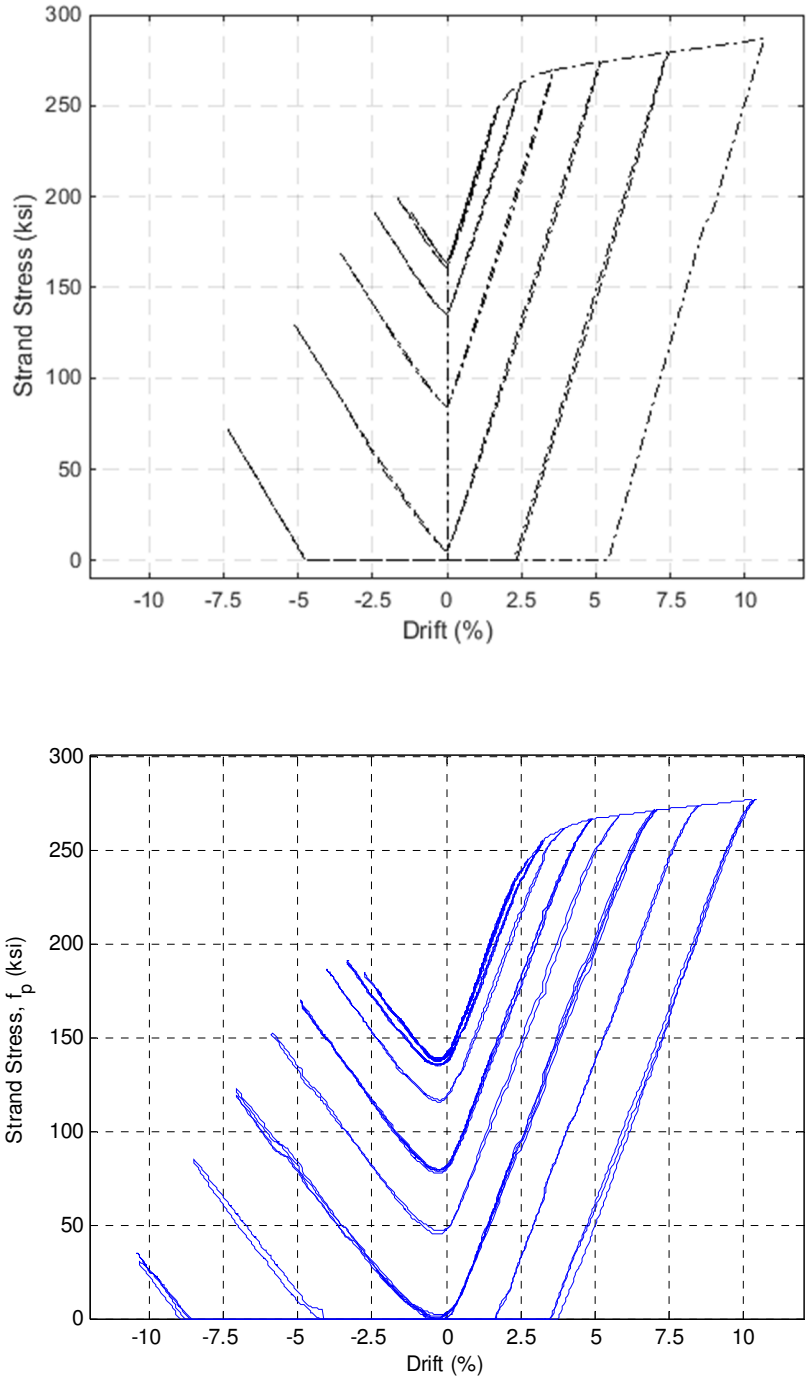

Figure 7.19 The stress vs. drift response for the NE/NW strand of the FEA model (top), and the stress analysis results for the NW strand (bottom).

The modeled response for strand stress was very similar to that for the experimental analysis given in Section 6.7.2. In particular, the FEA model predicted transitions from tension to compression stress, but the fuse elements prevented the strands from actually taking on compressive loads. This modeling result supported the theory of strand buckling during the test. However, the model predicted first buckling after the seventh cycle (drift ratio of 7.40%), whereas the strand strain gauge data suggested buckling after higher drift ratios. This discrepancy was also likely due to the slipping of the strands in the specimen, which was not considered for the finite element model.

7.4.2.3.4 Residual Grout Pad Rounding

The rounding of the grout pad edges was also captured by the FEA model. Figure 7.20 shows the grout pad elements during the last iteration of the analysis, when convergence failed and the analysis stopped. The figure shows the contours for vertical displacement.

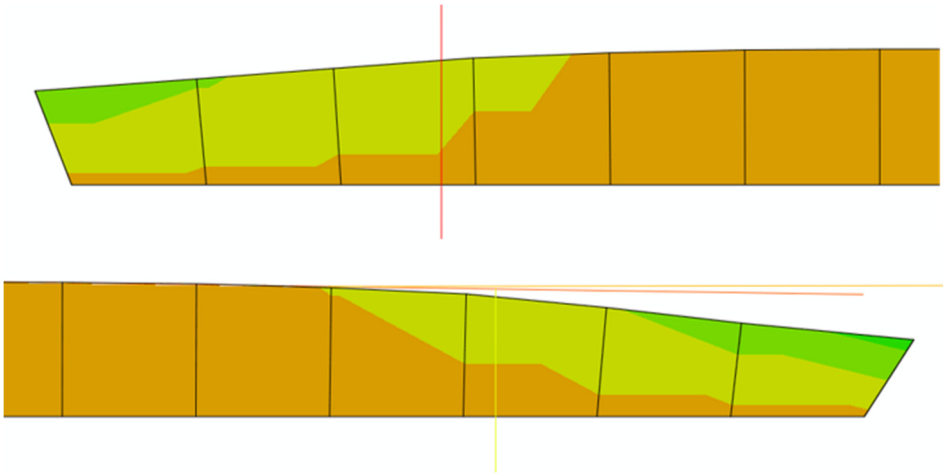

Figure 7.20 The permanent compression of the grout pad elements; vertical displacement contours are shown.

Figure 7.21 shows the residual gap (converted to millimeters) between the column base and grout pad, as a function of drift. For comparison, it includes the physical measurements from the experimental test. On the plot, the final data point is the gap at the south face of the column; all other data points are the average between the north and south faces.

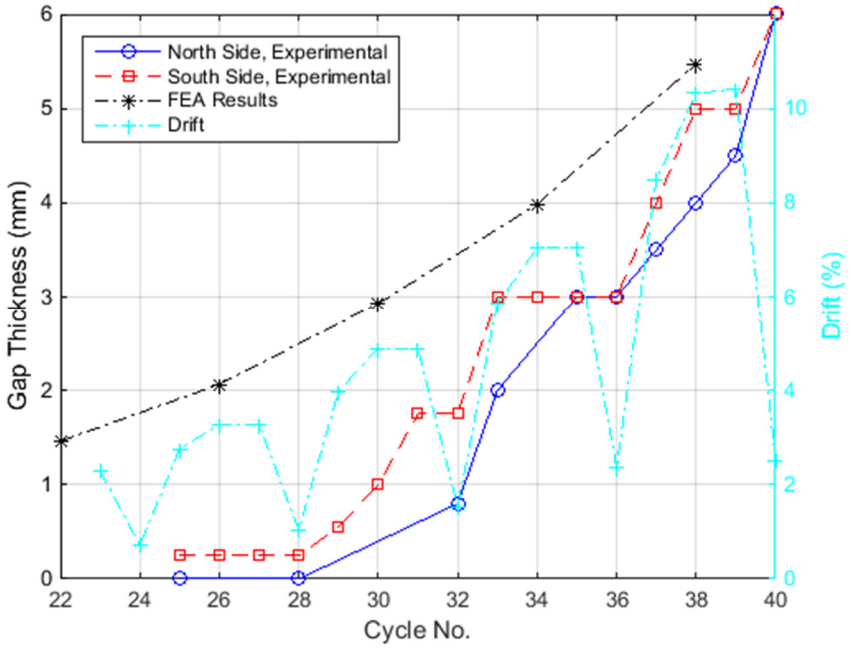

Figure 7.21 The residual gap between the column base and the grout pad.

When the analysis failed at the cycle 10 transition from positive to negative drift, the gap on the south face of the column was 5.47 mm and the gap on the north side was 3.95 mm. These results roughly coincided with the observed gaps of 6 mm at the end of the experimental test.

7.4.3 Summary of Flexural Modeling

Table 7.5 provides a summary of the predicted and measured peak moment strengths for PreT-CB-ROCK. The results showed that the two flexural models predicted very similar strengths to the experimental specimen.

Table 7.5 Comparison of experimental and moment-rotation strength results.

Measured/Modeled Strength	**Comparison Strength** (corresponding drift)	**Ratio** (Model : Experimental)
Experimental - South Direction	+3802 kip-in. (+10.33%)	-
Experimental - North Direction	– 3628 kip in. at Set 10-Cycle 2 (-10.30%), -3510 kip-in. at Set 9 – Cycle 2 (-7.01%)	-
Experimental - Average	3715 kip-in.	-
Moment-Rotation Model	3585 kip-in. (10.68%)	0.965 (compared to average)
FEA – South Direction	+3775 kip-in. (+10.65%)	0.993
FEA – North Direction	-3682 kip-in. (-7.40%)	1.05 (compared to Set 9 – Cycle 2)

It is noted that the minimum strength for the FEA analysis corresponded to -7.40% drift (the analysis failed before the north drift of the final cycle). However, the envelope showed that the post-secondary stiffness of the model was close to zero. Therefore, that result was assumed to be indicative of the model's peak strength in the north direction.

7.5 COMPARISON WITH DAMAGE PROGRESSION MODELS

The damage to PreT-CB-ROCK was primarily cosmetic (with the exception of rebar fracture at large drifts). However, previous researchers of precast, pre-tensioned systems have compared their observed damage to the predictive damage progression models of Berry et al., (2004 and 2005). These models were developed and calibrated for conventional, cast-in-place, reinforced concrete columns. Davis et al. (2012) and Finnsson (2013) compared the model's prediction for the onset of spalling, bar buckling, and bar fracture. The model's equations for these damage states are given in Equation 7.36 through Equation 7.38.

Spalling: $$\frac{\Delta_{calc,sp}}{h_1}[\%] = 1.6 \cdot \left(1 - \frac{P_{total}}{A_g \cdot f_c}\right)\left(1 + \frac{h_1}{10D}\right) \quad \textbf{Equation 7.36}$$

Bar buckling: $$\frac{\Delta_{calc,bb}}{h_1}[\%] = 3.25 \cdot \left(1 + 150 \cdot \rho_{eff} \cdot \frac{d_b}{D}\right)\left(1 - \frac{P_{total}}{A_g \cdot f_c}\right)\left(1 + \frac{h_1}{10D}\right) \quad \textbf{Equation 7.37}$$

Bar fracture: $$\frac{\Delta_{calc,bf}}{h_1}[\%] = 3.5 \cdot \left(1 + 150 \cdot \rho_{eff} \cdot \frac{d_b}{D}\right)\left(1 - \frac{P_{total}}{A_g \cdot f_c}\right)\left(1 + \frac{h_1}{10D}\right)$$ **Equation 7.38**

Where the variables are defined as:

- P_{total} – axial load (including the total prestressing force)
- A_g – the gross area of the column cross-section
- f_c – the concrete compressive strength
- h_1 – the distance between the connection interface and the centroid of the horizontal actuator
- D – the column diameter
- $\rho_{eff} = {\rho_s f_{yt}}/{f_c}$ - the effective transverse reinforcing ratio
  - ρ_s – volumetric spiral reinforcing ratio, as defined by *ACI 318-11*
  - f_{yt} – the yield stress of the spiral
- d_b – the longitudinal bar diameter

Equation 7.36 to Equation 7.38 were evaluated for the PreT-CB-ROCK design. The models were developed without consideration of prestressing in the column. Therefore, the prestressing force of the experimental specimen was added to the axial load term, "P_{total}", which was consistent with Davis's and Finnsson's formulation. However, the prestressing load varied as the strands were cyclically strained. Therefore, the damage progression calculations were completed separately for the initial prestressing force, and for the yield prestressing force. Furthermore, the presence of the steel tube at the base of the column was not included in the ρ_{eff} term of the calculations (only the volume of spiral was considered).

Table 7.6 compares the damage model's predictions for spalling, bar buckling, and bar fracture to damage observations made during tests. It is noted that the model outputs the first drift at which a specified damage state would be reached.

Table 7.6 Comparison of predicted versus observed damage states for initial prestressing force.

Specimen	**PreT-CB-CONC**			**PreT-CB-ROCK**			**PreT-SF-ROCK**		
Drift Ratio (%)	*Model*	*Obs.*	*Obs./ Model*	*Model*	*Obs.*	*Obs./ Model*	*Model*	*Obs.*	*Obs./ Model*
Spalling	1.88	1.11	0.59	1.92	N/A	N/A	1.93	N/A	N/A
Bar Buckling	5.00	3.20	0.64	4.87	N/A	N/A	4.67	N/A	N/A
Bar Fracture	5.35	3.95	0.73	5.26	7.05	1.34	5.03	5.80	1.15

Table 7.7 also compares the damage model for spalling, bar buckling, and bar fracture to experimental observations. However, the predicted drifts were calculated by assuming the prestressing force to be at its yield force.

Table 7.7 Comparison of predicted versus observed damage states for yield prestressing force.

Specimen	PreT-CB-CONC			PreT-CB-ROCK			PreT-SF-ROCK		
Drift Ratio (%)	*Model*	*Obs.*	*Obs./ Model*	*Model*	*Obs.*	*Obs./ Model*	*Model*	*Obs.*	*Obs./ Model*
Spalling	1.85	1.11	0.60	1.88	N/A	N/A	1.90	N/A	N/A
Bar Buckling	4.88	3.20	0.66	4.81	N/A	N/A	4.60	N/A	N/A
Bar Fracture	5.26	3.95	0.74	5.18	7.05	1.36	4.96	5.80	1.17

Generally speaking, the models have over predicted the durability of the pre-tensioned specimens. That is, the models predict reaching damage states at higher drifts than those observed during testing. However, several key points should be noted:

- The models were calibrated for reinforced concrete columns, and they have been applied without modification to prestressed concrete columns equipped with a steel confining tube.
- The "spalling" that was observed during the rocking specimen tests was cosmetic (caused by the section transition at the top of the steel tube). The "spalling" damage state of the models refers to the loss of cover concrete and the exposure of longitudinal reinforcing – which was not observed in either rocking specimen.
- Essentially, the model begins with a calculation for the "spalling drift", which is then linearly scaled for later damage states (the subsequent equations use the same terms as the initial spalling equation). The drift calculation for "bar fracture" is a scaling of the equation for "bar buckling" (it simply predicts 3.5/3.25 = 1.077 times more drift capacity before fracture). This implies that the bar fracture is directly dependent on, and shortly follows, the "buckling drift". This damage progression, which is typical for traditional reinforced concrete systems, was not observed for the rocking systems because the steel tube maintained the integrity of the column at its base (preventing loss of cover concrete). Therefore, the bar fractures observed during the rocking tests were due to the cyclic elongation of the rebars, not to the progressive loss of cover.
- Available damage progression models do not adequately address the performance and durability of the rocking system, and new damage progression models could be formulated with additional testing data.

7.6 COMPARISON OF DAMPING TO CONVENTIONALLY REINFORCED CONCRETE

It has been suggested (Priestley and Tao, 1993) that, during dynamic loading, unbonded systems will experience larger displacements than regular reinforced concrete systems. The fact that the restoring force of unbonded systems is elastic results in lower energy dissipation. Such

performance can be quantified with the calculation of an equivalent viscous damping coefficient for the cyclic response. These calculated damping coefficients are likely to be lower than for conventional, bonded, reinforced concrete columns. In this section, the peak displacement responses of the hybrid column tested here are compared with the peak predicted displacements of three possible models. The models are the AASHTO Seismic Isolation Specification model, the Priestley-Tao model, and Mole's model.

7.6.1 AASHTO Isolation Specification

AASHTO's Guide Specifications for Seismic Isolation Design (2000) provides an equation that relates the displacement of an elastic system with arbitrary damping to the response with 5% damping. It is based on work by Newmark et al. (1982) for a general elastic system, not necessarily an isolation system, subjected to earthquake loading. It was used here to estimate the increase in peak displacement of an unbonded prestressed concrete column compared with that of a conventional bonded, rebar column. Both systems were treated as elastic systems with damping levels estimated from the values given in Section 6.4. The spectral displacement is given by Equation 7.39.

$$d_{deck} = \frac{10 * A_{accel} * S_{site} * T_{eff}}{B_{damping}} \qquad \textbf{Equation 7.39}$$

Where:

d_{deck}	-	The displacement of the deck (in inches)
A_{accel}	-	A design acceleration coefficient
S_{site}	-	A site coefficient
T_{eff}	-	Period of a seismically isolated structure
$B_{damping}$	-	A constant related to the damping coefficient

The damping constant, $B_{damping}$, is provided by a design table (Table 7.1-1 in the specification). The table gives discrete values for $B_{damping}$ for discrete values of damping. The damping constant increases for increasing levels of damping, and can be approximated with Equation 7.40, a best-fit line for the table values:

$$B_{damping} = 0.64 * \zeta[\%]^{0.29} \qquad \textbf{Equation 7.40}$$

The best fit line is plotted in Figure 7.22, along with the corresponding values of AASHTO Table 7.1-1.

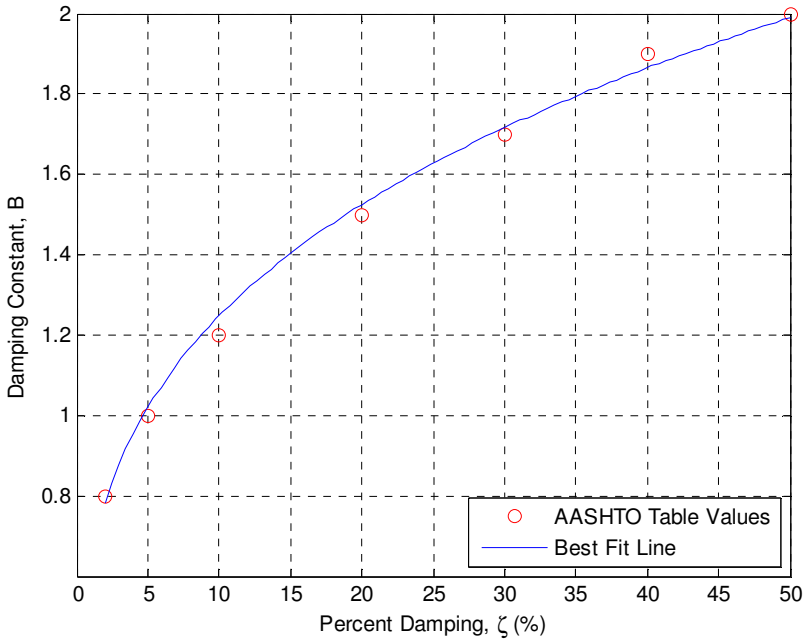

Figure 7.22 Damping constant, $B_{damping}$, as a function of percent damping, ζ, as defined by the AASHTO Isolation Specification.

It leads to prediction of smaller displacements for systems with higher damping. It was used to convert the equivalent viscous damping values shown in Figure 6.17 and Figure 6.18 into drift magnitudes relative to a system with 25% damping. That value was used as an arbitrary datum because it is commonly used to represent the response of reinforced concrete. The results are shown in Figure 7.23. It shows that, for experimental damping levels calculated at 2% drift, both the PCC-SF-THK2 (Haraldsson et al., 2011b) and the more recently tested PreT- specimens would have higher drifts than the hypothetical 25% damped system, and that the displacements of the PreT- systems would be about 1.1 times those of the PCC- specimen tested by Haraldsson. At 4% drift, the ratio would be about 1.2. These results are broadly in agreement with, but slightly lower than, those found by Priestley and Tao (1993).

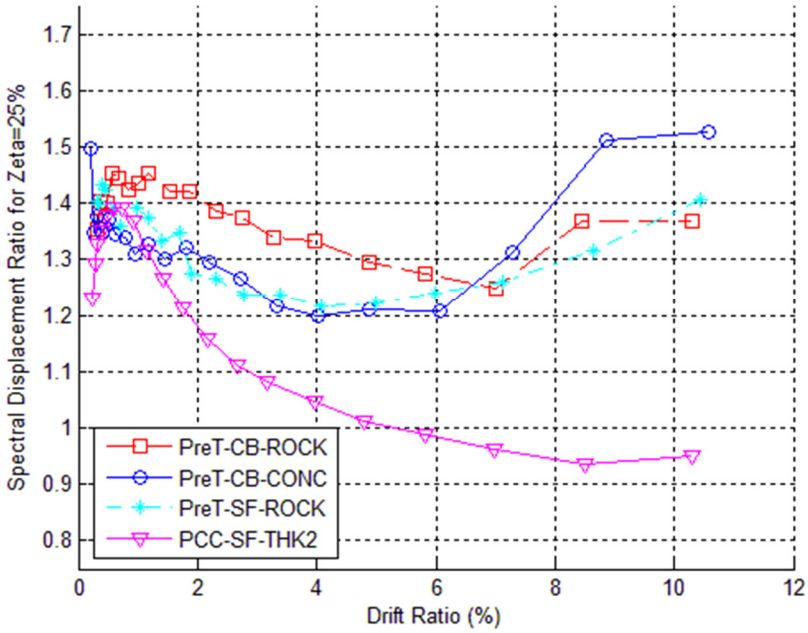

Figure 7.23 Displacements (relative to a 25% damped structure) of test specimens for various drifts according to the AASHTO Isolation Specification.

7.6.2 Nonlinear Dynamic Analyses of Unbonded Systems

Priestley and Tao (1993) investigated the dynamic response of prestressed concrete frames with partially debonded tendons. The design left unbonded tendons crossing the interface between column and beam. Yielding elements, such as conventional rebar, were not used in the connection. Therefore, if the tendons were designed to remain elastic, the connection theoretically offered no energy dissipation. Priestley formulated four force-deflection responses to represent different structural systems:

Linear elastic	-	Baseline response.
Bilinear elastic	-	Unbonded, elastic system with initial stiffness and secondary, decompression stiffness.
Bilinear elasto-plastic	-	Conventional reinforced concrete.
Bilinear degrading	-	Bonded, prestressed system with severe, cyclic, stiffness degradation.

The models were used in nonlinear, single degree of freedom, dynamic analyses. Priestley found that, for typical structural periods, the unbonded model had 38% larger deflections than the corresponding reinforced concrete model (on average). However, Priestley conceded that actual unbonded systems would likely have more than 5% damping assumed in the analyses. It was also acknowledged that the bilinear elasto-plastic response had a more ideal hysteretic response than that of typical reinforced concrete. For these reasons, it was concluded that actual displacement differences between unbonded and monolithic connections was likely less than the 38% model

prediction. Furthermore, the bilinear elastic model represented an unbonded connection as opposed to the hybrid connection of PreT-CB-ROCK (which can dissipate energy through cyclic yielding of longitudinal reinforcement).

Mole (1993) modeled the dynamic behavior of various hybrid connections with inelastic dynamic analyses. He also analyzed elastic and elastic-perfectly-plastic systems in order to compare the performance of the hybrid connections. Mole found that story drifts are only 0.5% larger for building frames with hybrid connections versus conventional reinforced concrete (so long as the hybrid connection is designed for the same strength). Mole found that particular kinds of ground motions most affect hybrid systems, and concluded that hybrid systems were most negatively affected by ground motions that were periodic in nature, and which had periods longer than that of the structure.

7.6.3 Other Considerations

Other general considerations should be noted. Bridge structures are unlikely to behave as single degree of freedom systems. However, the pre-tensioned specimens considered in this thesis were essentially tested in a single degree of freedom configuration. While relatively low levels of energy dissipation (and corresponding damping) were calculated from the PreT-CB-ROCK testing, in the prototype bridge other structural components such as abutments, superstructure elements, and bearings would provide some additional energy dissipation. Additionally, it is generally difficult to predict a full system response from the test properties of a subassembly. That is to say, after a rocking column was connected at both ends into a full bridge bent, a cast-in-place diaphragm poured on top of the bent, longitudinal girders erected, and the system tied into abutments, the system response may differ from the laboratory response of the SDOF column.

8 Summary and Conclusions

8.1 SUMMARY

A cantilever subassembly (PreT-CB-ROCK) was tested in order to evaluate a precast, prestressed column-to-cap beam connection. The design of the specimen was intended to be constructible and to accelerate bridge construction. The specimen represented the top half of a prototype bridge bent, and was tested under a constant vertical load and cyclic lateral displacements. The system's design included unbonded, prestressed tendons in order to re-center the column after a seismic event. Furthermore, the base of the column had a steel tube to provide concrete confinement and a baseplate to permit rocking behavior.

The design and detailing of the specimen was influenced by the findings of previous work at the University of Washington. Davis et al. (2012) tested a prestressed, column-to-cap beam connection that had re-centering behavior, but also experienced significant damage at lower drifts than for comparable reinforced concrete systems. Schaefer et al. (2014a) examined a nearly identical, column-to-footing design that used a similar rocking detail. He observed delayed rebar fracture and cosmetic concrete damage during cyclic loading.

The connection was made by grouting a reduced diameter extension and protruding rebars from the column into ducts that were set into the precast cap beam. The column's longitudinal rebars and prestressing strands were anchored within the depth of the cap beam, which resulted in a hybrid connection. The rebars and strands were intentionally unbonded in order to better distribute cyclic, axial strains along their lengths. The rebars were debonded on the cap beam side of the connection, and the strands were unbonded for a significant length of the column.

The rocking detail was composed of a steel tube (that matched the column diameter) welded to a circular, steel baseplate. That plate had a central hole through which the prestressing strands passed. A ½ in. thick, fiber-reinforced grout pad was used to create a bearing interface between the rocking plate and the cap beam.

The response of PreT-CB-ROCK was analyzed and compared to several similar experimental columns in order to evaluate the effects of the rocking detail. This detail resulted in cosmetic concrete damage only. The experimental response was also compared to damage progression models and strength modeling.

8.2 CONCLUSIONS

The following conclusions were drawn:

1. Adding the steel confining tube eliminated structural concrete spalling. The only damage to the concrete was cosmetic, and could probably be avoided by changing the detailed geometry at the transition from the circular tube to the octagonal, concrete cross-section.

2. Adding the baseplate allowed the column to rock on the cap beam, which concentrated the system deformation at the interface between column and cap beam. The body of the column then underwent essentially rigid body rotation.
3. System deformations were mostly accommodated by the concentrated rotation of the rocking connection, as opposed to cumulative bending curvature from distributed cracking.
4. The fiber-reinforced grout pad provided a suitable bearing interface between the column and cap beam.
5. The steel tube remained elastic and provided confining stiffness to the column concrete for the entire test. Tube yielding or "bulging" was not observed during the test.
6. Debonding the column's longitudinal rebar for a longer length (with respect to PreT-SF-ROCK) delayed bar fracture from cyclic loading.
7. The system design resulted in a very ductile connection; peak strength was observed at drifts exceeding 10% and no significant reduction in strength was observed.
8. The column exhibited good re-centering when the transverse load was removed.
9. The equivalent damping ratio of the system was lower than that of a similar, precast, non-prestressed column.
10. Peak displacements of the unbonded, hybrid system could be larger than for an equivalent, conventional, bonded, reinforced concrete structure for the same ground motion.
11. The cap beam of the system was not damaged during the loading.
12. Debonding rebars within buckle-restraining steel tubes, rather than plastic pipes, did not delay the fracture of the bars. All column rebars fractured at approximately the same drift levels (half were debonded with steel tubes, and half were debonded with ordinary PVC piping).
13. The cap beam connection was constructible, but alignment of the rebar in the cap beam was significantly affected by the commercial availability of duct sizes. This is likely to be less of a problem at full scale than at lab scale.
14. The cap beam connection (PreT-CB-ROCK) had a nearly identical response to a similarly designed spread footing connection (PreT-SF-ROCK). The reduction in column diameter at the socket connection appears to have no effect on performance under cyclic load.
15. Conventional construction materials can be used to produce a system that re-centers and has negligible damage even after large drift excursion. The implication is that these performance attributes can be achieved with the same material costs as the state-of-the-practice.
16. The unbonded prestressing strands exhibited unusual behavior when the column was returned to center after being displaced to higher drifts. This behavior could have been the result of strand buckling within the unbonded length.

17. The concrete bond strength with the prestressing strands was correlated to the casting orientation of the strands. That is, the top-cast strands had weaker bond with the concrete and were more susceptible to bond slip than bottom-cast strands.
18. The calculated moment contributions of the internal resisting forces to rotation of joint seemed reasonable. The No. 4 bars had a low contribution at low drifts, because of they were unbonded across the joint. The ratio between reinforcing strengths was roughly in-line with Davis's original design of the PreT- system. Furthermore, the discrete moment contributions of the unbonded strands and bonded reinforcement were used to demonstrate the theoretical behavior of the hybrid connection.
19. Shear damage was not observed during the test, and the amount of spiral reinforcement within the column could be reduced.
20. The dowel bar that was included to transfer shear forces from the column to the cap beam provided a negligible contribution to the shear resistance. The actual behavior was not understood, and it probably did not perform as intended. It could be abandoned in future designs.
21. The column shear force was likely transferred to the cap beam/footing entirely through friction between the baseplate and underlying concrete.
22. The models used to predict the damage progression of PreT-CB-ROCK and –SF-ROCK were not suitable for the unbonded, prestressed, rocking system design. They were originally developed for conventionally reinforced concrete columns.
23. The drift at first rebar yield was similar to the previous pre-tensioned specimens that did not have the rocking detail. However, the initial stiffness of the rocking systems were largely a function of the joint decompression, not of rebar yield alone.
24. The measured stiffnesses (pre-decompression, post-decompression, and yield) of the footing connection were consistently greater than for the cap beam connection. This could be attributable to the cap beam connection's grout pad, smaller base, longer reinforcement debonding lengths, or less stiff concrete.
25. Stiffness degradation due to yielding was under predicted by models. However, the pre-tensioned systems all exhibited similar levels of stiffness degradation.
26. The location of the rocking neutral axis was near the center for low drifts, and then settled to ~2.75 in. away from either column face for high drifts. Also, its cross-sectional location can be well approximated with a trigonometric function (an inverse tangent was used in the analysis).
27. The fiber-element, moment-rotation program produced good results for the moment-drift response. It is assumed that such a program could be developed with a spreadsheet coding or another code language (MATLAB 2014b was used in this thesis).
28. The moment-rotation program predicted a similar trend for the neutral axis location as what was observed from the data analysis. However, the model resulted in too quick a transition from the primary to secondary response.
29. The moment-rotation program also produced strength contribution results that were in general agreement with the analysis of the measured response.

30. A finite element analysis was used to model the rocking behavior of the specimen. It produced decent results for the strength envelope, but was altogether too stiff.
31. The finite element analysis predicted a transition from tension to compression stresses in the strands at high drifts. This was attributed to strand buckling in the analysis of the measured response.
32. The finite element analysis predicted a similar behavior for the neutral axis location (as a function of drift). However, the FEA model also resulted in too quick a transition from the primary to secondary response.
33. The finite element analysis predicted a similar magnitudes of permanent compression of the grout pad, compared to what was physically measured during the test.

8.3 RECOMMENDATIONS

8.3.1 Recommendations for Design and Practice

The socket connection with the footing has been observed to be very constructible (PreT-SF-CONC and PreT-SF-ROCK, for example). However, Davis observed difficulty during the fitting of the connection for PreT-CB-CONC, and recommended that larger ducts be used for the rebars in order to give greater alignment tolerance. But the reduced diameter column extension was 2 in. wider for PreT-CB-ROCK than for PreT-CB-CONC, and so it required a minimum 10-$^{5}/_{8}$ in. diameter duct to complete the socket connection. However, a duct of that size was not commercially available, so a nominal 12 in. duct was used. That larger duct (coupled with the larger, 2 in. diameter rebar ducts) created significant conflicts with the cap beam's longitudinal reinforcement. Therefore, it is recommended that a designer carefully consider the sizes of available ducts when detailing the connection region. However, this problem is likely to be less severe for full-scale construction.

The rocking specimens resulted in cosmetic damage only. However, the corner cracking above the steel tube would still be unsightly damage, which would be difficult to patch. Therefore, it is suggested that the designer specify a tapered detail where the 20 in. diameter octagon transitions to the top of the steel tube. Therefore, the geometric incompatibility between the two sections could be mitigated, along with the potential damage.

The cap beam was cast in the same orientation as it was tested. The ducts used for the socket connection were secured to the main formwork with bracing. However, that bracing prevented the striking of the concrete near the connection, and hand finishing the exposed crevices between the ducts was somewhat difficult. An inconsistent top finish resulted, which led to a non-uniform grout pad thickness (the connection was aligned so that the column and beam were orthogonal to one another). It is suggested that the cap beam be cast so that the bottom face is against flat formwork, and will guarantee a flat bearing surface for the future alignment.

Furthermore, the full implementation of this system will require consideration of maintenance and health monitoring. Previous tests have observed that a large crack is formed at the base of the column, which is a likely location for water to accumulate. The exposed steel of the rocking detail could be protected from corrosion with an additional, sacrificial layer of steel or some other material. Furthermore, damage detection methods (for determining the condition of the rebar) should be tested with this design. Such efforts were beyond the scope of this thesis.

8.3.2 Further Consideration of the PreT-SF-ROCK and PreT-CB-ROCK Subassembly Tests

8.3.2.1 Data Analysis

The following proposals are offered for additional analysis of the pre-tensioned rocking tests:

1. Isolate and quantify the sources of flexibility for the rocking systems. That is, determine how much of the applied displacement resulted from column bending deformation, baseplate frictional sliding, grout pad compression, concentrated joint rotation, and base deformation/rotation. In particular, determine why the calculated, uncracked stiffness for the columns were much higher than the measured pre-decompression stiffnesses (2.90 times higher on average).
2. Use the curvature data in order to determine the effective bending stiffness of the column as a function of drift and column height. That is, according to Euler-Bernoulli beam theory, moment and curvature are linearly related through bending stiffness. The moment at every column height could be determined with the effective force data, and the column curvature was determined with the Optotrak camera system.
3. Determine how the bilinear nature of the strength envelope was specifically affected by the transition between pre- and post-decompression behaviors. Essentially, PreT-CB-ROCK can be considered as a combination of two structures: a pre-decompression system and a post-decompression system.
4. Further compare the measured responses of the rocking columns to other unbonded column systems with similar conceptual designs. In this thesis and in Schaefer's report (2014a), the responses of PreT-CB-ROCK and –SF-ROCK were extensively compared to previous iterations of the University of Washington's precast column project. Comparing the rocking design to other, externally developed systems could provide valuable insights regarding any unforeseen strengths or weaknesses for the rocking design.
5. Investigate the effects of the neutral axis transition. In this thesis, it was generally assumed or implied that the neutral axis behavior was a function of the joint decompression. However, this was never explicitly quantified or investigated.
6. Investigate the abrupt increase in the measured, post-secondary stiffness and strength at ~±7.5%. This occurred for most of the previously tested, pre-tensioned specimens at the University of Washington. Determining the source of the inconsistency would shed additional light on the behavior of the pre-tensioned design. A preliminary examination of this issue suggested that the strands nearer to the compression face may have "unbuckled" at that drift ratio (and therefore suddenly contributed a resistive force to the joint's rotation), but that analysis was inconclusive.
7. Use the tube potentiometer data from the residual cycles to estimate the rounded profile of the permanently compressed grout pad. Furthermore, any analysis of the residual cycles could offer a better understanding of the system (this data was simply presented in this thesis, without analysis).
8. Further investigate the slip of the strands. The stand strains could be estimated by calculating their elongations with the tube potentiometer data, and dividing the result

by the strand unbonded length (which was done to estimate first rebar yield). Any difference between the calculated and measured strains would be indicative of strand slip.

9. Complete the moment contribution analysis for the PreT-SF-ROCK specimen, and compare against the results for the cap beam connection. The prestressing strands were identical in each specimen, and much of the column geometry was the same. Therefore, it is assumed that such an analysis could be readily performed. Furthermore, footing connection's rebar gauges were properly read during that test, so it is possible that the rebar contribution to the joint strength could be directly evaluated (as opposed to being indirectly calculated from the axial load, strands, and total moment).
10. Use the moment contribution analysis to produce an experimentally derived re-centering ratio. If the moment contribution of each specimen were known throughout the entire test, then the forces resisting re-centering (the rebars) could be related to the forces promoting re-centering (the axial load and strands). Then, this experimental result could be used to evaluate the design equation.
11. Use the moment contribution analysis to quantify the actual energy dissipations of the rebars and strands.
12. Evaluate the residual stiffness of the system, following of peak loads. This was the intention of the reduced drift, fourth cycles of each set, but this analysis was not performed for either rocking connection.
13. Use the two-dimensional stress analysis of the tube to estimate the hoop and longitudinal stresses as a function of tube location. The function should be easily related to tube elevation (two strain-gauge rosettes were applied at different elevations) and perimeter location (as stress data was calculated for both positive and negative drifts). Developing an experimentally derived stress field could be used to evaluate finite element analysis of the confining tube. Furthermore, such efforts could then be used to determine the tube elevation at which the No. 3 AWG spiral could adequately provide the entire confining force to the concrete. With that result, the required tube height could be evaluated, and its design optimized.
14. Estimate the triaxial confinement from the rocking detail. The two-dimensional stress state was determined by analyzing the strain-gauge rosette data. The approximate bearing area of the baseplate was given in the neutral axis analysis. The required compressive force could be determined with a section analysis, similar to that used for the moment contribution analysis. Using these results, it may be possible to quantify the actual confining force at the toe of the column.
15. Complete an analysis to determine any net, axial elongation of the column.
16. Finally, develop a reliable, robust, and objective data correction scheme for the improperly acquired strain gauge output. Investigation of the resulting, corrected data could provide additional and useful insights into the behavior of the system.

8.3.2.2 Modeling

The following tasks could improve modeling efforts of the rocking specimens:

1. Use the fiber-element, moment-rotation analysis to investigate the transition from primary to secondary response. The moment-rotation and finite element analyses predicted too stiff responses during the transition. This may have been due to bar slip, which was not considered in the model, and was not evaluated for the specimens. However, the transition was also observed to be a function of the assumed Mander confinement model for the underlying grout pad (the Mander model output the near peak compressive strength well before the specified strain). It is possible that the constitutive response of the grout/concrete underneath the rocking baseplate dictated the stiffness transition of the connection.
2. Predict the column deformation with modeling. The finite element model used a rigid, non-deformable body to represent the column, and the moment-rotation model assumed a uniform, equivalent bending stiffness for the entire column height. However, the transition from the top of the steel tube and the 20 in. wide octagon produced a concentrated source of curvature. Such considerations could help to improve the structural models.
3. Further develop the finite element analysis. The moment contribution analysis could be performed on the FEA results, and the energy dissipated by the FEA model could be compared to the experimental specimen. It was observed that the finite element analysis predicted far larger energy dissipation loops, which was not quantitatively investigated or assessed.
4. Use other non-linear analysis programs, such as OpenSees, to model the experimental testing of the rocking specimens.
5. Develop non-linear, dynamic models for the rocking specimens, in order to further investigate and analyze the behavior. It has been suggested that a system with low energy dissipation (such as an unbonded structure) would exhibit larger dynamic displacements than conventionally reinforced concrete system. The issue was only briefly addressed in this thesis.
6. Detailed, non-linear modeling of several of the system components would be helpful in further refining the design. Specifically, the transition between tube and 20 in. octagon would help to quantify the effect of the discontinuous No. 6 bars. Detailed modeling of the grout pad and the contact between the pad and baseplate could lend insight into the response. Finally, modeling the confinement provided by the rocking detail could corroborate the experimental stress analysis of the tube element.

8.3.2.3 Design Guidelines

Finally, the subassembly test results could be used to begin the development of design guidelines and equations. For example:

1. Relate the specimen design parameters (material properties, reinforcing ratios, sectional geometry, unbonded lengths, axial load, etc.) to the system performance (pre- and post-decompression stiffnesses, moment strength, energy dissipation, and equivalent viscous damping, etc.). After developing a parametric understanding of the

design vs. response, generate relatively simple, linear, predictive equations for use in design practice.

2. Develop new predictive damage models for the rocking system. The damage progression model used in this thesis was originally developed for conventionally reinforced concrete columns. However, the rocking, hybrid connection is likely different enough in composition that a new model should be produced. This may require additional parametric testing of the rocking design.

8.3.3 Future Development for the –ROCK Design

8.3.3.1 Full System Testing

Extensive pseudo-static, subassembly testing at the University of Washington has preceded the work described in this thesis. In 2014, a three bent bridge with pre-tensioned, rocking columns was tested at the NEES facility at the University of Nevada-Reno (Thonstad et al., 2015).

Those experiments were fully dynamic tests. The bents each had two rocking columns at full heights (the top cap beam connection and the bottom footing connection). Furthermore, superstructure components and typical bridge masses were included in the specimen design. The analysis of that test is expected to provide insight into the full system response of a bridge with rocking, prestressed columns.

8.3.3.2 Dynamic Testing

As previously discussed, the 25% scale, full system tests at the University of Nevada-Reno were dynamic.

However, additional dynamic testing of the connection subassemblies would help to isolate and determine their dynamic behavior, properties, and performances.

8.3.3.3 Parametric Studies

Several parametric studies are proposed here, which may be addressed with additional subassembly or component testing.

1. A detailed experimental analysis of the grout pad would be useful. Accurately determining the grout's highly confined, constitutive response would help in modeling efforts (the measured response was used to assume an appropriate constitutive relation). The effect of pad thickness on connection performance should be determined (it has been suggested in this thesis that it was a source of pre-decompression flexibility). In the PreT-CB-ROCK test, the column shear force was probably transferred to the cap beam base through friction with the grout pad alone. This was certainly true for the footing connection, as it did not have the dowel bar. However, the frictional interaction should be investigated, because for squat columns or bridge columns with a low axial load, the connection friction may not be enough for the full transfer (Hewes and Priestley, 2002). Finally, the material design for the grout should be optimized. The material selection for PreT-CB-ROCK's grout pad was primarily influenced by the experimental testing of rocking, post-tensioned, concrete filled tubes at UC San Diego (Restrepo et al., 2011 and Guerrini et al., 2012).

2. The required height and thickness of the steel tube, relative to the column dimensions, could be determined. For this round of testing, the height was conservatively designed at 10 inches.
3. The design of the six discontinuous No. 6 bars that were welded to the steel baseplate could be optimized (length, bar size, number).
4. The prestressing design could be further refined. Specifically, a greater area of prestressing strand could be introduced (either with larger strands or more of them), but pre-tensioned to give the same total prestressing force. Therefore, the re-centering offered by the strands would be maintained, but they would not need to be initially strained as much. This arrangement would likely delay strand yield to higher drift ratios.

8.3.3.4 Additional, Pseudo-Static, Subassembly Testing

Additional subassembly testing (to be conducted under similar experimental setups), is proposed here:

1. Other geometric configurations should be evaluated. That is, columns of different aspect ratios, cross-sectional shapes, and reinforcing details should be tested. With the exception of their debonding lengths, PreT-SF-ROCK and PreT-CB-ROCK had identical designs. Therefore, if new design guidelines or damage prediction models were developed for these two specimens, they may only be valid for 20 in. diameter, octagonal columns with six No. 4 reinforcing bars, and six $^{3}/_{8}$ in. diameter strands, etc. Therefore, if additional columns with different details were tested, it could lead to better, more robust predictive models for the rocking system.
2. The rocking columns examined in this thesis were octagonal, primarily due to fabrication considerations. Additional subassembly testing should be considered for circular, square, and rectangular columns. If such geometries were determined to be constructible and have adequate seismic performance, then it would offer greater flexibility to bridge owners and increase the practical feasibility of the system.
3. If, for whatever reason, a bridge owner did not want the externally visible tube of the rocking detail (perhaps from fear of corrosion or due to aesthetic concerns), it is possible that the behavior could be replicated with another detail. If the spiral at the top and bottom of the column were well anchored and tied with no spacing, it may provide the same level of local confinement as the tube. Adding an embedded steel baseplate would then provide a natural crack plane and a rocking mechanism for the element. Admittedly, such a column would be susceptible to losing its cover, and thereby exposing the spiral steel. However, some bridge owners may prefer such a structure (if they are comfortable with cosmetic, patching type repairs), and this alternative, if feasible, would offer greater flexibility for the PreT- design.
4. The substructure (i.e., spread footing) of this system has been thoroughly investigated. Haraldsson et al. (2011b) showed that the precast column does not need protruding steel tying it into the cast-in-place footing, which greatly simplified the socket connection. The footing design was further refined by Davis, Finnsson, and Schaefer's efforts. The cap beam, on the other hand, was initially designed by Davis for his project, and it has not been seriously reconsidered since. Granted, precast, non-

prestressed beam design does not necessarily need to be researched – but the same argument could have been made regarding cast in place spread footings. Essentially, the cap beam for PreT-CB-ROCK was far, far stronger than necessary (in order to ensure "failure" of the connection). Therefore, further developing the cap beam would help to optimize the overall design efficiency of the system.

5. The effort to absolutely guarantee re-centering and absolutely eliminate column damage should be carefully approached. That is, bar fracture was delayed until ~6.0% drift for the footing connection, and not until the second ±7.40% drift cycle for the cap beam connection (such drift ratios are very unlikely to occur in real structures). This delay in bar fracture was attributed to the intentional debonding of the No. 4 reinforcement across the rocking joint. However, the moment contribution analyses (both experimental and from the fiber-element model) indicated that the No. 4 reinforcing was nearly inactive for low drifts, which would have reduced the system's available energy dissipation (EVD ranged from 7-12% for drifts less than 2%). With these points in mind, the actual debonding length of the rebars or the relative percentage of bonded reinforcement could be reconsidered. Essentially, the goals of column re-centering and damage elimination are at odds with the performance criterion of energy dissipation, and it may be worthwhile to optimize the tradeoff. For example, in the subassembly test, the design re-centering ratio was ~3.4 in order to ensure re-centering behavior in the test specimens. However, even with additional, energy dissipating, bonded reinforcement, the columns would have likely re-centered. Nonlinear dynamic modeling and dynamic testing would assist in this endeavor.
6. Finally, additional pseudo-static tests of rocking columns with non-conservative designs are suggested. PreT-SF-ROCK and PreT-CB-ROCK were both very conservatively (and similarly) designed. The goal for this round of tests was to observe and quantify the connections' rocking behavior, and many of the components were conservatively designed in order to eliminate the possibility of premature or otherwise unrelated failure. For example, the tube was ~1.5 times longer than what was thought required, the No. 6 bars were likely longer and larger than they needed to be, preliminary analysis suggested that the dowel bar was unnecessary, the design re-centering ratio was 3.4 (far greater than 1.0), the spiral reinforcement was not reduced (even in lieu of the confining tube), the surface of the of the reduced diameter extension was given the roughened surface detail (even though it was probably unnecessary), etc. If more aggressively designed specimens were still shown to work, then the required detailing and fabrication methods for the pre-tensioned, rocking columns could be simplified. If, on the other hand, a less conservative design failed prematurely, it would provide definitive evidence for the initial design's conservatism.

8.3.3.4.1 General Construction and Testing Recommendations

1. Directly measure the horizontal displacement of the sliding bearing plate (i.e., the location of the vertical load). This dimension was estimated from the measured displacement at the horizontal load application, which may not be an absolutely accurate method.
2. Directly measure the rotation of the base, either with inclinometers or additional Optotrak LED targets. This thesis, and much of the preceding experimental work at

the University of Washington, has assumed the base to be perfectly rigid. However, knowing the base deformation would help in isolating the initial stiffness of the column from the entire subassembly.

3. Use additional linear potentiometers to measure the kinematics of the confining tube. Four potentiometers were used for this experiment, but one of them did not give plausible results for the entire test. Adding instruments would improve redundancy and output resolution.
4. Physically measure the bearing depth during the test. Such measurements could corroborate the neutral axis calculation. Furthermore, such measurements could illustrate the difference between the *apparent* neutral axis location and the *actual* location of bearing (i.e., the error that is caused by the permanent rounding to of the grout pad).
5. Extensively measure the grout pad rounding. This exact behavior was not anticipated at the onset of this test, and therefore the grout pad rounding was not quantified as well as it could have been (measurements were taken as a residual gap appeared between the pad and baseplate).
6. After running the first set, analyze the results to ensure that the data acquisition system is properly recording the instrumentation signals. Preferably, this should be done during the preceding trial cycle (most of PreT-CB-ROCK's instrumentation was not installed at the time of its trial cycle).
7. Re-examine the frictional model for high drifts. Brown (2008) developed the model from displacement measurements of the Baldwin loading head and the sliding plate at very low drifts. It may need to be adjusted for the higher drifts of these pre-tensioned column tests.
8. Construct and cast the cap beam on its side, in order to produce a flat "bottom" face for the cap beam. This would ensure a more uniform grout pad thickness.
9. Measure the slip of the strands at the release. For example, Peterman (2007) described a method to quantify the slip and corresponding bond strength for prestressing strands following release.
10. Use strand load cells at both the top and bottom of the column. If the bonded lengths vary between the column ends, then differences in the measured slip could provide insight on the bond properties of the system.

8.3.3.5 Additional Design Features to Consider

The following design features are suggested for the system:

1. Using a more ductile variety of steel for the bonded reinforcement, such as stainless steel. Finnsson (2013) tried stainless steel rebar for this columns, but it was determined that those specimens still exhibited the same damage progression of: concrete spalling, bar buckling, bar fracture. Therefore, stainless steel was abandoned after Finnsson's efforts (buckling is dependent on material stiffness, not ductility). However, the rebars of the rocking connections fractured from cyclic, tensile elongations, and likely did not freely buckle (buckling was not observed during the test, and the bars were likely well constrained within their debonding tubes). Therefore, the rocking design might make

better use out of a more ductile steel than a conventionally reinforced concrete structure. Using more ductile reinforcement could be coupled with shorter local debonding lengths (which would improve energy dissipation at low drifts).

2. An engineered material could be considered for the bearing pad (as opposed to the cementitious, fiber-reinforced grout pad used for PreT-CB-ROCK). It is possible that using such a material for the pad would improve energy dissipation at low drifts.
3. Finally, it has been suggested to achieve the pre-tensioning through the use of specially manufactured, post-tensioning strands (e.g., what is used for unbonded floor slabs). Using such an element for the design would allow the strands to be mechanically anchored at the top and bottom of the column, as opposed to relying on bond with the concrete. Even though such elements would be manufactured for post-tensioned construction, the stressing could still be done at the precast facility in order to deliver a whole, finished product to the site, and to mitigate onsite construction activities.

8.3.3.6 Initiate Analytical Efforts

The pre-tensioned, precast column project at the University of Washington has been primarily focused on experimentation (along with some modeling). A thorough analytical investigation of this system may provide to insights that have otherwise been missed during the experimental analyses. Finally, analytically deriving relations between design geometry and structural performance would bolster the production of robust and reliable design guidelines.

References

AASHTO Technical Committee for Seismic Design (2009). *AASHTO Guide Specifications for LRFD Seismic Bridge Design*. American Association of State Highway and Transportation Officials, Washington, D.C..

AASHTO T-3 Task Group (2000). *Guide Specifications for Seismic Isolation Design*, American Association of State Highway and Transportation Officials, Washington D.C..

Abaqus 6.13-4 (2013). Dassault Systèmes Simulia Corp., Providence, RI.

ACI Committee 318 (2011). *Building Code Requirements for Structural Concrete and Commentary, ACI 318-11,* American Concrete Institute, Farming Hills, MI.

ASTM International (2011). *Standard Test Methods for Tension Testing of Metallic Materials, ASTM E8/E8M – 11*, ASTM International, West Conshohocken, PA.

Berry M.P., Eberhard M.O. (2005). Practical performance model for bar buckling, *Journal of Structural Engineering*, ASCE, 131(7): 1060-1070.

Berry M.P., Parrish M., Eberhard M.O. (2004). *PEER Structural Performance Database: User's Manual (Version 1.0),* Pacific Earthquake Engineering Research Center, University of California, Berkeley, CA.

Billington S.L., Yoon J.K. (2004). Cyclic response of unbonded posttensioned precast columns with ductile fiber-reinforced concrete. *Journal of Bridge Engineering*, ASCE, 9(4): 353-363.

Brown W. (2008). Bar buckling in reinforced concrete bridge columns, Master's Thesis, University of Washington, Seattle, WA.

Building Seismic Safety Council for the FEMA. (2004). *NEHRP Recommended Provisions for Seismic Regulations for New Buildings and Other Structures (FEMA 450-1 / 2003 Edition),* National Institute of Building Sciences, Washington, D.C..

Chopra A.K. (2007). *Dynamics of Structures – Theory and Applications of Earthquake Engineering, Third Edition,* Pearson Prentice Hall, Upper Saddle River, NJ.

Cohagen L.S., Pang J.B.K., Eberhard M.O., Stanton J.F. (2008). A precast concrete bridge bent designed to re-center after an earthquake, *Washington State Department of Transportations. Report No. WA-RD 684.3*, Washington State Department of Transportation, Olympia, WA.

Cousins T.E., Johnston D.W., Zia P. (1990). Transfer and development length of epoxy coated and uncoated prestressing strand, *PCI Journal*, Precast/Prestressed Concrete Institute, 35(4): 92-103.

Dassault Systèmes Simulia Corp. (2012). Abaqus 6.12 Document Collection, *10.2 Plasticity in ductile metals*, Providence, RI.

Davis P.M., Janes T.M., Eberhard M.O, Stanton J.F. (2012). Unbonded pre-tensioned columns for bridges in seismic regions, *PEER Report No. 2012/04*, Pacific Earthquake Engineering Research Center, University of California, Berkeley, CA.

Davis P.M. (2013). Re-stressing operation on reduced diameter section, Message to the author, E-mail.

Dayton Superior (2011). Sure-Grip® High Performance Grout – Technical Data Sheet, *Section 16: Grouts*, Dayton Superior Corporation, Miamisburg, OH.

Dayton Superior (2015). Sure-Grip® High Performance Grout, *Products – Chemicals,* Dayton Superior Corporation, Web.

Elwood K.J., Eberhard M.O. (2009). Effective stiffness of reinforced concrete columns, *ACI Structural Journal*, American Concrete Institute, 106(4): 476-484.

Finnsson G. (2013). Unbonded pre-tensioned bridge columns with hybrid fiber-reinforced concrete shells, Master's Thesis, University of Washington, Seattle, WA.

Guerrini G., Restrepo J.I., Massari M., Vervelidis A. (2012). Self-centering precast concrete dual-shell steel columns, *Proceedings of the Fifteenth World Conference on Earthquake Engineering*, Paper No. 2552, Lisbon, Portugal.

Haraldsson O., Eberhard M.O., Stanton J.F., Berry M. (2011a). Accelerating bridge construction to reduce congestion, *Transportation Northwest Final Report, TNW2011-08*, University of Washington, Seattle, WA.

Haraldsson O., Janes T.M., Eberhard M.O., Stanton J.F. (2011b). Laboratory tests of column-to-footing socket connections, *Highways for LIFE Technology Partnership Program*, Federal Highway Administration, Washington, D.C..

Hewes J.T., Priestley N.M.J. (2002). Seismic design and performance of precast concrete segmental bridge columns, *California Department of Transportation Report No. SSRP-2001/15*, State of California Department of Transportation, Sacramento, CA.

Hieber D., Wacker J., Eberhard M.O., Stanton J.F. (2005). Precast concrete pier systems for rapid construction of bridges in seismic regions, *Washington State Department of Transportation Report No. WA-RD-511.1*, Washington State Department of Transportation, Olympia, WA.

Janssen D.J. (2013). Fiber reinforced grout, Message to the author, E-mail.

Jimenez J.G. (2012). Bond capacity of steel epoxy-coated and uncoated pre-stressing strands, *Earthquake Engineering for Resilient Communities: 2012 PEER Internship Program Research Report Collection, PEER Report No. 2012/07*, Eds. Tremayne H., Mahin S., Pacific Earthquake Engineering Research Center, University of California, Berkeley, CA.

Khaleghi B., Schultz E., Seguirant S., Marsh L., Haraldsson O., Eberhard M.O., Stanton J.F. (2012). Accelerated bridge construction in Washington State: From research to practice, *PCI Journal*, Precast/Prestressed Concrete Institute, 57(4): 34-49.

Kumar P., Jen G., Trono W., Panagiotou M., Ostertag C. (2011). Self compacting hybrid fiber reinforced concrete composites for bridge columns, *PEER Report No. 2011/106*, Pacific Earthquake Engineering Research Center, University of California, Berkeley, CA.

Lee J.R. (2011). Experimental investigation of embedded connections for concrete-filled steel tube columns subjected to combined axial-flexural loading, Master's Thesis, University of Washington, Seattle, WA.

Mander J.B., Priestley M.J.N., Park R. (1988). Theoretical stress-strain model for confined concrete, *Journal of Structural Engineering*, ASCE, 114(8): 1804-1826.

Matsumoto E. (2009). Emulative precast bent cap connections for seismic regions: Component test report – Cap pocket full ductility specimen (unit 3). *Report No. ECS-CSUS-2009-03*. California State University, Sacramento, CA.

MATLAB 2012b (2012). The MathWorks, Inc., Natick, MA.

MATLAB 2014b (2014). The MathWorks, Inc., Natick, MA.

Menegotto M., Pinto P.E. (1973). Method of analysis for cyclically loaded reinforced concrete plane frames including changes in geometry and non-elastic behavior of elements under combined normal force and bending, *Proceedings of IASBE Symposium on Resistance and Ultimate Deformability of Structures Under Well-Defined Repeated Loads*, Lisbon, Portugal.

Mole A. (1994). Seismic response of hybrid connections in precast concrete frames, Master's Thesis, University of Washington, Seattle, WA.

Naaman A.E. (2012). *Prestressed Concrete Analysis and Design, Third Edition*, Techno Press 3000, Ann Arbor, MI.

Newmark N. M., Hall W.J. (1982). Earthquake spectra and design, *Earthquake Engineering Research Institute,* Berkeley, CA.

Northern Digital Inc. (2014). Optotrak Certus motion capture system, *Optotrak Certus Research-Grade Motion Capture System Technical Specifications*, Waterloo, Ontario, Canada.

Pang J.B.K., Eberhard M.O., Stanton J.F. (2010). Large-bar connection for precast bridge bents in seismic regions. *Journal of Bridge Engineering*, ASCE, 15(3): 231-239.

Pang J.B.K., Steuck K.P., Cohagen L., Eberhard M.O., Stanton J.F. (2008). Rapidly constructible large-bar precast bridge-bent seismic connection. *Washington State Department of Transportation Report No. WA-RD 684.2*, Washington State Department of Transportation, Olympia, WA.

Park R., Paulay T. (1975). *Reinforced Concrete Structures*, John Wiley & Sons, New York City, NY.

Paulay T., Priestley M.J.N. (1992). *Seismic Design of Reinforced Concrete and Masonry Buildings*, John Wiley & Sons, New York City, NY.

Peterman R. (2007). The effects of as-cast depth and concrete fluidity on strand bond, *PCI Journal*, Precast/Prestressed Concrete Institute, 52(3): 72-101.

Priestley M.J.N., Tao J.R. (1993). Seismic response of precast prestressed concrete frames with partially debonded tendons, *PCI Journal*, Precast/Prestressed Concrete Institute, 38(1): 58-69.

Priestley M.J.N., Verma R., Xiao Y. (1994). Seismic shear strength of reinforced concrete columns, *Journal of Structural Engineering*, ASCE, 120(8): 2310-2329.

Restrepo J.I., Tobolski M.J., Matsumoto E.E. (2011). Development of precast bent cap systems for seismic regions. *NCHRP Report 681,* Transportation Research Board, Washington, D.C.

Riley W.F., Sturges L.D., Morris D.H. (2002). *Statics and Mechanics of Materials: An Integrated Approach, Second Edition*, John Wiley & Sons, New York City, NY.

Rodriguez M., Betero J., Villa J. (1999). Cyclic stress-strain behavior of reinforcing steel including effect of buckling, *Journal of Structural Engineering*, ASCE, 125(6), 605-612.

Sargin M. (1971). Stress-strain relationship for concrete and the analysis of structural concrete sections, *Study No. 4, Solid Mechanics Division*, University of Waterloo, Waterloo, Ontario, Canada.

Schaefer J.S., Kennedy B., Eberhard M.O., Stanton J.F. (2014a). Unbonded pre-tensioned bridge columns with rocking detail, *PEER Report No. 2014/08*, Pacific Earthquake Engineering Research Center, University of California, Berkeley, CA.

Schaefer J., Thonstad T., Kennedy B., Eberhard M., Stanton J. (2014b). Cyclic testing of an unbonded pre-tensioned bridge column with rocking detail: footing specimen 01, *Network for Earthquake Engineering Simulation* (distributor), Dataset, DOI:10.4231/D3G737473.

Stanton J.F., Stone W.C., Cheok G.S. (1997). Hybrid reinforced precast frame for seismic regions, *PCI Journal*, Precast/Prestressed Concrete Institute, 42(2): 20-32.

Stanton J.F., Nakaki S.D. (2002). Design guidelines for precast concrete structural systems. *PRESSS Report No. 01/03-09*.

Stephens M.T. (2014). UW Baldwin loading setup, Message to the author. E-mail.

Steuck K.P., Eberhard M.O., Stanton J.F. (2009). Anchorage of large-diameter reinforcing bars in ducts, *ACI Structural Journal*, 106(4): 506-513.

Thonstad T., Mantawy I., Stanton J., Eberhard M., Sanders D. (2015). Shake table testing of a two-span bridge specimen with unbonded, pre-tensioned rocking columns, *Network for Earthquake Engineering Simulation* (distributor), Dataset, DOI:10.4231/D33B5W88M.

Tobolski M.J. (2010). Improving the design and performance of concrete bridges in seismic regions, PhD Thesis, University of California-San Diego, La Jolla, CA.

Wight J.K., MacGregor J.G. (2011) *Reinforced Concrete: Mechanics and Design, Sixth Edition*, Prentice Hall, Upper Saddle River, NJ.

WSDOT Engineering and Regional Operations (2013). Precast prestressed concrete piles standard plan E-4, *WSDOT Standard Plans Manual,* Washington State Department of Transportation, Olympia, WA.

Appendix A: Materials Testing

This appendix provides the materials testing results for the construction materials used for specimen PreT-CB-ROCK.

CONVENTIONAL CONCRETE

The conventional concrete was supplied by CalPortland. Both column and cap beam were cast from the same concrete batch. Table A.1 gives engineering properties for the concrete, which were determined from materials testing at the University of Washington. The compressive strength was determined from 6 in. diameter cylinder tests. The splitting tension strength was determined with 6 in. diameter, split cylinder tension tests. The modulus of rupture was determined with 6 in. by 6 in. by 21 in. beam, four point loading tests. The modulus of elasticity was determined by compressively loading a 6 in. diameter cylinder to 40% of its ultimate strength. A line was fitted to digitally recorded data from these tests (from 50με to 40% of ultimate strength); the reported elasticity value was the slope of the line. With the exception of modulus of elasticity, every property in the table was the average of three testing results (the same two cylinders were used for all of the modulus of elasticity tests). The actual age of the concrete at time of the material test is given in parenthesis, below the actual result.

Table A.1 Concrete material properties.

Nominal Age	Compressive Strength, $\bar{f}_c$	Cylinder Splitting Tension, $\bar{f}_{ct}$	Modulus of Rupture, $\bar{f}_r$	Modulus of Elasticity, $\bar{E}_c$
7 days	6,690 psi (7 days)	498 psi (7 days)	N/A	4,620 ksi (7 days)
14 days	7,530 psi (14 days)	491 psi (14 days)	N/A	4,770 ksi (15 days)
28 days	8,420 psi (33 days)	577 psi (28 days)	817 psi (33 days)	4,990 ksi (33 days)
Test Day	9,030 psi (57 days)	560 psi (57 days)	909 psi (57 days)	4,930 ksi (64 days)

GROUT

Dayton Superior's Sure-Grip® High Performance grout was used for the grout pad and to grout the column's longitudinal reinforcement and reduced diameter extension into the cap beam ducts. Table A.2 provides compression results for the grouts used on the project. The grout used for the rebar duct and central duct had the same design, but were batched on different days. Unless noted, the reported strengths were calculated from the average of three 2 in. mortar cube tests. A result at 28 days for the grout used in the rebar ducts is not reported because there were not enough available cubes on that day.

Table A.2 Grout compressive strength.

Nominal Age	Grout Identification		
	Fiber-Reinforced Grout Compressive Strength, $\bar{f}_c$	**Rebar Duct Grout Compressive Strength, $\bar{f}_c$**	**Central Duct Grout Compressive Strength, $\bar{f}_c$**
7 days	7,200 psi (7 days)	6,230 (6 days)	5,980 psi (4 days)
14 days	9,630 psi (14 days)	7,760 (13 days)	6,700 psi (11 days)
28 days	9,830 psi (28 days)	N/A	9,740 psi (25 days)
Test Day	6,875 psi (31 days)	9,200 psi (30 days)	9,220 psi (28 days)
Makeup Materials Testing	6,105 psi (37 days, *5 cubes ranging from 4.7-7.8 ksi*)	11,200 psi (51 days, *1 cube*)	10,400 psi (49 days)

The strengths for the specimen test day appeared to be inconsistent with previous results. More specifically, the measured strength on test day was lower than when measured at 28 days (37.8% reduction for the fiber-reinforced grout, and a 5.3% reduction for the grout used in the central duct). Therefore, additional materials tests were completed. The makeup results for the duct grouts confirmed the typical strength gain over time for cementitious materials, but the results for the fiber-reinforced grout were again lower than what was measured on test day. The reasons for this discrepancy are unknown.

REINFORCEMENT

Monotonic Pull Tests

Monotonic pull tests on the specimen's steel reinforcement were completed with the 300-kip Baldwin at the University of Washington. The specimens (strands, rebar steel, or spiral) were instrumented with a 3.5-in. gauge length extensometer (a linear potentiometer with a clamp on either end). The rebars and strands were also instrumented with pairs of two-wire strain gauges. The results of these tests were used to generate stress versus strain relations for the steel, which are provided in Figure A.1 to Figure A.7; results are summarized in Table A.3. Strains were calculated from the extensometer readings by dividing the measured elongation by the 3.5-in. gauge length. The data for the red, dashed, strain gauge line in the figures was calculated by taking the average reading between the two strain gauges (unless otherwise noted). Two separate tests were completed for each size of the mild steel reinforcement, spiral, and strand; the specimens were anchored in the jaws of the Baldwin for each of these tests.

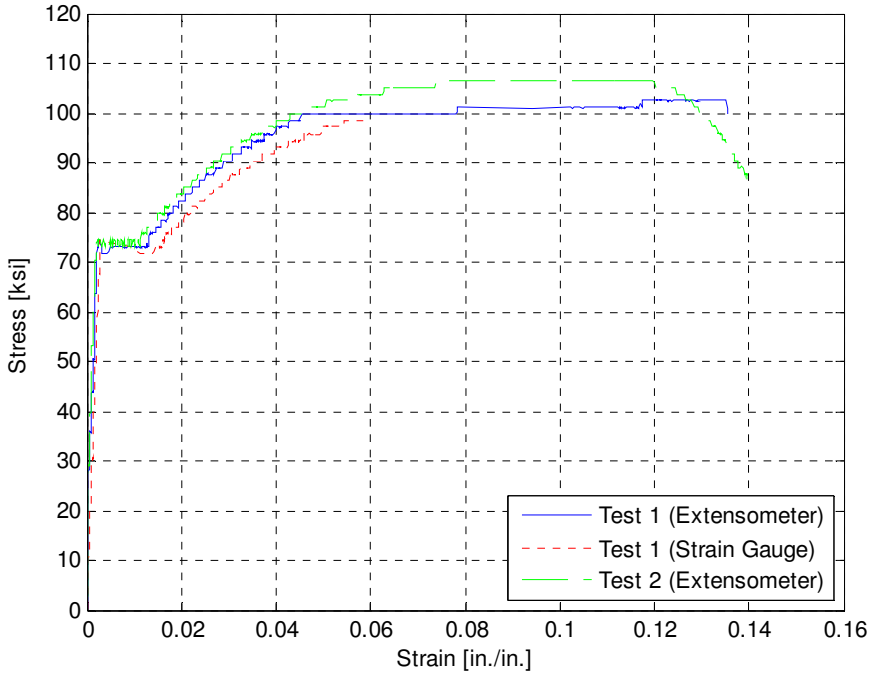

Figure A.1 Stress vs. strain relation for No. 3 bars.

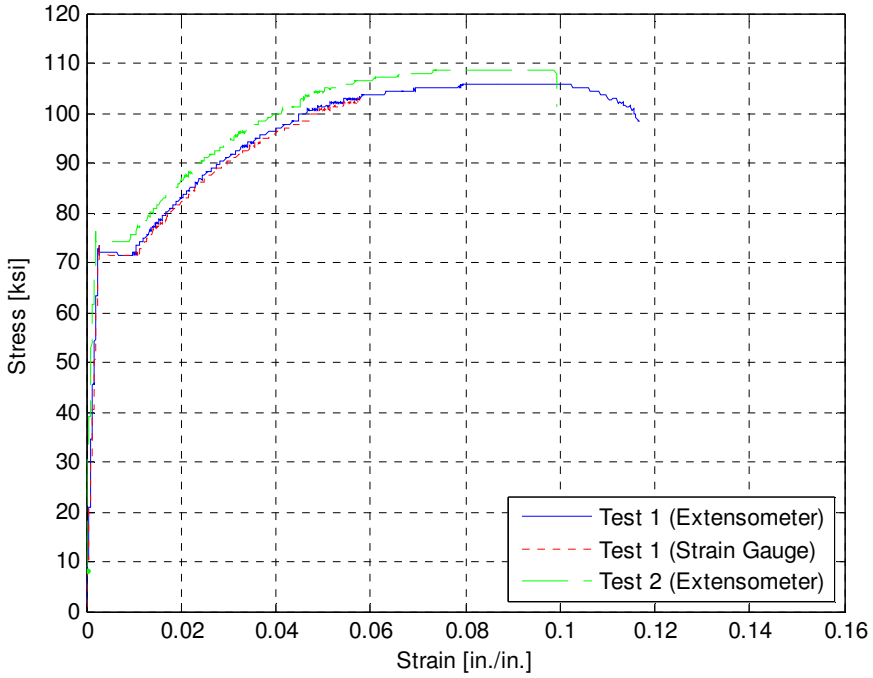

Figure A.2 Stress vs. strain relation for No. 4 bars.

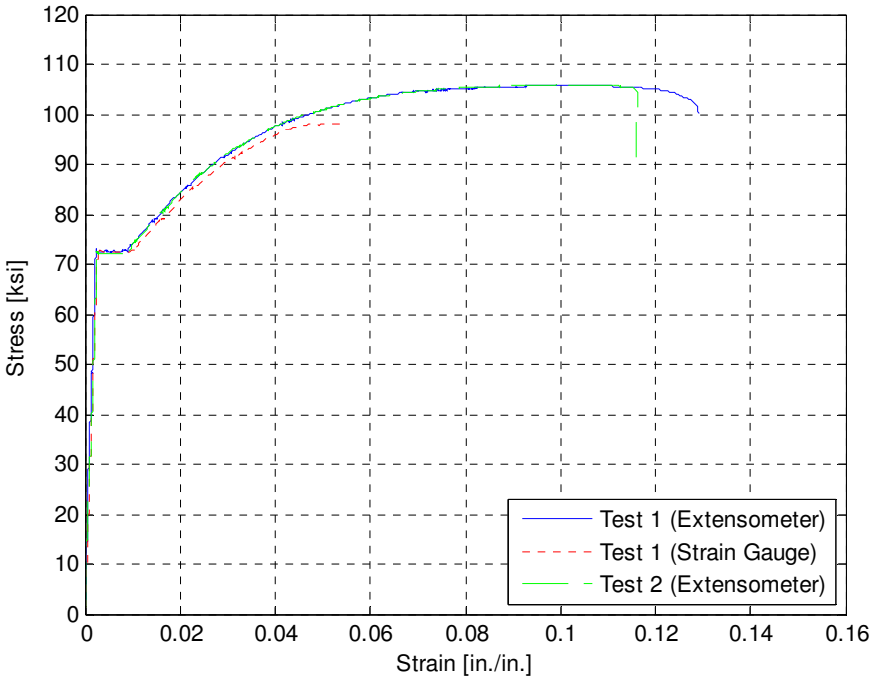

Figure A.3 Stress vs. strain relation for No. 6 bars.

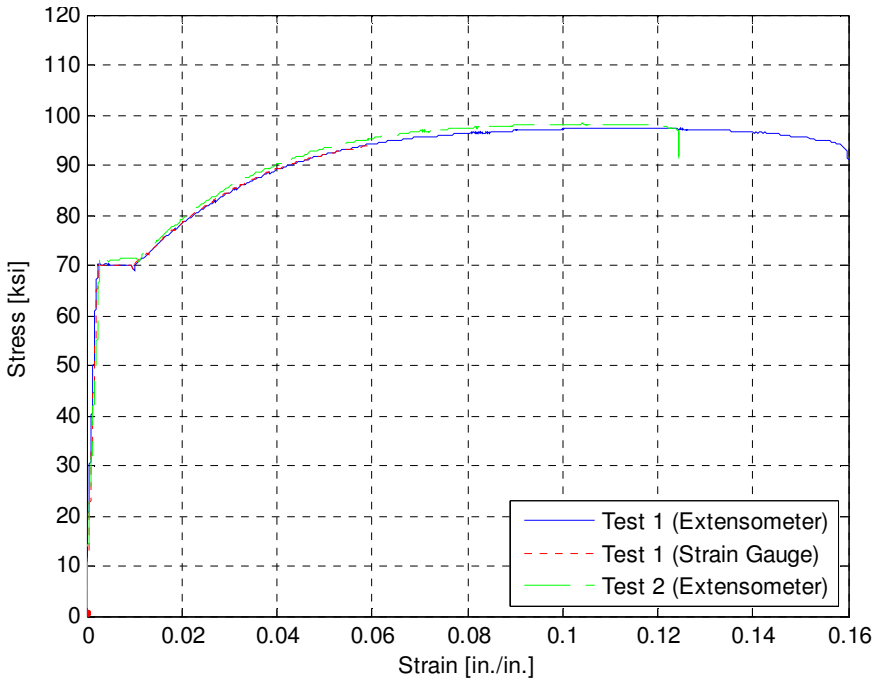

Figure A.4 Stress vs. strain relation for No. 7 bars.

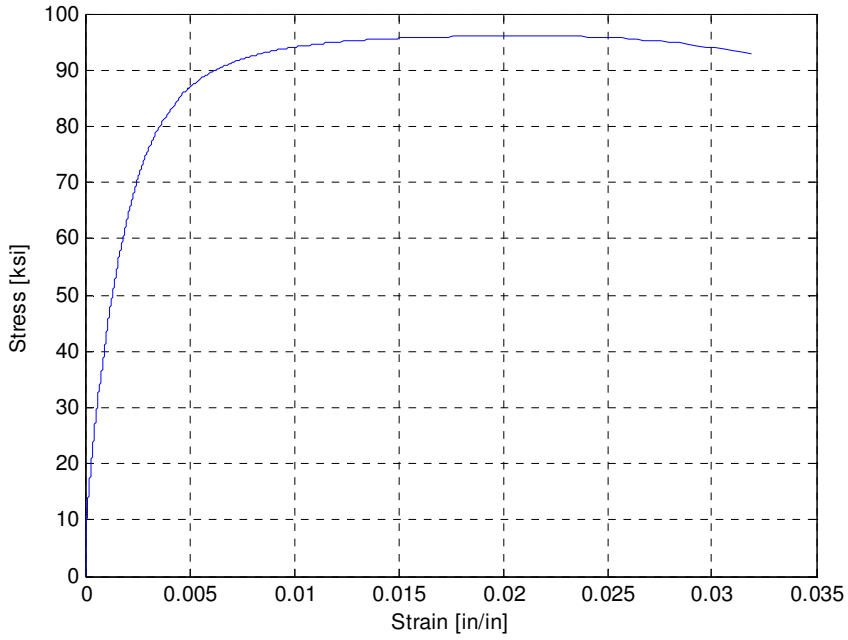

Figure A.5 Stress vs. strain relation for No. 3 AWG (Finnsson, 2013).

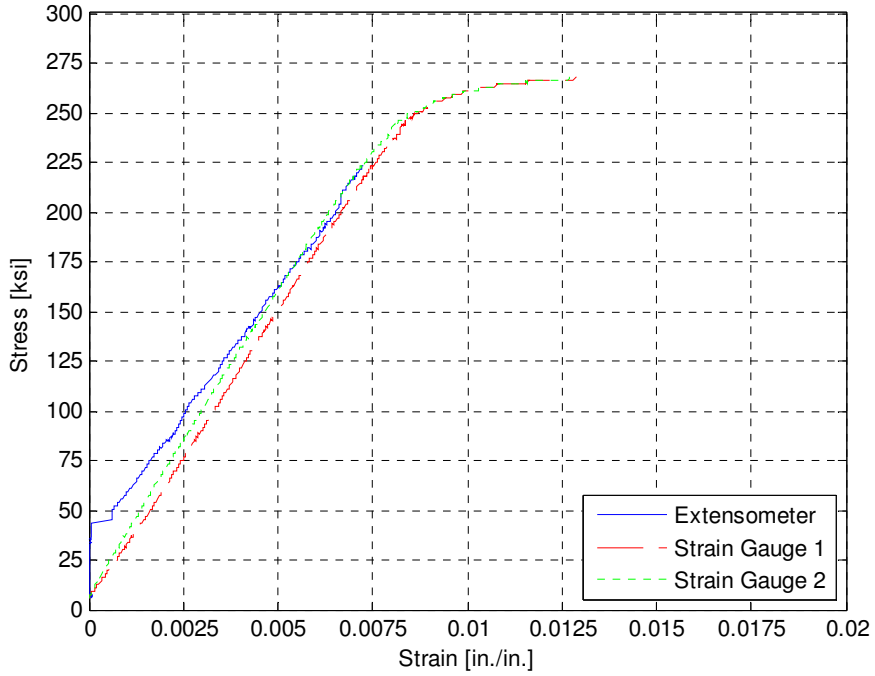

Figure A.6 Test 1 stress vs. strain relation for prestressing strand.

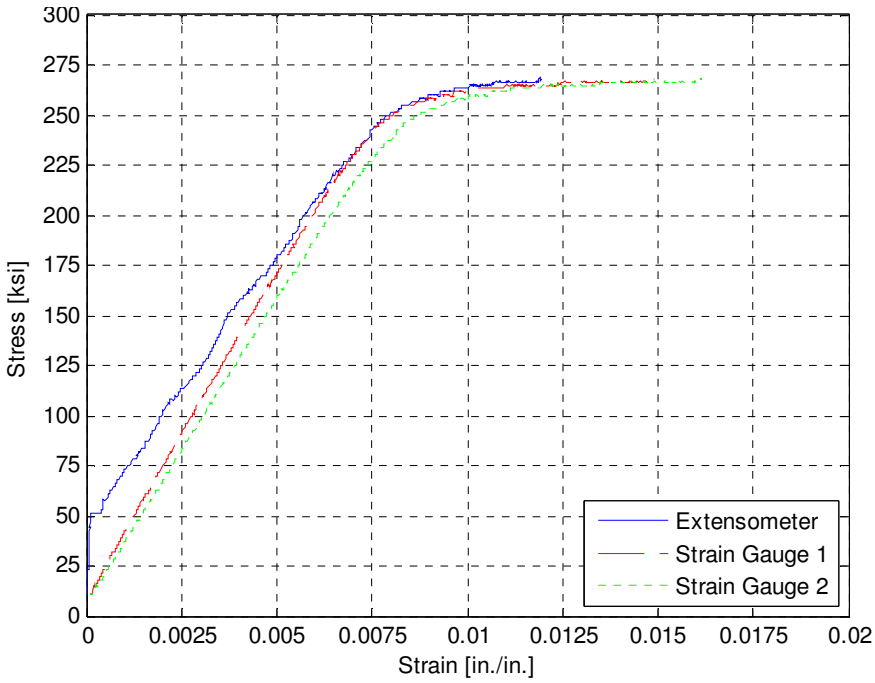

Figure A.7 Test 2 stress vs. strain relation for prestressing strand.

Table A.3 Summary of monotonic pull tests.

Size and Type	Main Construction Use	Tensile Yield Strength, $\bar{f}_y$ (ksi)	Ultimate Tensile Strength, $\bar{f}_u$ (ksi)	Modulus of Elasticity, $\bar{E}_s$ (ksi)
No. 3 Bar	Cap beam transverse reinforcement	73.4	105.3	35,600
No. 4 Bar	Column longitudinal reinforcement	73.1	107.3	31,000
No. 6 Bar	Column longitudinal reinforcement	72.4	106.0	29,600
No. 7 Bar	Cap beam longitudinal reinforcement	70.5	97.8	27,100
No. 3 AWG*	Column spiral reinforcement	86.3*	96.0*	30,500*
3/8 in., Epoxy Coated Strand	Prestressing strand	248.3‡	268.2	30,800 ♦

*Results for No. 3 AWG from Finnsson (2013).
‡Result determined by multiplying ultimate tensile strength by proportion of nominal yield to nominal ultimate strengths (250/270 ksi).
♦Result determined from strain gauge data.

Cyclic Tension Tests

Cyclic, tension tests were also completed for the prestressing strands. These tests were done in order to evaluate the point at which the strand stress was lost after increasing cyclic elongations of the strand; which was intended to lend insight on the suggested buckling behavior of the strands during the cyclic displacement of the column. The tests were conducted under a combination of load, deformation, and displacement control. The tests began by first elongating the strand to the designed effective prestressing force (approximately 14.0 kip). The strand was then elongated to increasing levels of strain (controlled by monitoring the strain gauge readings). After reaching an

increased level of strain, the strand was "unstretched" until the elongation of the strand returned to the elongation at the original 14.0 kip prestressing force (controlled by monitoring the displacement of the 300-kip loading head with a linear potentiometer). After returning the strand to its original prestressing length, the strand was then tensioned to a strain that was higher than the previous cycle. The first test was conducted by anchoring the strand in the jaws of the 300-kip Baldwin. This resulted in a local stress concentration at the jaws, and a relatively low level of measured ductility for the strand. The second test was conducted by anchoring the strand with $^{3}/_{8}$ in. diameter strand chucks (the same that were used during the construction of the PreT-CB-ROCK). This anchorage mitigated the local stress concentration and resulted in a much higher measured tensile strength and ductility (when compared to Baldwin jaws anchorage). Due to geometric constraints of the loading machine and test setup, it was not possible to fracture the strand that was anchored with strand chucks. Figure A.8 and Figure A.9 give stress versus strain results from these tests. The strand strain in the figures was calculated by taking the average between two strain gauge readings, the stress was calculated by dividing the force reading from the Baldwin by the nominal area of the strand. Table A.4 provides a summary of the results, it is noted that the reported values for the modulus of elasticity were calculated using readings from the initial loading.

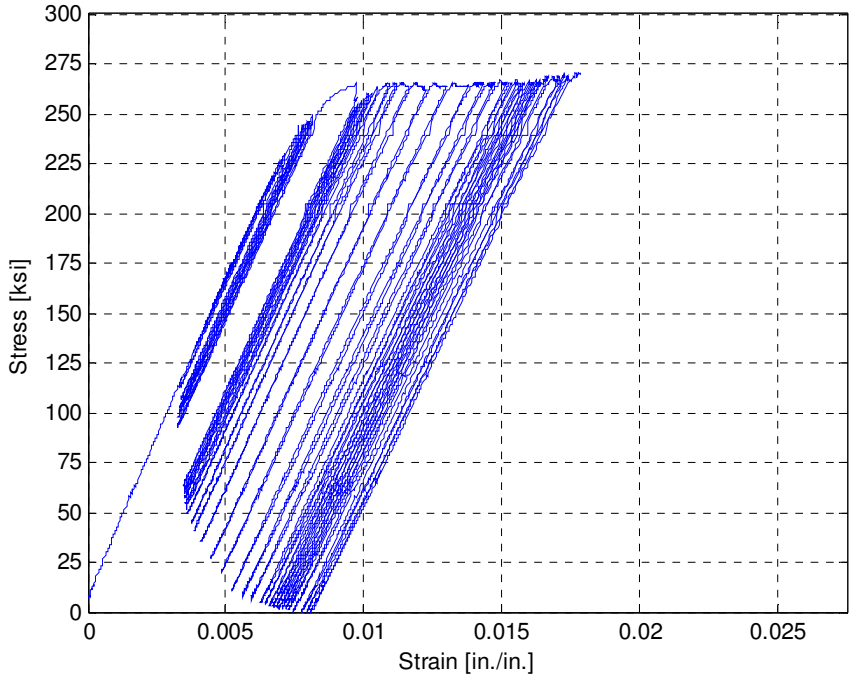

Figure A.8 Baldwin jaws anchored, cyclic strand test using strain gauge readings.

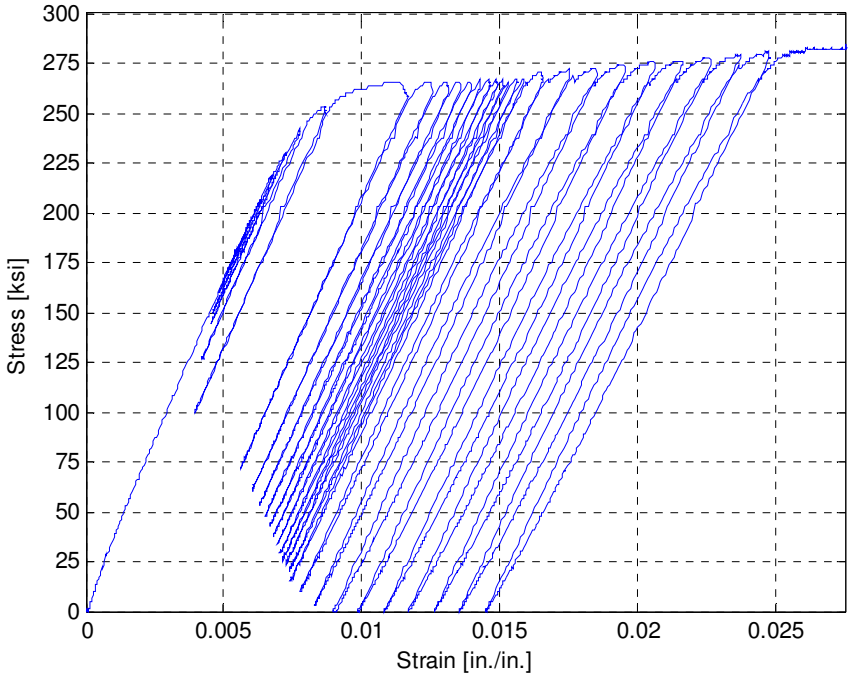

Figure A.9 Chuck anchored, cyclic strand test using strain gauge readings.

Table A.4 Summary of cyclic strand tests.

Size and Type	Anchorage	Tensile Yield Strength, f_y (ksi)	Ultimate Tensile Strength, f_u (ksi)	Modulus of Elasticity, E_s (ksi)
3/8 in., Epoxy Coated Strand	Baldwin jaws	250.4‡	270.4	32,100
3/8 in., Epoxy Coated Strand	Strand chucks	N/A	>301.4*	32,600

*Strand was unable to be fractured due to geometric configuration of the test setup. The reported stress was the highest measured during the test.

‡Result determined by multiplying ultimate tensile strength by proportion of nominal yield to nominal ultimate strengths (250/270 ksi).

In the plots of Figure A.8 and Figure A.9, it was observed that the measured strain did not return to the same reading at the "valley" of each elongation cycle. That is, when the strand was elongated to a strain that was larger than the maximum of the previous cycle, and the loading head of the Baldwin was then moved to the position at the design effective prestressing force, the strain gauge measurement did not return to the same minimum value as was read from the previous cycle. Therefore, the following two plots, Figure A.10 and Figure A.11, give stress versus strain results using displacement readings from a linear potentiometer that was attached to the loading head of the Baldwin (in these plots, strain was calculated by dividing the original specimen length by the

displacement reading of the potentiometer. These plots show that the strand elongation was indeed returned to the same value at the "valley" of every cycle, but the resulting stiffness appeared to be highly non-linear. This was likely a result of the strand slipping in the anchorage of the Baldwin jaws or chuck (the loading head was displaced which suggested increasing strain, but this measured elongation was not matched with an incremental increase in force due to the slipping).

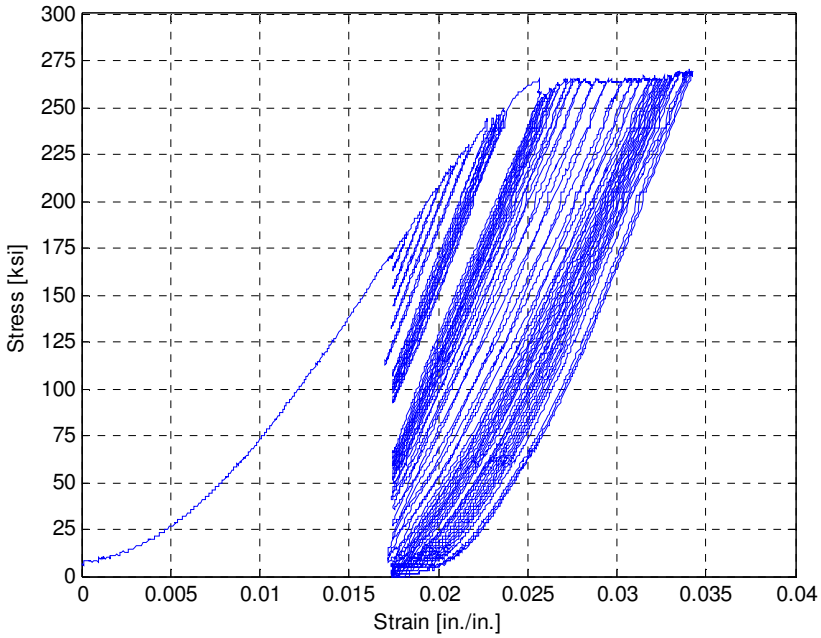

Figure A.10 Baldwin jaws anchored, cyclic strand test using loading head displacement to calculate strain.

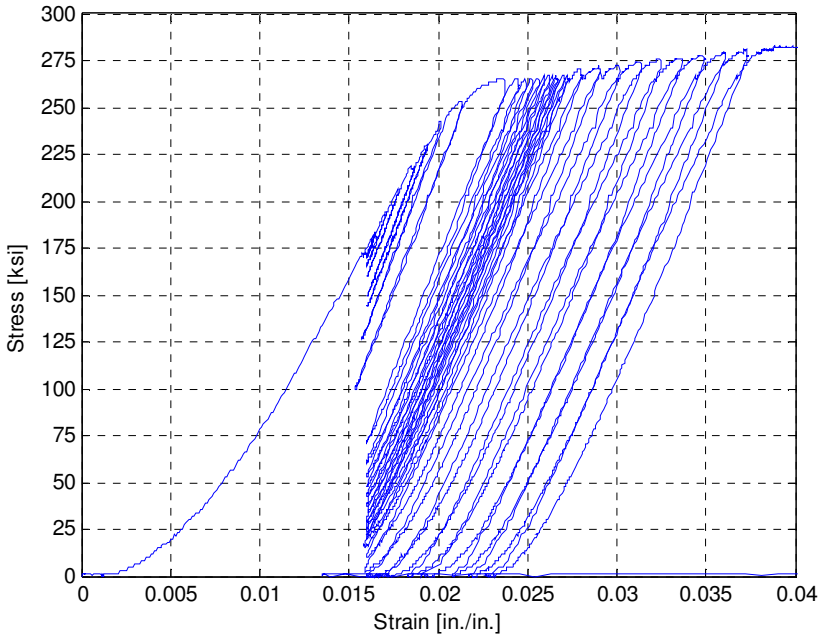

Figure A.11 Chuck anchored, cyclic strand test using loading head displacement to calculate strain.

Appendix B: Specimen Drawings

COLUMN

Figure B.1 Column isometric.

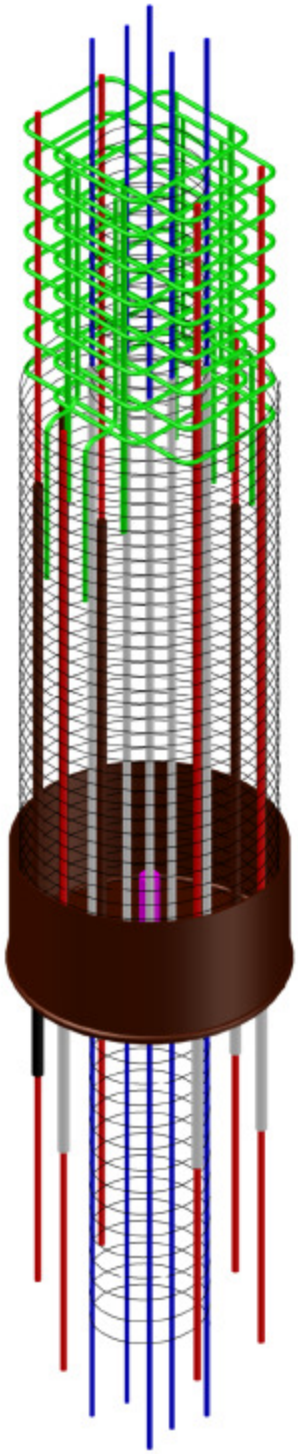

Figure B.2 Column reinforcement isometric.

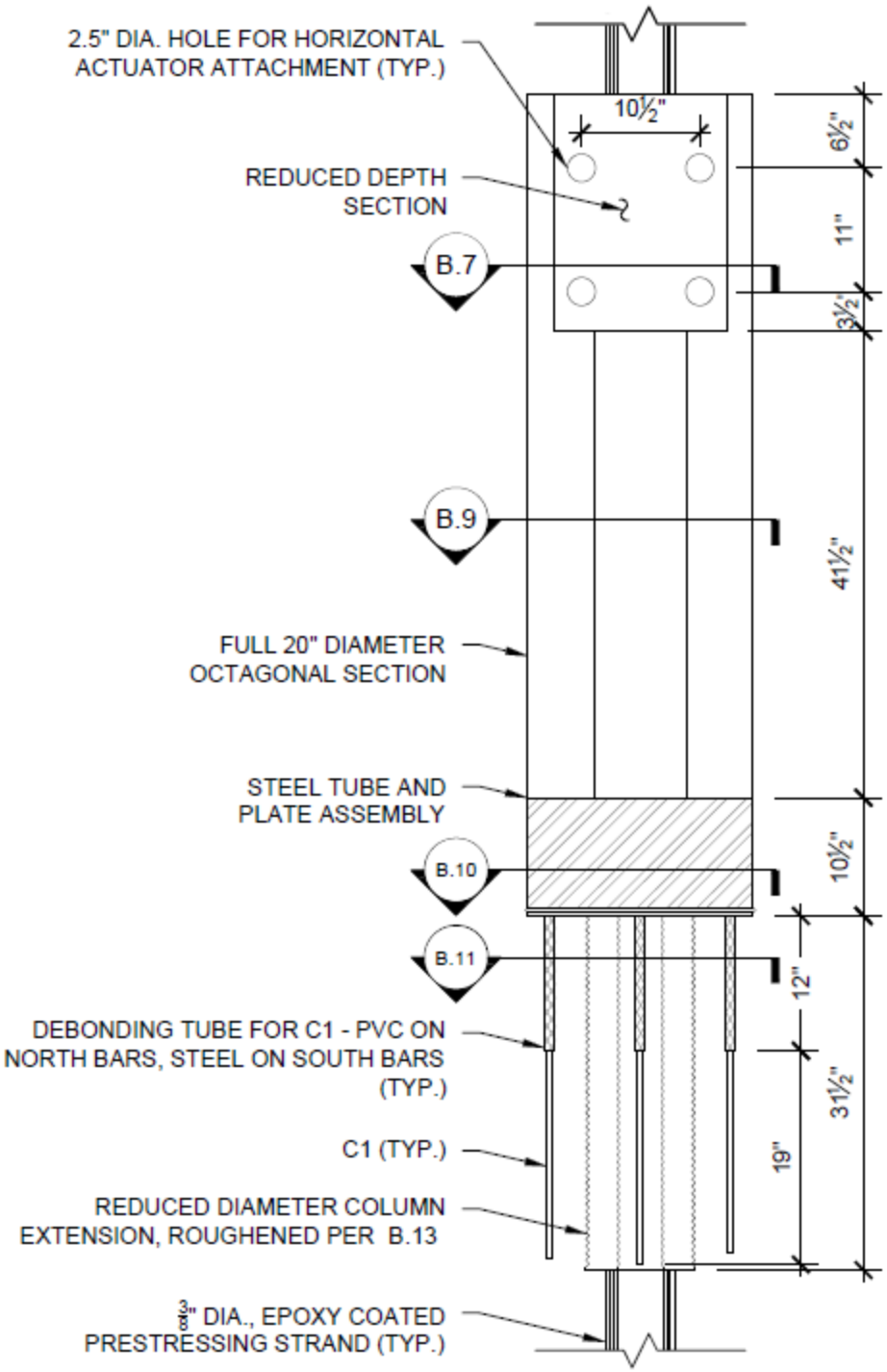

Figure B.3 Column north elevation.

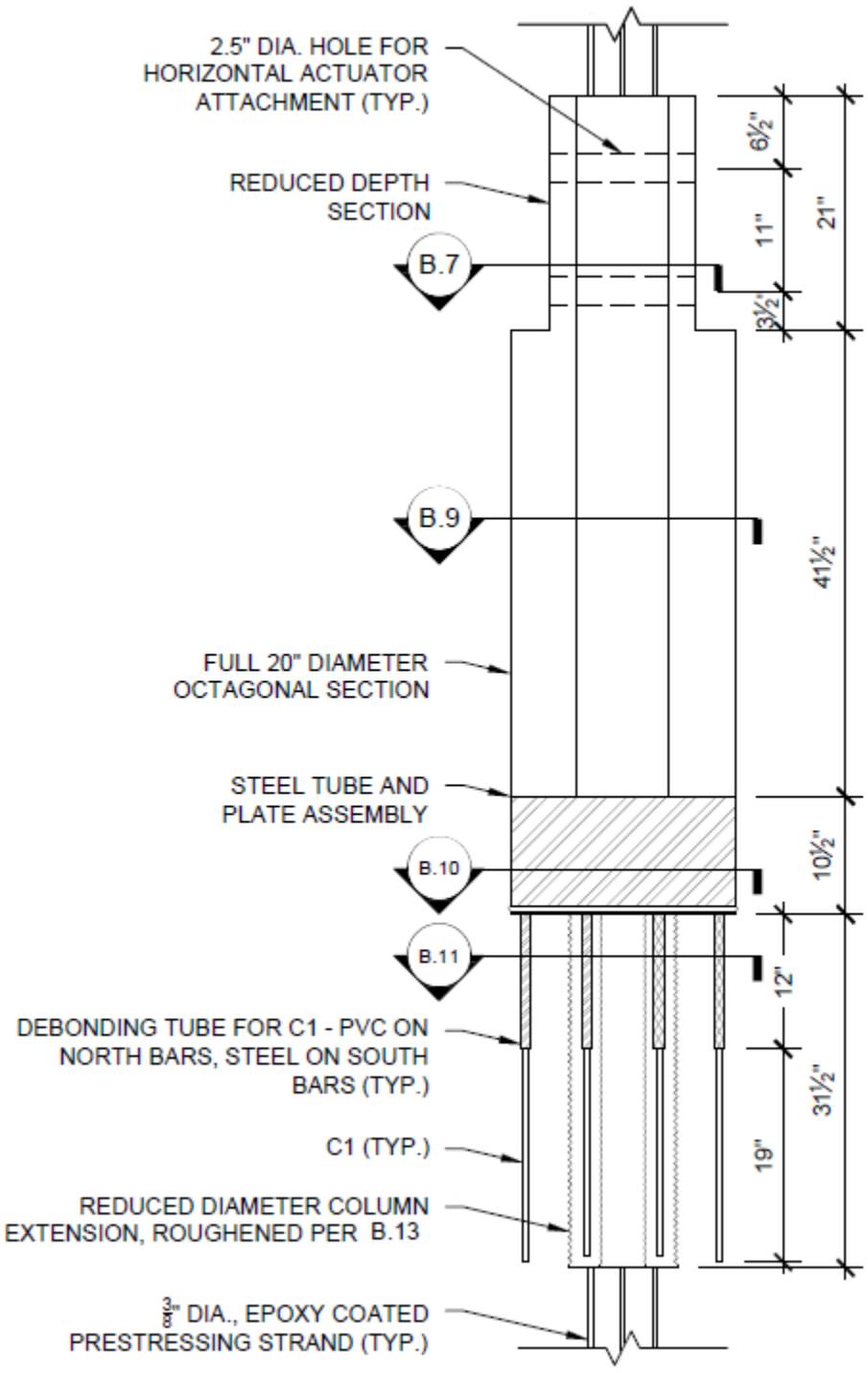

Figure B.4 Column east elevation.

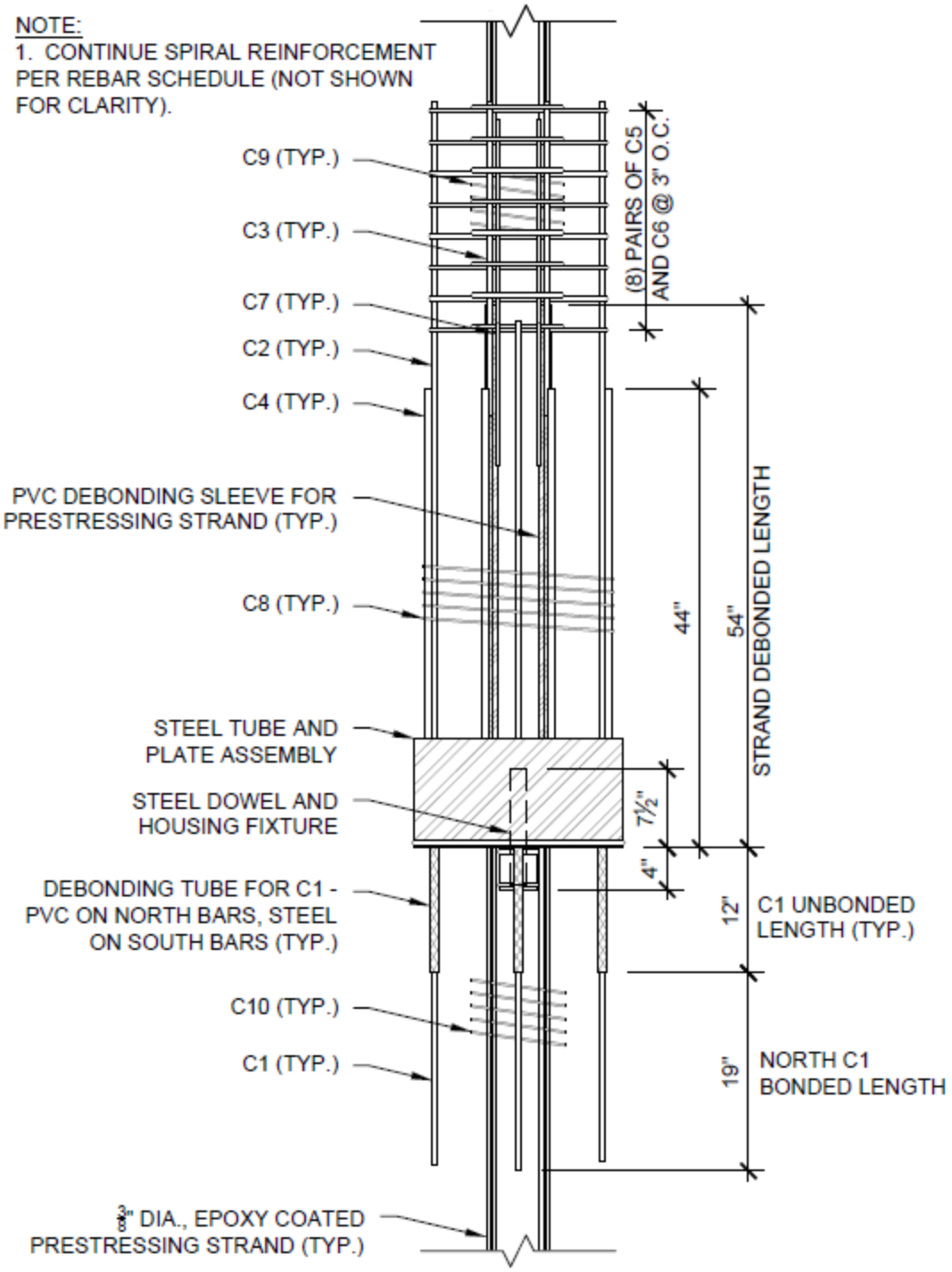

Figure B.5 Column reinforcement north elevation.

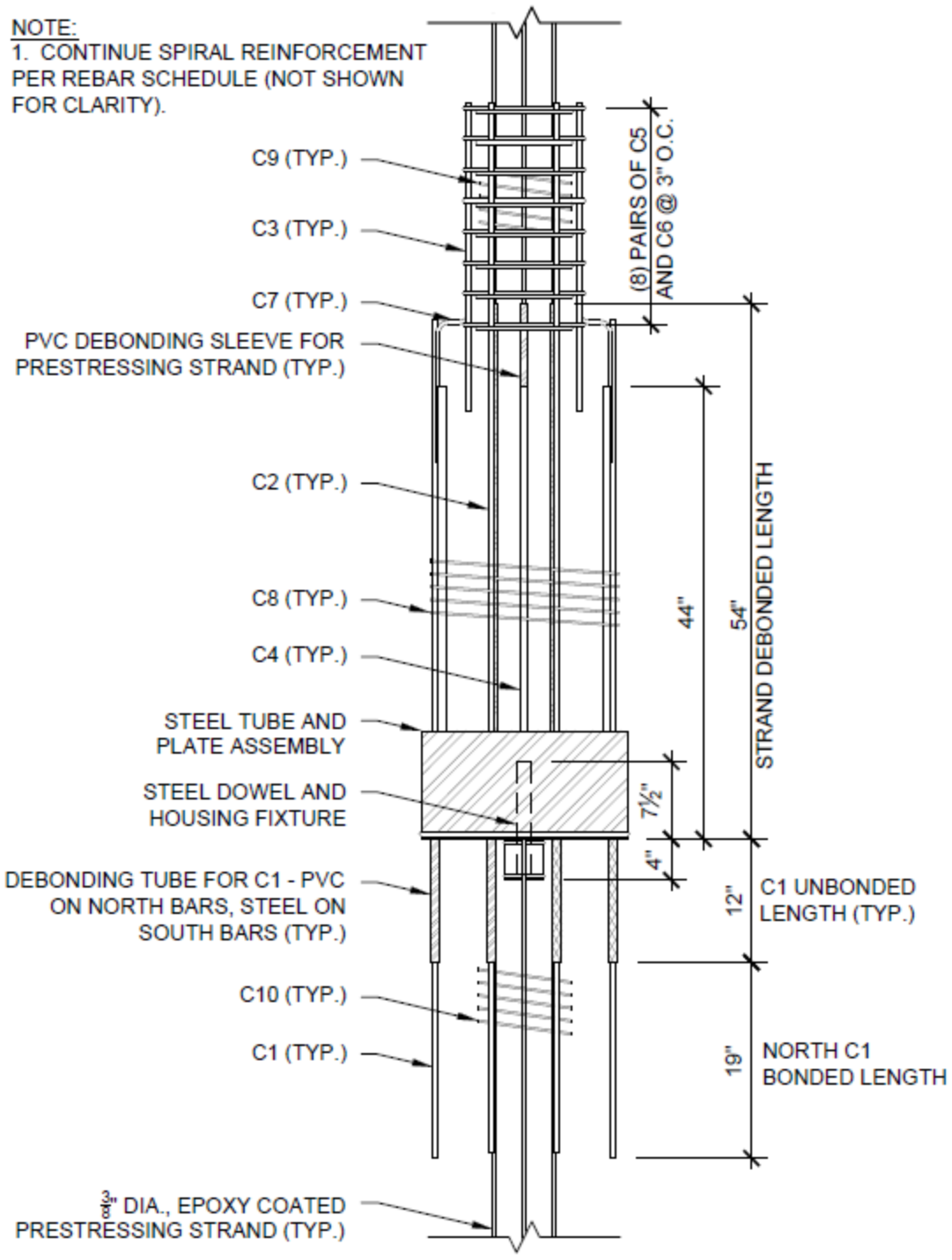

Figure B.6 Column reinforcement east elevation.

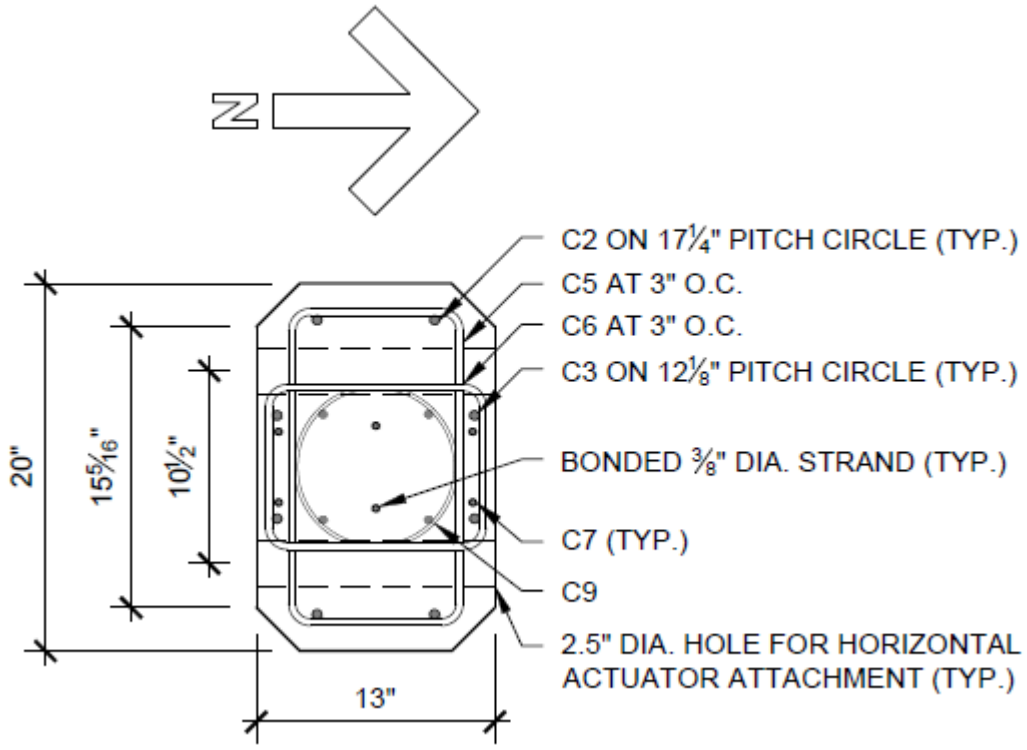

Figure B.7 Column section – reduced depth.

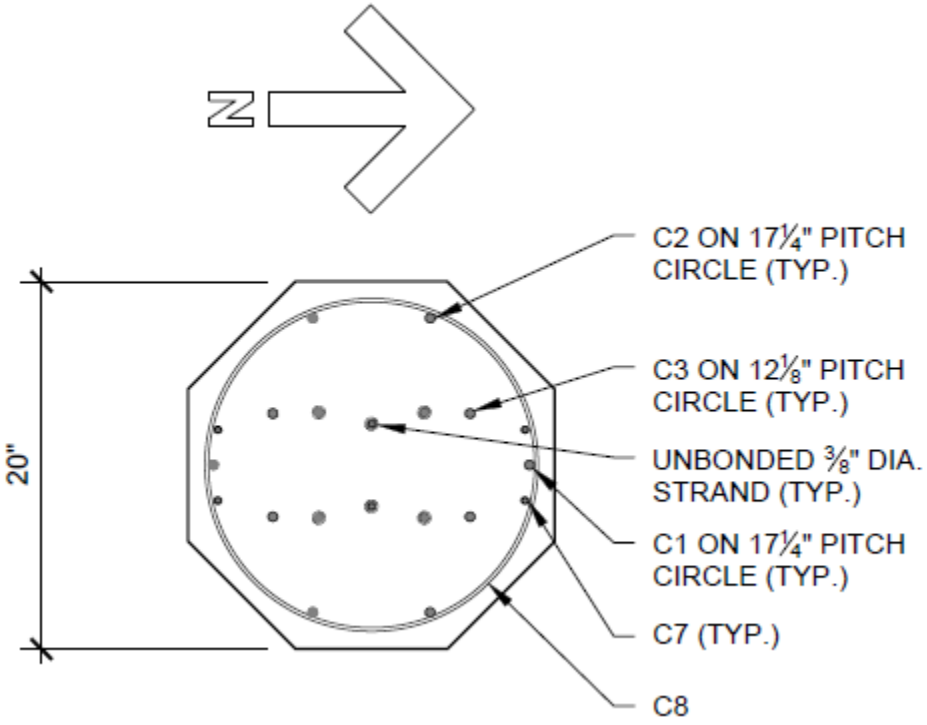

Figure B.8 Column section – over reinforced top.

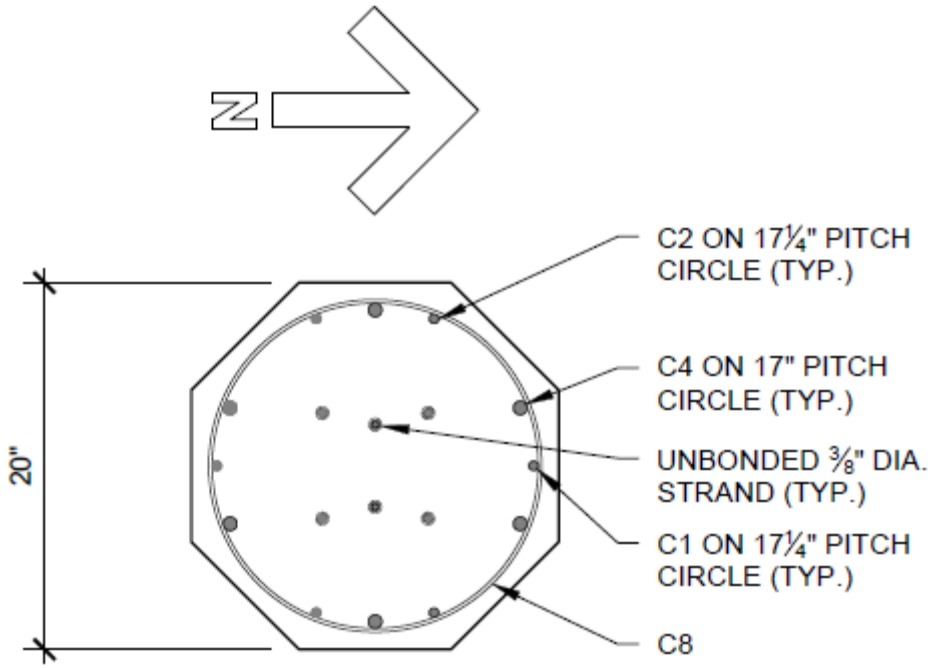

Figure B.9 Column section – typical.

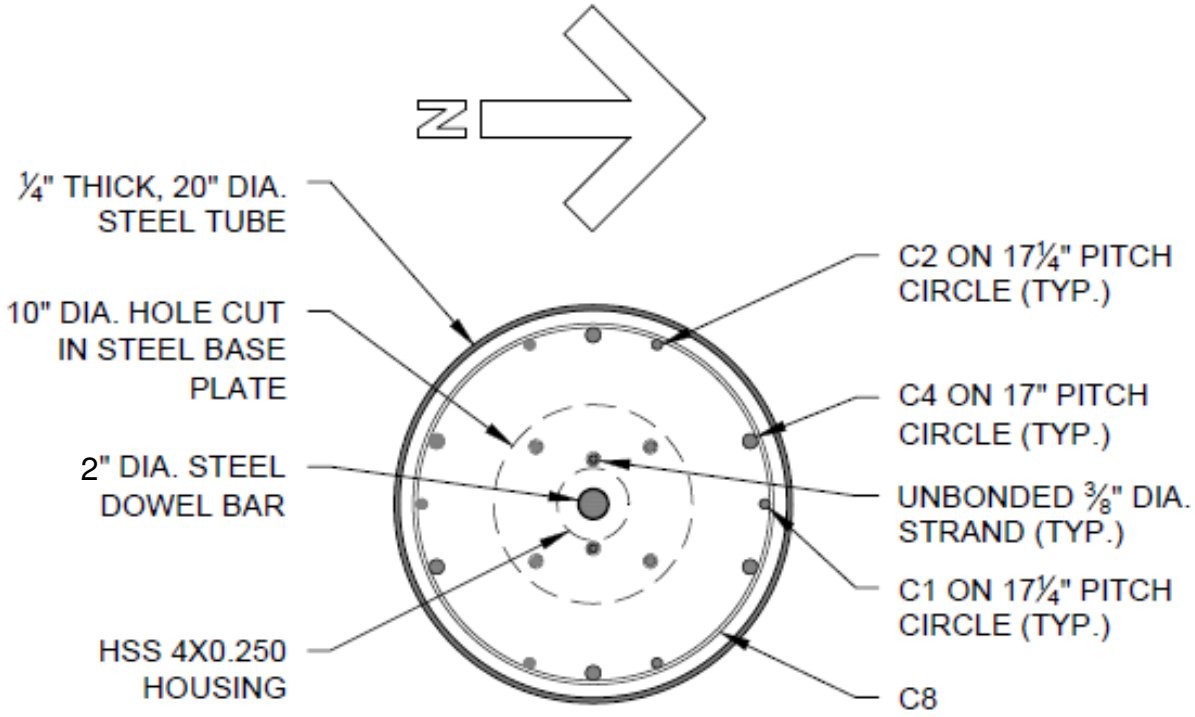

Figure B.10 Column section – steel tube.

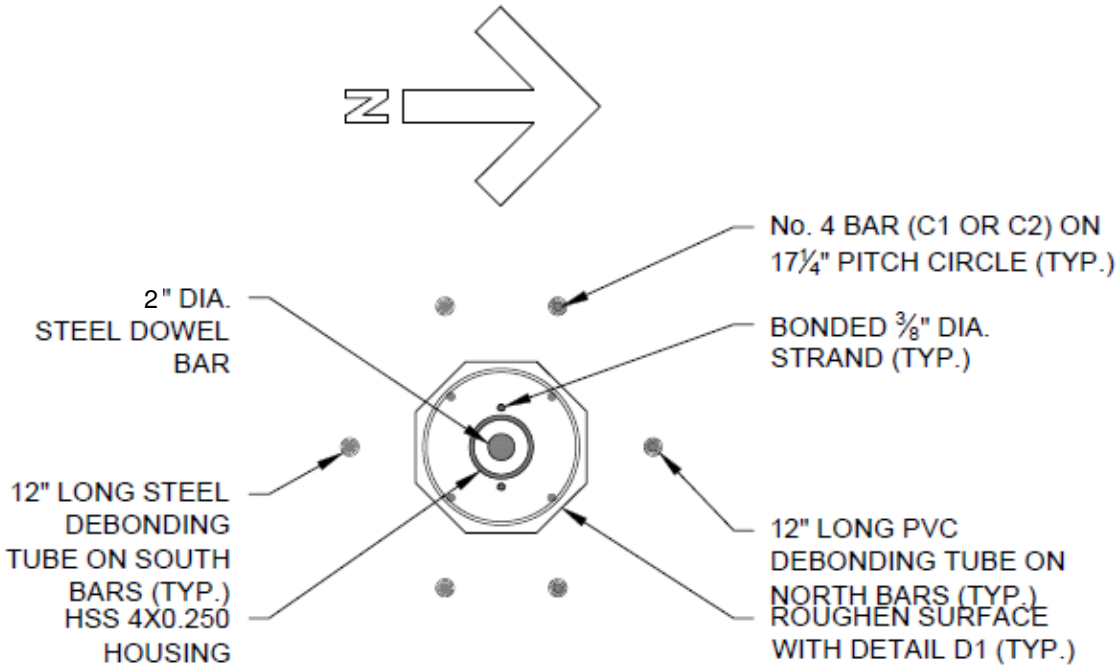

Figure B.11 Column section – reduced diameter.

COLUMN DETAILS

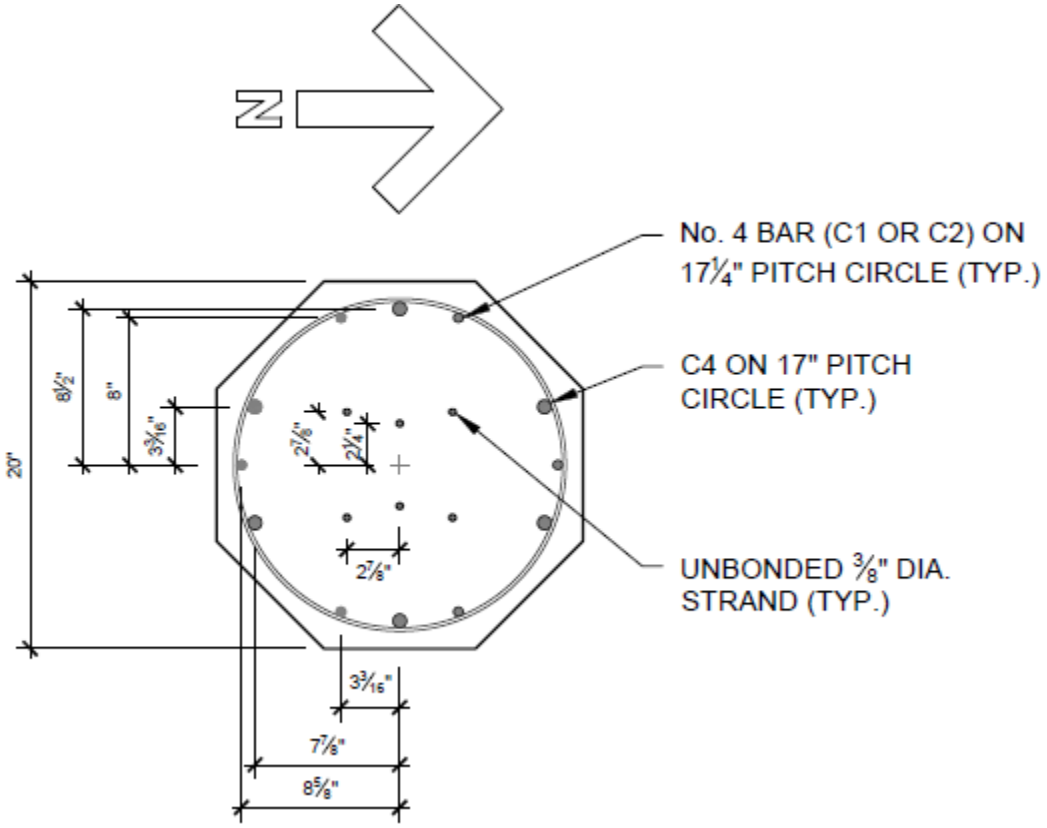

Figure B.12 Detail – column reinforcing layout.

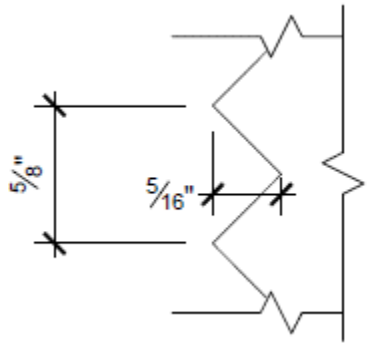

Figure B.13 Detail – roughened surface.

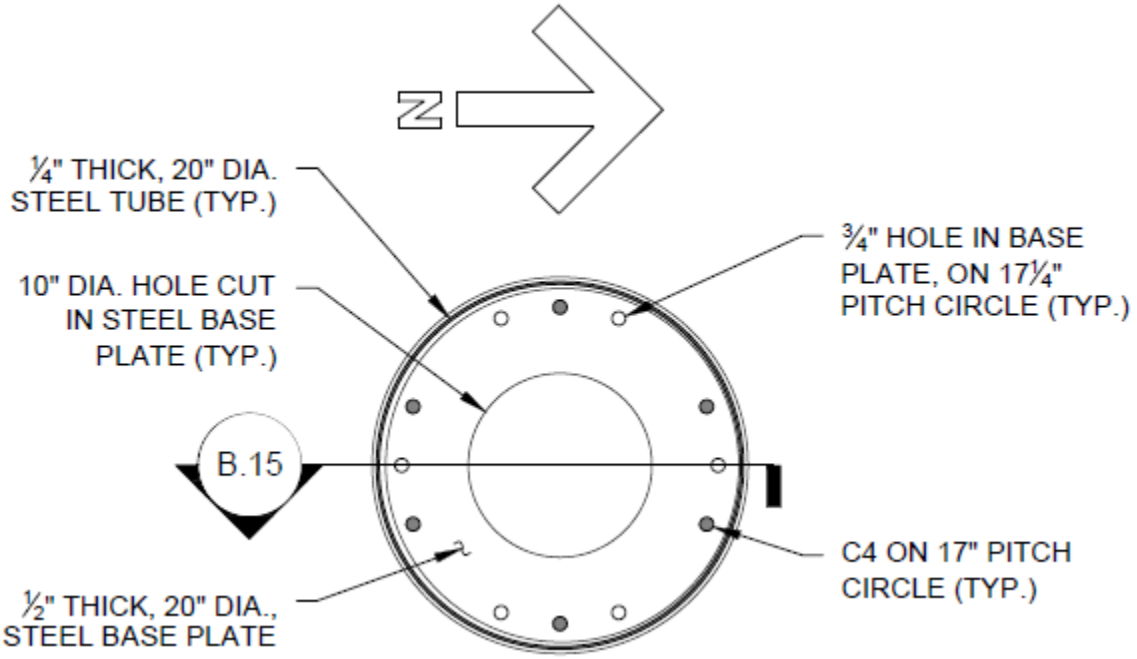

Figure B.14 Detail – steel tube and plate plan view.

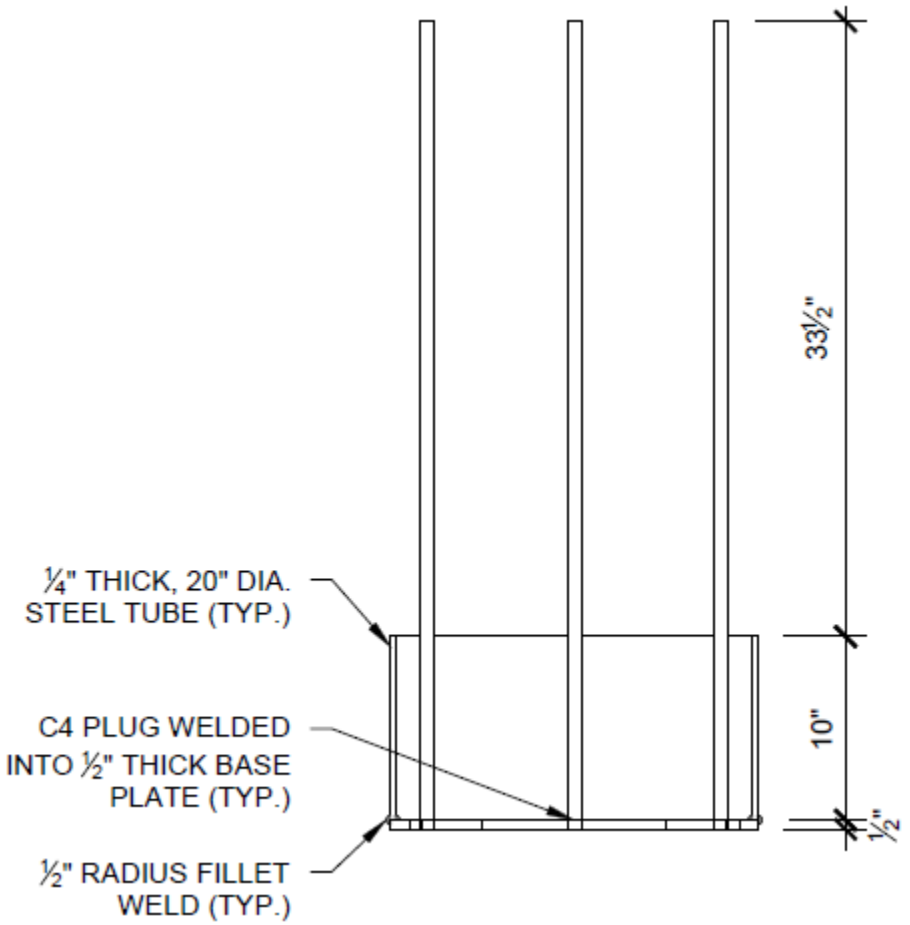

Figure B.15 Detail – steel tube and plate section.

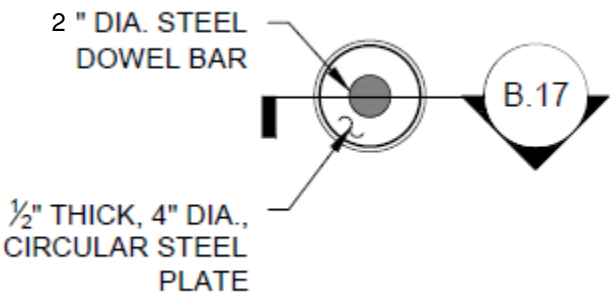

Figure B.16 Detail – dowel plan.

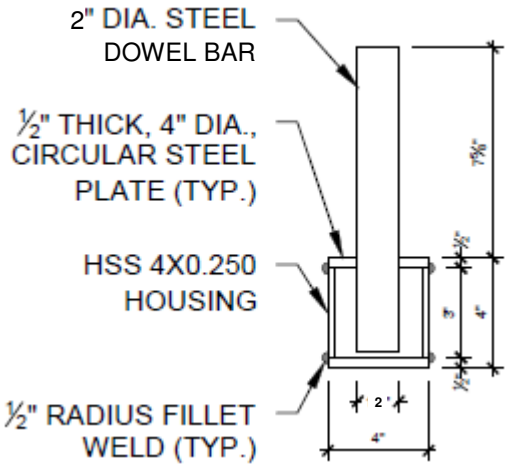

Figure B.17 Detail – dowel section.

CAP BEAM

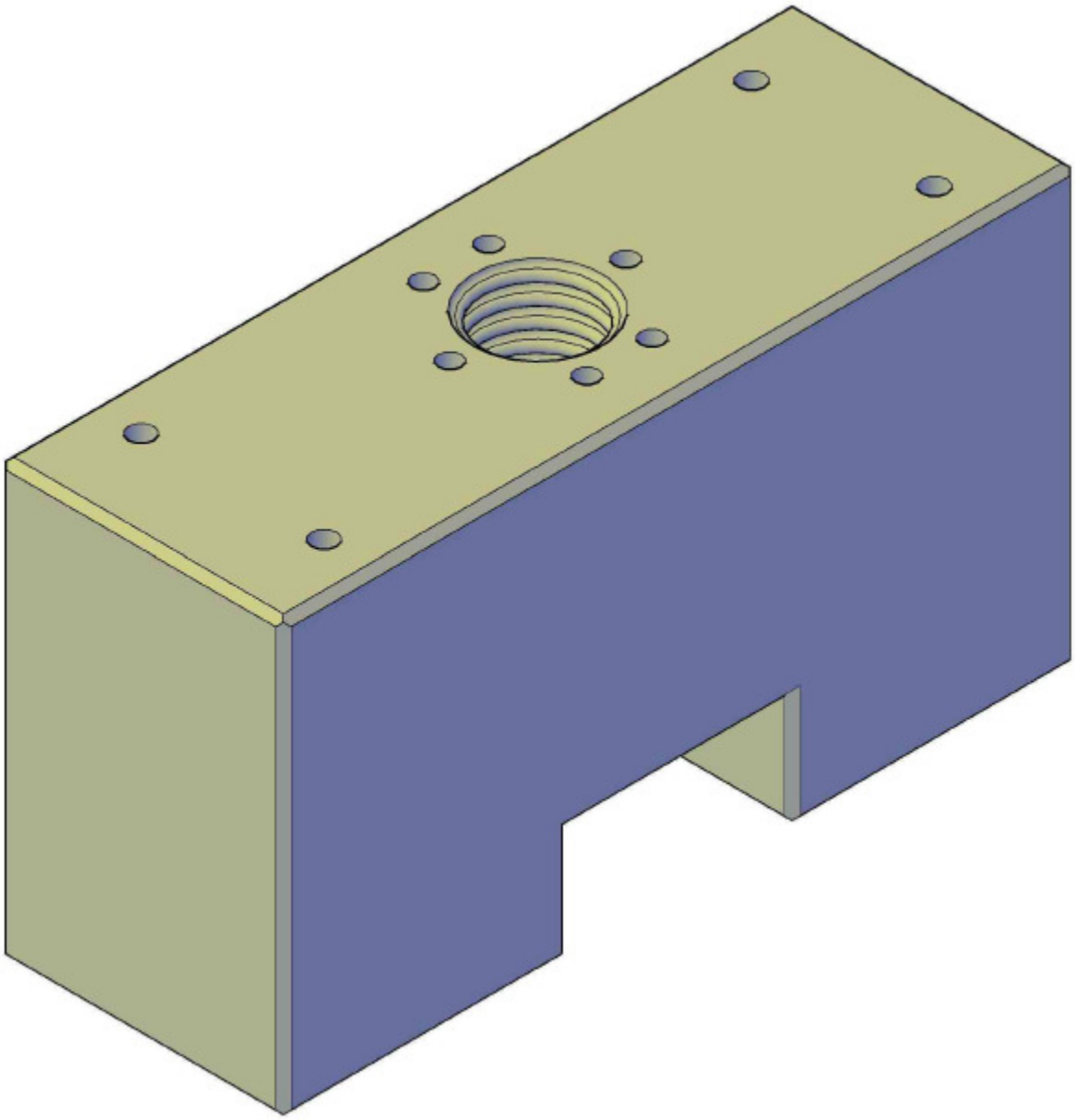

Figure B.18 Cap beam isometric.

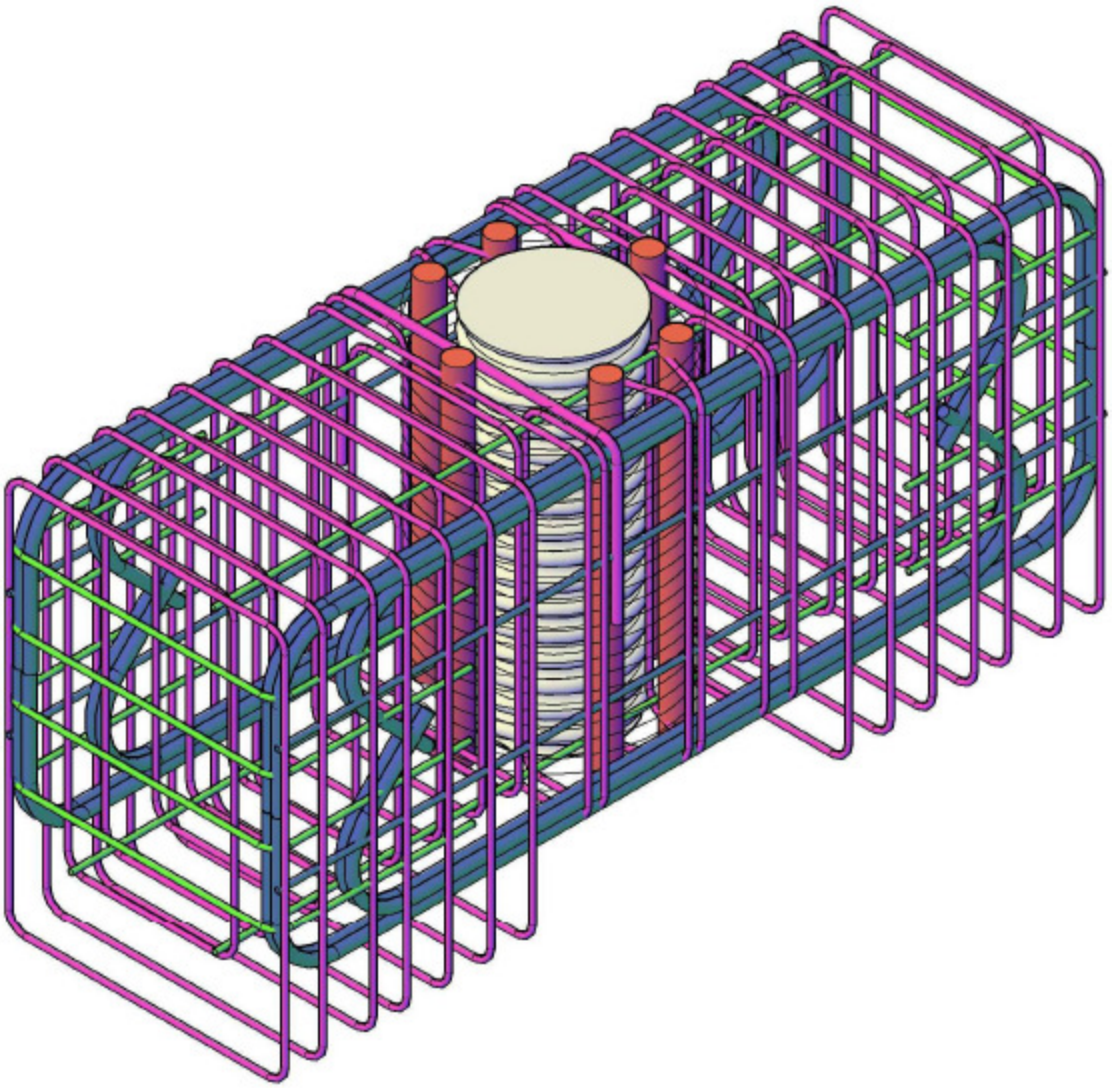

Figure B.19 Cap beam reinforcement isometric.

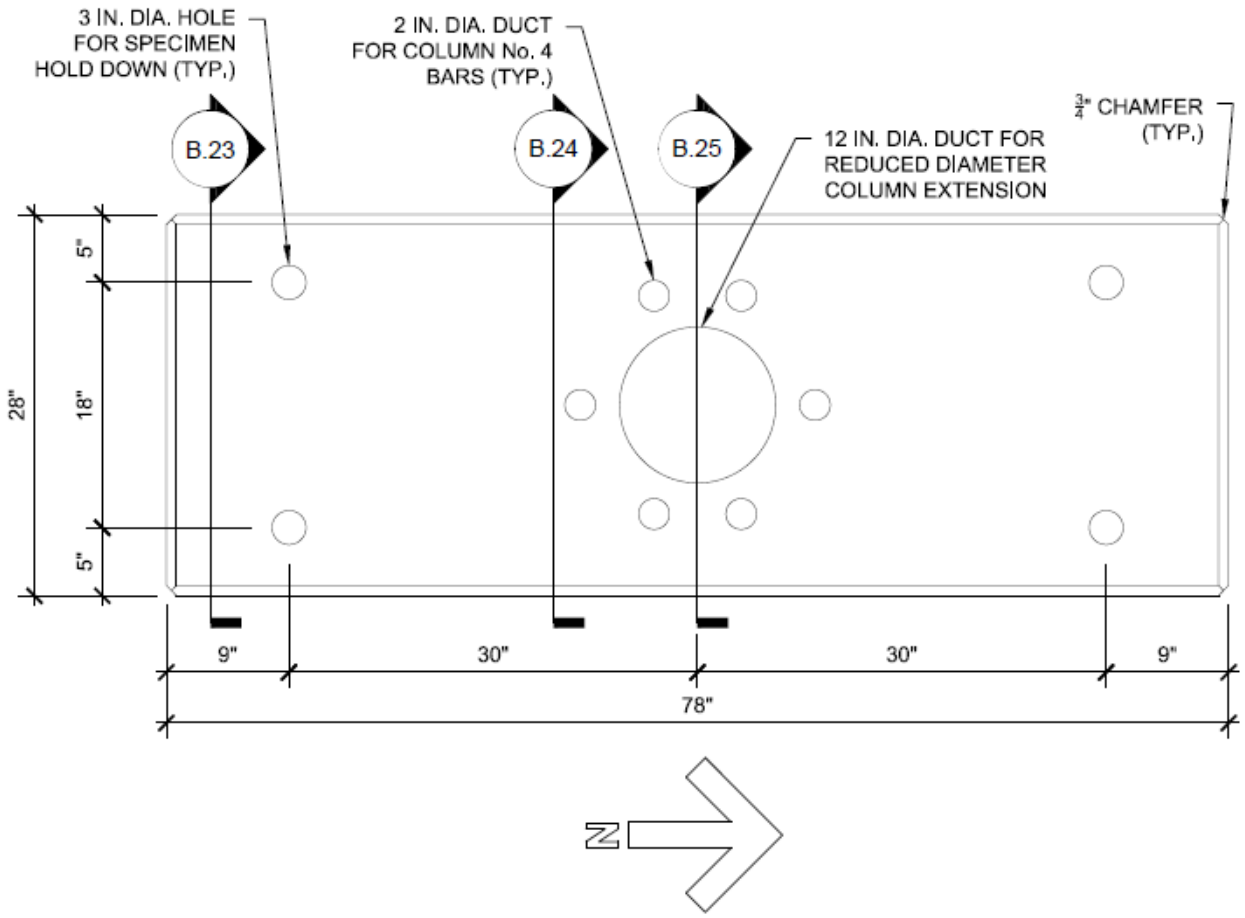

Figure B.20 Cap beam plan.

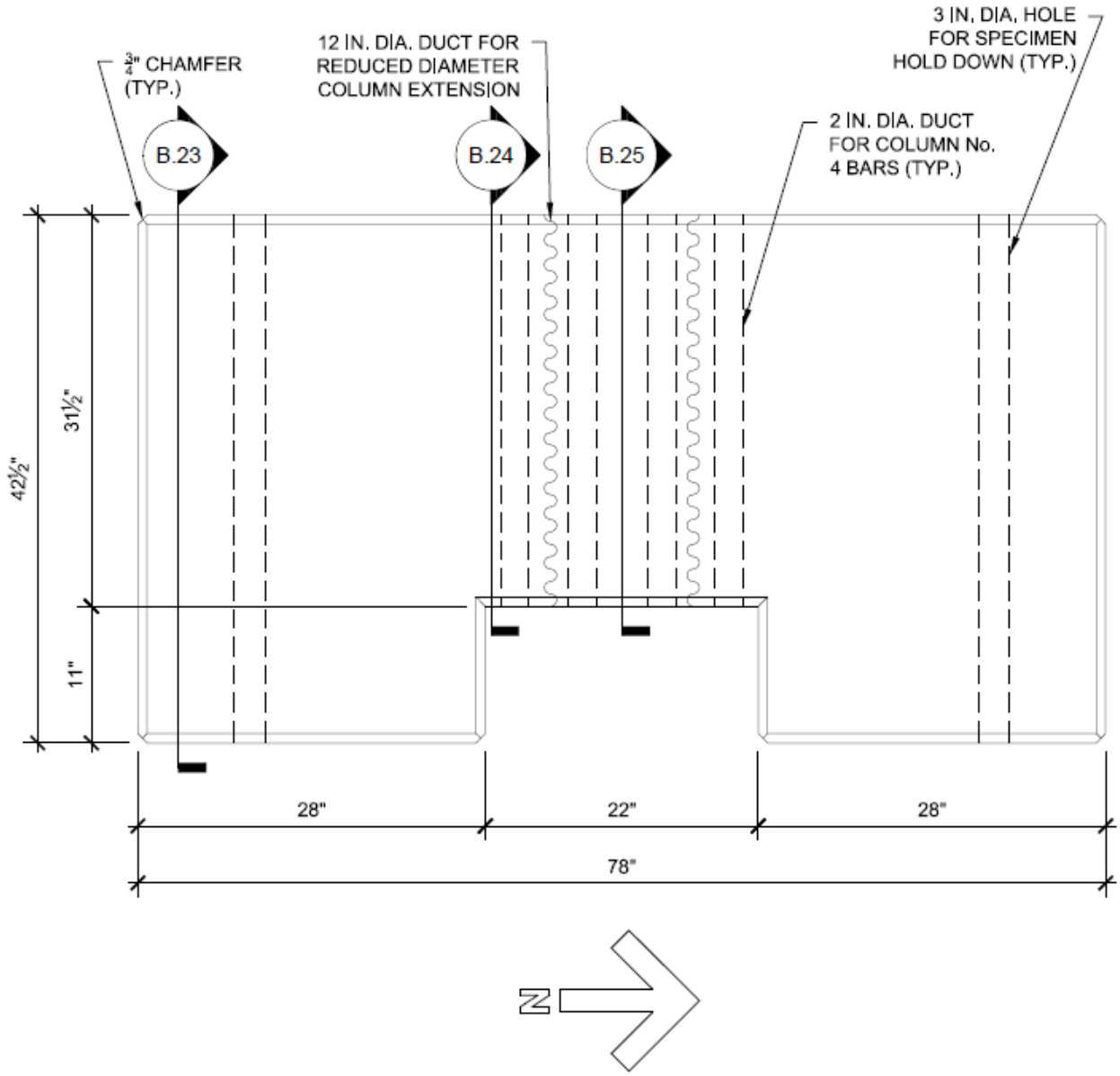

Figure B.21 Cap beam east elevation.

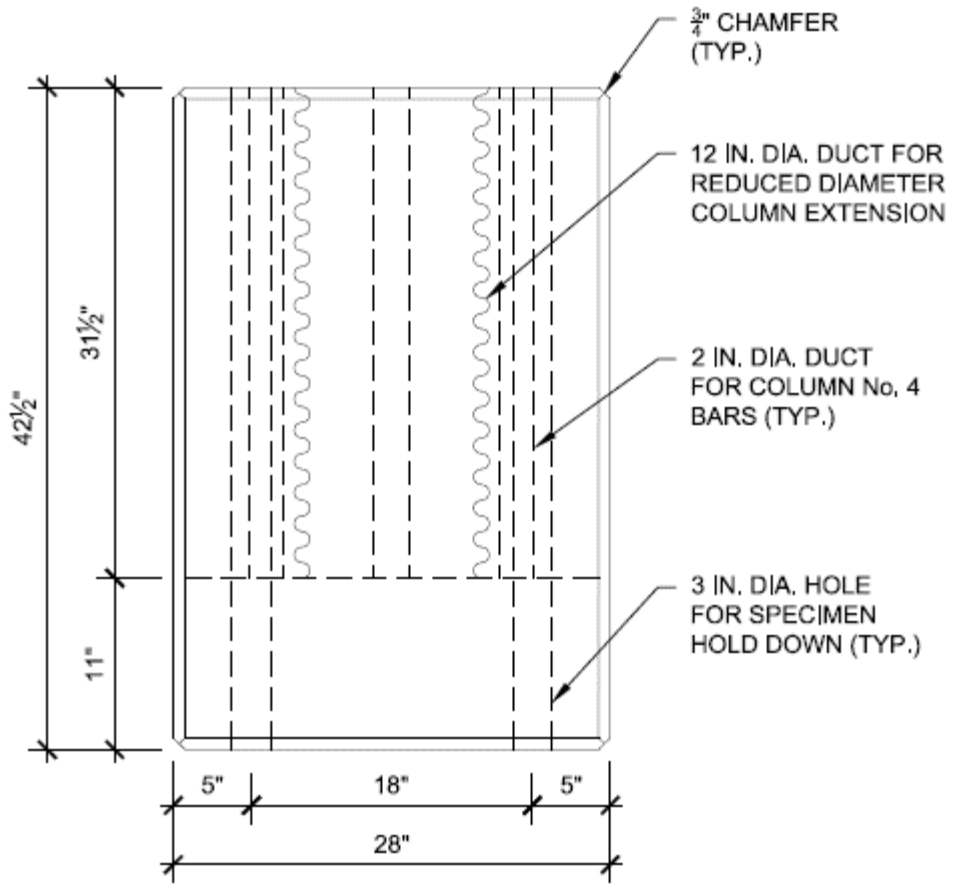

Figure B.22 Cap beam north elevation.

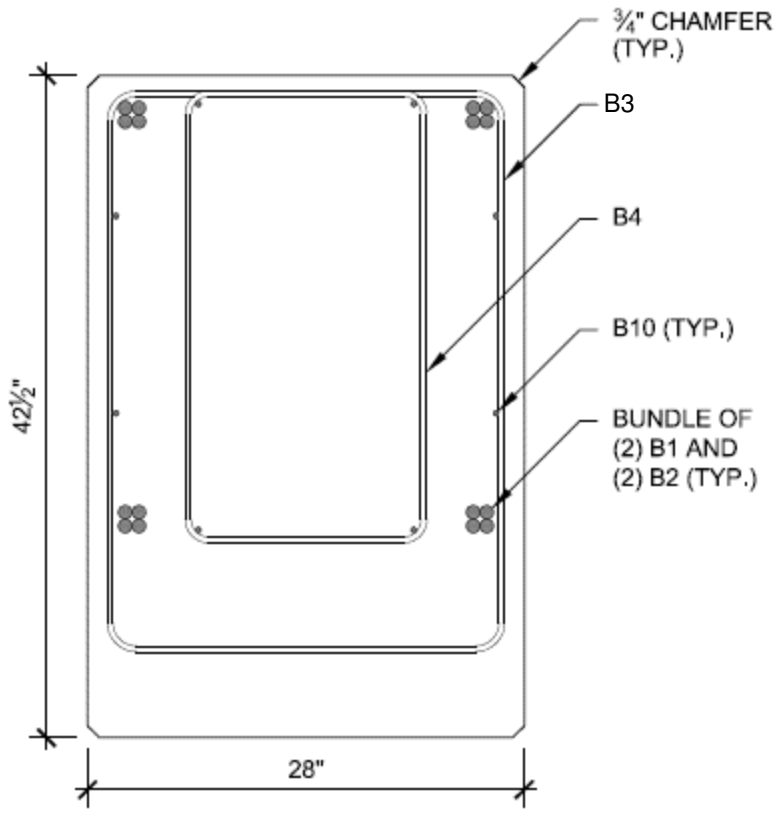

Figure B.23 Cap beam section at 42.5 in. depth.

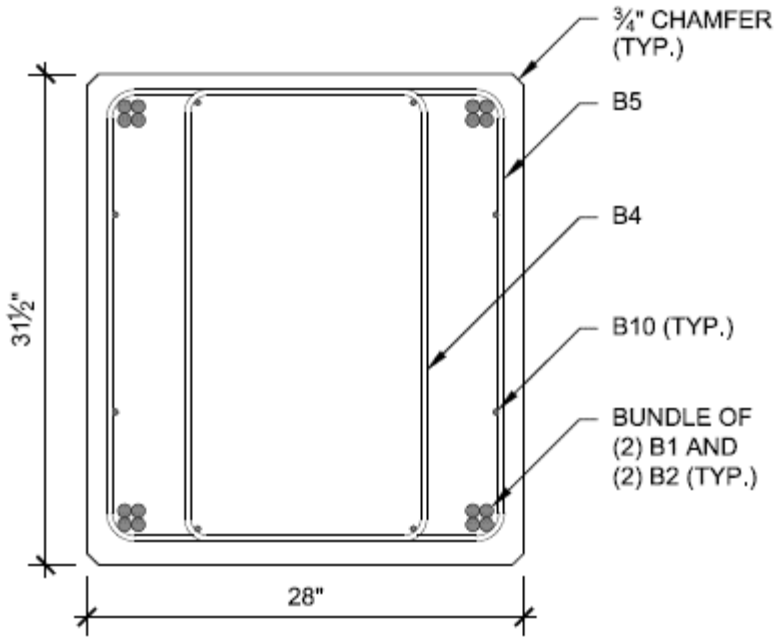

Figure B.24 Cap beam section at 31.5 in. depth.

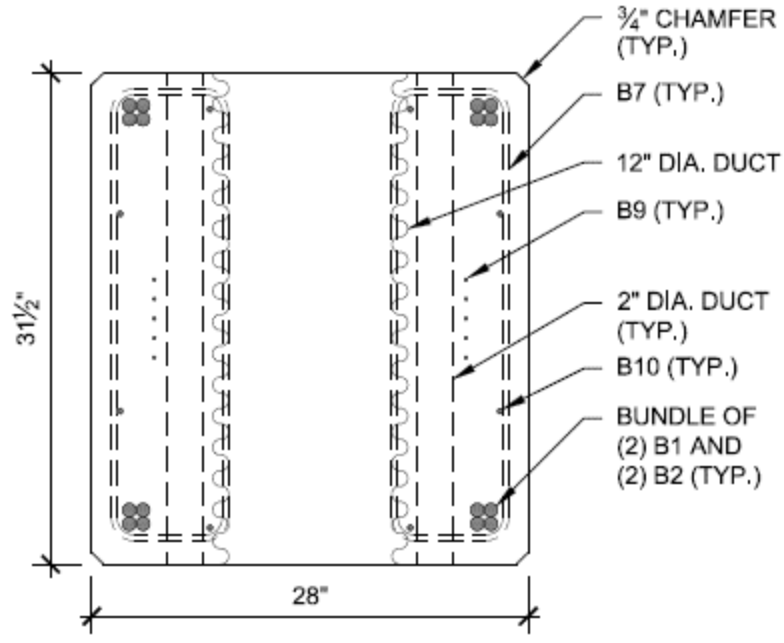

Figure B.25 Cap beam section at central duct.

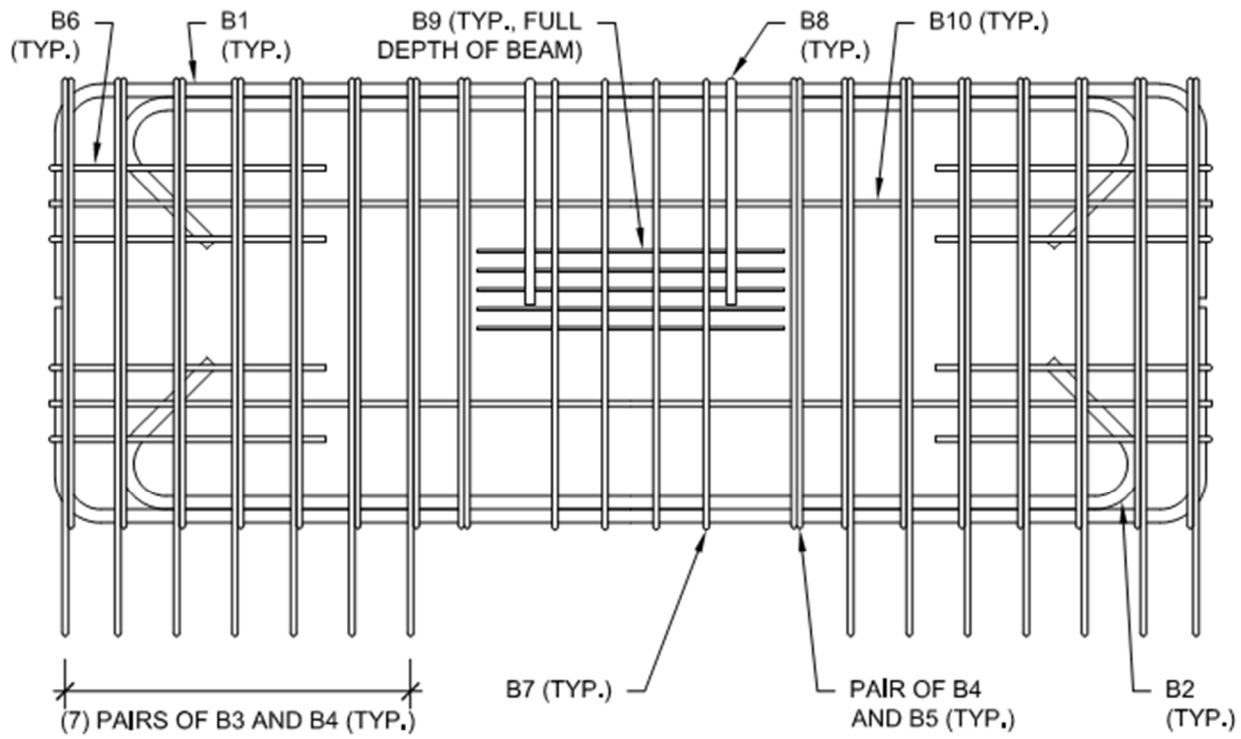

Figure B. 26 Cap beam reinforcement elevation.

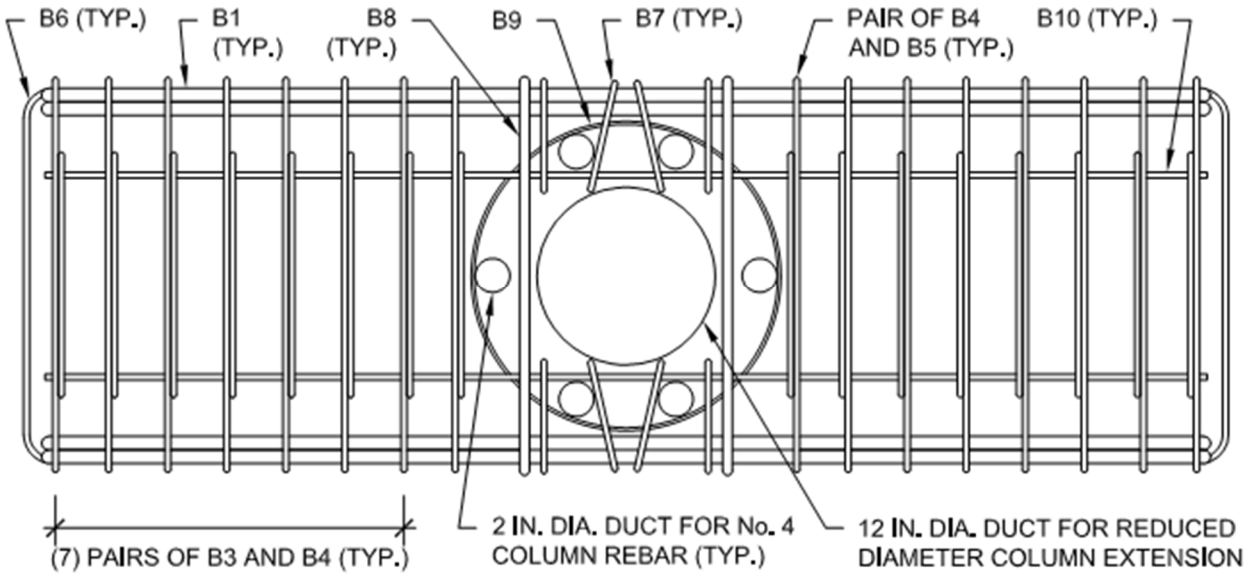

Figure B. 27 Cap beam reinforcement plan.

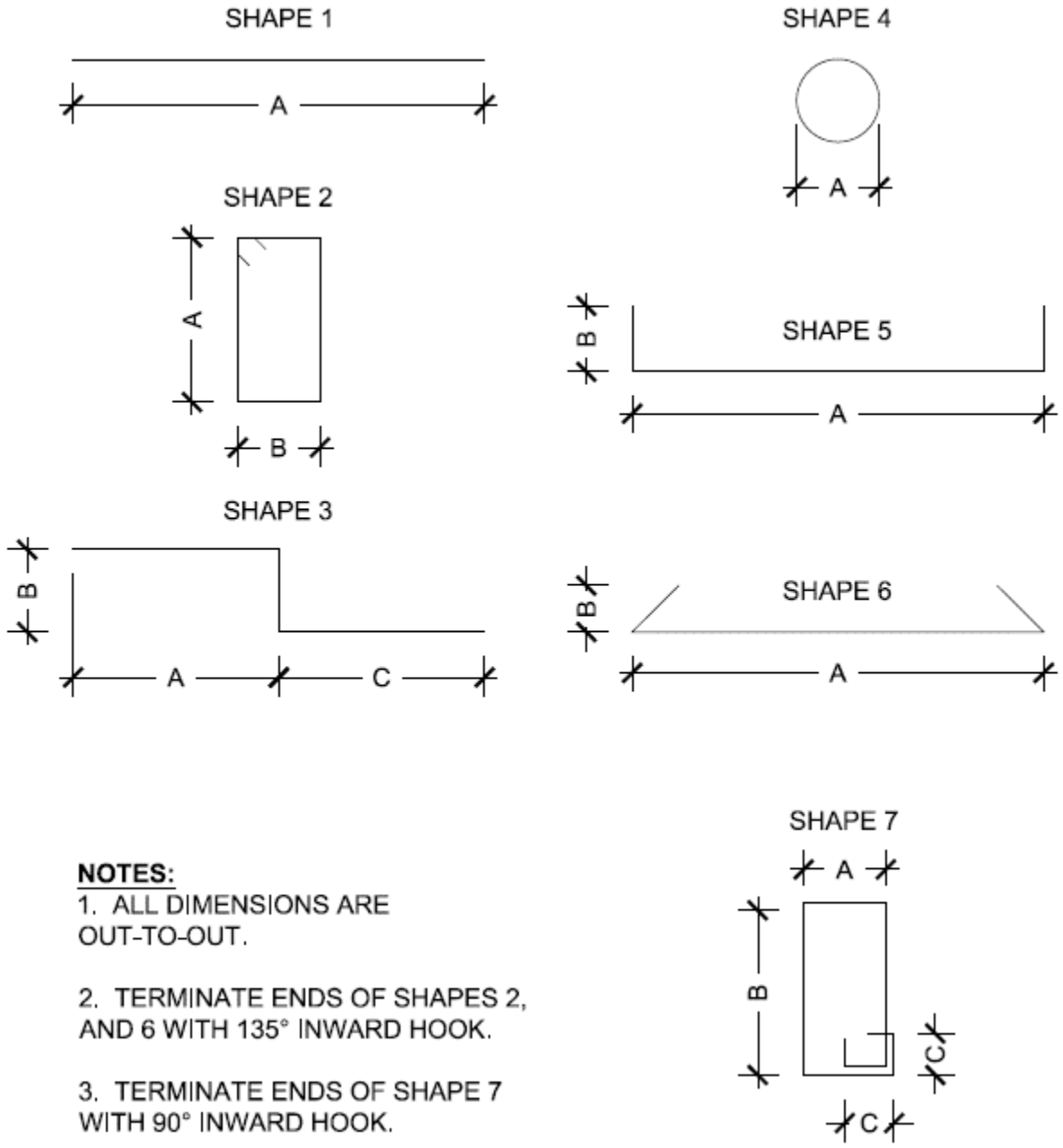

Figure B.28 Reinforcement shapes.

REBAR SCHEDULE

Table B.1 Reinforcing schedule.

Name	Qty.	Size	Shape	Dimensions (in.)			Notes
				A	B	C	
C1	2	No. 4	1	81.5	-	-	Column longitudinal reinforcement.
C2	4	No. 4	1	102	-	-	Column longitudinal reinforcement.
C3	4	No. 4	1	30	-	-	Additional reinforcement for reduced depth section.
C4	6	No. 6	1	44	-	-	One end plug-welded into steel baseplate.
C5	8	No. 3	2	17.25	9.5	-	Transverse reinforcement for reduced depth section.
C6	8	No. 3	2	12	9	-	Transverse reinforcement for reduced depth section.
C7	4	No. 3	3	13.75	3.5	20	Additional reinforcement for reduced depth section. Field bent to size and set into rebar cage.
C8	1	No. 3 AWG	4	18.3125	-	-	Tied in continuous spiral at 1.25 in. pitch. Extended from steel baseplate to reduced depth section of column.
C9	1	No. 3 AWG	4	9	-	-	Tied in continuous spiral at 1.25 in. pitch. Located in top 25 in. of column.
C10	1	No. 3 AWG	4	9	-	-	Tied in continuous spiral at 1.25 in. pitch. Located in bottom 37.5 in. of column.
B1	8	No. 7	5	74.75	14	-	Cap beam longitudinal reinforcement.
B2	8	No. 7	6	62	14	-	Cap beam longitudinal reinforcement.
B3	14	No. 3	2	36	25.5	-	Cap beam transverse reinforcement.
B4	16	No. 3	2	29	15.5	-	Cap beam transverse reinforcement.
B5	2	No. 3	2	29	25.5	-	Cap beam transverse reinforcement.
B6	8	No. 3	5	24.75	18	-	Cap beam end ties.
B7	8	No. 3	7	29	7.5	3.25	Joint transverse reinforcement.
B8	2	No. 5	5	25.5	14.5	-	Additional joint transverse reinforcement.
B9	25	No. 3 AWG	4	20	-	-	Tied in singular hoops at 1.25 in. O.C., full 31.5 in. height of cap beam. 10 in. end overlap.
B10	12	No. 3	1	75	-	-	Skin steel and cage steel.

Appendix C: Test Photos

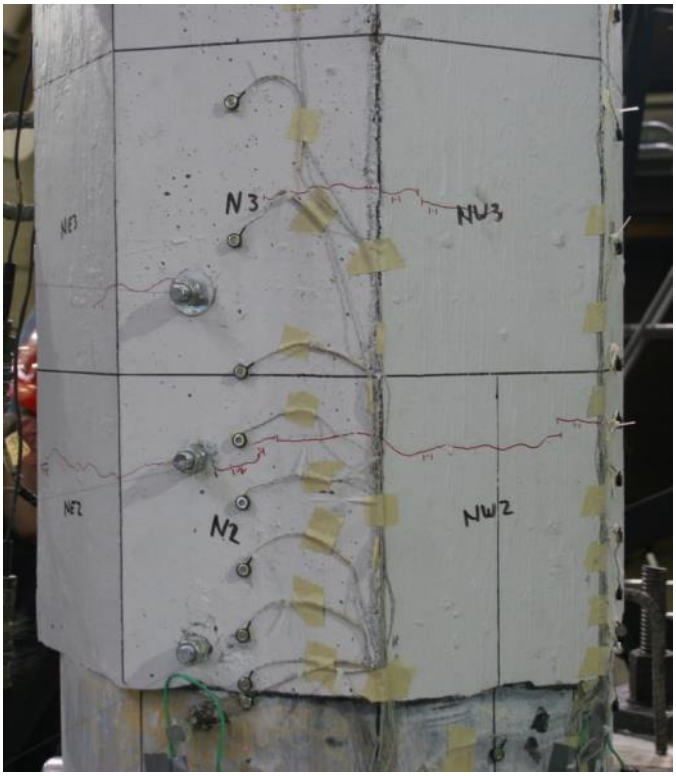

Figure C.1 Early hairline cracking in column. Most cracks remained hairline.

Figure C.2 Column rocking during peak (left) and valley (right) displacements of maximum drift ratios of test (±10.41%).

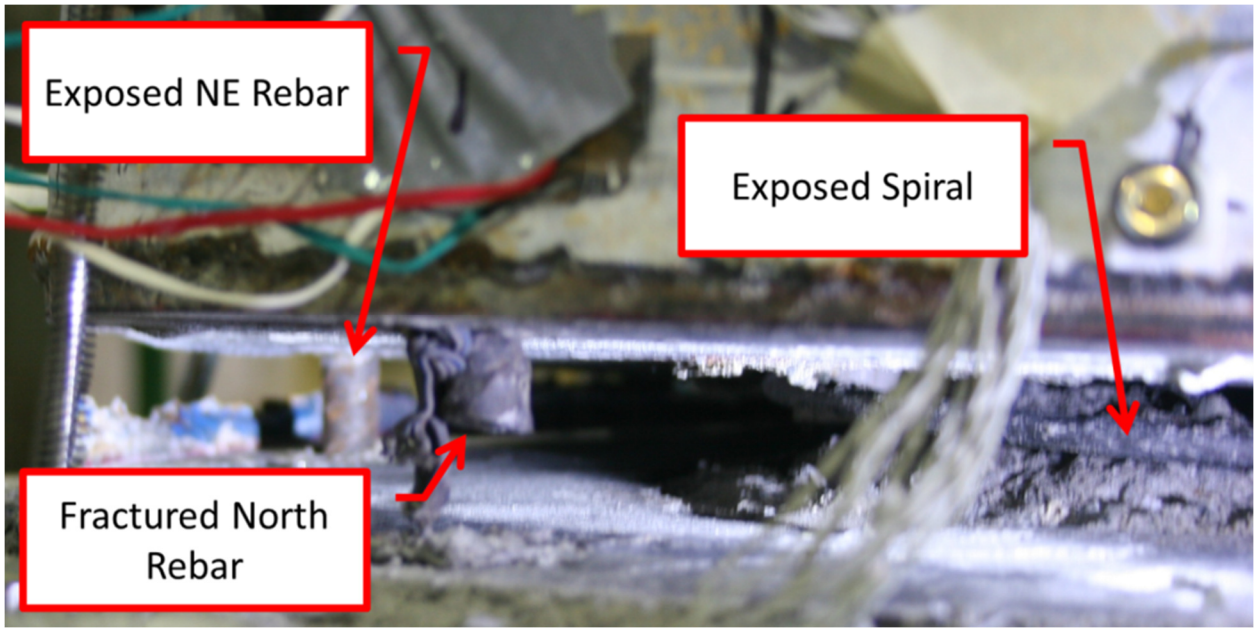

Figure C.3 Exposed and fractured reinforcement.

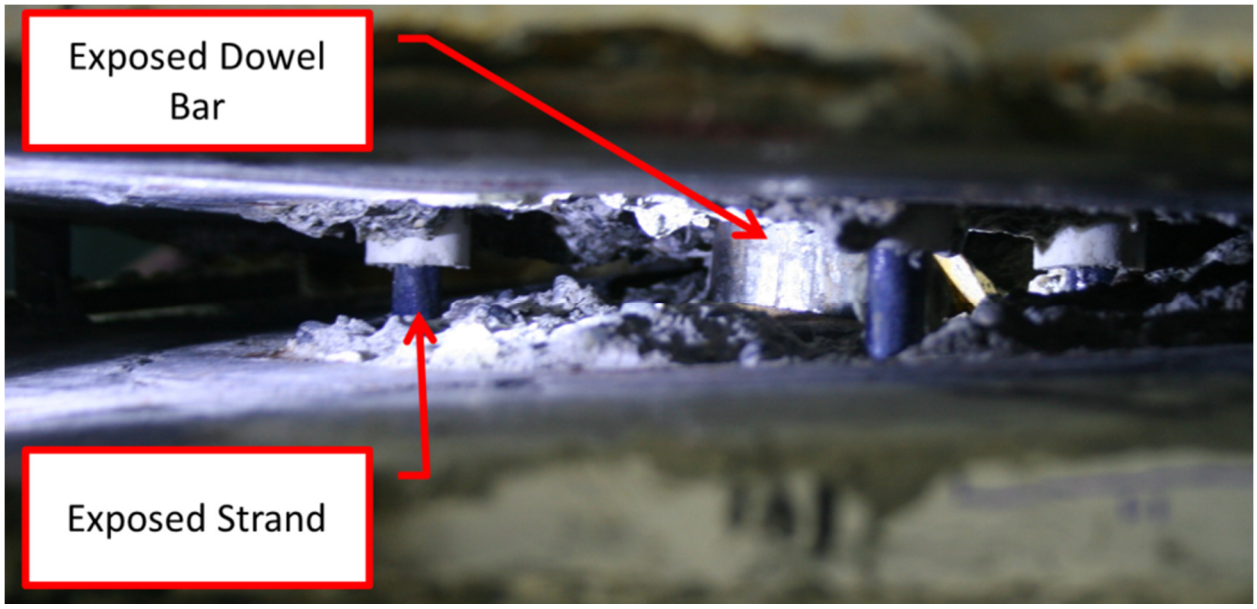

Figure C.4 Exposed dowel bar and prestressing strand.

Figure C.5 Grout pad at end of test.

Appendix D: Construction Photos

COLUMN

Figure D.1 Column cage and formwork (isometric).

Figure D.2 Steel tube region of column cage.

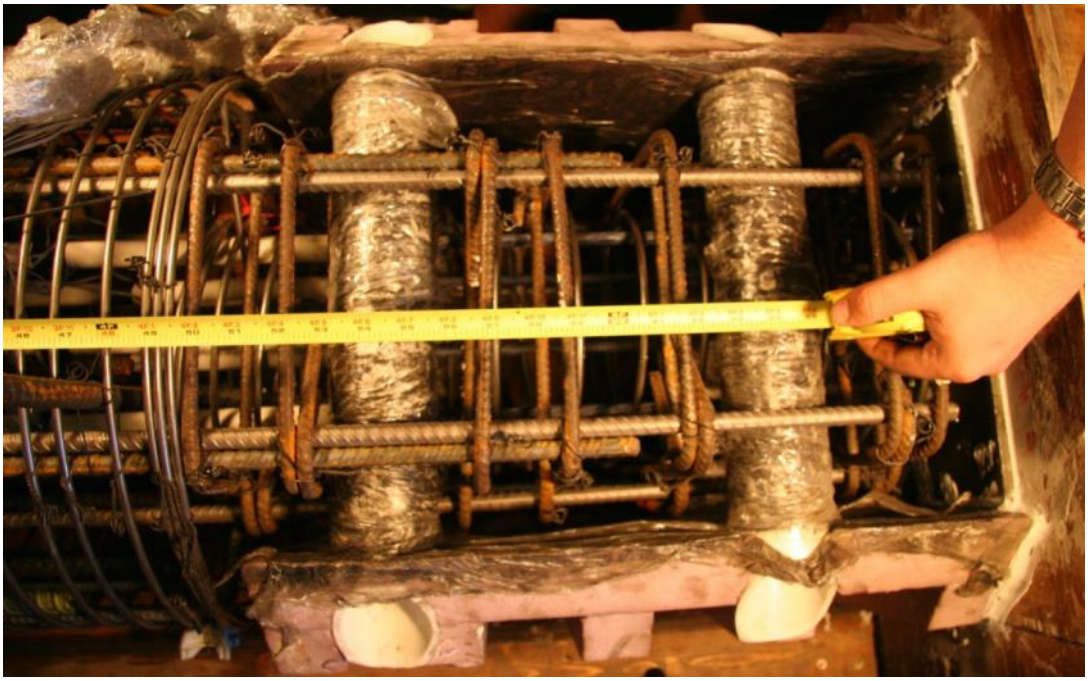

Figure D.3 Reduced depth segment for actuator attachment.

Figure D.4 Formwork for reduced diameter segment.

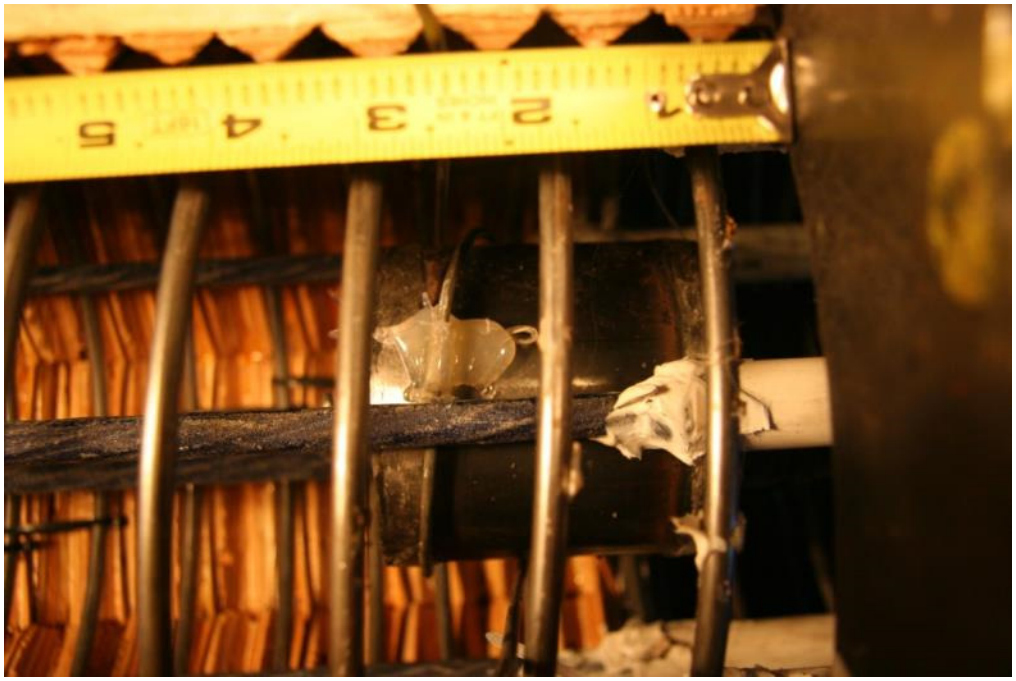

Figure D.5 Tubular housing for dowel bar.

Figure D.6 Crane lift of cast column.

CAP BEAM

Figure D.7 Cage elevation view.

Figure D.8 Cage isometric view.

Figure D.9 Cage end elevation.

Figure D.10 Cap beam ductwork.

Figure D.11 Cast cap beam isometric view.

Figure D.12 Socket connection ductwork.

SOCKET CONNECTION

Figure D.13 Fitting of column extensions into cap beam ducts.

Figure D.14 Placement of fiber-reinforced, ½ in. thick, grout pad.

Figure D.15 Column was dropped onto fresh grout, and material was allowed to squeeze out from gap.

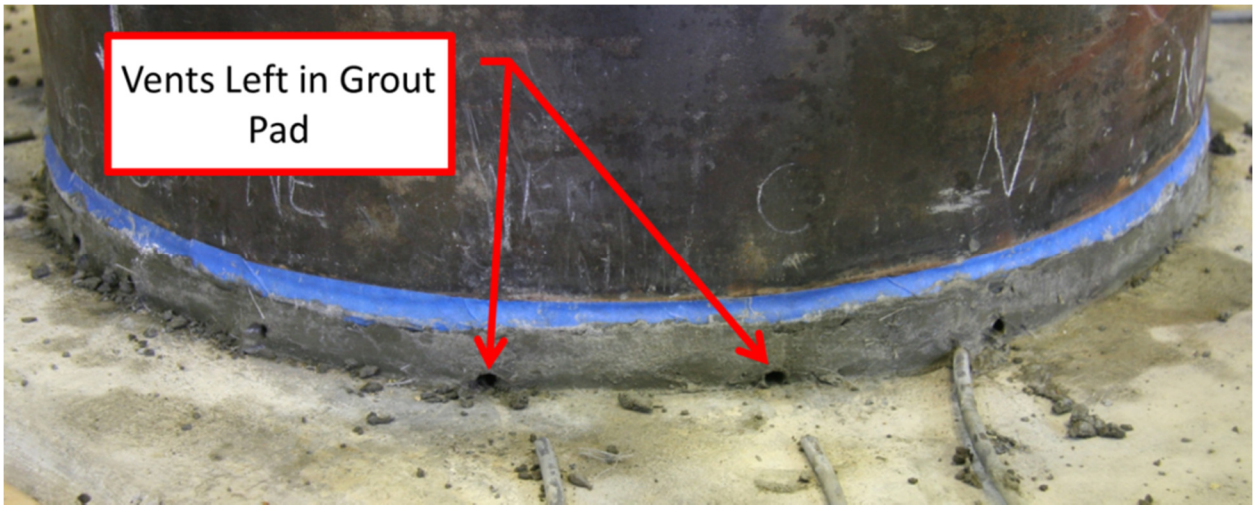

Figure D.16 After setting up, the perimeter of the pad was cut to the tube circumference and the tubes were removed, leaving vents in grout pad.

Figure D.17 Specimen during grout pumping operation.

Figure D.18 Grout was pumped into ducts until it flowed out of vents left in pad, which then filled temporary reservoirs formed on top of the cap beam.

Figure D.19 Grout was pumped into ducts until reservoirs outside of vents were filled. This overflowing grout was allowed to setup and was then removed.

Appendix E: Calculations

SPECIMEN		**PreT-CB-CONC**							
CROSS SECTION		20 in. wide octagon, reinforced with six No. 4 and six No. 6							
CALCULATION		Transformed Moment of Inertia, I_t							
MATERIAL PROPERTIES									
Steel Modulus of Elasticity		E_s	29000	ksi					
Concrete Modulus of Elast		E_c	4776	ksi					
Modular Ratio		n	6.072						
CONCRETE AREAS									
$Element_i$	b_i	h_i	y_i	A_i	y_i*A_i	$I_{i,self}$	$(y_i-y_c)^2$	A_{i*} x d_i^	$I_{i,total}$
1	8.2843	20	10	165.69	1656.9	5522.8	3E-30	5E-28	5522.8
2	5.8579	5.8579	16.095	17.157	276.14	32.708	37.146	637.33	670.03
3	5.8579	5.8579	16.095	17.157	276.14	32.708	37.146	637.33	670.03
4	5.8579	8.2843	10	48.528	485.28	277.54	3E-30	2E-28	277.54
5	5.8579	8.2843	10	48.528	485.28	277.54	3E-30	2E-28	277.54
6	5.8579	5.8579	3.9052	17.157	67.003	32.708	37.146	637.33	670.03
7	5.8579	5.8579	3.9052	17.157	67.003	32.708	37.146	637.33	670.03
STEEL AREAS									
$Element_i$	b_i	h_i	y_i	$A_{t,i}$	$y_i*A_{t,i}$	$I_{t,i,self}$	$(y_i-y_c)^2$	$A_{t,i*}$ x d_i^	$I_{t,i,total}$
8	0.5		1.375	1.2144	1.6698	0.0031	74.391	90.34	90.343
9	0.5		6.8125	2.4288	16.546	0.0061	10.16	24.677	24.683
10	0.5		13.188	2.4288	32.03	0.0061	10.16	24.677	24.683
11	0.5		18.625	1.2144	22.618	0.0031	74.391	90.34	90.343
NEGATIVE CONCRETE AREAS									
$Element_i$	b_i	h_i	y_i	A_i	y_i*A_i	$I_{i,self}$	$(y_i-y_c)^2$	A_{i*} x d_i^	$I_{i,total}$
-8	0.5		1.3125	-0.2	-0.263	-0.003	75.473	-15.09	-15.1
-9	0.5		5.6563	-0.4	-2.263	-0.003	18.868	-7.547	-7.55
-10	0.5		14.344	-0.4	-5.738	-0.003	18.868	-7.547	-7.55
-11	0.5		18.688	-0.2	-3.738	-0.003	75.473	-15.09	-15.1
RESULTS									
ΣA_i	337.46		$\Sigma I_{i,total+}$	8988.1					
Σy_i*A_i	3374.6		$\Sigma I_{i,total-}$	-45.3					
y_c	10		**I_t**	**8942.8**					

SPECIMEN		**PreT-CB-ROCK**							
CROSS SECTION		20 in. wide octagon, reinforced with six No. 4 and six No. 6							
CALCULATION		Transformed Moment of Inertia, I_t							
MATERIAL PROPERTIES									
Steel Modulus of Elasticity		E_s	31000	ksi					
Concrete Modulus of Elast		E_c	4930	ksi					
Modular Ratio		n	6.288						
CONCRETE AREAS									
$Element_i$	b_i	h_i	y_i	A_i	y_i*A_i	$I_{i,self}$	$(y_i-y_c)^2$	A_{i*} x d_i^	$I_{i,total}$
1	8.2843	20	10	165.69	1656.9	5522.8	0.0056	0.9337	5523.8
2	5.8579	5.8579	16.095	17.157	276.14	32.708	36.237	621.72	654.43
3	5.8579	5.8579	16.095	17.157	276.14	32.708	36.237	621.72	654.43
4	5.8579	8.2843	10	48.528	485.28	277.54	0.0056	0.2735	277.81
5	5.8579	8.2843	10	48.528	485.28	277.54	0.0056	0.2735	277.81
6	5.8579	5.8579	3.9052	17.157	67.003	32.708	38.067	653.12	685.83
7	5.8579	5.8579	3.9052	17.157	67.003	32.708	38.067	653.12	685.83
STEEL AREAS									
$Element_i$	b_i	h_i	y_i	$A_{t,i}$	$y_i*A_{t,i}$	$I_{t,i,self}$	$(y_i-y_c)^2$	$A_{t,i*}$ x d_i^	$I_{t,i,total}$
8	0.5		1.375	1.2576	1.7292	0.0031	75.691	95.19	95.193
9	0.5		6.8125	2.5152	17.135	0.0061	10.644	26.773	26.779
10	0.5		13.188	2.5152	33.169	0.0061	9.6872	24.365	24.372
11	0.5		18.625	1.2576	23.423	0.0031	73.101	91.933	91.936
12	0.75		2.125	5.5335	11.759	0.0311	63.204	349.74	349.77
13	0.75		10	5.5335	55.335	0.0311	0.0056	0.0312	0.0622
14	0.75		17.875	5.5335	98.911	0.0311	60.839	336.65	336.68
NEGATIVE CONCRETE AREAS									
$Element_i$	b_i	h_i	y_i	A_i	y_i*A_i	$I_{i,self}$	$(y_i-y_c)^2$	A_{i*} x d_i^	$I_{i,total}$
-8	0.5		1.3125	-0.2	-0.263	-0.003	76.783	-15.36	-15.36
-9	0.5		5.6563	-0.4	-2.263	-0.003	19.526	-7.81	-7.813
-10	0.5		14.344	-0.4	-5.738	-0.003	18.222	-7.289	-7.292
-11	0.5		18.688	-0.2	-3.738	-0.003	74.174	-14.83	-14.84
-12	0.75		2.125	-0.88	-1.87	-0.031	63.204	-55.62	-55.65
-13	0.75		10	-0.88	-8.8	-0.031	0.0056	-0.005	-0.036
-14	0.75		17.875	-0.88	-15.73	-0.031	60.839	-53.54	-53.57
RESULTS									
ΣA_i	351.68		$\Sigma I_{i,total+}$	9684.7					
Σy_i*A_i	3543.2		$\Sigma I_{i,total-}$	-154.6					
y_c	10.075		**I_t**	**9530.2**					

SPECIMEN		**PreT-SF-ROCK**							
CROSS SECTION		20 in. wide octagon, reinforced with six No. 4 and six No. 6							
CALCULATION		Transformed Moment of Inertia, I_t							
MATERIAL PROPERTIES									
Steel Modulus of Elasticity			E_s	29100	ksi				
Concrete Modulus of Elast			E_c	5620	ksi				
Modular Ratio			n	5.1779					
CONCRETE AREAS									
$Element_i$	b_i	h_i	y_i	A_i	y_i*A_i	$I_{i,self}$	$(y_i-y_c)^2$	A_{i*} x d_i^	$I_{i,total}$
1	8.2843	20	10	165.69	1656.9	5522.8	0.0058	0.9567	5523.8
2	5.8579	5.8579	16.095	17.157	276.14	32.708	36.226	621.53	654.24
3	5.8579	5.8579	16.095	17.157	276.14	32.708	36.226	621.53	654.24
4	5.8579	8.2843	10	48.528	485.28	277.54	0.0058	0.2802	277.82
5	5.8579	8.2843	10	48.528	485.28	277.54	0.0058	0.2802	277.82
6	5.8579	5.8579	3.9052	17.157	67.003	32.708	38.078	653.32	686.03
7	5.8579	5.8579	3.9052	17.157	67.003	32.708	38.078	653.32	686.03
STEEL AREAS									
$Element_i$	b_i	h_i	y_i	$A_{t,i}$	$y_i*A_{t,i}$	$I_{t,i,self}$	$(y_i-y_c)^2$	$A_{t,i*}$ x d_i	$I_{t,i,total}$
8	0.5		1.375	1.0356	1.4239	0.0031	75.707	78.401	78.405
9	0.5		6.8125	2.0712	14.11	0.0061	10.65	22.059	22.065
10	0.5		13.188	2.0712	27.314	0.0061	9.6815	20.052	20.058
11	0.5		18.625	1.0356	19.288	0.0031	73.086	75.686	75.69
12	0.75		2.125	4.5566	9.6827	0.0311	63.218	288.06	288.09
13	0.75		10	4.5566	45.566	0.0311	0.0058	0.0263	0.0574
14	0.75		17.875	4.5566	81.449	0.0311	60.825	277.15	277.18
NEGATIVE CONCRETE AREAS									
$Element_i$	b_i	h_i	y_i	A_i	y_i*A_i	$I_{i,self}$	$(y_i-y_c)^2$	A_{i*} x d_i^	$I_{i,total}$
-8	0.5		1.3125	-0.2	-0.263	-0.003	76.799	-15.36	-15.36
-9	0.5		5.6563	-0.4	-2.263	-0.003	19.534	-7.814	-7.817
-10	0.5		14.344	-0.4	-5.738	-0.003	18.214	-7.286	-7.289
-11	0.5		18.688	-0.2	-3.738	-0.003	74.158	-14.83	-14.83
-12	0.75		2.125	-0.88	-1.87	-0.031	63.218	-55.63	-55.66
-13	0.75		10	-0.88	-8.8	-0.031	0.0058	-0.005	-0.036
-14	0.75		17.875	-0.88	-15.73	-0.031	60.825	-53.53	-53.56
RESULTS									
ΣA_i	347.41		$\Sigma I_{i,total+}$	9521.5					
Σy_i*A_i	3500.5		$\Sigma I_{i,total-}$	-154.6					
y_c	10.076		**I_t**	**9367**					

Appendix F: Experimental Instrumentation

This appendix details some of the instrumentation that was used for the experiment.

STRAIN GAUGES

The application procedure used to apply strain gauges to reinforcing bars has the potential to affect the performance and behavior of the bar. A general summary of this procedure follows:

1. Mill or grind flat spot on bar (and then polish) for the application of strain gauge. See Figure E.1.

Figure E.1 Milled and polished spot on rebar for application of strain gauge.

2. Adhere strain gauge to bar with cyanoacrylate.
3. Coat strain gauge with waterproofing. See Figure E.2

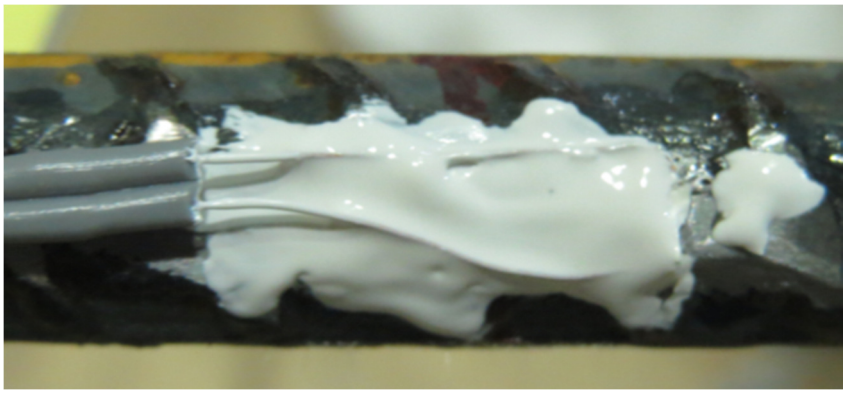

Figure E.2 Waterproof coating applied to back of strain gauge and folded over lead wires.

4. Wrap with contact tape. See Figure E.3.

Figure E.3 Waterproof coating applied to strain gauge and folded over lead wires.

This instrumentation process was selected because it produces good results (due to the polishing of the bar) and the gauge is protected while the bar slips through the surrounding concrete (due to the wrapping of tape), which extends the life of the gauge. However, the process results in a net reduction in the cross-sectional area of the bar (due to the milling), and the rebar is effectively debonded for a length of approximately 1 in. (due to the tape wrap).

OPTOTRAK MOTION CAPTURE SYSTEM

A motion capture system was used to measure the kinematics of the specimen. The system tracked the positions of LED targets with two three-dimensional cameras. The system was acquired from Northern Digital Inc. (NDI), their Optotrak Certus® Motion Capture System.

The system has a 3D accuracy of 0.1 mm, and a resolution of 0.01 mm (Northern Digital Inc., 2014). An analysis was completed in order to determine if the Optotrak camera could detect rotations caused by hairline cracking within the column. An individual, hairline crack (first observed during the peak drift of Set 7-Cycle 2), was examined for this analysis. The crack was at a column elevation of approximately 29 in., in-between the top two Optotrak targets. The crack is identified in Figure E.4.

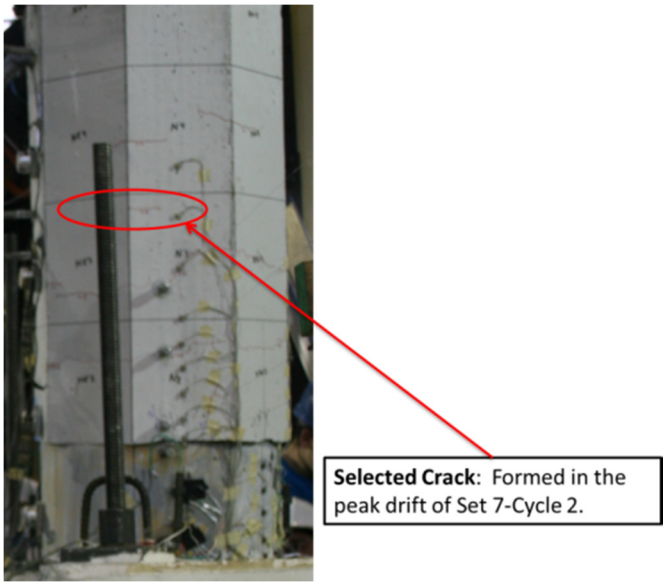

Figure E.4 Identification of hairline crack for Optotrak resolution analysis.

The rotation record (measured by the Optotrak targets and calculated with the process described in Section 5.5.3) is given in Figure E.5. The difference in rotation record between the two pairs of LED targets is given in Figure E.6.

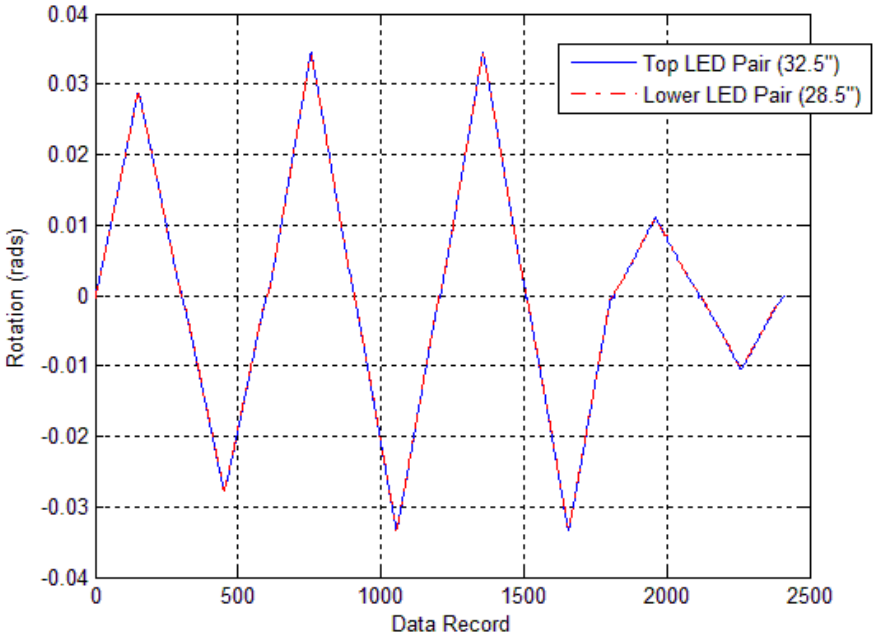

Figure E.5 Rotation records for Set 7-Cycle 2 for the target rows above and below hairline crack.

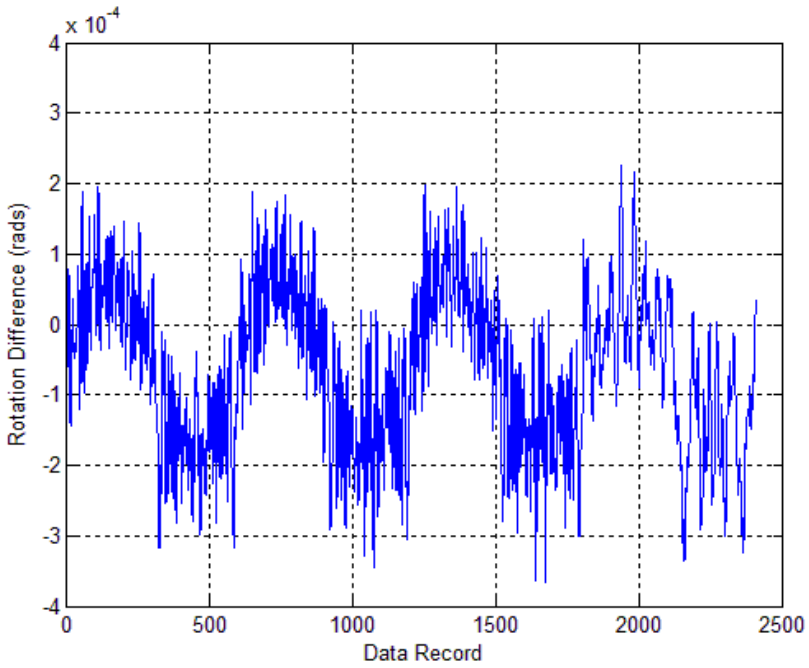

Figure E.6 Difference in rotation record between two LED target rows.

This result of this analysis (the lack of any distinct "jump" in the difference between the rotation records) suggests that the Optotrak cameras used in this experiment were not able to detect rotations caused by individual, hairline cracking.

MEASUREMENT OF COLUMN TOP DISPLACEMENT

The drift of the column was determined using the displacement recorded by the LVDT in the horizontal MTS actuator. The readings from the LVDT were corrected by subtracting the deflection of the beam that supported the actuator. That displacement was measured with a linear potentiometer that was attached to a stationary reference tower. The actuator LVDT was used for the top column displacement because it offers finer data resolution than string potentiometers. However, the data from a string potentiometer attached at the point of horizontal load application can be compared to the corrected readings from the LVDT in the actuator. Figure E.7 plots these two displacement measurements. The strong correlation between these two independent measurements suggests that the displacement of the top of the column was properly measured throughout the test.

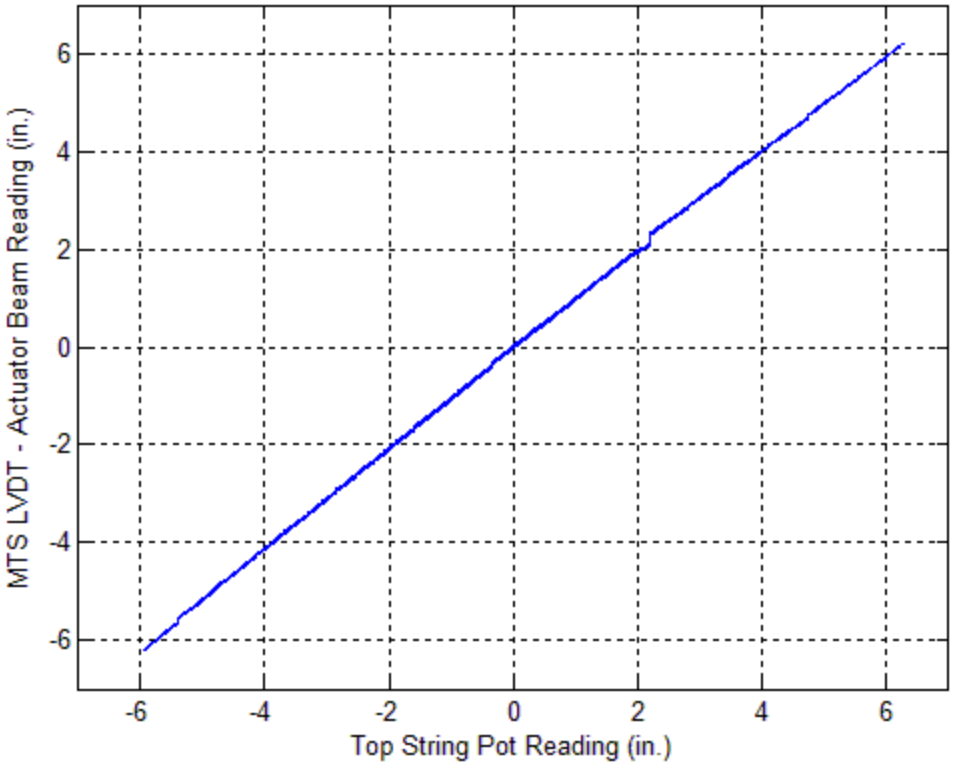

Figure E.7 Displacement measured by top string potentiometer vs. actuator LVDT (after correcting for deflection of rig).